DISSERTATION

STUDY AND DESIGN OF MINIMALLY INSTRUMENTED MICROFLUIDIC UNIT OPERATIONS FOR A PORTABLE BIOSENSOR: MIXING, PUMPING, AND REACTION

Submitted by

Nicholas Scott Lynn Jr.

Department of Chemical and Biological Engineering

In partial fulfillment of the requirements

For the Degree of Doctor of Philosophy

Colorado State University

Fort Collins, Colorado

Summer 2009

COLORADO STATE UNIVERSITY

June 25, 2009

WE HEREBY RECOMMEND THAT THE DISSERTATION PREPARED UNDER OUR SUPERVISION BY NICHOLAS SCOTT LYNN JR. ENTITLED STUDY AND DESIGN OF MINIMALLY INSTRUMENTED MICROFLUIDIC UNIT OPERATIONS FOR A PORTABLE BIOSENSOR: MIXING, PUMPING, AND REACTION BE ACCEPTED AS FULFILLING IN PART REQUIREMENTS FOR THE DEGREE OF DOCTOR OF PHILOSOPHY.

Committee on Graduate Work

Laurence Belfiore

Kenneth F. Reardon

Charles S. Henry

Advisor and Department Head: David S. Dandy

ABSTRACT OF DISSERTATION

STUDY AND DESIGN OF MINIMALLY INSTRUMENTED MICROFLUIDIC UNIT OPERATIONS FOR A PORTABLE BIOSENSOR: MIXING, PUMPING, AND REACTION

This research involves the detailed study and design of several microfluidic unit operations that combined together, passively deliver analyte to a local, evanescent array coupled (LEAC) sensor. Specifically, this dissertation is focused on minimally instrumented mixing, pumping, and heterogeneous reaction strategies regarding fluids confined to microchannels whose widths and heights are less than 100 microns. These microfluidic platforms present many advantages over their traditional macroscale counterparts, including reduced sample volumes, analysis times, costs, and overall device size. The minimally instrumented unit operations studied in this dissertation work such that no external control is required and power inputs are small enough to be handled by small battery systems. When combined with the LEAC sensor, the unit operations within this dissertation will provide a unique device able to detect a wide variety of biological markers or small molecules with a high degree of portability.

For microfluidic mixing, both the optimization of previous mixing methods as well as the development of a novel mixing strategy are studied in detail. Previously, there have been several reports involving microfluidic mixing via the creation of helical flow in microchannels from a series of patterned grooves on the channel floor. Due to the

enhancement of surface effects at the microscale, these grooves remain a state of the art method to induce chaotic flows within a pressure driven system. Here a new geometrical factor is presented that significantly affects the strength of helical flow over patterned grooves. By varying the ratio of the length of the grooves to the neighboring ridges, helical flow can be optimized for a given groove depth and channel aspect ratio, with up to 50% increases in transverse flow possible. A full numerical study of over 700 cases details the magnitude of helical flow over unsymmetrical patterned grooves in a slanted groove micromixer, where the optimized parameters for the slanted groove mixer can be translated to the staggered herringbone mixer. The optimized groove geometries are shown to have a large depend strongly on the channel aspect ratio, the groove depth ratio, and the ridge length.

Furthermore, a new micromixer that utilizes integrated electrodes to induce a localized, perpendicular electric field within pressure driven axial flow is presented. The presence of the electric field drives electro-osmotic flow in the transverse direction along the channel walls, creating helical motion that serves to mix the fluid. A numerical model is used to describe the three-dimensional flow field, where characterization is performed via particle tracking of passive tracer particles, and the conditional entropy is utilized to approximate the extent of mixing within cross-sectional planes. The geometrical parameters and operating conditions of the numerical model are used to fabricate an experimental device, and fluorescence microscopy measurements are used to verify mixing of rhodamine B across the width of the microchannel for a wide range of fluid flow rates. The results demonstrate that under certain operating conditions and selective placement of the electrode gaps along the width of the microchannel, efficient mixing can be achieved within 6 mm of the inlet.

As a result of very large surface area to volume ratios, evaporation is of significant importance when dealing with microfluidic devices that possess open air/liquid interfaces. For devices utilizing a reservoir as a fluid delivery method to a microfluidic

network, excessive evaporation can quickly lead to reservoir dry out and overall device failure. Predicting the rates of evaporation from these reservoirs is difficult because the position of the air/liquid interface changes with time as the volume of liquid in the reservoir decreases. Here a two-step method to accurately predict the rates of evaporation of such an interface over time is presented. First, a simple method is proposed to determine the shape of an air/liquid meniscus in a reservoir given a specific liquid volume. Second, computational fluid dynamics simulations are used to calculate the instantaneous rate of evaporation for that meniscus shape. It is shown that the rate of evaporation is strongly dependent on the overall geometry of the system, enhanced in expanding reservoirs while suppressed in contracting reservoirs, where the geometry can be easily controlled with simple experimental methods. Using no adjustable parameters, the model accurately predicts the position of the inner moving contact line as a function of time following meniscus rupture in poly(dimethylsiloxane) reservoirs, and predicts the overall time for the persistence of liquid in those reservoirs to within 0.5 minutes. The methods in this study can be used to design holding reservoirs for lab-on-a-chip devices that involve no external control of evaporation, such that evaporation rates can be adjusted as necessary by modification of the reservoir geometry.

Controlled pumping of fluids through microfluidic networks is perhaps the most important unit operation within microfluidic based applications. Although there have been a number of studies involving the creation of passive flows within lab-on-a-chip devices, none have shown the ability to create temporally stable flows for periods longer than several minutes. In this study, a passive pumping approach is presented in which a large pressure differential arising from a small, curved meniscus situated along the bottom corners of an outlet reservoir serves to drive fluid through a microfluidic network. The system quickly reaches steady state and is able to provide precise volumetric flow rates for periods lasting over an hour. A two-step mathematical model provides accurate predictions of fluid and mass transport dynamics in these devices, as validated by particle

tracking in laboratory systems. Precise flow rates spanning an order of magnitude are accomplished via control of the microchannel and outlet reservoir dimensions. This flow mechanism has the potential to be applied to many micro-total analytical system devices that utilize pressure-driven flow; as an illustrative example, the pumping technique is applied for the passive generation of temporally stable chemical gradients.

Lastly, the dynamics of a complete device utilizing microfluidic delivery of analyte to a sensor surface are explored. The use of microfluidic passive pumping methods for the capture of analyte molecules onto the LEAC sensor has the potential to greatly aid in the development of a simple, robust, point-of-care diagnostic device. Unfortunately, devices involving multiple binding regions concerning similar analytes suffer from the formation of an analyte concentration boundary layer adjacent to the sensor surface. As a result, the time required to achieve equilibrium hybridization states for all binding surfaces is strongly dependent on both the convective flow conditions within the microchannel and the geometry of the channel itself. For optimal assay times that utilize minimal sample volumes, there is a delicate balance between the convective flow rate through the microchannel and potential for interaction between the analyte and sensor surface. This dissertation explores the relationships between microchannel geometries and assay response via computational fluid dynamics.

Nicholas Scott Lynn Jr.
Department of Chemical and Biological Engineering
Colorado State University
Fort Collins, Colorado 80523
Summer 2009

ACKNOWLEDGEMENTS

I would like to acknowledge my advisor, Dr. David Dandy, and my committee members, Dr. Kenneth Reardon, Dr. Laurence Belfiore, and Dr. Charles Henry, for their time and input throughout the project. I would also like to extend my thanks to Dr. Dandy for his support, guidance, and trust through the last five years. I am certain that both this dissertation and my scientific abilities would not be the same if I was not afforded the freedoms granted to me during my stay under his watch. It has been an honor and a privilege to work with Dr. Dandy.

I would like to thank Claire Lavelle and Marilyn Gross for their limitless patience with my numerous and prolonged visits to Glover 100, "is Dave in?" I would also like to thank Dr. Derek Johnson for his friendship, advice, and technical guidance over the initial years of my graduate career. Thanks also to the members of the Henry and Reardon labs, both past and present, for their assistance and friendship through the years. I

I would like to extend my deepest thanks to Stephen Gensits, my high school chemistry teacher. In addition to his seemingly perfected teaching method, "Mr. G." possessed unparalleled levels of enthusiasm, approachability, and willingness to go the extra mile. In my 25+ years as a student he undoubtedly remains the greatest teacher I have ever had the privilege of studying under. If it were not for the two years I had spent in his classroom, I am certain that either I would have never moved to study the physical sciences in college – nor if I would have enrolled in college at all.

Finally, I would like to thank all my family and friends who have provided me with countless hours of entertainment guided me through the ups and downs all these years. And a very special thank you to my wife and best friend, Christina, for all of her love, encouragement, and support through the last 5 years. Enrolling in graduate school is perhaps the best decision I have ever made. Without you, this would have never happened. I owe you the world.

TABLE OF CONTENTS

Chapter 1

Introduction

1.1 Motivation

By providing accurate and timely care for patients, ensuring the safety of blood supplies, and contributing to short- and long-term public health care strategies, diagnostics play critical roles in health care in both the developed and undeveloped world.[1] Diagnostic devices for health care vary in their capabilities, including the detection of biomarkers associated with cancer, cardiovascular and sexually transmitted diseases, the isolation and identification of infectious microbes or viruses, the detection of genetic disease markers, and the detection of toxic compounds in aqueous media or blood serum. In the developed world, traditional diagnostic tests are typically carried out in centralized laboratories by trained technicians using expensive, specialized equipment. Although there exists a large effort to develop hardware and software technologies to automate these processes, laboratory environments are still required and associated costs remain high.[2] In addition, the time between sample collection (e.g., blood, saliva, urine) and eventual diagnosis is often on the order of days to weeks. Traditional diagnostics can demand whole blood sample volumes of $O(100)$ mL, and human-induced errors concerning sample storage, pretreatment, and processing are the most problematic steps in the entire diagnostic process.[3] It is therefore desirable to develop diagnostic instruments that combine all the aspects of a traditional laboratory assay into a single device for use in point-of-care (POC) settings. These assay steps include sample handling, pretreatment, and separation as well as signal transduction and detection. Areas

of focus for these instruments include accuracy, reliability, portability, automation, low power requirements, low sample volume requirements, and high degrees of robustness.[4]

In the past decade a large amount of work has been dedicated to the miniaturization of individual unit operations that when combined, recreate the multiple steps included in a variety of clinical assays. These unit operations are carried out on a microfluidic platform, where traditional microfabrication processes are utilized to create microchannels with characteristic lengths ranging from 1 to 1000 μm for the containment and delivery of fluid volumes ranging from 10^{-6} to 10^{-15} L.[5, 6] Initial research in microfluidic systems focused on gas chromatography or capillary electrophoresis in microchannels fabricated from glass or silicon with either dry or wet etching procedures.[7, 8] These early systems, although successful in operation, are expensive and generally require advanced microfabrication technologies and use of a semiconductor processing clean room. Work on microfluidic analysis systems was fairly stagnant until the late 1990s, when the development of soft lithography allowed the rapid fabrication of microfluidic channel networks (μFN) using simple procedures in a traditional laboratory.[9] Since this pioneering work, interest in microfluidics has been explosive, as there are currently several journals and conferences dedicated to the subject. Peer-reviewed articles on microfluidics currently number well above 1500 articles per year.

Due to their inherent high surface area to volume ratios, microfluidic platforms present many advantages over their traditional macroscale counterparts. These advantages include reduced sample volume requirements, reduced times for sample analysis, reduced cost as devices are scaled out, precise control over temperature with low power consumption, and a reduction in the overall device size. Furthermore, transport and electronic phenomena on the microfluidic scale are well understood, allowing for accurate prediction and optimization of devices without the need for laboratory experiment.[10] Due to these many benefits, microfluidic systems are currently

utilized nearly universally within the fields of physical, medical, and biological sciences for a variety of applications.

The development of microfluidics for analytical and diagnostic purposes is analogous to that of micro-electro-mechanical systems (MEMS). Although many of the fabrication methods utilized to create application-specific MEMS had been developed by the middle half of the 20th century, it was not until 1982 that a combination of micro-mechanical functions were integrated with electronic components to create a working device.[11] Similarly, the integration of microfluidic unit operations to form a complete analytical package did not occur until the mid 1990s, nearly 15 years after the seminal work on microfluidics. Systems integrating multiple microfluidic unit operations onto a single device have since been termed micro-total-analysis-systems (μTAS) or lab-on-a-chip (LOC) devices. Due to the advantages inherent to microfluidic systems, these devices have the potential to increase the availability and reliability of POC diagnostics in multiple locations, including (*i*) centralized hospitals and first response emergencies, (*ii*) offices of the primary care physician, (*iii*) home testing via disposable kits, and (*iv*) low-resource settings in developing countries.

The small characteristic size of microchannels and LOC devices is not without drawbacks, as multiple phenomena can contribute to potential device failure: these include the effects of evaporation, fluid leakage, and unwanted introduction of particulate matter, gas bubbles, or emulsions. Furthermore, since surface chemistry plays an enhanced role within microfluidic systems, increased attention must be paid to the fabrication processes for devices to possess high repeatability. Nevertheless, there has been significant progress towards addressing these issues, and interest in the field remains very high.

As a part of a multidisciplinary project, this work is concerned with the detailed study, design, and optimization of microfluidics based unit operations regarding analyte delivery to a local, evanescent array coupled (LEAC) sensor. Specifically, this

dissertation is focused on mixing and pumping strategies in microchannels of heights and widths less than 50 μm that can be easily integrated with the LEAC technology. This dissertation details the operational requirements of such a device when applied to heterogeneous affinity interactions between the sensing surface and the aqueous solutions containing an analyte of interest. In parallel to this work, the department of electrical engineering has focused on the design, fabrication, and operation of the LEAC sensor and the study of its capabilities and limitations. The department of chemistry has focused on methods to perform heterogeneous immunoassays on the silicon nitride surface of the LEAC sensor. Details of these parallel efforts can be found in the literature.[12-15]

1.2 Microfluidic Unit Operations

As with their traditional macroscopic counterparts, LOC devices are composed of a series of individual fluidic unit operations that when combined in an appropriate manner, complete an application-specific chemical process utilizing the fundamentals of separation, reaction, and detection.[16] In the case of diagnostic or analytical assays, these unit operations generally include fluid storage, pretreatment, pumping, metering, mixing, dilution, and concentration along with heat exchangers, chemical reactors, separation units, and appropriate valve units. The small length scales associated with microfluidic devices present several challenges with the design of each unit operation. For aqueous fluids with density ρ and viscosity μ, obtainable linear velocities v in a microchannel of width w, height h, and hydraulic diameter $D_h = 4wh/(2w+2h)$ will be such that the Reynolds number $Re = \rho D_h v/\mu < 1$ and the fluid will be well within the laminar regime; therefore, reaction and mixing chambers need to be designed to work without the enhanced mixing characteristics of turbulent flow. Futhermore, soft lithographic fabrication procedures generally prohibit the utilization of moving parts, functionalities that are vital to macroscale valves, pumps, and other devices. Unless expensive three dimensional micro-milling machines are available, all unit operations must be designed

using the "bottom up" methodology utilizing standard microfabrication procedures. Despite these difficulties, there has been a tremendous amount of work dedicated to a wide variety of fundamental microfluidic unit operations. Several important microfluidic unit operations are briefly discussed here, and more information can be found in a variety of reviews.[17-22]

1.2.1 A Note on Paper Based LOC Devices

This dissertation is limited to unit operations for microfluidic LOC devices and does not include material concerning capillary driven test strips or paper based microfluidics. Paper based LOC diagnostic devices, such as those seen in home pregnancy test kits, have been in commercial use for more than 40 years; however, little to no information concerning the details of these devices exists in the literature.[23] There has, however, been an upsurge in studies focused on the fabrication and operation of these types of devices in recent years,[24] as advantages of portablility, low cost, and ease of use of such devices remains extremely high. Although these devices have great potential for advanced LOC systems, they possess numerous complexities inherent to the paper structures composing the fundamental unit operations of each device. Methods of detection are generally limited to electrochemical and colorimetric methods, as the capillary forces present within the test strip and the optical opacity of the paper precludes the use of analytics based on optical and electrokinetic phenomena. Futhermore, these devices are generally limited to a single biomarker present in relatively high concentrations and as such are limited to hormones, antibodies, or abundant pathogenic antigens.[25] Continuous flow in these devices is limited in time by the total volume of the test strip, and there is generally low sample-to-sample repeatability and sensitivity. Numerous reviews on this subject can be found in the literature.[26, 27]

1.2.2 Microfluidic Pumping

Methods for fluid pumping and metering are perhaps the most studied, as well as most complex, unit operation for microfluidic devices. Encompassing a very wide region of research, a review on microfluidic pumping methods is beyond the scope of this dissertation; however, there are several thorough reviews on the subject.[18, 19] Microfluidic pumping methods are generally classified as active or passive. Active (or actuated) pumping mechanisms utilize external power sources or pumps, pressurized chambers, mechanical actuation, or electrokinetic phenomena to drive fluid between neighboring regions of a device. These active methods encompass a wide variety of mechanisms and can provide large dynamic ranges of flow (nL min^{-1} to mL min^{-1}) for extended periods of time (hours to days), where the flow rates can be modulated with time. Active pumping methods are by far the most common mode of fluid transport within LOC devices; however, nearly all require bulky equipment (e.g., power sources, syringe pumps) or complex fabrication methods, restricting the portability and cost of such devices.

In contrast, flow within devices utilizing passive pumping methods requires no external equipment, where the eventual dynamics of flow are a function of the microchannel geometry, surface chemistry, and external conditions. Temporal modulation of the flow is not available on demand for these methods, although some systems can be designed such that the flow is modulated passively.[28] Traditional mechanisms for passive microfluidic flows include surface tension forces,[29, 30] evaporation,[31, 32] osmotic pressures,[33] and fluid permeation into the microchannel.[34, 35] These devices are spontaneous in nature and require only fluid delivery to an inlet region, most commonly a micro-reservoir. Previously, there has been a gap in the ability for passive pumping mechanisms to deliver constant flow rates for extended periods of time. Chapter 4 details the design and operation of a new passive pumping method that possesses both of these crucial traits.

1.2.3 Microfluidic Mixing

Along with microfluidic pumping, mixing is often a necessary unit operation in LOC devices. Because of the lack of turbulent flows, mixing in microfluidic systems becomes dominated by molecular diffusion unless something is done to modify the dynamics of flow. Traditional fabrication methods for microfluidic systems are generally planar, thus when two fluid streams are combined into one, occurring at a T-junction, the two streams initially remain segregated and the important dimension of the system is the channel width. For continuous flow systems it is useful to estimate the axial channel length for a fluid stream to be regarded as well mixed. Typically, the mass transfer Péclet number $Pe = vw/D$ is very high for microfluidic systems containing a solute with molecular diffusivity D. The time for a solute to diffuse across the channel width is on the order of $t_{mix} \propto w^2/D$, and it follows that the axial channel mixing length is $L_{mix} \propto w \cdot Pe$. For solutions containing high molecular weight solutes such as deoxyribonucleic acid (DNA), ribonucleic acid (RNA), or large proteins, molecular diffusion coefficients are inherently small ($D < 10^{-10}$ m^2 s^{-1}) and axial mixing lengths become impractically large. In addition to reducing the overall length of a μFN, a shorter mixing length allows for faster analysis times regarding homogeneous reaction systems, a reduction in required sample volumes, and a reduction in Taylor dispersion along the axial length of the microchannel.

To reduce this mixing length, the microchannel components must be stirred in a manner such that the area of interfacial contact for two initially segregated streams is increased as a function of the axial distance. In the best case scenario a microfluidic mixing mechanism produces a chaotic flow profile, where even though the velocity field $\mathbf{v} = \mathbf{v}(x, y, z, t)$ can be predicted throughout the device, one-dimensional integration of the velocity field along fluid streamlines yields non-deterministic results. In this optimal case, the mixing length then scales as $L_{mix} \propto \log(Pe)$ and the overall length of the microchannel is substantially reduced.[36] Active mixing strategies utilize numerous

mechanisms, including electroosmotic, electrophoretic, electrohydrodynamic, and magnetohydrodynamic phenomena, as well as temporal pressure pertebations. In contrast, passive mixing strategies rely on the geometry of the device to perturb the fluid streamlines into a mixing state. These strategies are generally based on channel geometries that stir the fluid within a planar microchannel or channel arrangements such that the fluid is systematically split and recombined. There are several reviews dedicated to the study of microfluidic mixing strategies.[20, 22, 37] Chapter 2 details the geometrical optimization of the staggered herringbone mixer (SHM), a passive micromixing method introduced in 2002 by Stroock *et al.* that remains state of the art.[38] Chapter 3 details the fabrication and optimization of a new microfluidic mixing method, which combines axial pressure driven flow with transverse electroosmotic flows to rapidly mix fluids in microchannels.

1.3 Lab-on-a-Chip Devices

Although the majority of microfluidics based literature has been focused on the study of a single unit operation, there is a significant amount of work that integrates multiple unit operations into a single device for a variety of end uses. One of the earliest complete LOC systems is found in the integrated nanoliter DNA analysis device developed by Burns *et al.*[39] This early device utilized a hydrophilic microchannel partitioned with hydrophobic regions combined with an external pressure control device to meter 120 nL aqueous droplets containing relatively small DNA concentrations. The small droplet was combined with a second droplet containing restriction and polymerase enzymes, after which integrated microheaters cycled the droplets in temperature consistent with macroscopic polymerase chain reaction (PCR) tecniques. The resulting droplet containing amplified DNA was then mixed with a third droplet containing intercalating fluorescent dye and electrokinetically loaded onto a capillary gel electrophoresis channel. The DNA products were then separated via gel electrophoresis, where the separation products were

measured using an external detector via both an integrated laser emitting diode (LED) and long pass filter. Although the individual components for this device (integrated electrodes, LED, hydrophobic patches, filter, glass microchannel) required complex fabrication procedures, associated costs regarding the large scale fabrication of such devices is predicted to be small.

The device shown by Burns *et al.* required the use of microfabrication techniques within a clean room environment. In contrast, several complete LOC devices have since been constructed utilizing the soft lithographic techniques developed by Xia *et al.*[9] Using these techniques, microchannels composed of poly(dimethylsiloxane) (PDMS) can created in multiple layers as to create a series of controllable gate valves by exploiting the elastomeric properties of the microchannel structures.[40, 41] These multi-layered devices have since been used for a variety of purposes, including: nanoliter PCR,[42] single-cell enzyme screening,[43] and protein crystallization.[44] Recently, these types of devices have been used to isolate mRNA from a single cell.[45] After isolation of a single cell into a nanoliter sized chamber near the microchannel inlet, pressure driven flow (from external sources) through a series of valve arrangements is used to relocate the cell into a central chamber, where the cell is lysed by active convection of a recirculating lysing buffer. The cell components are then directed towards a monolithic filter to collect mRNA components of interest. An elution buffer then directs the concentrated mRNA towards a port where the solution can be collected for further analysis.

In addition to the two devices described above, there are many such LOC devices incorporating multiple unit operations onto a microfluidics based chip. The functionalities of these devices are wide ranging and can be found in a variety of review articles.[1, 3, 4, 16, 23, 46, 47] Despite the prevalence of these devices, nearly all require additional equipment that is much larger than the size of the LOC component. For example, the device utilized by Burns *et al.* possesses a size footprint roughly 3 cm wide and 15 cm long; however, several ancillary tools are needed to run the operation

including a computational device (overall control), pressurized sources and solenoid valves (fluid metering), electrical power supplies and relay switches (temperature control), and a photodetection unit. It is very common to see an LOC device the size of a credit card situated on an inverted fluorescence microscope with fluid delivery lines running to a syringe pump, electric wires leading from power supplies and conductance detectors to the device, as well as electrical wires running to Peltier elements, solenoid valves, and relay switches. The ancillary equipment utilized with LOC devices can easily take several linear feet of bench space, and severely restricts the portability of such a device. Furthermore, nearly all existing LOC devices require a trained technician operating the device through the use of a microscope.

As a result, there is considerable focus on the engineering of diagnostic devices that are truly point-of-care. This can be accomplished by the integration of unit operations such that a device works passively and without the need of a technician. These minimally instrumented devices can be either a stand alone disposable unit, or a reusable, portable monitoring unit that uses disposable analysis cartridges.[25] By providing passive methods for both microfluidic pumping and mixing, the results of this dissertation can be used along with the sensing technologies developed at Colorado State University to provide a platform that meets these minimally instrumented needs. Nevertheless, there remain significant challenges with the design of minimally instrumented LOC devices.

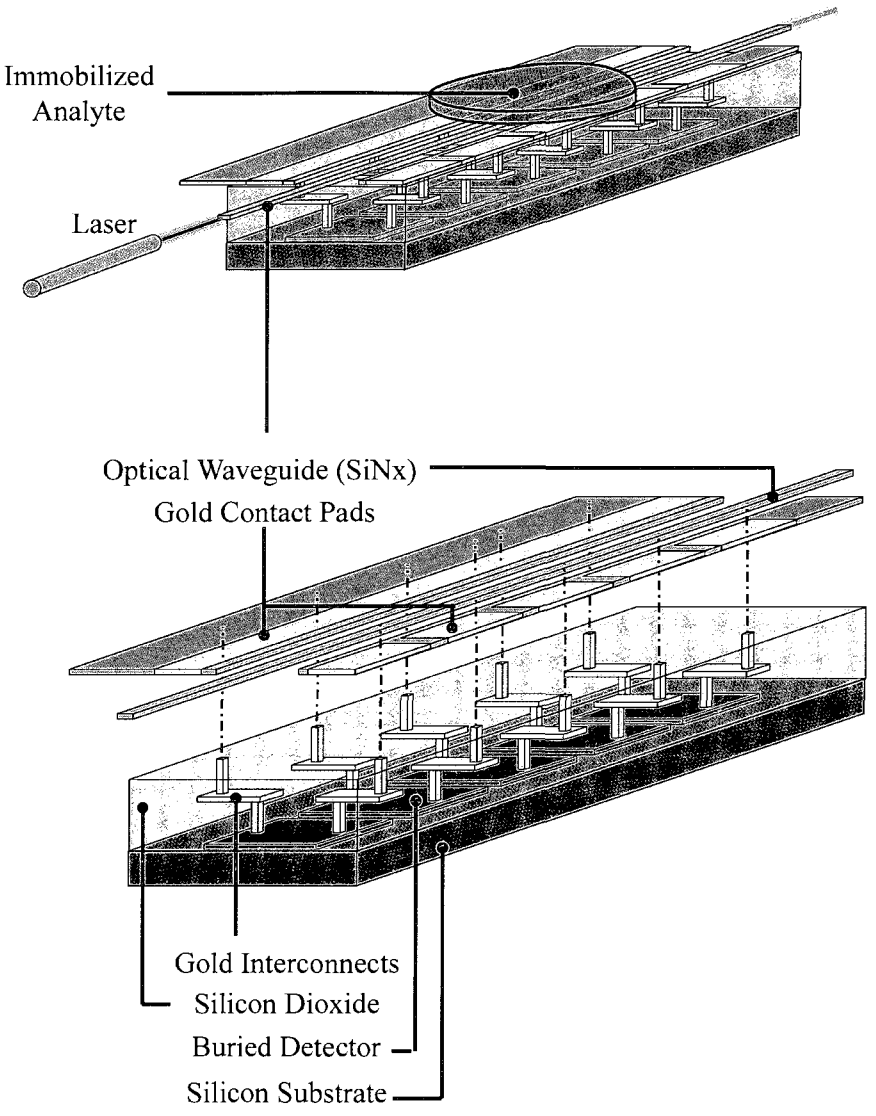

Figure 1.1. The local evanescent array coupled (LEAC) biosensor developed at Colorado State University.

1.4 Local Evanescent Array Coupled (LEAC) Biosensor

Colorado State University has recently developed a reagentless, multi-analyte sensor based on the evanescent field response to local changes in the refractive index (RI) of a region near the surface of a planar waveguide.[15] This local evanescent array coupled (LEAC) biosensor is displayed in Fig. 1.1, and works as follows. A laser diode focuses light into a planar silicon nitride waveguide where the dimensions of the waveguide are such that the electromagnetic profile of the light is confined to the fundamental mode. A series of discrete, buried polysilicon detectors, fabricated below the waveguide separated by a silicon dioxide layer, generate a small photocurrent upon exposure to the evanescent field of the waveguide. The asymmetric evanescent field decays exponentially as a function of distance from the waveguide core, where shifts in the field can be induced by local changes to the RI from an aqueous solution present on top of the waveguide. A diagram of the sensing mechanism can be found in Fig. 1.2. By immobilization of capture bodies (antibodies or antigens) on discrete regions of the waveguide top surface, the LEAC sensor can act as a reagentless immunosensor when exposed to a solution containing solutes having an affinity for the immobilized probes, as long as the remaining waveguide surfaces have been passivated against non-specific adsorption. Because the sensing surfaces exist along the length of the waveguide core, the LEAC can be used for multiple analytes, where immobilized capture bodies corresponding to different analytes need to be separated by a distance along the waveguide determined by the dimensions of the system. This system has been shown to accurately detect the presence of dry organic biofilms situated on top of the waveguide.[14] When combined with an on chip LED source as well as integrated circuitry for signal amplification, the LEAC sensor possesses a high portability, low cost, and high sensitivity means of detection for POC purposes.

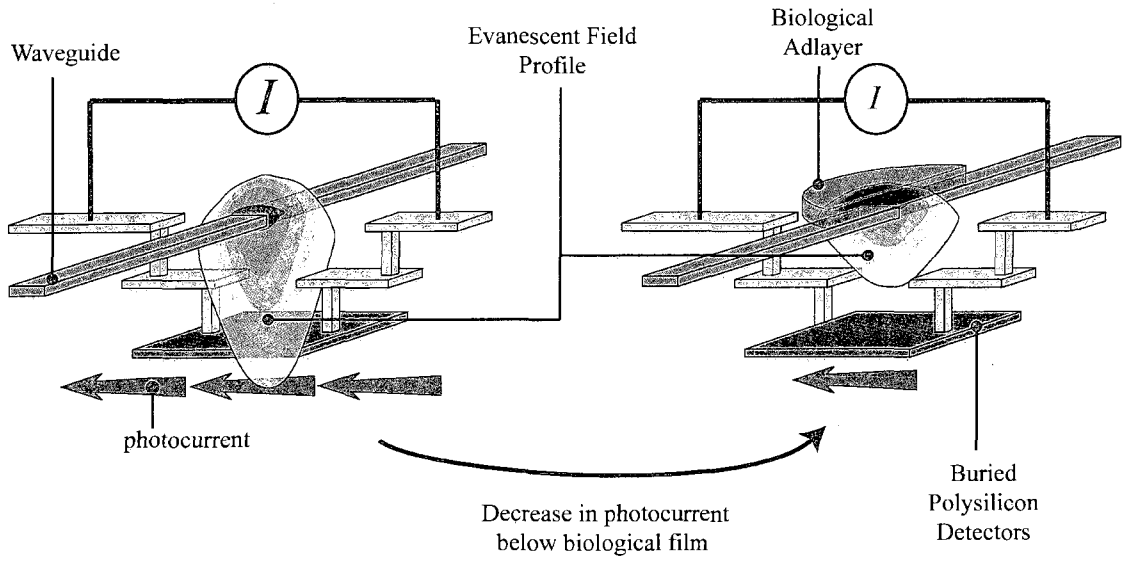

Figure 1.2. Sensing mechanism of the LEAC. Before a capture event, the evanescent intensity profile through the silicon dioxide layer exists to create a photocurrent in a buried polysilicon detector where the photocurrent is a function of the fluid RI local to the top waveguide surface. When biological material is immobilized onto the waveguide surface (e.g. binding of antigens to immobilized antibodies), the evanescent profile shifts away from the buried detector resulting in an observed decrease in photocurrent.

1.5 Research Objectives

The LEAC sensor can be operated in an extremely simple manner by exposing the sensor (with pre-immobilized capture probe molecules) to a static solution with an unknown analyte concentration *C*. For this system, aqueous target analyte species are free to diffuse throughout the solution such that they become "captured" by the affinity relationship between the analyte and capture body and remain on the surface. For analytes with low molecular diffusivity and present in small concentrations, the system becomes severely mass-transfer limited and the times required to complete the assay can be impractical, taking as long as 24 hours to achieve an equilibrium state.[48] This problem can be alleviated by actively transporting the aqueous solution of interest over the waveguide surface.

Due to the ease of fabrication and operation, we have chosen a microfluidics approach to actively deliver analytes to the LEAC sensor. In this approach a PDMS μFN will be utilized to both immobilize capture bodies onto the LEAC surface and perform the affinity assays under convective flow conditions. We require the system to be minimally instrumented, where no external equipment will be used for fluid delivery and pumping, and electrical requirements will be such that is available with the currents and voltages available from simple battery systems.

The integration of a microfluidic platform with the LEAC sensing technology would be similar in design to the heterogeneous immunoassay techniques first demonstrated by Bernard *et al.* and summarized as follows.[49] After a surface pretreatment step, a μFN will be used to immobilize capture probes in discrete regions aligned perpendicular to the planar waveguide. The μFN would consist of PDMS oxidized in a manner such that a reversible bond is formed with the silicon nitride/gold surface. After immobilization, the first μFN would be removed for the entire surface to be passivated against non-specific adsorption of analyte to regions other than the capture spots. These passivation agents include bovine serum albumin (BSA) or polyethylene glycol (PEG). A second μFN would then be bonded to the LEAC sensor (reversibly or irreversibly) with the regions of μFN near the outlet consisting of microchannels channel aligned over the waveguide, such that the channel intersects the regions of immobilized capture agents by 90°. At this point a baseline reading of the discrete buried LEAC detectors is established due to the immobilized capture bodies and passivating agents present on the waveguide surface. As reported in several studies, it is expected that the device can be stored for several months before the immobilized bodies begin to degrade.[1] When the device is required for analyte measurement, all that is required is reagent and sample delivery to the inlet reservoirs. Upon introduction of the aqueous solutions to the inlet reservoirs, the μFN will be designed such that the analyte is mixed with any required reagents (e.g. a competitive immunoassay) and fluid convection over the sensing regions is passive. As analyte is

captured over the sensing surface, photocurrent within the discrete buried silicon detectors will reduce in a manner such that the amount of material captured can be quantified when compared to baseline readings.[15]

In this study, I am interested in affinity systems such as those possessed in immunoglobulins, aptamers, and complementary strands of DNA or RNA, where the analyte of interest includes small molecules, proteins, viruses or pathogens, and DNA/RNA oligiomers. Because the LEAC sensor was not available for a majority of this dissertation, the unit operations shown here were studied independently from one another as well as the LEAC sensor. It is not expected, however, that the integration of these components into a complete device will possess any adverse effects with respect to one another. All potential problems with a fully functional device are addressed in the individual chapters.

An efficient μFN utilizing the LEAC sensing technology will have to address the following issues.

- **Sample Storage**. Affinity systems under consideration, in general, will have reached at least 50% of equilibrium coverage in less than an hour as long as the system is within a reaction limited regime.[50] Therefore, a sample storage system capable of containing aqueous volumes of $V < 10$ μL for the extent of these assays will be required. The storage vessel will need to be connected to the μFN serving to deliver fluid to the sensor surface. Due to the small liquid volumes present in the reservoir, the effects of evaporation will need to be examined such that the reservoir does not dry out before the assay is completed. To date, little to no information concerning the evaporation rates from small reservoirs has been studied.
- **Fluid Pumping**. To reduce the overall assay times, it is desirable to keep the immunoassay within the reaction limited regime. To accomplish this, the aqueous solution containing an analyte of interest must be pumped past a region of the

sensor where capture bodies have been immobilized. The critical rate of convection above which the system will be reaction limited will be dictated by the geometry of the microchannels, the concentration of analyte, and the association constant of the affinity interaction. Because we require the device to be minimally instrumented, a passive pumping mechanism will be examined, where a mechanism is required such that steady flows are produced at controlled rates dictated by the geometries of the system. Because of the small size of the microchannels, capillary forces will be ideal for this task. There are several studies examining passive microfluidic pumping methods utilizing capillary forces as the driving mechanism;[30, 51] however, all produce flows that are neither steady nor can maintain continuous flows for extended times. Therefore, novel pumping approaches will be required for study.

- **Fluid Mixing**. There are several operational cases that will require microfluidic mixing strategies: (1) In the case that an aqueous analyte stream requires pretreatment before passing over the sensing regions of the waveguide, additional reagents will need to be added to the analyte solution. Mixing strategies will be required such that the overall size of the microfluidic network remains small. (2) In the case that there is a small amount of available sample volume the analyte solution must be recirculated over the sensing regions. Mixing strategies must be utilized as to eliminate the boundary layers created by the heterogeneous immunoreaction at the sensing surface. It is possible that active mixing methods can be of use in this situation if the overall power requirements remain such that the electric potential ϕ and current i remain low ($\phi < 6$ V, $i < 1$ mA). Approaches to this problem will include optimization of previous mixing methods as well as the development of a novel mixing strategy.
- **Analyte Reaction**. The speed at which the sensing region captures analytes from the aqueous solution will be dictated by the kinetics of the affinity interaction, the

molecular diffusion of the analyte, the rate of convection over the sensing surface, and the geometries of the microchannel and immobilized capture regions. The chemistry involving the immobilization of capture bodies to the LEAC sensor, pretreatment of analyte, and passivation of the nonsensing LEAC surfaces have been handled by a separate group.[12, 13] Because it is desirable to limit the assay to times of less than an hour, the dependence on the heterogeneous reaction rate on the parameters describing the system must be examined to ensure the system remains reaction limited. In systems where a single microchannel delivers an analyte to multiple sensing regions, analyte boundary (depletion) layers created by the first capture spot serve to decrease the amount of captured material on the downstream sensing regions. Although there have been several computational and experimental studies concerning these types of heterogeneous affinity reactions in microfluidic systems,[50, 52-54] none have placed emphasis either on the geometries of the microchannels nor have any discussed possible methods of alleviation to the depletion effects in systems with multiple sensing regions.

1.6 Organization of the Dissertation

Brief outlines of each chapter are given below.

- **Chapter 2.** "*Geometrical optimization of helical flow in grooved micromixers.*" This chapter is dedicated to optimizing a state of the art passive micromixer, the staggered herringbone mixer (SHM). The SHM works by incorporating a series of herringbone shaped grooves on the floor of a microchannel. When pressure or electrokinetic driven flow is forced over the grooves, regions of fluid become directed along the orientation of the grooves along the channel floor and an overall bi-helical flow pattern is observed. By alternating the asymmetry of the grooves along the length of the microchannel, chaotic flow is realized and required mixing lengths are reduced substantially. Preceding this study were over

20 computational and experimental studies involving the optimization of the geometry of the SHM channel, however, none addressed the optimal geometry of the grooves themselves and how the optimal groove geometries change with the overall channel geometry. This chapter involves the optimization of helical flow within a SHM, providing optimal groove geometries for channels of any dimension.

- **Chapter 3**. "*Design of a new microfluidic mixer – mixing via transverse electrokinetic effects in a planar microchannel.*" This chapter is dedicated to the development of a novel mixing strategy, where pressure driven flows are subjected to DC electroosmotic flows perpendicular to the channel axis created by a small potential drop across integrated microelectrodes. This study involves the theoretical optimization of electrode geometries and the experimental operation of a device under a variety of conditions. To date, this study details the only experimental device utilizing this mixing strategy.
- **Chapter 4**. "*Passive microfluidic pumping using coupled capillary/evaporation effects.*" This chapter is dedicated to the creation of long term steady state flow rates in microchannels connected to a cylindrical outlet reservoir. A theoretical model to predict the time dependent flow rate in such systems is developed that utilizes (*i*) a model to account for the shape of an air/water interface in a micro-reservoir under varying conditions and reservoir geometries, (*ii*) a model that predicts the rate of evaporation from said interface, and (*iii*) a model to predict the pressure drop between multiple reservoirs with varying liquid volume. I show that this model gives excellent predictions towards experimental systems of a microchannel connected to an inlet and outlet reservoir. This passive pumping mechanism stands alone in its ability to create steady state flows for time periods lasting hours or more.

- **Chapter 5**. "*Optimization of microchannel geometries applied to heterogeneous immunoassays*." This chapter studies the effects of microchannel geometry and convective flow on the rate of reaction in microfluidics based heterogeneous immunoassays. Using computational fluid dynamics we study the response of the system to changes in microchannel height, capture spot length, and solution flow rate over the sensor surface. Furthermore, I study the ability of the SHM to alleviate analyte boundary layer effects on downstream capture spots.

1.9 References

1. P. Yager, G. J. Domingo and J. Gerdes, (2008) Point-of-care diagnostics for global health *Annual Review of Biomedical Engineering*, **10**, 107-144.
2. C. C. Sanders, M. Peyret, E. S. Moland, S. J. Cavalieri, C. Shubert, K. S. Thomson, J. M. Boeufgras and W. E. Sanders, (2001) Potential impact of the VITEK 2 system and the advanced expert system on the clinical laboratory of a university-based hospital *Journal of Clinical Microbiology*, **39**, 2379-2385.
3. D. D. Cunningham, (2001) Fluidics and sample handling in clinical chemical analysis *Analytica Chimica Acta*, **429**, 1-18.
4. C. D. Chin, V. Linder and S. K. Sia, (2007) Lab-on-a-chip devices for global health: Past studies and future opportunities *Lab on a Chip*, **7**, 41-57.
5. G. M. Whitesides, (2006) The origins and the future of microfluidics *Nature*, **442**, 368-373.
6. D. Janasek, J. Franzke and A. Manz, (2006) Scaling and the design of miniaturized chemical-analysis systems *Nature*, **442**, 374-380.
7. A. Manz, J. C. Fettinger, E. Verpoorte, H. Ludi, H. M. Widmer and D. J. Harrison, (1991) Micromachining of Monocrystalline Silicon and Glass for Chemical-Analysis Systems - a Look into Next Century Technology or Just a Fashionable Craze *Trac-Trends in Analytical Chemistry*, **10**, 144-149.
8. S. C. Terry, J. H. Jerman and J. B. Angell, (1979) Gas-Chromatographic Air Analyzer Fabricated on a Silicon-Wafer *Ieee Transactions on Electron Devices*, **26**, 1880-1886.
9. Y. N. Xia and G. M. Whitesides, (1997) Soft lithography. *Abstracts of Papers of the American Chemical Society*, **214**, 348-PMSE.
10. M. Gad-el-Hak, (1999) The fluid mechanics of microdevices - The Freeman Scholar Lecture *Journal of Fluids Engineering-Transactions of the Asme*, **121**, 5-33.
11. P. L. Chen, R. S. Muller, R. D. Jolly, G. L. Halac, R. M. White, A. P. Andrews, T. C. Lim and M. E. Motamedi, (1982) Integrated Silicon Microbeam Pi-Fet Accelerometer *Ieee Transactions on Electron Devices*, **29**, 27-33.
12. B. M. Murphy, D. S. Dandy and C. S. Henry, (2009) Analysis of oxidative stress biomarkers using a simultaneous competitive/non-competitive micromosaic immunoassay *Analytica Chimica Acta*, **640**, 1-6.
13. B. M. Murphy, X. Y. He, D. Dandy and C. S. Henry, (2008) Competitive immunoassays for simultaneous detection of metabolites and proteins using micromosaic patterning *Analytical Chemistry*, **80**, 444-450.
14. R. Yan, S. P. Mestas, G. Yuan, R. Safaisini, D. S. Dandy and K. L. Lear, (2009) Label-free silicon photonic biosensor system with integrated detector array *Lab on a Chip*. DOI: 10.1039/b902111f
15. R. J. Yan, G. W. Yuan, M. D. Stephens, X. Y. He, C. S. Henry, D. S. Dandy and K. L. Lear, (2008) Evanescent field response to immunoassay layer thickness on planar waveguides *Applied Physics Letters*, **93**, -.
16. K. Ohno, K. Tachikawa and A. Manz, (2008) Microfluidics: Applications for analytical purposes in chemistry and biochemistry *Electrophoresis*, **29**, 4443-4453.

17. K. W. Oh, R. Rong and C. H. Ahn, (2005) Miniaturization of pinch-type valves and pumps for practical micro total analysis system integration *Journal of Micromechanics and Microengineering*, **15**, 2449-2455.
18. D. J. Laser and J. G. Santiago, (2004) A review of micropumps *Journal of Micromechanics and Microengineering*, **14**, R35-R64.
19. P. Woias, (2005) Micropumps - past, progress and future prospects *Sensors and Actuators B-Chemical*, **105**, 28-38.
20. C. C. Chang and R. J. Yang, (2007) Electrokinetic mixing in microfluidic systems *Microfluidics and Nanofluidics*, **3**, 501-525.
21. N. T. Nguyen and Z. G. Wu, (2005) Micromixers - a review *Journal of Micromechanics and Microengineering*, **15**, R1-R16.
22. J. M. Ottino and S. Wiggins, (2004) Introduction: mixing in microfluidics *Philosophical Transactions of the Royal Society of London Series a-Mathematical Physical and Engineering Sciences*, **362**, 923-935.
23. S. Haeberle and R. Zengerle, (2007) Microfluidic platforms for lab-on-a-chip applications *Lab on a Chip*, **7**, 1094-1110.
24. A. W. Martinez, S. T. Phillips and G. M. Whitesides, (2008) Three-dimensional microfluidic devices fabricated in layered paper and tape *Proceedings of the National Academy of Sciences of the United States of America*, **105**, 19606-19611.
25. B. Weigl, G. Domingo, P. LaBarre and J. Gerlach, (2008) Towards non- and minimally instrumented, microfluidics-based diagnostic devices *Lab on a Chip*, **8**, 1999-2014.
26. P. von Lode, (2005) Point-of-care immunotesting: Approaching the analytical performance of central laboratory methods *Clinical Biochemistry*, **38**, 591-606.
27. W. A. Zhao and A. van den Berg, (2008) Lab on paper *Lab on a Chip*, **8**, 1988-1991.
28. J. Ju, J. Y. Park, K. C. Kim, H. Kim, E. Berthier, D. J. Beebe and S. H. Lee, (2008) Backward flow in a surface tension driven micropump *Journal of Micromechanics and Microengineering*, **18**, -.
29. E. Berthier and D. J. Beebe, (2007) Flow rate analysis of a surface tension driven passive micropump *Lab on a Chip*, **7**, 1475-1478.
30. M. Zimmermann, H. Schmid, P. Hunziker and E. Delamarche, (2007) Capillary pumps for autonomous capillary systems *Lab on a Chip*, **7**, 119-125.
31. C. S. Effenhauser, H. Harttig and P. Kramer, (2002) An evaporation-based disposable micropump concept for continuous monitoring applications *Biomedical Microdevices*, **4**, 27-32.
32. N. Goedecke, J. Eijkel and A. Manz, (2002) Evaporation driven pumping for chromatography application *Lab on a Chip*, **2**, 219-223.
33. J. Y. Park, C. M. Hwang, S. H. Lee and S. H. Lee, (2007) Gradient generation by an osmotic pump and the behavior of human mesenchymal stem cells under the fetal bovine serum concentration gradient *Lab on a Chip*, **7**, 1673-1680.
34. X. Noblin, L. Mahadevan, I. A. Coomaraswamy, D. A. Weitz, N. M. Holbrook and M. A. Zwieniecki, (2008) Optimal vein density in artificial and real leaves *Proceedings of the National Academy of Sciences of the United States of America*, **105**, 9140-9144.

35. G. C. Randall and P. S. Doyle, (2005) Permeation-driven flow in poly(dimethylsiloxane) microfluidic devices *Proceedings of the National Academy of Sciences of the United States of America*, **102**, 10813-10818.
36. S. Wiggins and J. M. Ottino, (2004) Foundations of chaotic mixing *Philosophical Transactions of the Royal Society of London Series a-Mathematical Physical and Engineering Sciences*, **362**, 937-970.
37. V. Hessel, H. Lowe and F. Schonfeld, (2005) Micromixers - a review on passive and active mixing principles *Chemical Engineering Science*, **60**, 2479-2501.
38. A. D. Stroock, S. K. W. Dertinger, A. Ajdari, I. Mezic, H. A. Stone and G. M. Whitesides, (2002) Chaotic mixer for microchannels *Science*, **295**, 647-651.
39. M. A. Burns, B. N. Johnson, S. N. Brahmasandra, K. Handique, J. R. Webster, M. Krishnan, T. S. Sammarco, P. M. Man, D. Jones, D. Heldsinger, C. H. Mastrangelo and D. T. Burke, (1998) An integrated nanoliter DNA analysis device *Science*, **282**, 484-487.
40. S. R. Quake and A. Scherer, (2000) From micro- to nanofabrication with soft materials *Science*, **290**, 1536-1540.
41. M. A. Unger, H. P. Chou, T. Thorsen, A. Scherer and S. R. Quake, (2000) Monolithic microfabricated valves and pumps by multilayer soft lithography *Science*, **288**, 113-116.
42. J. Liu, M. Enzelberger and S. Quake, (2002) A nanoliter rotary device for polymerase chain reaction *Electrophoresis*, **23**, 1531-1536.
43. T. Thorsen, S. J. Maerkl and S. R. Quake, (2002) Microfluidic large-scale integration *Science*, **298**, 580-584.
44. C. L. Hansen, E. Skordalakes, J. M. Berger and S. R. Quake, (2002) A robust and scalable microfluidic metering method that allows protein crystal growth by free interface diffusion *Proceedings of the National Academy of Sciences of the United States of America*, **99**, 16531-16536.
45. J. W. Hong, V. Studer, G. Hang, W. F. Anderson and S. R. Quake, (2004) A nanoliter-scale nucleic acid processor with parallel architecture *Nature Biotechnology*, **22**, 435-439.
46. M. Toner and D. Irimia, (2005) Blood-on-a-chip *Annual Review of Biomedical Engineering*, **7**, 77-103.
47. E. Verpoorte, (2002) Microfluidic chips for clinical and forensic analysis *Electrophoresis*, **23**, 677-712.
48. G. Bhanot, Y. Louzoun, J. H. Zhu and C. DeLisi, (2003) The importance of thermodynamic equilibrium for high throughput gene expression arrays *Biophysical Journal*, **84**, 124-135.
49. A. Bernard, B. Michel and E. Delamarche, (2001) Micromosaic immunoassays *Analytical Chemistry*, **73**, 8-12.
50. M. Zimmermann, E. Delamarche, M. Wolf and P. Hunziker, (2005) Modeling and optimization of high-sensitivity, low-volume microfluidic-based surface immunoassays *Biomedical Microdevices*, **7**, 99-110.
51. G. M. Walker and D. J. Beebe, (2002) A passive pumping method for microfluidic devices *Lab on a Chip*, **2**, 131-134.
52. J. Bishop, S. Blair and A. Chagovetz, (2007) Convective flow effects on DNA biosensors *Biosensors & Bioelectronics*, **22**, 2192-2198.

53. H. Parsa, C. D. Chin, P. Mongkolwisetwara, B. W. Lee, J. J. Wang and S. K. Sia, (2008) Effect of volume- and time-based constraints on capture of analytes in microfluidic heterogeneous immunoassays *Lab on a Chip*, **8**, 2062-2070.
54. M. Wolf, D. Juncker, B. Michel, P. Hunziker and E. Delamarche, (2004) Simultaneous detection of C-reactive protein and other cardiac markers in human plasma using micromosaic immunoassays and self-regulating microfluidic networks *Biosensors & Bioelectronics*, **19**, 1193-1202.

Chapter 2

Geometrical Optimization of Helical Flow in Grooved Micro-mixers

Portions of this chapter appear in the following:

- Lynn N.S. and Dandy D.S. (2008) Geometrical Optimization of Helical Flow in Grooved Micromixers *Lab on a Chip*, **7,** 580-587

2.1 Introduction

It is recognized that mixing plays an important role in the growing use of micro-fluidic devices for lab-on-a-chip applications.[1, 2] For applications ranging from DNA separation and amplification to protein crystallization and kinetics studies, the performance of a lab-on-a-chip device is directly related to the rate at which two or more fluids can be mixed. Due to the small dimensions of micro-channels as well as the limited range of obtainable linear flow rates, flow in micro-channels is confined to the laminar regime and mixing is dominated by molecular diffusion. Micro-fluidic mixing may be accomplished using a variety of approaches. Active mixers may rely on external energy sources, such as electro-osmotic flow,[3-5] external pressure gradients,[6, 7] and electrokinetic instabilities[8, 9] to perturb fluid streamlines into a mixing state. Unlike their active counterparts, passive mixers utilize existing geometries within a micro-channel to mix externally pumped fluids. Efficient passive mixing in planar micro-channels may be accomplished via flow through spiral-type microchannels,[10, 11] as well as via gas-liquid[12] or liquid-liquid[13] multiphase flow. More complicated three-dimensional micro-channel

systems have also been used to mix fluids via chaotic advection[14] and other split and recombine methods.[15, 16]

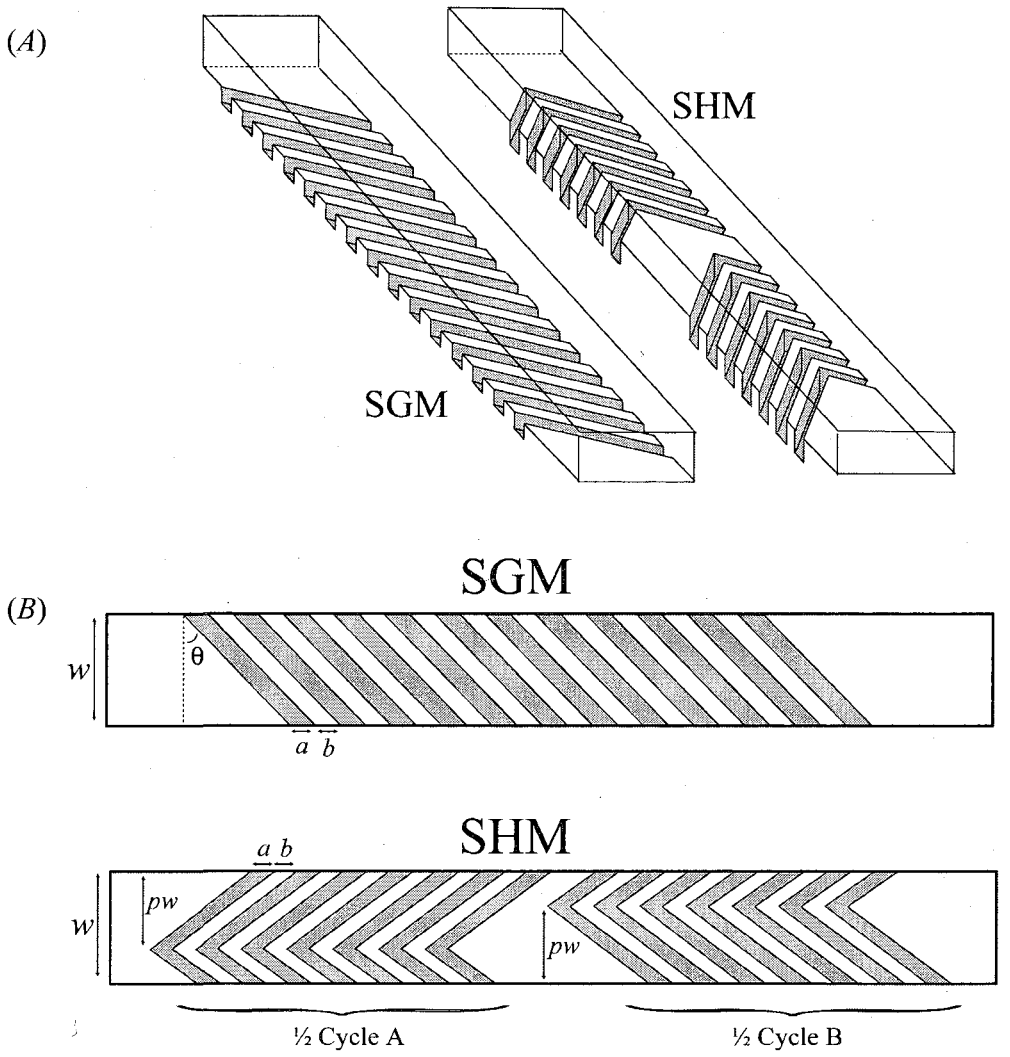

Figure 2.1. (*A*) Overall geometries of the SGM and SHM. (*B*) Top down view of both geometries, as well as some geometric parameters. The darker regions indicate the presence of a groove.

Perhaps the best known examples pertaining to passive micro-fluidic mixing are the staggered herringbone mixer (SHM)[17] and the slanted groove micro-mixer (SGM).[18] The geometries of the SGM and SHM can be seen in Fig. 2.1. The SGM consists of diagonal grooves embedded into the floor of a micro-channel situated at an angle θ with respect to the axial direction, whereas the SHM grooves exist in a herringbone pattern. The oblique grooves serve to transport fluid from the apex of the groove structure to the downstream edges of the micro-channel. As a result, fluid near the top of the channels will re-circulate in the opposite direction, and an overall helical flow pattern is created. The herringbone pattern on the SHM serves to generate two counter-rotating helical flows, such that a chaotic flow profile may be created by alternating the asymmetry of the herringbones along the length of the micro-channel. Typically, less than 10 full cycles are needed for complete mixing of the fluid within the micro-channel, regardless of the overall flow rate.[17, 19] Due to its simple planar design, the SHM is readily fabricated using standard soft lithographic methods,[20] thus making a convenient choice for lab-on-a-chip applications requiring rapid mixing of two or more liquids, such as the lysis of whole blood using de-ionized water.[21] Several passive mixer designs have evolved from the original SGM design: Kim *et al.* placed alternating barriers above the slanted grooves to achieve enhanced mixing effects with the barrier embedded mixer (BEM),[22] and Sato *et al.* fabricated PDMS micro-channels with slanted grooves on the sidewalls as well as the channel floor to achieve increases in bulk helical flow.[23, 24]

To date, there have been a number of theoretical, experimental, and numerical studies aimed at the optimization of SHM- and SGM-type devices. Stroock *et al.* developed an analytical solution to the Stokes equations to quantify non-axial flow over sinusoidal modulated surfaces,[18] and later showed that flow over oblique grooves may be accurately modeled using a superposition of the analytical 2D lid-driven cavity solution with the Fourier series solution to Poiseuille flow in rectangular ducts.[19] Due to the low Reynolds number flows and simple geometries, the SHM and SGM are perfect candidates for study

via computational fluid dynamics (CFD), usually via finite element or finite volume methods. Flow in these microchannels can also be studied with the lattice Boltzmann method, based on simplified kinetic models incorporating the essential physics of microscopic processes such that the averaged fluid properties obey the desired macroscopic continuum equations.[25] Several CFD studies on the SHM report consistent mixing profiles between computational and experimental methods via the solution of the convection-diffusion equation for the concentration field.[26, 27] Although these methods are particularly useful for visualization of the flow field, numerical diffusion errors are typically high and quantification of the mixing efficiency is difficult. To avoid these numerical errors, several studies have utilized particle tracking methods to characterize the mixing properties of the SGM and SGM in more detail. Kang *et al.* utilized colored particle tracers to display excellent resolution of the multi-cycle SHM mixing profile,[28] Camesasca *et al.* utilized statistical entropy of particle tracers to evaluate the mixing efficiency of the original SHM design,[29] and Aubin *et al.* displayed Poincaré maps for the original SHM and SGM designs in addition to an analysis of the magnitude of the rate of deformation tensor along the length of the mixer.[30]

In addition to validation of the flow field, recent work has been focused on the optimization of SGM and SHM devices. Both Wang *et al.*[31] and Hassell *et al.*[32] studied the effects of the groove depth to channel height ratio in SGM designs. Li *et al.* used a lattice Boltzmann method to study effects of the width fraction of the long arm and the number of grooves per half-cycle on SHM designs.[33] Additionally, Aubin *et al.* used particle tracking methods to study the effects of the groove spacing on the same SHM designs.[5] In the most complete optimization study to date, Yang *et al.* used the Taguchi method to study the effects of the groove depth ratio, the width fraction of the long arm, the channel height to width aspect ratio, and the groove intersection angle on helical flow within the SHM.[34] These studies agree on several conclusions: (1) The mixing properties of the SHM are much more efficient than that of the SGM, (2) the mixing properties of

the SHM are optimized when the width fraction of the long arm is approximately 2/3, (3) non-axial flow is maximized over a groove intersection angle of 45°, (4) the magnitude of helical flow is weakly dependent on the channel aspect ratio, and (5) the magnitude of helical flow is strongly dependent (asymptotically) on the groove depth ratio. It is consistently observed that as helical flow increases (or the magnitude of flow within the grooves), the rate of mixing within the SHM increases, and the overall SHM length needed for complete mixing decreases. Although a number of different numerical studies exist concerning the SHM, little is known regarding the effect of the groove spacing on helical flow, and there are no comprehensive design parameters associated with the overall SHM geometries.

At the time of this work, all published experimental and numerical studies concerning flow over patterned grooves involved symmetric grooves, for which the groove and ridge lengths are equal. Here, we utilize computational fluid dynamics to demonstrate that the magnitude of helical flow is strongly dependent on the groove spacing within a SGM, and that the equal spacing used in all previous studies does not provide an optimum design. Further, the optimum groove spacing is strongly dependent on both the channel aspect ratio and the groove depth to channel height ratio. A full numerical study details the magnitude of helical flow over uneven patterned grooves in the SGM, where the optimized parameters can be used to optimize flow within the SHM. Helical flow over 800 different SGM geometries were computed within this study.

2.2 Qualitative Flow Visualization – Particle Pathline Plots

Previous computational studies on flow within the SHM have shown particle pathline plots in which there is a small scale helical motion, similar to a corkscrew, situated directly over the patterned grooves.[31, 33, 34] In these studies, no characterization of this flow mode was carried out. An example of this flow pattern is shown in figure 2.2, illustrating pathline plots within a SGM (computed in this study with methods discussed below), and can be described as follows: via viscous interaction, fluid streamlines situated directly over the grooves are effected by the flow within the grooves directed towards the channel walls, whereas fluid streamlines between the grooves (over the ridges) are effected by the fluid near the top of the channel recirculating in the opposite direction. The fluid directly over the ridges appears to inhibit the overall non-axial transport of fluid in the direction of the grooves, thus limiting the total magnitude of helical flow within the device. Because the overall goal is to maximize the non-axial convective transport of fluid within the grooves, it is reasonable that the ridge length should be minimized to acceptable lengths that can be readily fabricated.

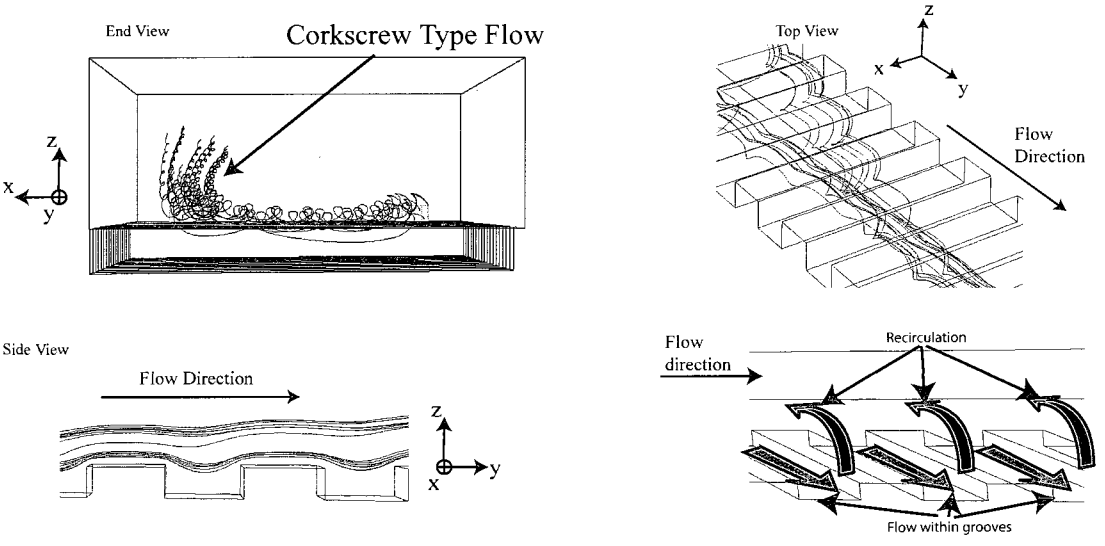

Figure 2.2. Simulated pathlines of fluid flow over patterned grooves. Flow just over the grooves is shown in blue, and the resulting re-circulation profile is shown in red.

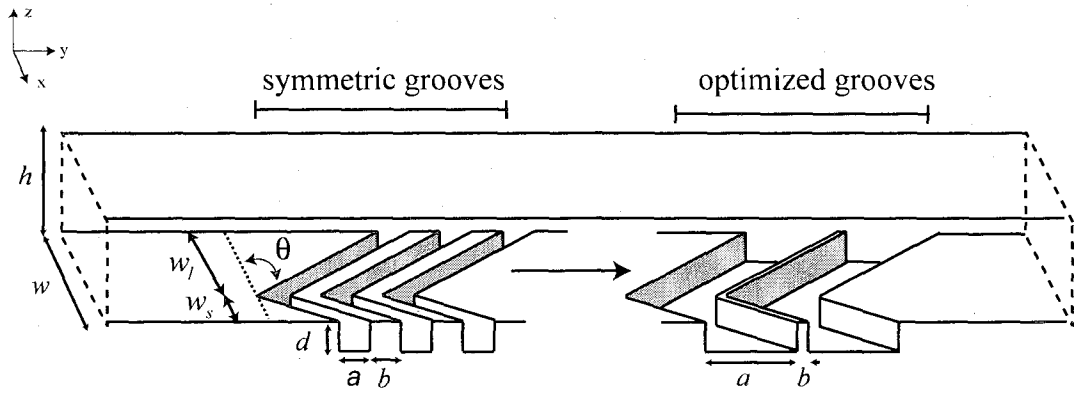

Figure 2.3. The geometric parameters used within this study. These parameters apply to both the SGM and SHM.

Figure 2.3 displays the geometries considered in this study. Rather than utilize notations described in previous studies, a new set of geometries has been adopted that are directly related to the fabrication of SHM type devices, namely the spin coat thickness and photo-mask design. Previous studies have shown that helical flow is maximized when the groove intersection angle $\theta = 45°$, thus that value has been used in this study. Along with the channel height (h) and width (w), additional geometric parameters are the groove depth (d), the groove width (a), and the ridge width (b). Mixers are classified here according to their groove depth to channel height ratio (d/h), the channel aspect ratio (h/w), and the groove and ridge to width ratios (a/w, b/w). Because the limits of $b/a \rightarrow 0$ and $b/a \gg 1$ will produce Poiseuille flow profiles containing no helical flow, there must exist an optimum ratio b/a that maximizes helical flow over the grooves for a specific value of b. Thus, this study involves finding the optimized groove spacing (a/w) for a given SHM type device, and how that groove spacing relates to channels with specific d/h, h/w, and b/w ratios.

2.3 Numerical Methodology

Because of its geometrical simplicity, the slanted groove mixer is utilized for the study of geometrical effects on the magnitude of helical flow. The magnitude of helical flow within the SGM is closely related to that within the SHM, where optimized geometries for the SHM can be derived from those optimized from the SGM (to be further discussed later). The finite volume CFD package FLUENT was used to simulate the 3D velocity field through a planar SGM device consisting of one inlet and one outlet. The entry and exit lengths of the channel were constant at $w/2$, and the length of the channel containing grooves was a minimum of $7w$, the minimum lengths to produce a fully developed flow profile. The CFD preprocessing package Gambit® was used to discretize the SGM into 6-node trihedral elements with typical cell dimensions of $w/50$. For geometries with small features (small b/w, a/w, d/h values), a minimum of 8 elements were placed along the groove and ridge walls (x and z-directions), which has been determined in this system to be sufficient resolution to ensure the predicted flow field is independent of the mesh density. The top face was meshed with a tri/pave scheme, where the face was split into several domains dictated by a projection of the grooves below. The volume of the SGM was then discretized with a structured mesh with nodes placed at equal z-values. This mesh density corresponds to a minimum of 1.5 million elements per computational simulation. The boundary conditions for the channel inlet was v_y = constant, $v_x = v_z = 0$, where it was determined that the constant velocity inlet condition had no impact on the magnitude of helical flow downstream. A constant pressure condition on the outlet was used along with a no-slip condition on all surfaces, with water at 25°C and 1 atm used for the operating fluid. The SIMPLE-Consistent method was used to couple the momentum and continuum equations, with a second-order upwind discretization scheme for the velocity calculations. The simulations were considered converged when the normalized residuals for the velocities and continuity fell below 10^{-7} and 10^{-4}, respectively.

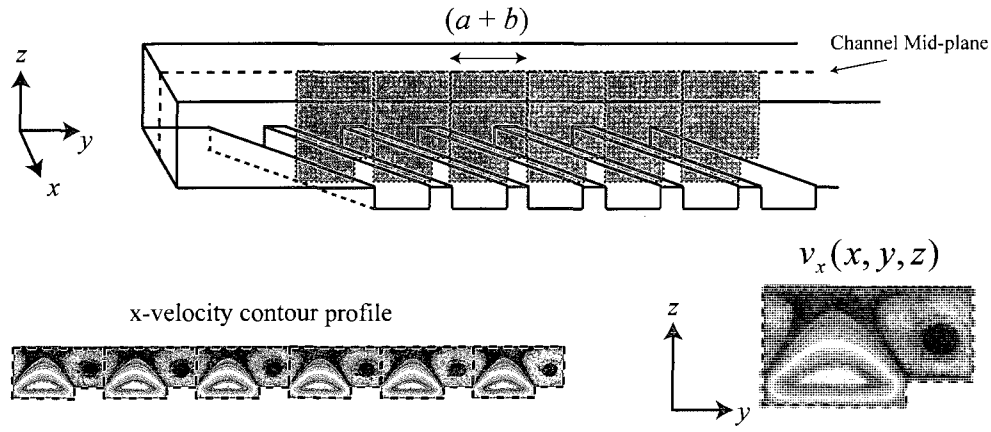

Figure 2.4. Typical domain of the SGM used in this study. Numerical data is exported from the mid-plane of the SGM. The x-velocity contour profile used with Eqn. (1) is shown below.

For purposes of consistency, the magnitude of non-axial flow within the SGM has been analyzed by calculating the magnitude of re-circulating flow towards the center of the channel. Figure 2.4 displays a computational domain of a typical SGM in this study, together with the non-axial (x) velocity contour profile in the center of the channel. The x-velocity profile along the mid-plane of the SGM is divided into planes correlating to one groove and its neighboring ridge.

For each individual plane the non-axial volumetric flow (Q_n) is

$$Q_n = \int_y \int_z [v_x(x, y, z)]_{v_x<0} \, dydz \,, \tag{2.1}$$

where restricting the integration to values of $v_x < 0$ ensures the quantification of fluid passing through the mid-plane in one direction only. To quantify the magnitude of helical flow within the SGM, the ratio of non-axial (Q_n) to axial flow (Q_a) is calculated as

$$\eta = \frac{Q_n w}{Q_a (a+b)} = \frac{Q_n}{\langle v_y \rangle h(a+b)}, \tag{2.2}$$

where Q_n and $Q_a = \langle v_y \rangle wh$ have been normalized by the groove-ridge length ($a + b$) and channel width w, respectively. The ratio η provides a reliable measure of the relative magnitude of secondary re-circulation flow, and thus the total magnitude of helical flow, above the grooves. Also, η is independent of the volumetric flow rate through the SGM (for $Re < 100$, where $Re = \langle v_y \rangle w / \nu$ for a fluid with kinematic viscosity ν, highlighting the insensitivity of the flow profile to the Reynolds number within SHM-type devices. Because axial velocities v_y are much higher than the non-axial velocities v_x and v_z, it is convenient to use v_y in the calculation of *Re*. Similarly, the magnitude of axial flow situated in the rectangular section described by h and w is much higher than the magnitude of non-axial flow situated within the grooves, therefore the characteristic length is chosen as w. Choosing the hydraulic or equivalent diameter of the channel yields similar order-of-magnitude values of *Re,* and is unimportant for values of $Re < 100$ as η is independent of *Re*. For all cases considered in this study, $Re = 0.02$. Figure 2.5 displays η as a function of groove number for several typical SGM geometries in this study; η reaches a maximum value within w axial lengths from the start and end of the groove cycle, where the variation between the maximum value and that in the center of the groove cycle varies by less than 5%. The drop off in the magnitude of η as the groove cycle ends is due to the dissipation of the effects of the flow rate through the grooves, as non-axial flow in the opposite direction is spread out along the axial length of the channel. This observation is consistent with the work by Yang *et al.*,[34] in which the volumetric flow rate through the first and last grooves per half-cycle were higher than the center grooves. The values of η reported in this study are the maximum values of η vs. groove number (as shown in figure 2.5).

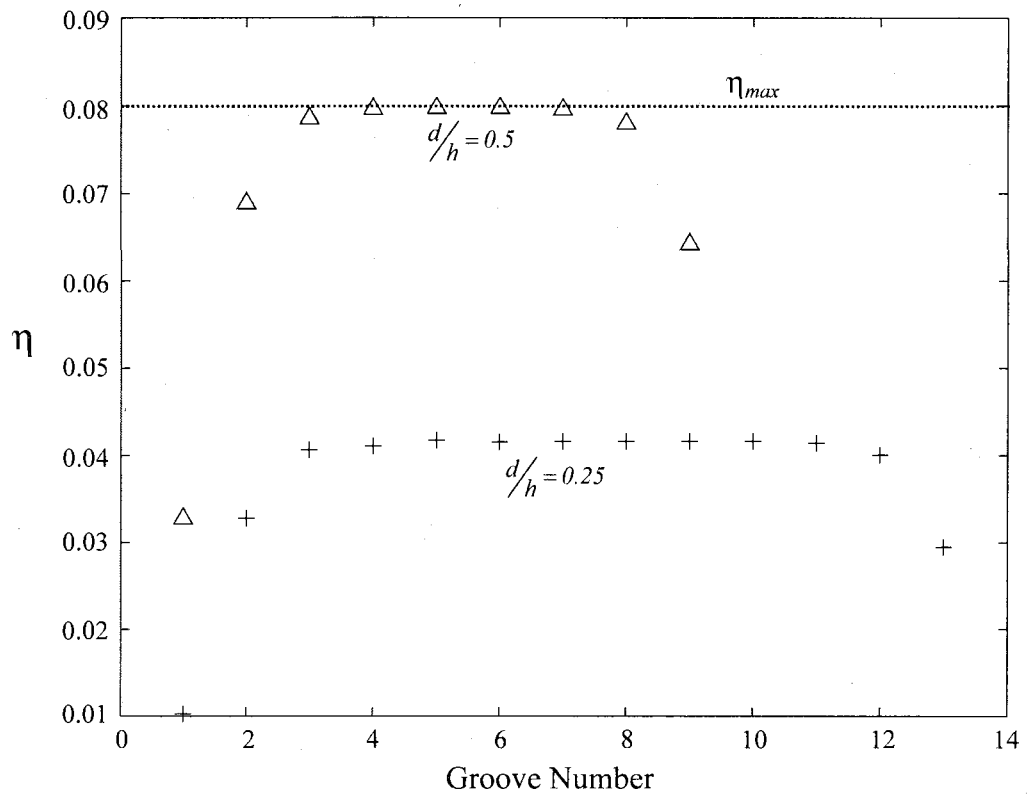

Figure 2.5. Ratio of non-axial to axial flow η vs. the groove number for several SGMs with a/w = 0.4, b/w = 0.1, and h/w = 0.4.

2.4 Comparison with Previous Characterization Methods

Previous characterization of helical flow over patterned grooves included the maximum velocity ratio $(v_x/v_y)_{max}$, located near the top of the channel.[18, 26] Although $(v_x/v_y)_{max}$ is easy to calculate both computationally and experimentally, there are certain mixer geometries with notably different helical flow magnitudes that possess the same value of $(v_x/v_y)_{max}$.

Figure 2.6*A* displays η vs. $(v_x/v_y)_{max}$ for the 800+ SGM geometries within this study. For devices which exhibit low magnitudes of helical flow, η is proportional to $(v_x/v_y)_{max}$. However, as the magnitude of helical flow increases, there exists many cases where the same value of $(v_x/v_y)_{max}$ leads to different flow behavior. For example, there exists more

than 5 SGM geometries within this study that possess the same value of $(v_x/v_y)_{max}$ = 0.235, however, these same devices demonstrate a range of calculated η values of $0.32 \leq \eta \leq 0.42$. This effect is highlighted in figure 2.6*B*, which shows (v_x/v_y) values along the normalized height of two SGMs, where the (v_x/v_y) values were averaged over one groove cycle length $(a + b)$ along the channel mid-plane. Both devices display the same $(v_x/v_y)_{max}$ value, located near the top wall of the SGM. The (v_x/v_y) profile of the two SGMs are very similar near the top of the micro-channel; however, this similarity changes drastically near the bottom of the micro-channel, close to the grooves. The discrepancy between the profiles of the two generic SGMs is further highlighted in Fig. 2.6*C*, which displays the *y*-averaged normalized *x*-velocity profile of the same two mixers shown in Fig. 2.6*B*. The quantitative helical flow pattern for the SGM can be seen in Fig. 2.6*C*, as values of v_x are positive near the top of the microchannel and negative near the grooves. It is obvious that the magnitude of helical flow is greater in the 2nd simulation (shown in the red data). In general, geometrical changes in the SGM produce similar trends in both $(v_x/v_y)_{max}$ and η; however, characterization via η gives a more accurate representation of helical flow within a SGM (and SHM).

Equation 1 is similar to the methods of helical flow characterization employed by Yang *et al.* in their analysis of the volumetric groove flow rate for different mixer geometries.[34] Rather, this approach taken accounts for the *effects* of the flow within the grooves, furthermore accounting for changes in the groove geometries, to provide a common, platform-independent metric for the comparison of different mixers. The relationship between helical flow rates and mixing efficiency within SHM type devices have been previously reported.[5, 19, 34] Larger values of η translate to higher rates of mixing in a SHM within the individual cycles, which correlates to a smaller length of a SHM needed for complete mixing.

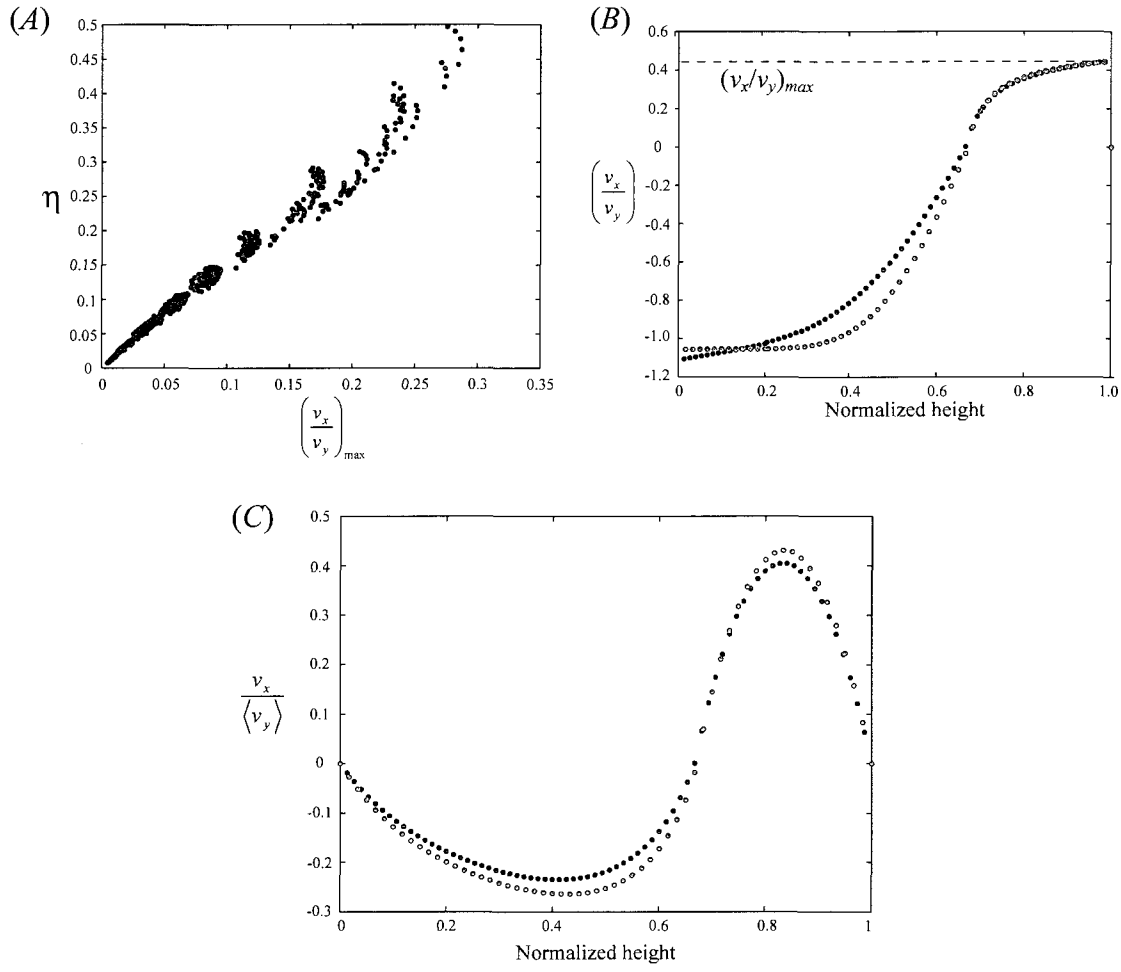

Figure 2.6. (*A*) Values of η vs. values of $(v_x/v_y)_{max}$ for the range of SGM geometries in this study. (*B*) *y*-averaged (v_x/v_y) vs. the normalized height for two generic SGMs exhibiting the same value of $(v_x/v_y)_{max}$. (C) Normalized *y*-averaged *x*-velocity profile vs. the normalized height for the SGMs shown in (*B*).

2.5 Helical Flow within a SGM

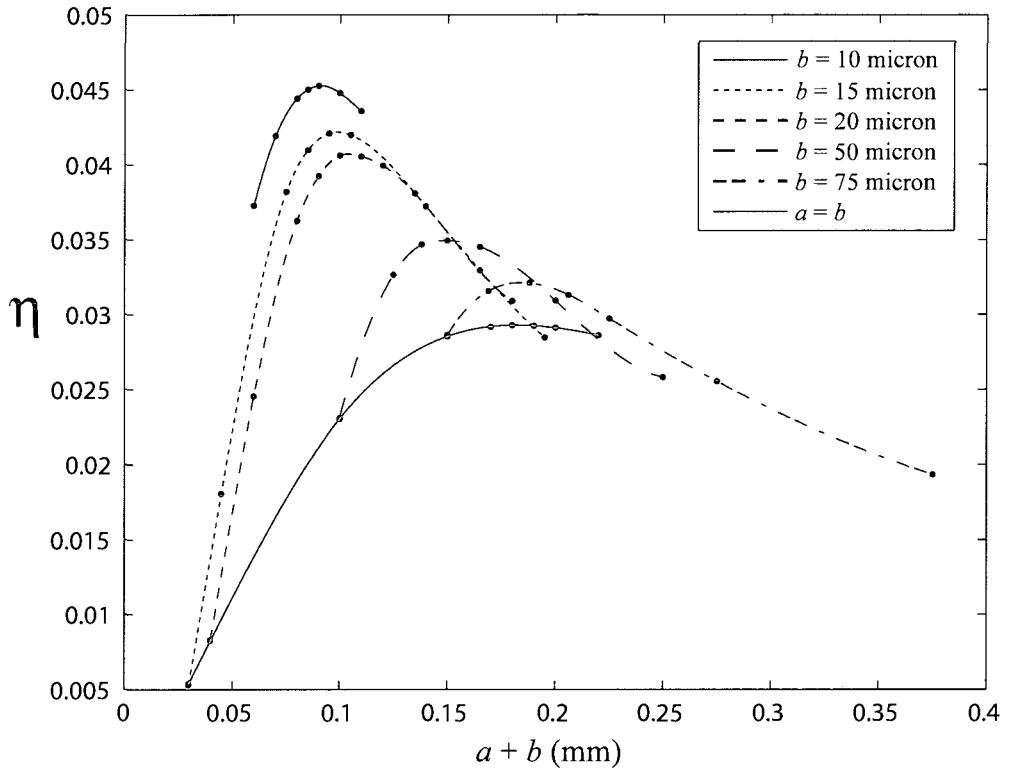

Figure 2.7. η vs. the total groove length ($a + b$) for several SGMs with h = 80 μm, w = 200 μm, and d = 20 μm. The red line indicates the constrained SGM, with $a = b$.

For a SGM with specific d/h and h/w ratios, there will exist an optimum groove spacing that maximizes helical flow. To determine this optimum spacing, helical flow within several SGMs with varying groove geometries (constant d/h and h/w ratios) is calculated. Figure 2.7 displays η versus ($a + b$) for several values of a set ridge length b (including the case $a = b$) for a SGM with dimensions h = 80 μm, w = 200 μm, and d = 21 μm. The channel aspect ratio h/w = 0.4 and groove depth ratio d/h = 0.2625 correspond well to previous experimental and numerical studies.[10, 17]

From Fig. 2.7 it is observed that, as b decreases, the maximum obtainable value of η increases by up to 50% of the base ($a = b$) case. For example, the SGM base case yields a maximum ratio $\eta = 0.03$ at a groove spacing of $a = b = 78$ μm, whereas the optimized SGM ($b = 10$ μm) exhibits a maximum ratio $\eta = 0.045$ at a groove spacing of $a = 78$ μm. It can be seen that as b is minimized, the maximum obtainable value of η increases, and the total groove spacing ($a + b$) at which this maximum value occurs decreases, allowing for an increase in grooves per cycle length. To further highlight this effect of optimizing the groove spacing, figure 2.8 displays normalized concentration distributions along two SGMs, one of which has been optimized for helical flow. The CFD simulation pertains to a generic solute (diffusion coefficient $D = 10^{-10}$ m^2 s^{-1}, $Pe_{mesh} = 4$) initially segregated on one side of the SGM inlet ($\langle v_y \rangle = 1$ mm/s), where the SGM has dimensions $h = 60$ μm, $w = 200$ μm, and $d = 30$ μm. Flow through the optimized SGM undergoes an approximately 360° twist ($\eta = 0.09$) within 2 mm of axial length, whereas flow through a SGM with symmetric grooves ($a = b$) undergoes only a 180° twist ($\eta = 0.047$) for the same axial channel length. Figure 2.8 displays the relationship between η and the total magnitude of helical flow within a SGM, where it appears that η is proportional to the fluid twist per axial length of channel; however, this relationship has yet to be further clarified.

It is now clear that an increase in helical flow within a SGM can be accomplished in a straightforward manner by optimizing the geometrical parameters of the grooves present on the micro-channel floor. These optimized grooves lead to an increase in the re-circulatory flow above the grooves, as well as flow within the grooves themselves. Figure 2.7 highlights the optimized parameters for a channel with geometric ratios $h/w = 0.4$ and $d/h = 0.2625$. Optimized groove geometries of micro-channels with varying h/w and d/h, along with the resulting effects on η, will be discussed further in the next section.

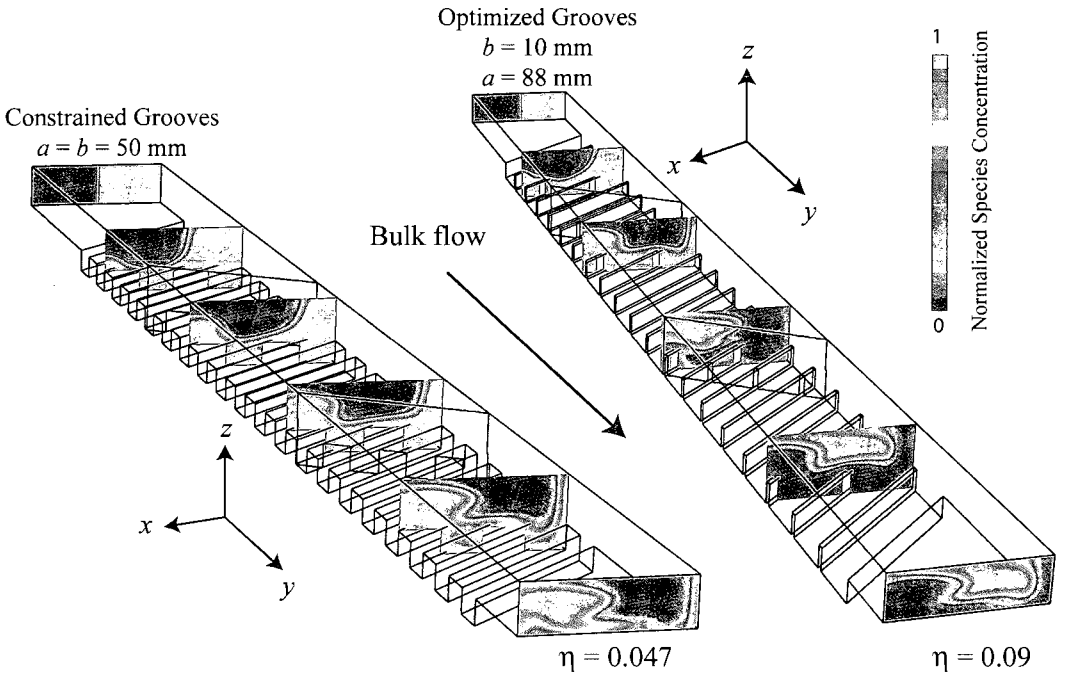

Figure 2.8. Comparison of concentration distributions displaying helical flow between a SGM with constrained grooves (left) and optimized grooves (right). The SGM has absolute dimensions of w = 200 μm, h = 60 μm, and d = 30 μm.

2.6 Geometric Optimization

It remains important to maintain flexibility in SHM or SGM geometries during the design of lab-on-a-chip processes, and to this end a wide range of geometric ratios were chosen for this study. The range of channel aspect ratios for this study was chosen as $0.2 < h/w < 0.45$. For each h/w value, a range of groove depth ratios was chosen as $0.09 < d/h < 2$, at which three b/w values were studied: $b/w = 0.05$, 0.10, and 0.15. Some of the parameter space was not studied due to the potential fabrication difficulties associated with high aspect ratio grooves (channels with low b/w and high d/h ratios). A minimum of 6 CFD cases corresponding to geometries with varying a/w were computed for each microchannel geometry (h/w, d/h, b/w). For these cases, a cubic spline function was fit to η as a function of a to evaluate the optimized a/w value for that geometry (The cubic spines are shown along with the CFD data in figure 2.7). For randomly selected channel geometries, the difference between the optimized a/w value computed from 6 CFD cases and the value utilizing 10 or more cases was less than 4%.

2.6.1 Optimization of Groove Geometry with Depth Ratio d/h

The groove depth ratio has previously been found to be the most sensitive parameter affecting the magnitude of helical flow over grooved surfaces.[5, 31, 32, 34] At the time of this work there had been no study on the dependency of the groove geometries on the d/h ratio. Figure 2.9 displays the optimized groove geometries, shown as a/w versus d/h, for a wide range of h/w and b/w values. As expected, a/w increases asymptotically with increasing d/h, due to the fact fluid near the bottom of deeper grooves has less impact on the flow profile through the SGM. The groove length is also dependent on the ridge length used, as for constant h/w and d/h values, a/w increases with increasing values of b/w. For precise fabrication of optimized mixing devices between the data points shown in figure 2.9, the optimized groove geometries may be fit to the asymptotic relationship:

$$\frac{a}{w} = a_0\left[1-\exp\left(-a_1\left(\frac{d}{h}\right)^{a_2}\right)\right]. \tag{2.3}$$

Non-linear regression was used to calculate the parameters a_0, a_1, and a_2, and these values are shown in table 2.1. All of the curves (constant *h/w*, *b/w*) resulting from Eqn. (2.3) yielded non-linear regression R^2 coefficient values greater than 0.992. The asymptotic value a_0 is found to be proportional to *h/w*, as seen in figure 2.9*C*; however, this relationship has yet to be confirmed for values outside the range considered in this study. Equation (2.3) is not meant to elucidate the physical relationships between the parameters important to helical flow within a SGM, it is simply a sizing guide for optimized fabrication of these devices.

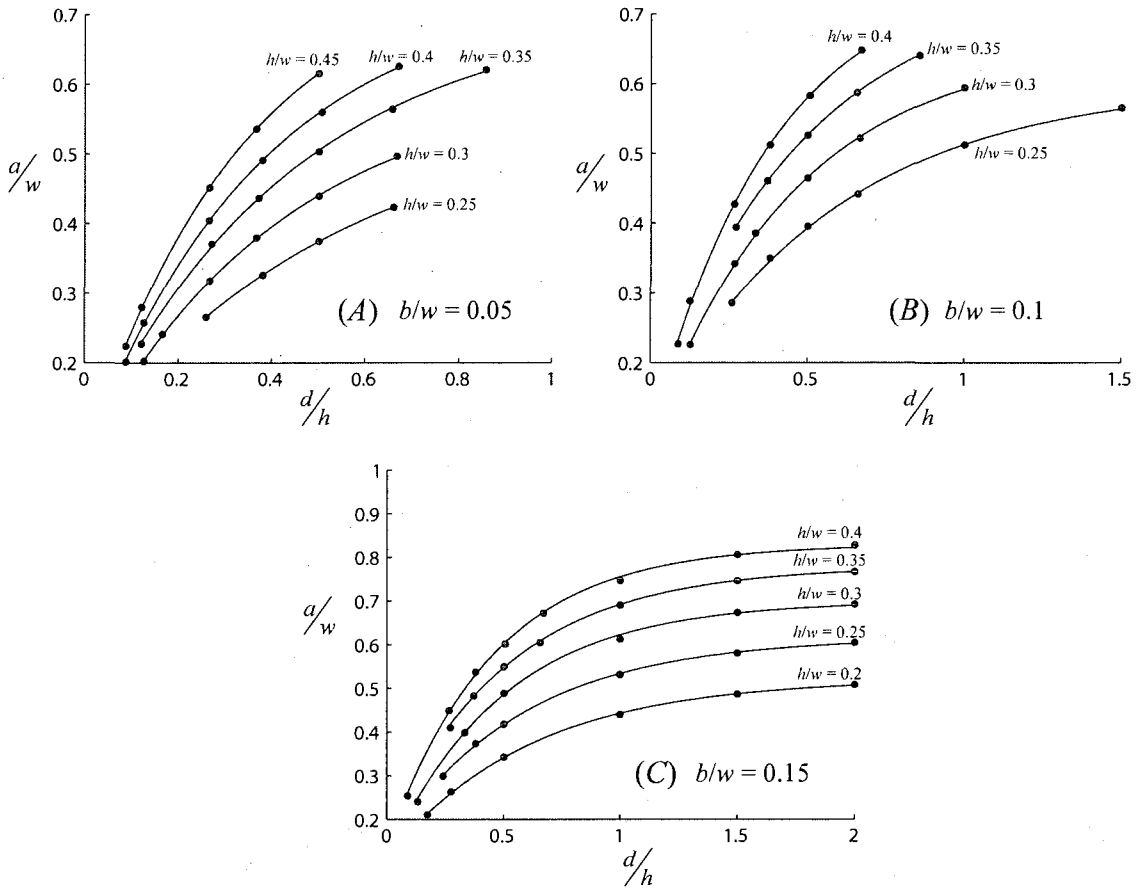

Figure 2.9. Optimized groove geometries, shown as *a/w* vs. *d/h*, for several different channels of varying *h/w* and *b/w*.

h/w	b/w	a_o	a_1	a_2
0.25	0.05	0.661 (0.19)	1.39 (0.77)	0.741 (0.14)
0.30	0.05	0.70 (0.030)	1.70 (0.13)	0.777 (0.019)
0.35	0.05	0.793 (0.010)	1.72 (0.049)	0.772 (0.008)
0.4	0.05	0.824 (0.023)	1.96 (0.128)	0.802 (0.016)
0.45	0.05	0.878 (0.047)	2.13 (0.25	0.816 (0.030)
0.25	0.1	0.637 (0.020)	1.62 (0.138)	0.743 (0.039)
0.30	0.1	0.733 (0.027)	1.67 (0.147)	0.734 (0.027)
0.35	0.1	0.814 (0.030)	1.74 (0.160)	0.74 (0.032)
0.4	0.1	0.915 (2.0e-6)	1.64 (4.9e-6)	0.718 (2.9e-6)
0.2	0.15	0.555 (0.019)	1.56 (0.150)	0.686 (0.041)
0.25	0.15	0.641 (0.010)	1.75 (0.096)	0.723 (0.029)
0.3	0.15	0.724(0.019)	1.87 (0.18)	0.772 (0.050)
0.35	0.15	0.793 (0.011)	2.03 (0.120)	0.787 (0.038)
0.4	0.15	0.865 (0.021)	1.97 (0.160)	0.726 (0.040)

Table 2.1. Non-linear regression parameters for Eq. (3). 95% confidence intervals shown in parentheses.

Figure 2.10 shows η as a function of *d/h* for the optimized *a/w* values shown in figure 2.9*C*; η increases linearly at low groove depth ratios ($d/h < 0.6$), followed by an asymptotic increase at higher *d/h* ratios. This result parallels that of Stroock *et al.*[18] along with previous numerical studies,[26, 31, 32] likely because η follows the same trends as the maximum velocity ratio (v_x/v_y) concerning flow over patterned grooves. As with the asymptotic relationship seen in figure 2.9, as *d/h* increases there is a limit to the obtainable volumetric flow within the grooves, and thus a limit to what values η can attain. Due to the mechanical stability of the ridges themselves, the asymptotic maximum helical flow strength with respect to the groove depth ratio is most likely out of the range of devices readily fabricated via soft lithographic methods; however, these structures very well may be obtainable utilizing other micro-channel substrates. Interestingly, for low aspect ratio channels, the asymptotic maximum for the groove length occurs at *d/h* values much lower than the maximum for helical flow. Thus, there is a limit for which the groove spacing becomes constant, yet η still increases with increasing *d/h*. Figure 2.10 highlights the effect of optimizing the groove spacing, and as for channels with $h/w = 0.3$,

a SGM with constant ridge ratio $b/w = 0.15$ displays helical flow magnitudes approximately 25% higher than a channel with symmetric ridges (red line). This increase in η for optimized groove spacing becomes greater as b/w is further minimized.

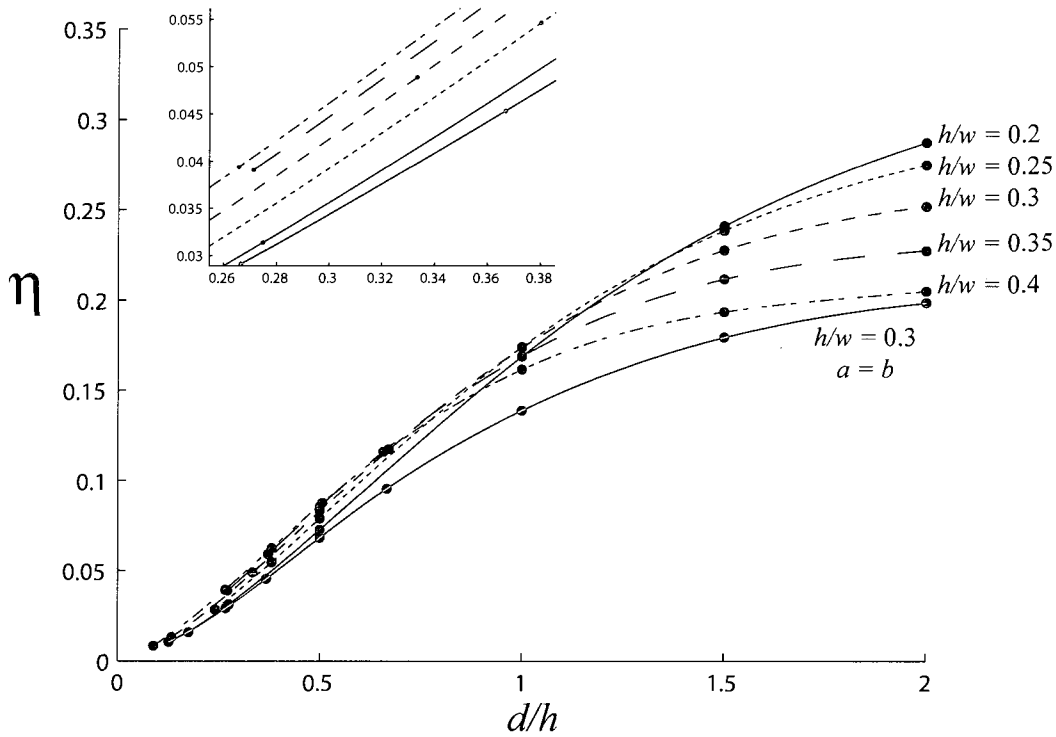

Figure 2.10. η vs. d/h shown for a SGM with $b/w = 0.15$, with optimized groove geometries corresponding to the points in figure 2.9 (c). The red line relates to a constrained SGM with ($a = b$).

2.6.2 Optimization of Channel Aspect Ratio *h/w* with Groove Depth Ratio

The sensitivity of helical flow on the channel aspect ratio can be seen in figure 2.10. At low groove depth ratio values ($d/h < 0.5$), higher aspect ratio channels exhibit the highest rates of helical flow. As the groove depth ratio is increased, an inversion occurs and helical flow becomes greater in lower aspect ratio channels. Thus for a specific groove depth ratio, there exists an optimum channel aspect ratio for maximizing helical flow.

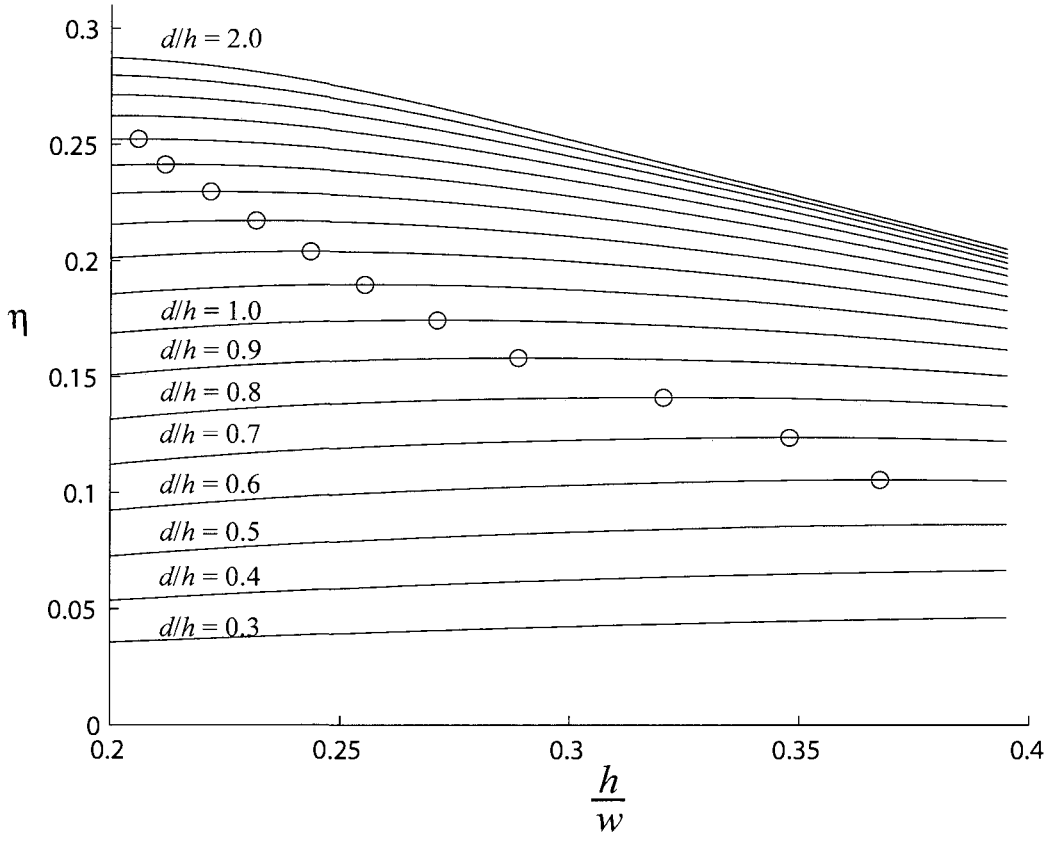

Figure 2.11. η vs. h/w for channels with $b/w = 0.15$ and d/h ranging in increments of 0.1 from $0.3 \leq d/h \leq 2.0$. The maximum values of η on each line are shown with the red circles.

Figure 2.11 shows helical flow strength as a function of the channel aspect ratio for several groove depth ratio values ($b/w = 0.15$). As the groove depth ratio is increased, the optimum channel aspect ratio decreases, where at groove depth ratios of $d/h > 1.6$ and $d/h < 0.6$, the maximum lies outside of the range considered in this study. Despite the lack of data for low values of d/h, it is apparent that the channel aspect ratio has a strong affect on helical flow. For example, for channels with $d/h = 0.4$, there is a 25% increase in helical flow from an aspect ratio $h/w = 0.2$ ($\eta = 0.053$) to an aspect ratio of $h/w = 0.4$ ($\eta = 0.066$). The maximum values of η shown in figure 2.11 are displayed in table 2.2.

For the range of parameters used in this study, the optimized h/w values are independent of b/w. A previous study, in which only three channel aspect ratios were

examined, determined that this parameter had minimal impact on helical flow.[34] The data in table 2.2 demonstrate that this conclusion is not correct. Not only does *h/w* have a strong impact on helical flow over patterned grooves, but the optimized *h/w* value is also dependent on *d/h*. Current work is focused on elucidating the limits of the optimized aspect ratio when $d/h \rightarrow 0$ or $d/h \gg 1$.

The results shown in figure 2.9, figure 2.10, and figure 2.11 display the effects of *d/h*, *h/w*, *b/w*, and *a/w* on the total helical flow magnitude η within a SGM. Of the four dimensionless parameters, helical flow is most sensitive to *d/h*; however helical flow can be significantly increased by minimizing *b/w* while simultaneously optimizing *h/w* and *a/w*. When designing devices that utilize patterned grooves for lateral transport of fluid, all of the above geometric parameters need to be taken into account for complete optimization of the device.

d/h	opt. h/w	η_{max}
0.3	> 0.4	n.a.
0.4	>0.4	n.a.
0.5	0.393	0.086
0.6	0.367	0.105
0.7	0.348	0.124
0.8	0.320	0.141
0.9	0.289	0.158
1.0	0.271	0.174
1.1	0.255	0.190
1.2	0.234	0.204
1.3	0.232	0.217
1.4	0.222	0.230
1.5	0.212	0.241
1.6	0.206	0.252
1.7	< 0.2	n.a.
1.8	< 0.2	n.a.
1.9	< 0.2	n.a.
2.0	< 0.2	n.a.

Table 2. η vs. *h/w* optimization parameters.

2.7 Implications for the Staggered Herringbone Mixer

The optimization procedure described in this study was specific to the SGM; however, these techniques can be applied to any device using patterned grooves for non-axial fluid transport purposes (specifically the BEM and SHM). Optimizing fluid in the BEM is straightforward, and the SHM can be though of as two SGM devices adjacent to one another with aspect ratios h/w_s and h/w_l (figure 2.3), where the asymmetry of the herringbone pattern is such that $w_l = p\,w$. For these two sections, $h/w_s = 2h/w_l$, and helical flow over the long arm will most likely be different than that over the short arm (cf. figure 2.11), in contradiction with the boundary conditions used in the analytical model developed by Stroock *et al.*[19] It is reasonable to expect that fluid flow within the long arm of the SGM is the primary mechanism for fluid mixing, thus the SHM should be sized via h/w_l, b/w_l, and a/w_l for flow optimization over the long arm, where the short arm retains the same groove geometries a, b, and d. Computational studies of helical flow on the long arm of the SHM varied by less than 3% of that within the SGM when $(a/w_l)_{SHM} = (a/w)_{SGM}$, $(h/w_l)_{SHM} = (h/w)_{SGM}$, and $(b/w_l)_{SHM} = (b/w)_{SGM}$ within SHM and SGM devices with the same d/h value (data not shown). For SHM type devices with grooves placed on more than one wall, such as those displayed by Sato et al.,[23, 24] we expect the optimization procedure to be equivalent to that shown above, where the defining ratios of such a mixer would remain d/h, h/w, and b/w.

2.8 Future Work

Although the magnitude of helical flow within a SHM device is important, other design properties also contribute significantly to the creation of chaotic flow. One important factor is the number of grooves per half-cycle (N_g). Several groups have studied the effect of N on the mixing performance of SHM-type devices.[5, 33] Li *et al.* found that the mixing performance was dependent on N_g, as long as N_g was above a particular value (in their case, $N_g \geq 4$). The values of N_g that Aubin *et al.* used were much

higher (N_g = 10, 20, and 30), and no dependence of the mixing performance on N_g was found. These results suggest that there exists not a critical value of N_g, but a critical length of each half-cycle (L_c), below which the mixing performance of the SHM will suffer. By optimizing the geometries of the SHM using the relationships found in figure 2.9 and 2.11, the rate at which fluid is transferred laterally across the floor, as well as the exchange of fluid between the two counter-rotating currents, will be maximized. This should serve to have a profound effect on the mixing performance of such devices, since the value of L_c for an optimized SHM should be well below that of previous SHM designs.

Unlike other passive mixing devices, curves of the extent of mixing vs. axial distance for the SHM are not smooth, containing discontinuities and plateaus.[5, 29] In these studies there are many cases where the extent of mixing concerning two mixers with different geometries follow unusual trends, where one mixer might display dominant mixing performance through the initial stages (e.g. first 4 mixing cycles) of the mixer, after which the second mixer dominates. It appears that a *minimum* of 5-10 complete cycles is needed for comparison of different mixer geometries. Low mesh densities can be used for the solution to the momentum and continuum equations with high accuracy; however, the same cannot be said for the solution to the convection-diffusion equation, where numerical artifacts enhance the rate of diffusion. Discretization schemes for accurate solutions to the convection-diffusion equation require roughly an order-of-magnitude more computational elements than those used in this study, and are unrealistic to assess the mixing performance of SHM geometries consisting of more than 4 cycles. Numerical determination of L_c for a given SHM geometry is therefore best accomplished through the use of particle tracking methods.

A brief description of these particle tracking methods are discussed here, where further details can be found chapter 3. First, the velocity field regarding both half-cycle SHM geometries, as shown in Fig. 2.1*A*, would be computed using the methods discussed

above. This would necessitate multiple CFD simulations with each simulation pertaining to set values of d/h, b/w, a/w, h/w, and N_g. After each simulation convergences to a solution of predetermined accuracy, solutions of $v = v(x, y, z)$ are exported from Fluent for use in particle tracking and computation of η via Eqn. (2.1). A series of massless tracer particles (on the order of 10^5-10^6 particles) are initialized in the flow field such that all particles occupy a small portion of mixer inlet, usually confined to half of the inlet cross-section. The positions of the particles are then calculated as a function of time via Lagrangian integration of the velocity field. The mixing characteristics of a multi-cycle SHM can be approximated tracking particles through multiple half-cycles, where the particle positions of the n^{th} half-cycle are used as inputs to the $(n+1)^{th}$ half-cycle. After computation of the particle positions throughout the mixer, the extent of mixing can be calculated with the statistical entropy methods discussed in Camesasca *et al.*[35] Relationships between the extent of mixing as a function of the SHM geometry (for a given cycle number) can then be used to calculate L_c. Current studies indicate that the values of L_c in optimized SHM devices may be as small as $L_c = w$, long enough to necessitate only several grooves per half-cycle. These optimized devices correlate to overall lengths that would be more than 50% lower than traditional SHM devices.

2.9 Conclusions

Helical flow is investigated within the slanted groove mixer (SGM), whose geometry can be completely described by the ratios d/h, h/w, a/w, and b/w. Relative helical flow magnitude is described by the parameter η, which the ratio of transverse to axial flow rate over individual grooves, normalized by the length of the groove and neighboring ridge as well as the width of the microchannel. Over 800 channels with differing geometries (as described by d/h, h/w, a/w, and b/w) were studied via computational fluid dynamics (CFD) using the commercial package Fluent®.

Helical flow within a SGM is found to be dependent on all four geometric ratios. For a SGM with specific values of d/h, b/w, and h/w, there exists an optimum groove geometry a/w that will maximize helical flow. By removing the constraint that grooves and ridges remain symmetric (i.e., the base case $a = b$), as has been used in all previous studies, non-axial fluid transport can be substantially increased. In particular, helical flow increases significantly as the ridge length ratio b/w is minimized, where the optimum value of a/w is further dependent on the specific ratios d/h and h/w. Figures 2.9 and 2.11, (or tables 1 and 2) may be directly applied as design criteria for a SGM. After the values for the groove depth (d) and channel height (h) are chosen (the two geometries defined by the Su-8 spin coating process, for example), the channel width can be optimized via table 2, and the groove geometries can be interpolated using table 1. Although the groove geometries will be dependent on specific lithographic capabilities, larger values of b/w can still provide a significant increase from symmetric grooves, providing the grooves are sized appropriately. For other fabrication methods, such as micro-milling, fabrication of small a/w ratios can be a challenge, as the smallest available cutting tool is approximately 100 μm. Thus micro-milling fabrication of optimized mixers whose overall size is relatively small might not be possible (for example, $w < 200$ μm).

While this study deals specifically with optimization of helical flow within a slanted groove mixer, it can also be used to optimize flow within a staggered herringbone mixer (SHM). Rather than normalizing geometric parameters with the total width w of the channel, the SHM is sized to the width of the long arm w_l. Thus a/w_l, h/w_l, and b/w_l are sized according to figures 2.9 and 2.11. By optimizing the long arm of the SHM, the critical length for each half-cycle of grooves is expected to decrease, however, this has yet to be confirmed. Regardless, optimized flow within a SHM correlates to a higher magnitude of non-axial flow located within the grooves, which has been shown in the past to provide faster mixing rates. This study presents the first sizing guide for optimization of flow over patterned grooves, such that the optimization procedure will

provide faster rates of non-axial transport—and hence, mixing—within the SGM, SHM and BEM.

2.10 References

1. J. M. Ottino and S. Wiggins, (2004) Introduction: mixing in microfluidics *Philosophical Transactions of the Royal Society of London Series a-Mathematical Physical and Engineering Sciences*, **362**, 923-935.
2. H. A. Stone, A. D. Stroock and A. Ajdari, (2004) Engineering flows in small devices: Microfluidics toward a lab-on-a-chip *Annual Review of Fluid Mechanics*, **36**, 381-411.
3. T. J. Johnson, D. Ross and L. E. Locascio, (2002) Rapid microfluidic mixing *Analytical Chemistry*, **74**, 45-51.
4. H. Y. Wu and C. H. Liu, (2005) A novel electrokinetic micromixer *Sensors and Actuators a-Physical*, **118**, 107-115.
5. J. Aubin, D. F. Fletcher and C. Xuereb, (2005) Design of micromixers using CFD modelling *Chemical Engineering Science*, **60**, 2503-2516.
6. A. Dodge, M. C. Jullien, Y. K. Lee, X. Niu, F. Okkels and P. Tabeling, (2004) An example of a chaotic micromixer: the cross-channel micromixer *Comptes Rendus Physique*, **5**, 557-563.
7. X. Z. Niu and Y. K. Lee, (2003) Efficient spatial-temporal chaotic mixing in microchannels *Journal of Micromechanics and Microengineering*, **13**, 454-462.
8. M. H. Oddy, J. G. Santiago and J. C. Mikkelsen, (2001) Electrokinetic instability micromixing *Analytical Chemistry*, **73**, 5822-5832.
9. N. Sundaram and D. K. Tafti, (2004) Evaluation of microchamber geometries and surface conditions for electrokinetic driven mixing *Analytical Chemistry*, **76**, 3785-3793.
10. F. Jiang, K. S. Drese, S. Hardt, M. Kupper and F. Schonfeld, (2004) Helical flows and chaotic mixing in curved micro channels *Aiche Journal*, **50**, 2297-2305.
11. A. P. Sudarsan and V. M. Ugaz, (2006) Multivortex micromixing *Proceedings of the National Academy of Sciences of the United States of America*, **103**, 7228-7233.
12. A. Gunther, S. A. Khan, M. Thalmann, F. Trachsel and K. F. Jensen, (2004) Transport and reaction in microscale segmented gas-liquid flow *Lab on a Chip*, **4**, 278-286.
13. H. Song, M. R. Bringer, J. D. Tice, C. J. Gerdts and R. F. Ismagilov, (2003) Experimental test of scaling of mixing by chaotic advection in droplets moving through microfluidic channels *Applied Physics Letters*, **83**, 4664-4666.
14. R. H. Liu, M. A. Stremler, K. V. Sharp, M. G. Olsen, J. G. Santiago, R. J. Adrian, H. Aref and D. J. Beebe, (2000) Passive mixing in a three-dimensional serpentine microchannel *Journal of Microelectromechanical Systems*, **9**, 190-197.

15. H. Chen and J. C. Meiners, (2004) Topologic mixing on a microfluidic chip *Biophysical Journal*, **86**, 482a-482a.
16. D. Therriault, S. R. White and J. A. Lewis, (2003) Chaotic mixing in three-dimensional microvascular networks fabricated by direct-write assembly *Nature Materials*, **2**, 265-271.
17. A. D. Stroock, S. K. W. Dertinger, A. Ajdari, I. Mezic, H. A. Stone and G. M. Whitesides, (2002) Chaotic mixer for microchannels *Science*, **295**, 647-651.
18. A. D. Stroock, S. K. Dertinger, G. M. Whitesides and A. Ajdari, (2002) Patterning flows using grooved surfaces *Analytical Chemistry*, **74**, 5306-5312.
19. A. D. Stroock and G. J. McGraw, (2004) Investigation of the staggered herringbone mixer with a simple analytical model *Philosophical Transactions of the Royal Society of London Series a-Mathematical Physical and Engineering Sciences*, **362**, 971-986.
20. Y. N. Xia and G. M. Whitesides, (1998) Soft lithography *Angewandte Chemie-International Edition*, **37**, 551-575.
21. P. Sethu, L. L. Moldawer, M. N. Mindrinos, P. O. Scumpia, C. L. Tannahill, J. Wilhelmy, P. A. Efron, B. H. Brownstein, R. G. Tompkins and M. Toner, (2006) Microfluidic isolation of leukocytes from whole blood for phenotype and gene expression analysis *Analytical Chemistry*, **78**, 5453-5461.
22. D. S. Kim, S. W. Lee, T. H. Kwon and S. S. Lee, (2004) A barrier embedded chaotic micromixer *Journal of Micromechanics and Microengineering*, **14**, 798-805.
23. H. Sato, S. Ito, K. Tajima, N. Orimoto and S. Shoji, (2005) PDMS microchannels with slanted grooves embedded in three walls to realize efficient spiral flow *Sensors and Actuators a-Physical*, **119**, 365-371.
24. H. Sato, D. Yagyu, S. Ito and S. Shoji, (2006) Improved inclined multi-lithography using water as exposure medium and its 3D mixing microchannel application *Sensors and Actuators a-Physical*, **128**, 183-190.
25. S. Chen and G. D. Doolen, (1998) Lattice Boltzmann method for fluid flows *Annual Review of Fluid Mechanics*, **30**, 329-364.
26. F. Schonfeld and S. Hardt, (2004) Simulation of helical flows in microchannels *Aiche Journal*, **50**, 771-778.
27. Y. Z. Liu, B. J. Kim and H. J. Sung, (2004) Two-fluid mixing in a microchannel *International Journal of Heat and Fluid Flow*, **25**, 986-995.
28. T. G. Kang and T. H. Kwon, (2004) Colored particle tracking method for mixing anlysis of chaotic micromixers *Journal of Micromechanics and Microengineering*, **14**, 891-899.
29. M. Camesasca, I. Manas-Zloczower and M. Kaufman, (2005) Entropic characterization of mixing in microchannels *Journal of Micromechanics and Microengineering*, **15**, 2038-2044.
30. J. Aubin, D. F. Fletcher, J. Bertrand and C. Xuereb, (2003) Characterization of the mixing quality in micromixers *Chemical Engineering & Technology*, **26**, 1262-1270.
31. H. Z. Wang, P. Iovenitti, E. Harvey and S. Masood, (2003) Numerical investigation of mixing in microchannels with patterned grooves *Journal of Micromechanics and Microengineering*, **13**, 801-808.

32. D. G. Hassell and W. B. Zimmerman, (2006) Investigation of the convective motion through a staggered herringbone micromixer at low Reynolds number flow *Chemical Engineering Science*, **61**, 2977-2985.
33. C. A. Li and T. N. Chen, (2005) Simulation and optimization of chaotic micromixer using lattice Boltzmann method *Sensors and Actuators B-Chemical*, **106**, 871-877.
34. J. T. Yang, K. J. Huang and Y. C. Lin, (2005) Geometric effects on fluid mixing in passive grooved micromixers *Lab on a Chip*, **5**, 1140-1147.
35. M. Camesasca, M. Kaufman and I. Manas-Zloczower, (2006) Quantifying fluid mixing with the Shannon entropy *Macromolecular Theory and Simulations*, **15**, 595-607.

Chapter 3

Design of a New Microfluidic Mixer – Mixing via Transverse Electrokinetic Effects in a Planar Microchannel

Portions of this chapter appear in the following:

- Lynn N.S., Henry C.S., and Dandy D.S. (2008) Microfluidic Mixing via Transverse Electrokinetic Effects in a Planar Microchannel *Microfluidics and Nanofluidics*, **5,** 493-505

3.1 Introduction

In recent years there has been a remarkable growth in research directed toward analytical devices on the micron scale. Lab-on-a-chip technology has the promise to fully integrate all stages of an analytical process, including chemical synthesis, characterization, separation, and detection within the confines of several square centimeters of area.[1] As in their macroscale counterparts, fluid mixing becomes a very important, albeit inherently difficult step on the microscale. The small characteristic length scale w, along with a limited range of obtainable average linear fluid velocities u, dictate that the Reynolds number ($Re = uw/\nu$) for a fluid with kinematic viscosity ν is constrained to values below 100. At these Reynolds numbers, fluid flow is well within the laminar regime, and without intervention, mixing relies principally on molecular diffusion. In a continuous flow device, the characteristic length needed for complete mixing of two fluid streams can be estimated by equating the characteristic times for convection in the axial direction $t_c = L/u$, and the time for diffusion across the channel width $t_c = w^2/D$, to estimate a mixing length $L_{mix} = t_{mix} \cdot u = w^2 u/D = Pe_m \cdot w$, where

Pe_m is the mass transfer Peclet number. Consequently, mixing of fluids with low molecular diffusivities D can require channel lengths on the order of tens of centimeters, too long for many lab-on-a-chip applications. One of the most effective methods to enhance diffusive mixing within a microchannel is to generate non-axial flow within the microchannel, stirring the fluid in a manner such that analyte concentration gradients will be increased within the channel, thus effectively decreasing the diffusion distance required for mixing.

Microfluidic mixing can be accomplished in an active or passive manner. Passive micromixers rely on the existing geometry of the microchannel to perturb a laminar flow field away from straight streamlines. The simplest conceptual design of a passive type micromixer is the lamination mixer. This mixer systematically splits and re-layers a fluid stream to geometrically increase the solute concentration gradients within the channel, and has been experimentally realized by several groups.[2-5] The lamination type mixer employs 3D geometries involving complicated, multiplanar microfabrication strategies, which are difficult to fabricate via standard soft lithographic methods.[6] Another type of passive mixing design is the rotational-type mixer, where non-axial flows are used in an attempt to efficiently stir the fluid cross-section of a microchannel. Several groups have investigated the use of spiral microchannels to promote fluid mixing, where non-axial flow is generated from the naturally occurring Dean vortices.[7-12] Efficient mixing can also be promoted by the use of oblique grooves on a channel surface, first demonstrated in the slanted groove micromixer (SGM)[13] and staggered herringbone mixer (SHM).[14] The SGM has since been extended to the include geometrical barriers in the center of the channel,[15] and oblique grooves on the sidewall of the channel in addition to those on the floor.[16] Both the SGM and SHM are studied in detail in chapter 3.

Unlike passive micromixers, active micromixers utilize external forces, such as electrokinetic and applied pressure forces, to achieve mixing. Active mixers have employed magnetic beads,[17] peristaltic wall movement,[18] and magnetohydrodynamic

actuation[19] as external forces. A well known example of active micromixing involves subjecting a continuous flow microchannel to multiple, pressure-driven, periodic, closed cross-channel currents.[20-22] External mechanical methods are then used to control the frequency and amplitude of the cross-channel currents.

Electrokinetic phenomena have been widely used in microfluidic mixing.[23] Several studies have utilized ac electric fields to promote an electrokinetic instability (EKI) within a microchannel.[24-27] Similarly, liquids exposed to transverse electro-hydrodynamic (EHD) forces have been used to promote a mixing environment.[28] In EKI and EHD, the use of high-voltage electric fields requires large, high-voltage power supply equipment. Electro-osmotic flow (EOF) can also be used to create mixing via non-axial flow generation in channels with oblique grooves[29] and heterogeneous channel surface charges, created by either active[30-32] or passive methods.[33-35] The use of EOF to mix fluids generally relies on an applied potential drop over the entire channel length, where fields of necessary strength require large potentials (> 1 kV), again requiring high-voltage power supplies.

To reduce the electric potential drop needed for relevant EOF flow magnitudes, integrated metal electrodes may be fabricated such that the distance between electrodes is on the order of the size of the microchannel. Electro-osmotic manipulation of fluids using integrated electrodes has recently been used for several applications. McKnight *et al.* used pairs of integrated electrodes to pump fluids in an open microfluidic device, in which EOF was demonstrated in an electrode gap as small as 60 μm.[36] Lammertink *et al.* used integrated electrodes to mix nanoliter volumes via recirculation in a closed microchannel.[37] These two studies capitalized on the principal of an electric field applied parallel to the microfluidic channel axis, thus inducing EOF in the axial direction. Gitlin *et al.* fabricated an electro-osmotic micropump using a pair of integrated electrodes situated below a microchannel with oblique grooves on the ceiling.[38] Transverse EOF

was observed between the electrodes, where the resulting recirculation across the anisotropic grooves served to pump fluid axially through the microchannel.

Transverse EOF can be efficiently utilized for microfluidic mixing strategies. Qian *et al.* first theorized an electro-osmotic stirrer in a two-dimensional cavity with heterogeneous surface charges on the cavity walls;[39, 40] however, it was not reported how the electric field was created, or possible three-dimensional implementations of such device. Pacheco *et al.* later theorized that efficient mixing could be achieved in three-dimensional channels by subjecting pressure driven flow to a transverse moving wall condition on the top and bottom microchannel walls.[41] The moving wall condition, created by a transverse electric field, could be controlled via multiple electrodes built into the channel sidewalls. Although efficient in design, this type of device presents several difficulties, as fabrication of multiple electrodes on the channel sidewalls can be not only difficult, but also costly and time intensive. To date, no mixer of this type has been experimentally realized.

Rather than place the integrated electrodes along the channel sidewalls, it is straightforward to use standard micro-fabrication processes to position integrated electrodes along the channel floor. In the present work a new method is described for achieving microfluidic mixing through application of a localized electric field perpendicular to the mean flow direction driven by a pressure gradient in a planar microchannel (Fig. 3.1). Integrated electrodes are fabricated such that there exists a small gap situated perpendicular to the channel axis. A potential drop across the gap drives EOF perpendicular to the primary flow direction, thereby creating several non-axial recirculation flow profiles. The three-dimensional velocity field of such a device may be described by a numerical model, and the resulting mixing characteristics may be characterized via particle tracking of passive tracers. The numerical results show that, through control of the electrode geometry-gap width, gap location, axial separation, and applied potential, it is possible to induce rapid micro-mixing in short axial distances.

Furthermore, this study details the operation of an experimental mixer, fabricated via standard micro-fabrication methods, which displays the same trends as predicted by the numerical model for the same geometry and operating parameters.

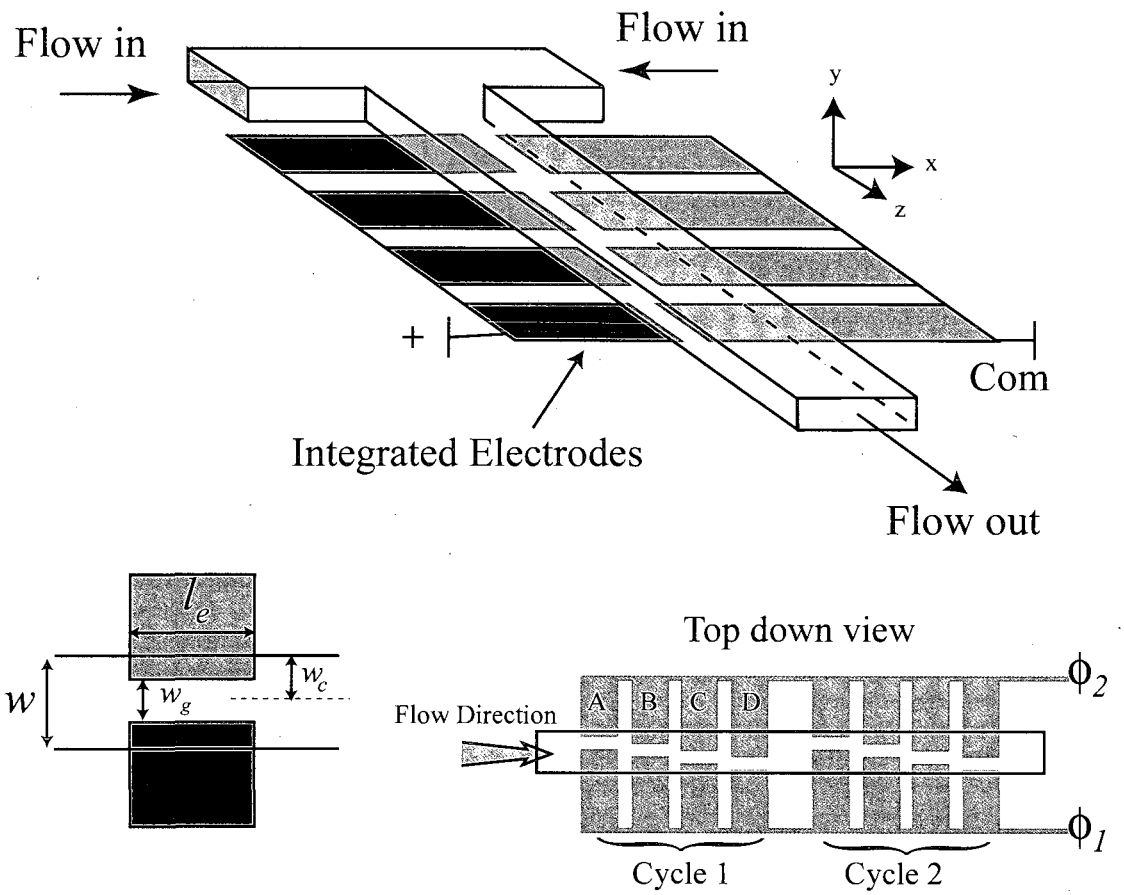

Figure 3.1. Schematic of the micro-mixing device described within this study. A microchannel with height h and width w is fabricated with a set of staggered integrated electrodes along the channel floor. The center of the electrode gap is situated at a distance w_c from the top wall, where each electrode pair has an axial length l_e and a separation gap w_g.

3.2 Numerical Methods

3.2.1 Governing Equations

In general, the potential distribution in a micro-cavity is composed of the externally applied potential (ϕ), and the potential (ψ) associated with the electrical double layer (EDL). For expected ion concentrations the Debye length (λ_d) is very small with respect to the size of a microchannel, and it is reasonable to assume that the total potential (Ψ) is a superposition of the two ($\Psi = \psi + \phi$). According to electrostatics theory, the potential distribution is a cavity is governed by the Poisson equation,[42]

$$\nabla^2 \Psi = \frac{\rho_e}{\varepsilon_o \varepsilon}, \tag{3.1}$$

where ρ_e is the net charge density of the electrolyte solution, ε is the dielectric constant of the liquid, and ε_o is the permittivity of vacuum. Equation (3.1) can thus be separated into two equations,

$$\nabla^2 \phi = 0, \tag{3.2}$$

and

$$\nabla^2 \psi = \frac{\rho_e}{\varepsilon_o \varepsilon}. \tag{3.3}$$

At thermodynamic equilibrium, the ion concentration can be described by the Boltzmann distribution,

$$n_{i\pm} = n_{io} \exp\left(\frac{\pm z_i e \psi}{k_b T}\right), \tag{3.4}$$

where n_i and z_i are the concentration and valence of the i^{th} ion, respectively, e is the elementary charge, k_b is the Boltzmann constant, and T is the temperature. The net charge density ρ_e of a symmetric electrolyte can thus be written as

$$\rho_e = (n_+ + n_-)ze = 2n_o ze \sinh\left(\frac{ze\psi}{k_b T}\right). \tag{3.5}$$

Combining equations (3.3) and (3.5) results in

$$\nabla^2\psi = \frac{2n_o ze}{\varepsilon_o \varepsilon}\sinh\left(\frac{ze\psi}{k_b T}\right), \tag{3.6}$$

which describes the potential in a microcavity associated with the EDL. For a symmetric electrolyte, the Debye-Hückel approximation can be used to simplify Eqn. (3.6)

$$\nabla^2\psi = \frac{n_o z^2 e^2}{\varepsilon_o \varepsilon k_b T}\psi = \kappa^2\psi, \tag{3.7}$$

where $\kappa^{-1} = \lambda_d$, the characteristic length of the EDL. The boundary conditions for equations (3.2) and (3.7) are

$$\phi_e = \phi_{applied}, \ \frac{\partial\phi_w}{\partial\hat{n}} = 0, \ \psi_e = 0, \ \psi_w = \zeta, \tag{3.8}$$

where the subscripts e and w represent electrode and wall surfaces, and ζ is the zeta potential for the charged wall surfaces. The electric field is then determined by the gradient of the total potential

$$\vec{E} = -\nabla(\psi + \phi). \tag{3.9}$$

Electro-osmotic flows in microchannels are generally restricted to small Reynolds numbers. Thus, combined pressure and electro-osmotic driven steady-state flow can be described using the modified steady-state Stokes equation (including an electric field term) along with the incompressible continuity equation,

$$-\nabla p + \mu\nabla^2\vec{u} + \rho_e\vec{E} = 0, \tag{3.10}$$

$$\nabla\cdot\vec{u} = 0, \tag{3.11}$$

where p is the fluid pressure, μ the viscosity of the electrolyte solution, and $\vec{v}$ is the fluid velocity. For electrolyte concentrations $C > 1$ mM in aqueous media, the Debye length will be such that $\lambda_d \ll w$, where $\rho_e \approx 0$ for regions of fluid positioned at a distance greater than λ_d from a charged surface. In this case it is appropriate to neglect the electric body

force in Eqn. (3.10) in favor of the Helmholtz-Smoluchowski boundary condition along a surface,[43]

$$u_{EOF,t} = \frac{\varepsilon_o \varepsilon \zeta}{\mu} E_t, \tag{3.12}$$

where E_t is the component of the electric field parallel to the surface. Using this approximation, the non-axial flow field in a plane of constant z-position between each electrode gap can be described by Eqns. (3.10) and (3.11) are solved as follows: two dimensional creeping flow of a viscous incompressible fluid can be described by the stream function φ, whose solution obeys the biharmonic equation

$$\nabla^4 \varphi = 0. \tag{3.13}$$

This relationship is described in detail by Meleshko.[44] The velocity field is obtained from φ via

$$u_x = \frac{\partial \varphi}{\partial y}, \; u_y = -\frac{\partial \varphi}{\partial x}, \tag{3.14}$$

with impermeable boundary conditions φ_e = constant on the electrode bearing surfaces. EOF on non-electrode surfaces is estimated using the Helmholtz-Smoluchowski equation along the top and bottom walls,

$$\frac{\partial \varphi_w}{\partial y} = u_{EOF,x} = -\frac{\varepsilon_o \varepsilon \zeta}{\mu} E_x, \tag{3.15}$$

and the channel sidewalls,

$$\frac{\partial \varphi_w}{\partial x} = -u_{EOF,y} = \frac{\varepsilon_o \varepsilon \zeta}{\mu} E_y, \tag{3.16}$$

where E_x and E_y are the x and y components of the electric field vector, respectively.

3.2.2 Numerical Approach

Figure 3.1 displays the structure of the electro-osmotic micromixer. The axial length of the electrode is denoted as l_e, and the width and center position of the electrode gap are w_g and w_c, respectively. For externally driven flow rates of aqueous electrolytes corresponding to an average linear velocity $\langle u_z \rangle < 5$ mm s^{-1} through a microchannel of width $w = 100$ μm, the Reynolds number ($Re = \langle u_z \rangle w/\nu$) will be $O(1)$. If the axial length of the individual electrodes is considerably larger than the width of the microchannel, the potential distribution along the axial direction within the individual electrodes may be assumed constant. Thus, if the spacing between the individual electrodes is considerably larger than w_g, the inter-electrode potential distributions and edge effects can be neglected, and the three-dimensional velocity field can be well approximated as a superposition of the velocity field given by Eqn. (3.14) and the axial velocity field, $\vec{u}_z\{x, y\}$, acquired from the Boussinesq series solution for flow in a rectangular duct. This approach is similar to that taken by Stroock *et al.* to describe fluid flow in the staggered herringbone mixer,[45] detailed in chapter 2.

A numerical approach is implemented to solve the governing Eqns. (3.2), (3.7) and (3.13) along with the corresponding boundary conditions (3.8), (3.15), and (3.16). Equations (3.2) and (3.7) were discretized with a second-order accurate finite difference scheme and solved via a successive over-relaxation (SOR) method, where the typical distance between nodes was 0.5 μm, a value was predetermined (data not shown) to ensure that the predicted concentration field was independent of the mesh density. The convergence requirements for the normalized residuals concerning ϕ and ψ was 10^{-12}. The electric field is then found via equation (3.9), and used as a boundary condition in equations (3.15) and (3.16). Equations (3.13) and (3.14) are solved simultaneously via a fourth-order accurate SOR scheme as discussed in Altas *et al.*,[46] where the convergence requirements for the normalized residuals for φ was 10^{-15}. The numerical methods in this

study were verified with the two-dimensional quasi-analytic flow profiles for the electrode geometries displayed by Qian *et al.*[39, 40]

3.2.3 Mixer characterization

To computationally characterize the mixing efficiency of a three-dimensional velocity field, non-interacting, massless tracer particles are injected into the mixer and their motion tracked in space and time. The passive tracers do not affect the flow field, and are considered diffusionless. The positions of the tracers are calculated as a function of time via integration of the three-dimensional velocity field:

$$\vec{x}(t) = \vec{x}(t_o) + \int_{t_o}^{t} \vec{u}(x, y, z)\mathrm{d}t\,, \tag{3.17}$$

where integration is carried out with a fourth-order Runge-Kutta scheme with a constant time step of $\Delta t = 0.001$ s. Advecting passive tracers forward in time through a non-homogeneous velocity field will introduce large gaps between tracers in fluid regions of high velocity. These gaps can create problematic artifacts when attempting to quantify the extent of mixing of the tracer particles in cross-sectional planes of the microchannels. To avoid these artifacts, a backtrace method similar to Stone *et al.* is employed for both imaging of downstream tracer distributions and mixing characterization.[47] The backtrace method involves initializing an ordered set of tracer particles on a cross sectional plane of interest ($z > 0$), and advecting each particle backward in time until the inlet plane ($z = 0$) is reached. Each tracer particle is then allocated a color (red, blue) based on the tracer position on the inlet plane. The initialization of the tracers at the mixer outlet is performed such that the distance between neighboring particles is constant, which allows for very fine resolution concerning the distribution of tracers and avoids the introduction of large gaps between tracers. In this study, the microchannel inlet is separated into two vertical regions, designating red or blue tracers, respectively, such that the tracer flow

resembles perfectly segregated tracer distribution at the channel inlet. The main drawback to the backtrace method is its intensive computational nature, as the time required for analysis of n evenly spaced cross-sectional planes scales as

$$t_{comp} = \sum_{i=1}^{n} nt_n , \tag{18}$$

where t_n is the average computational time required to advect particles between neighboring planes (as opposed to $t_{comp} = nt_n$ for forward advection).

Despite the extensive body of literature focused on the numerical characterization of mixing processes at the micro- and macro-scales using massless tracer particles, there is not unanimous agreement regarding the best method to calculate the extent of mixing of the dispersed particles in time or space. In this study, the extent of mixing within a distribution of tracer particles is characterized using the entropic methods of Camesasca *et al.*, which has been previously shown to be successful in the characterization of several mixing processes.[48, 49] In this method, the downstream x,y cross-sectional planes are divided into M equally sized spatial bins, and the conditional entropy S_{lc} is averaged over all bins as

$$S_{lc} = -\frac{1}{\ln(2)} \sum_{j=1}^{M} p_j \sum_{c=1}^{C} p_{c,j} \ln p_{c,j} , \tag{3.19}$$

where p_j is the probability that a particle is in bin j irrespective of species type, and $p_{c,j}$ is the probability that a particle is of the type c whose position is in bin j. For this study, two particle species are employed (red and blue). The conditional entropy S_{lc} is thus normalized by ln(2), as in Camesasca *et al.* A value of $S_{lc} = 0$ indicates that no mixing has occurred between the two species, and a value of $S_{lc} = 1$ indicates a well mixed solution on the scale of the typical size of the bin.

3.3 Experimental Methods

3.3.1 Fabrication of Experimental Mixers

Fabrication of the mixers was performed with a soft lithographic method using poly(dimethylsiloxane) (PDMS, Sylgard 184, Dow Corning) for the channel top and sidewalls, sealed to a glass bottom containing patterned, integrated thin film electrodes. The fabrication process is shown schematically in Fig. 3.2. The PDMS microchannels were cured over a raised Su-8 master developed onto a silicon wafer and subsequently subjected to a PDMS oligomer extraction process similar to Lee *et al.*,[50] which has been shown to stabilize the hydrophilic nature of oxidized PDMS for up to 7 days.[51] To prepare the electrodes, a bi-layer photoresist stack (Microchem LOR 10B, Shipley 1818) was spun onto a cleaned, dehydrated glass slide. Following UV exposure and development to expose the electrode sites, 30 nm of Au was deposited onto a 6 nm Ti adhesion layer using e-beam evaporation. After lift-off of the metal layer, holes were drilled into the glass slide to provide fluid access to the mixer through the use of Nanoport fittings (Upchurch). The glass slide and PDMS layer were then cleaned and exposed to O_2 plasma (25 W, 370 mTorr) to strengthen the PDMS/glass irreversible bond and minimize the contact angle between PDMS and water.[52] The two layers were then aligned and irreversibly bonded. Syringe pumps were used to deliver buffer solutions of 5 mM TES (N-[tris-hydroxymethyl]methyl-2-aminoethanesulfonic acid, Sigma), pH = 7.5, to both channel inlets, where one inlet contained 0.1 mM rhodamine B (Sigma) for mixing analysis. Exposed bonding pads on the periphery of the glass slide were used to connect the integrated electrodes to a power supply (HP 6217A) via patch clips.

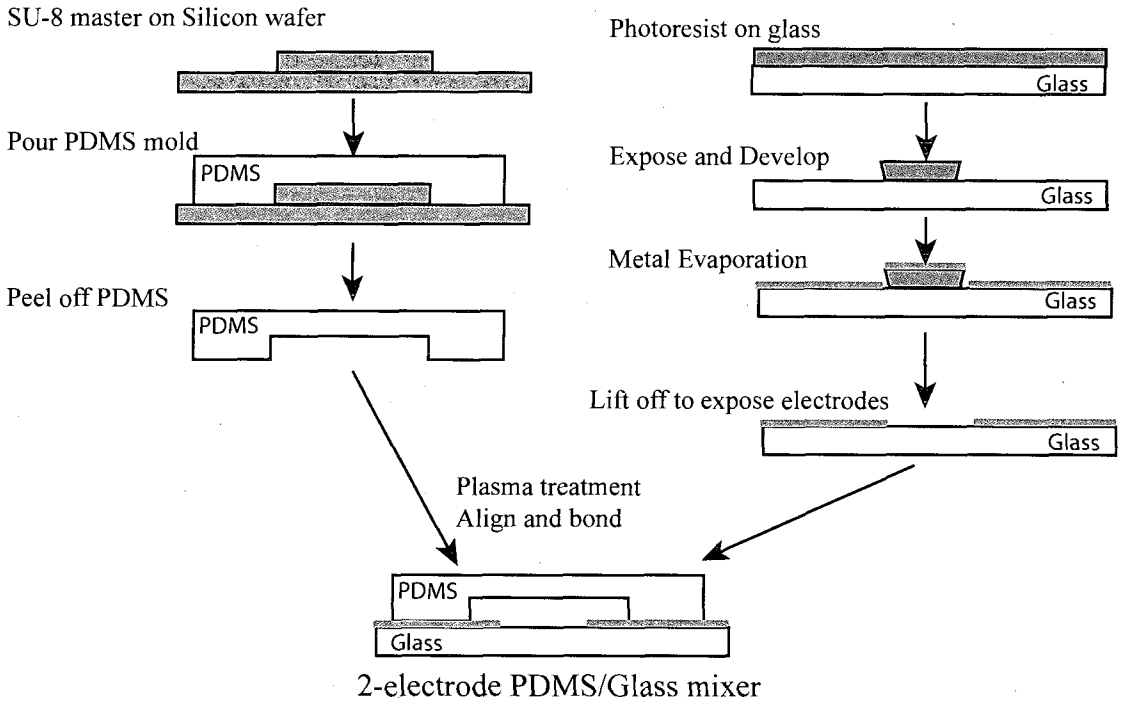

Figure 3.2. Fabrication process used to create the glass/PDMS mixer. The PDMS mold constitutes the channel top and sidewalls. The channel top and bottom is composed of the metal electrodes on a glass substrate.

3.3.2 Image acquisition

Fluid micromixing was monitored by fluorescence of rhodamine B using two-dimensional images captured by an inverted microscope equipped with an epifluorescence attachment (Nikon TE-2000U) and fitted with a CCD camera (Coolsnap fx). Fluorescence intensity images of the unmixed and mixed states were acquired at a fixed distance from the T-junction. To quantify the mixing performance, an adjusted extent of mixing (δ_a) is introduced as

$$\delta_a = 1 - \sqrt{\sum_{i=1}^{N}\left(I_i - \langle I_i \rangle\right)^2 \Big/ \sum_{i=1}^{N}\left(I_{i,o} - \langle I_{i,o} \rangle\right)^2} \quad , \tag{3.20}$$

where I_i is the intensity at pixel i during active mixing, $I_{i,o}$ is the intensity at pixel i if no active mixing occurs ($\Delta\phi = 0$), and N is the total number of pixels across the width of the

microchannel. The fluid passing through the *xy*-plane downstream of any integrated electrode has undergone a limited amount of diffusive mixing (no active mixing), thus the standard extent of mixing is adjusted to this unmixed state rather than the state corresponding to the plane at $z = 0$ (T-junction). The adjusted extent of mixing is defined such that $\delta_a = 1$ for well-mixed solutions (or solutions which display constant fluorescence intensity across the width of the micro-channel), whereas $\delta_a = 0$ for solutions which display no change from the unmixed state. The method of top down fluorescence analysis, although limited in the case of horizontally laminated fluorescent streams, has had previous success to characterize micro-mixing devices.[26, 29, 33]

3.4 Numerical Results

3.4.1 Two-Dimensional Flow Profiles

It is convenient to use equation (3.13) to calculate the flow field because the contours of the stream function represent the fluid streamlines in the domain of interest. Figure 3 displays the ϕ-potential distributions and fluid streamlines for several electrode arrangements in a two-dimensional microcavity. All simulations within this study pertain to a micro-cavity with dimensions $w = 140$ μm and $h = 60$ μm. The electrode arrangements in Fig. 3.3 correspond to an electrode gap of $w_g = 50$ μm, where the position of the gap was systematically staggered along the length of the microchannel. The ζ-potential of the cavity floor was assumed to be $\zeta = -0.05$ V, whereas the top and sidewalls are $\zeta = -0.08$ V, consistent with the values associated with the glass floor and PDMS cap.[53] In each of the electrode geometries shown in Fig. 3.3, there exists a primary recirculation region directly above the electrode gap, and a weaker, secondary, counter-rotating recirculation region in the remaining cavity domain. Because the electric field magnitude within the gap ($E \approx \Delta\phi / w_g$) is much larger than along the channel sidewalls

($E \approx \Delta\phi/(2h+w)$), fluid velocities are much higher within the primary recirculation regions.

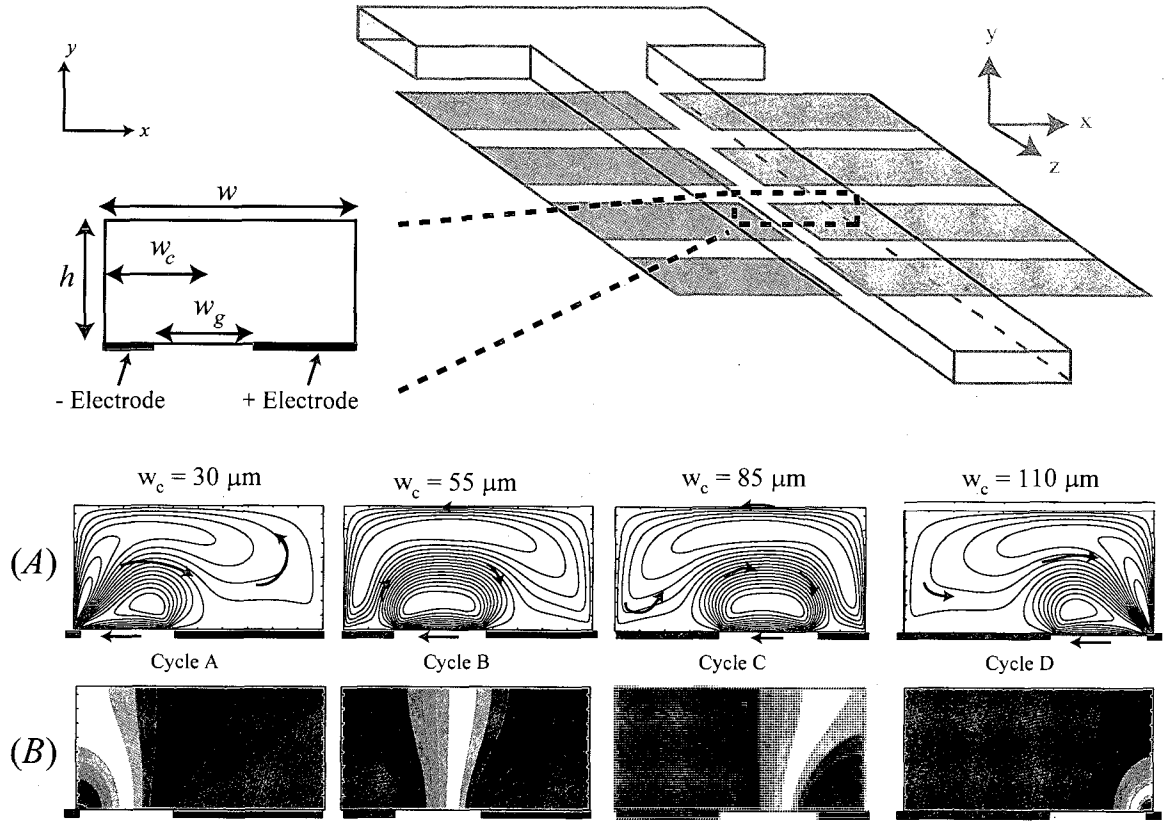

Figure 3.3. Two-dimensional streamlines (*A*) and contour plots of the applied potential ϕ (*B*) corresponding to the four electrode geometries considered in this study.

Subjecting a microchannel to only one of the cross-sectional flow profiles shown in Fig. 3.3 will not be sufficient to mix the cross-section of the channel, as the solution will only be stirred in a regular fashion. Combinations of the individual cycles must be used either in a temporal or spatial fashion to completely mix the microchannel constituents. Because the points of stagnation in the flow profiles shown in Fig 3.3*A* are all located in different positions from one another, it is expected that a combination of the four profiles together will not contain any zones of invariance where complete mixing will be

inhibited. Potential zones of invariance (regions of fluid that will not undergo sufficient mixing) can be found by subjecting a two-dimensional cavity to temporal changes in the cross-sectional with a period T while monitoring the evolution of tracer particles. In the case that a cavity could be subjected to periodic changes in the potential distributions, such as those shown in Fig. 3.3*B*, the instantaneous flow fields would be given by the streamline distributions shown in Fig. 3.3*A* as long as T is sufficiently greater than the viscous diffusion time of the fluid. For a microcavity of $w < 100$ μm, the viscous diffusion time ($\tau = w^2/\nu$) is on the order of milliseconds, and we can assume that the flow field responds nearly instantaneously from one state to another.

Figure 3.4 displays the evolution of 10^5 particles tracked over the overall cycle *ABCDABCDABCD*, where the individual mixing pattern for each cycle was held for $T =$ 1 second with a potential drop between the electrodes of $\Delta\phi = 1$ V. The initial positions of the particles were segregated uniformily along one-third of the width of the microcavity and were advected forward in time, thus the occurrence of void spots in regions of high fluid velocity. The stretching and folding of the initial blob is qualitatively characteristic of a chaotic process; however, no studies were carried out to determine the presence of a positive Lyapunov exponent. It should be noted there was no occurrence of any invariant mixing zones no matter the position of the initial blob of tracer particles, nor the overall size of the blob. The results from figure 3.4 are thus purely qualitative, yet helpful in determining the overall effectiveness of the staggered electrode placement. The temporal changes in the potential distribution of a two dimensional cavity are analogous to spatial changes in the potential distribution of a three-dimensional microchannel, such as that shown in Fig. 3.1. Any invariant zones in the two-dimensional situation would show up in the same region for a three dimensional mixer.

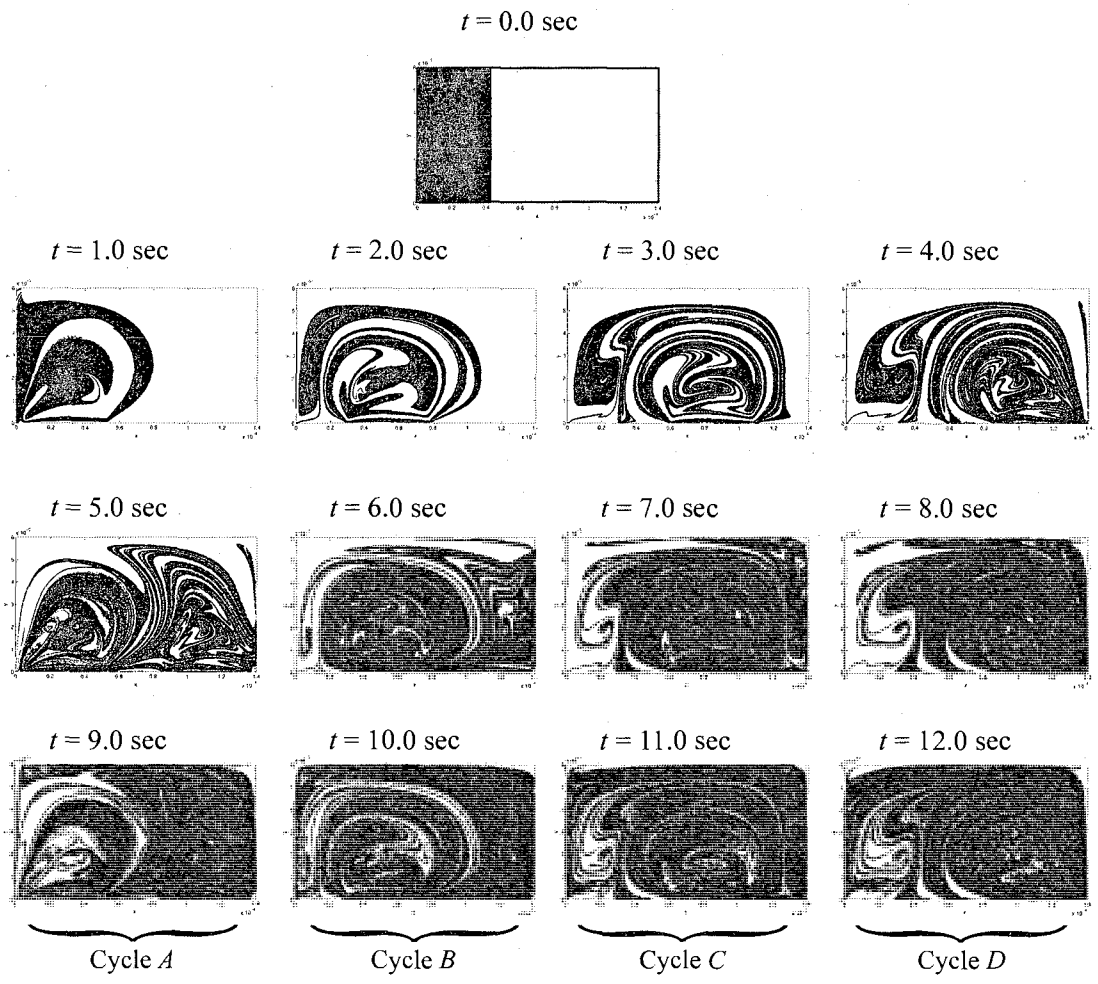

Figure 3.4. Deformation of a blob of 100,000 tracer particles initially segregated to the left third of a microcavity subjected to the flow fields of cycles *A*-*D* for 1 second each.

3.4.2 Three-Dimensional Flow

The three-dimensional velocity field of a mixing device shown in Fig. 3.1 can be described as follows:

$$\vec{u}(x, y, z) = \vec{u}_z(x, y) + \vec{u}_n(x, y), \tag{3.21}$$

where $\vec{u}_z(x, y)$ is obtained from a Boussinesq series solution for viscous flow in a duct, and the non-axial components $\vec{u}_n = \vec{u}_x + \vec{u}_y$ are obtained from the solution to equation (3.14) for an electrode cycle determined by the flow fields shown in Fig. 3.3 and assembled as:

$$\vec{u}_n(x, y) = \begin{cases} \vec{u}_A & l_i < z < l_i + l_e \\ \vec{u}_B & l_i + l_e < z < l_i + 2l_e \\ \vec{u}_C & l_i + 2l_e < z < l_i + 3l_e \\ \vec{u}_D & l_i + 3l_e < z < l_i + 4l_e \end{cases} \tag{3.22}$$

where l_i is the axial position of the start of the i-th electrode cycle. Equation (3.22) describes a mixer with an overall electrode cycle pattern $[ABCD]_n$, where n is the total number of electrode cycles within the mixer, and inter-electrode flow is neglected. This study involves the comparison of the four electrode cycle pattern $[ABCD]_n$ and the two electrode cycle pattern $[BC]_n$.

Figure 3.5 displays the distribution of 100,000 tracers corresponding to x,y-planes situated at the end the first 8 electrodes for a mixer with an overall electrode cycle pattern of $[ABCD]_2$. The bulk flow rates for the two cases correspond to $\langle u_z \rangle$ = 0.4 mm s^{-1} for Fig. 3.5*A*, and $\langle u_z \rangle$ = 1.6 mm s^{-1} for Fig. 3.5*B*. The red and blue tracers were initially segregated in equal proportions to the right and left sides of the microchannel inlet, respectively. The applied potential drop between the electrodes is $\Delta\phi$ = +2.0 V, and the length and dimension of each electrode gap is l_e =500 μm and w_g = 50 μm, where the associated values of w_c are given in Fig. 3.3.

Although small amounts of mixing occur for each individual electrode, the combined effect of the 2 mixing cycles is quite dramatic. For Fig. 3.5*A*, the channel cross-section appears visually well mixed at the outlet, positioned 4 mm downstream of the inlet. As expected, as the bulk flow rate increases, the magnitude of stirring over each electrode decreases, which is visually apparent in the figures. However, even though the channel cross-section at the outlet of Fig. 3.5*B* maintains a large level of heterogeneity, it may be concluded that only several more electrode cycles will be needed to achieve the level of mixing seen in the outlet of Fig. 3.5*A*. It should be noted that, because the backtrace method is employed to generate the tracer distributions shown in Fig. 3.5, the ratio of red to blue tracers does not remain constant as the tracers pass through x,y-planes of interest. However, this has a negligible effect on the conditional entropy of the tracer distribution in each x,y plane.

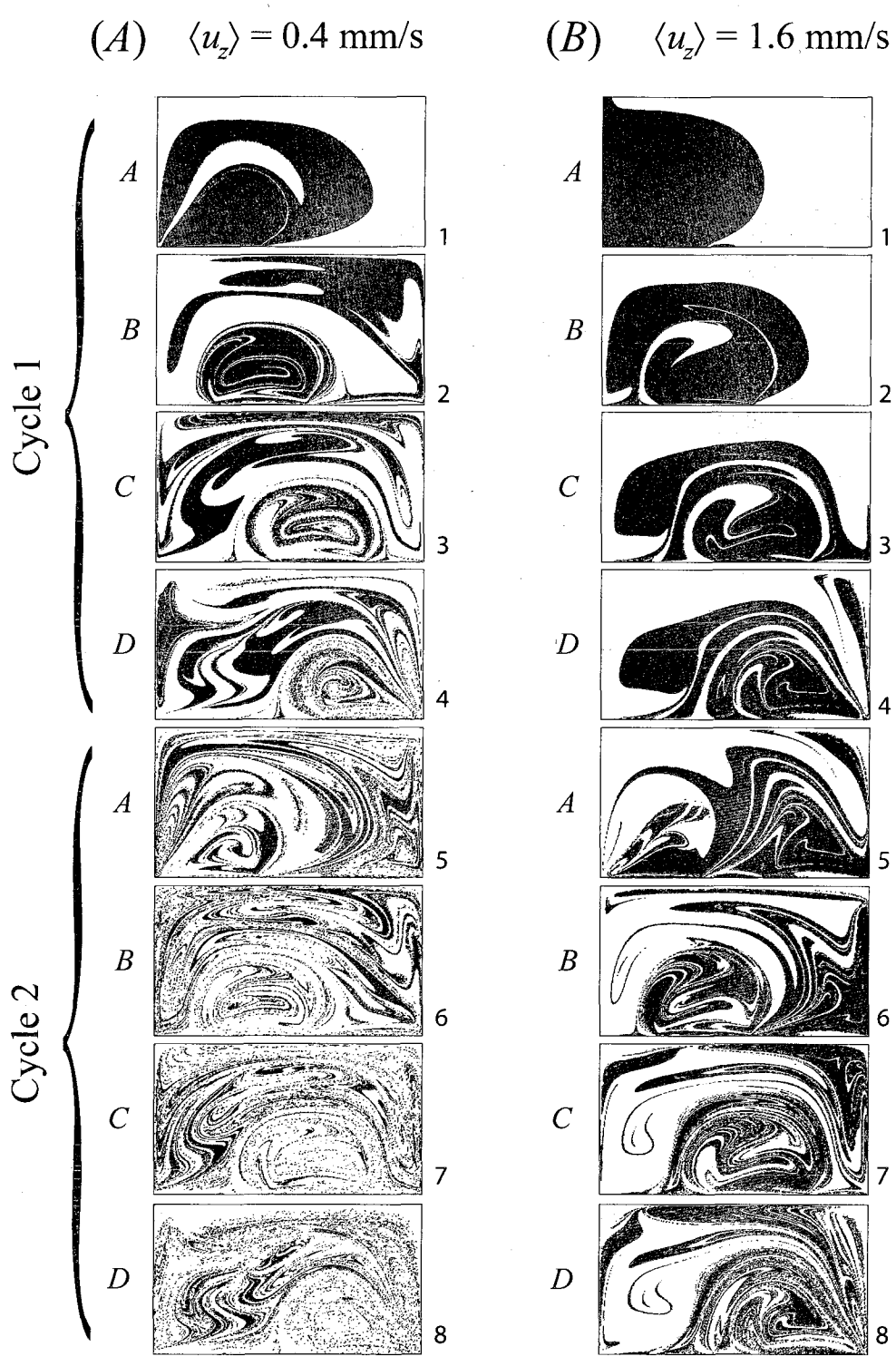

Figure 3.5. Tracer distributions (100,000 tracers) for two flow rates corresponding to the first eight electrodes for a mixer with an overall cycle pattern $[ABCD]_n$, and $\Delta\phi = 2.0$ V. The cross-sectional potential distributions and fluid streamlines are shown in Fig. 3.3.

3.4.3 Mixing Mechanism

The tracer distributions shown in Fig. 3.5 are important in qualitatively determining both where good mixing is occurring within x,y-planes and potential regions of invariance within overall electrode cycle patterns. It may be concluded from Fig. 3.5 that the overall mixing mechanism is composed of two parts:

Rapid mixing within the primary recirculation. Lamination of fluid occurs very rapidly within the primary recirculation region situated directly above the electrode gaps associated with the four electrode cycles shown in Fig. 3.3. The fluid is simultaneously stretched and folded within this region. Fluid breakup occurs as the electrode gap is staggered along the width of the mixer along periodic axial lengths. Because the primary recirculation occupies a region constrained to the lower part of the channel, only fluid within this region is subject to rapid mixing.

Non-axial transport within the secondary recirculation. The secondary recirculation region serves to transport fluid in opposite directions along the top and sidewalls of the channel. Due to the smaller magnitudes of velocity in the x and y-directions, little lamination occurs within this region. Thus it appears the benefit of this secondary recirculation is to transport regions of fluid to the lower half of the channel. As regions of fluid reach the lower parts of the channel there exists the probability that it will be entrained in a primary recirculation region upon entering a new electrode cycle.

It has been demonstrated here that an applied potential across a staggered electrode gap has the potential to rapidly mix fluids within short axial distances. Equation (3.19) can be used to quantify the extent of mixing in the x,y-planes located at the end of each individual electrode. The conditions associated with in Fig. 3.5 lead to a quantitatively well mixed solution within 4 mm of the inlet, as the conditional entropy at the eighth electrode is calculated as $S_{lc} = 0.95$ (1000 bins) for case (A), whereas a value of $S_{lc} = 0.75$ (1000 bins) is calculated for case (B).

When designing such a mixer for experimental study, it remains important to evaluate not only different operating conditions, but overall electrode cycles as well as operating polarities. Fig. 3.5 displays tracer distributions for a mixer with specific parameters l_e = 500 μm, w_g = 50 μm, and $\Delta\phi$ = 2.0 V for two values of $\langle u_z \rangle$. To optimize the mixing efficiency of such a device, it is necessary to test a variety of mixer designs and operating conditions.

3.4.4 Numerical Characterization

The parameters governing the operation of a mixer of this type are $\langle u_z \rangle$, l_e, w_g, $\Delta\phi$, the overall electrode cycle geometry, and the micro-channel substrate(s), i.e., the specific channel surface charge ζ. From the tracer distributions shown in Fig. 3.5, it appears that the effectiveness of each mixing cycle is related to the total magnitude of helical flow within the primary recirculation region. It is reasonable to assume that higher magnitudes of helical flow will lead to a greater degree of stirring within each recirculation region, thus leading to an increase in mixing efficiency. The magnitude of helical flow within the primary recirculation region can be estimated as the ratio of the average time taken for fluid to migrate down the axial length of an individual electrode and the average time for non-axial transport of fluid across the gap. A mixing effectiveness can therefore be calculated as

$$F = \frac{t_{\parallel}}{t_{\perp}} = \frac{l_e v_{EOF}}{w_g \langle u_z \rangle} = \frac{l_e \varepsilon_o \varepsilon \zeta (\Delta\phi)}{w_g^2 \mu \langle u_z \rangle} . \tag{3.23}$$

As F increases there exists a higher degree of stirring within the primary (and secondary) recirculation regions, which should lead to an increase in mixing efficiency and a decrease in L_{mix}. Because the simulated flow field is a linear superposition of Eqn. (3.14) and the solution for axial flow in a duct, the distribution of tracer particles at the outlet of a mixer (such as that shown in figure 3.1) operating at different conditions will

be identical should the two systems possess the same value of F. Thus for a first generation optimization effort it is only necessary to calculate the extent of mixing at the outlet of each individual electrode while varying the mixing effectiveness F. This provides a direct comparison of overall electrode cycles, and will allow for the optimization of such a mixing device.

Figure 3.6 displays the conditional entropy S_{lc} as a function of electrode number for several values of F for mixers similar to that in Fig. 3.1. The mixer shown in Fig. 3.6*A* has an overall electrode cycle pattern of $[ABCD]_n$, whereas the mixer shown in Fig. 3.6*B* has the overall electrode cycle pattern $[BC]_n$. The individual electrode geometries are shown in Fig. 3.3, and the values of S_{lc} are computed using $M = 1000$ equal sized bins. The dotted lines indicate the condition $S_{lc} = 0.9$, above which the cross-sectional planes are classified as well-mixed, i.e., on the order of the width of a bin, $w_b = 3$ μm. The data shown in Fig. 3.6 follow the same trends for the range of bin numbers $500 < M < 5000$. It is seen in Fig. 3.6 that higher magnitudes of F lead to higher rates of mixing, achieving a well mixed condition with fewer electrodes (thus requiring a shorter axial length). For example, for the pattern $[ABCD]_n$ and $F = 80$, only 5 electrodes are required to reach a value of $S_{lc} = 0.9$, whereas 14 electrodes are required for the same condition when $F = 20$. Figure 3.6 also includes the simulated mixing profiles for a mixer operated with the polarity reversed (filled symbols, $\Delta\phi < 0$). As seen in Fig. 3.6*A*, for the pattern $[ABCD]_n$, operation in positive polarity ($\Delta\phi > 0$) results in better overall mixing performance with respect to operation in negative polarity. However, the polarity of the electrodes has little effect on the mixing performance of the $[BC]_n$ electrode pattern. The tracer distributions for the $[BC]_n$ mixer at a effectiveness of $F = 40$ and $F = 10$ may be viewed in Fig. 3.7. For high values of F, all cases in Fig. 3.6*B* resulted in better mixing performance than their counterparts in Fig. 3.6*A*; however, for low values of F ($F < 5$) the reverse is true, as the $[ABCD]_n$ electrode cycle pattern displays better mixing performance over its $[BC]_n$ counterpart.

From Fig. 3.6, it is seen that for a specific electrode number there is a critical value of F, above which a well mixed solution ($S_{lc} > 0.9$) is obtained. Figure 3.8 shows the conditional entropy as a function of F along the outlet of the first 4 electrode cycles corresponding to the pattern $[ABCD]_n$. When the mixing effectiveness in on the order of $F = O(1)$, fluid located just above the electrode gap will complete less than one full recirculation, and only small amounts of stirring occur along the length of each electrode gap. As F increases, there exists more than one recirculation of fluid above the electrode gap, and the extent of mixing rises sharply due to the rapid lamination of fluid within this region. There is a point of diminishing returns for each cycle, however, where subsequent increases in F have little effect on the overall extent of mixing, since the decrease in the striation thickness between two regions of fluid become smaller with every fluid recirculation. In all cases, the addition of more electrode cycles will increase the total extent of mixing at the outlet of a mixer.

Utilizing Eqn. (3.23), the results shown in Fig. 3.8 can be transformed into data that are commonly acquired in a laboratory experiment. Figure 3.9 shows the expected conditional entropy values as a function of the average linear velocity for a mixer with l_e = 400 μm, h = 60 μm, w = 140 μm, $\Delta\phi$ = 2.0 V, and the overall cycle pattern $[ABCD]_n$. As may be expected, the performance of the mixer is somewhat poor at high linear velocities, $\langle u_z \rangle > 6$ mm s^{-1}, while mixing performance increases rapidly as $\langle u_z \rangle$ decreases. For bulk flow rates corresponding to $\langle u_z \rangle < 4$ mm s^{-1}, the extent of mixing of a device can be increased significantly by the addition of multiple electrode cycles. Each electrode cycle shown in Fig. 3.9 accounts for 1.6 mm of axial channel length; thus, a mixer of this type (operated such that $\langle u_z \rangle < 2$ mm s^{-1}) would be able to provide near complete mixing of a non-diffusive fluid in 6.4 mm of channel length.

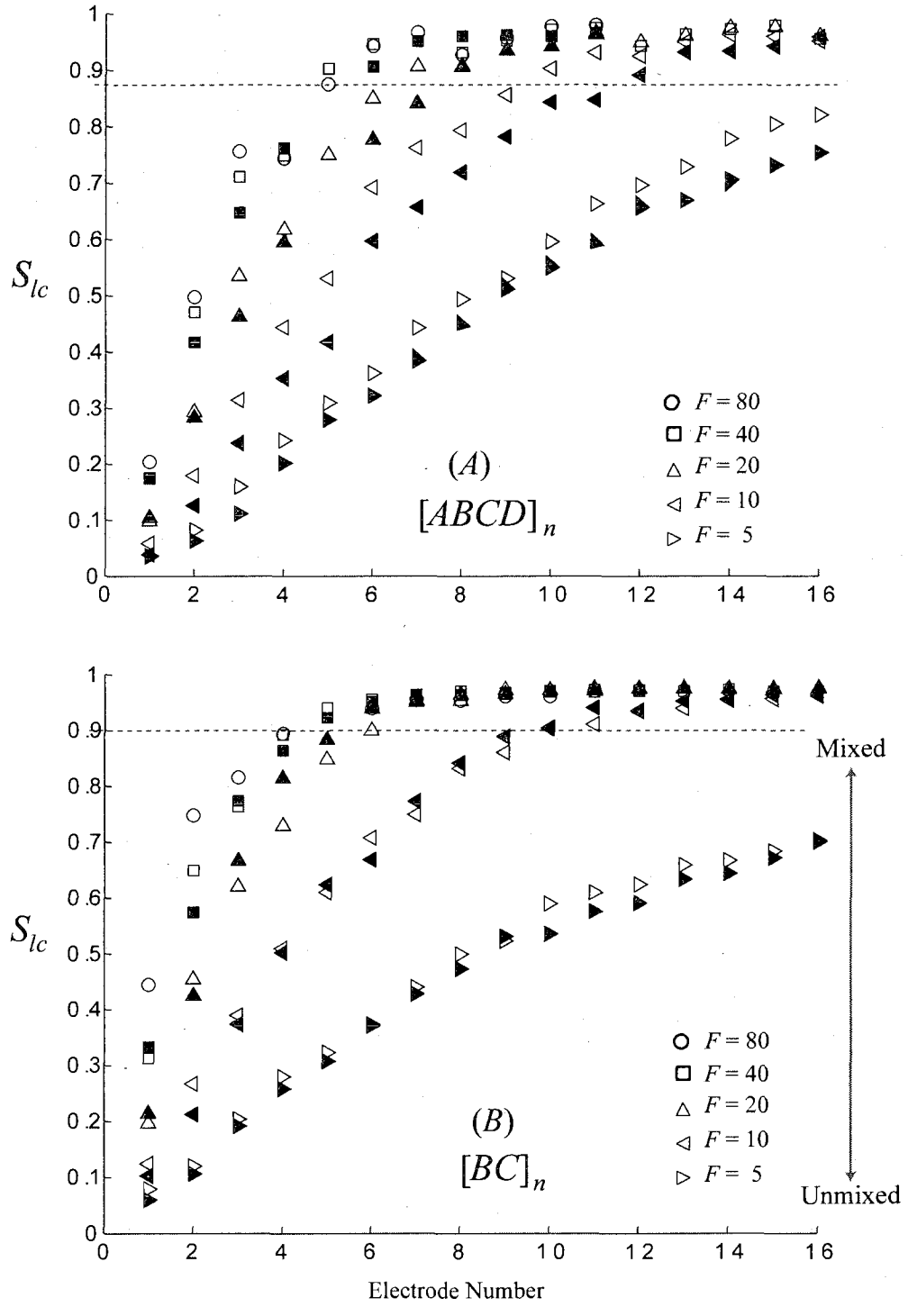

Figure 3.6. Comparison of overall cycle pattern (*A*) $[ABCD]_n$ and (*B*) $[BC]_n$ using the conditional entropy S_{lc} vs. electrode number for several values of F. The filled symbols indicate mixer operation in reversed polarity ($\Delta\phi < 0$).

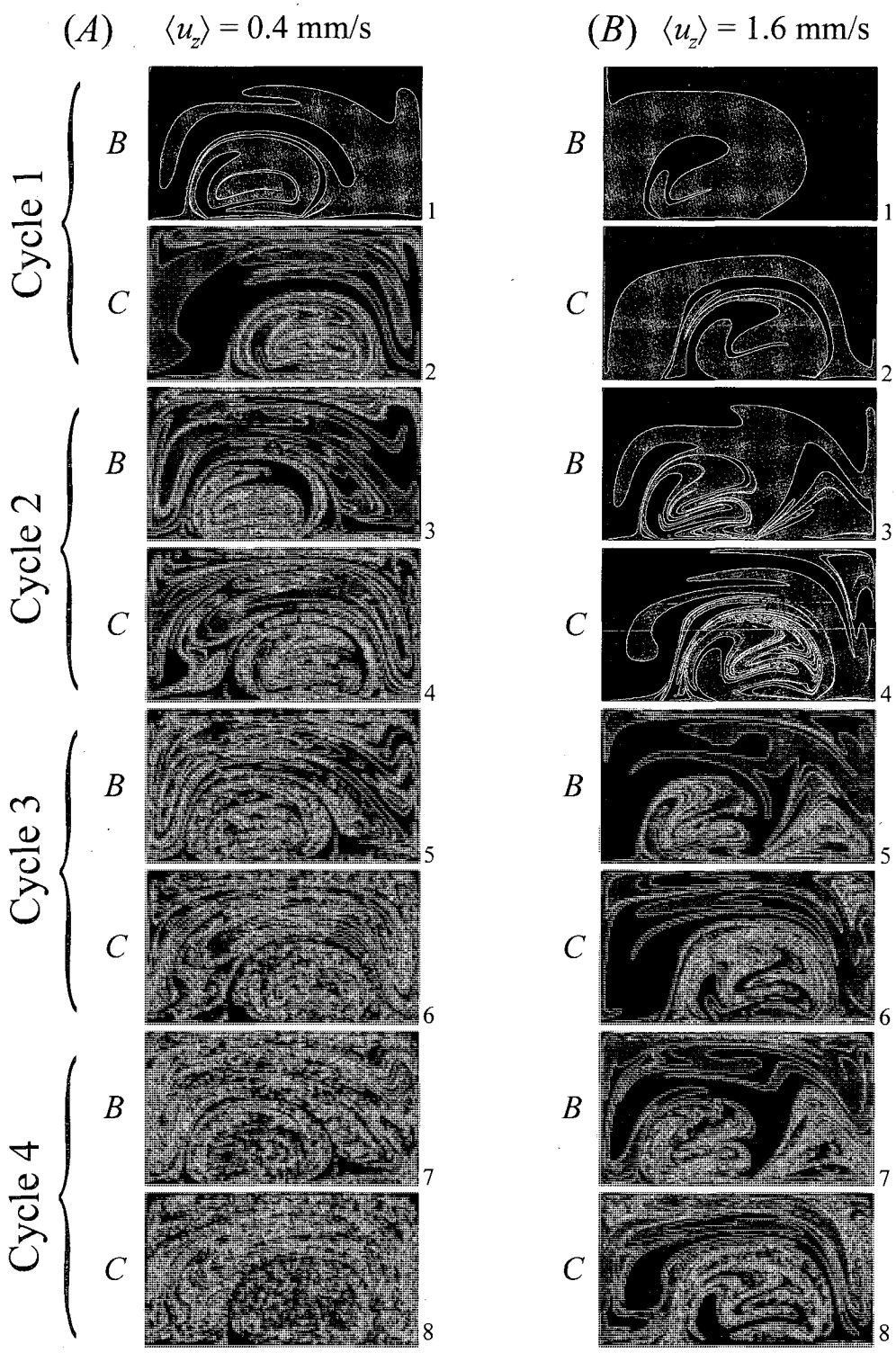

Figure 3.7. Tracer distributions (100,000 tracers) for two flow rates corresponding to the first eight electrodes for a mixer with an overall cycle pattern $[BC]_n$, and $\Delta\phi = 2.0$ V. The cross-sectional potential distributions and fluid streamlines are shown in Fig. 3.3.

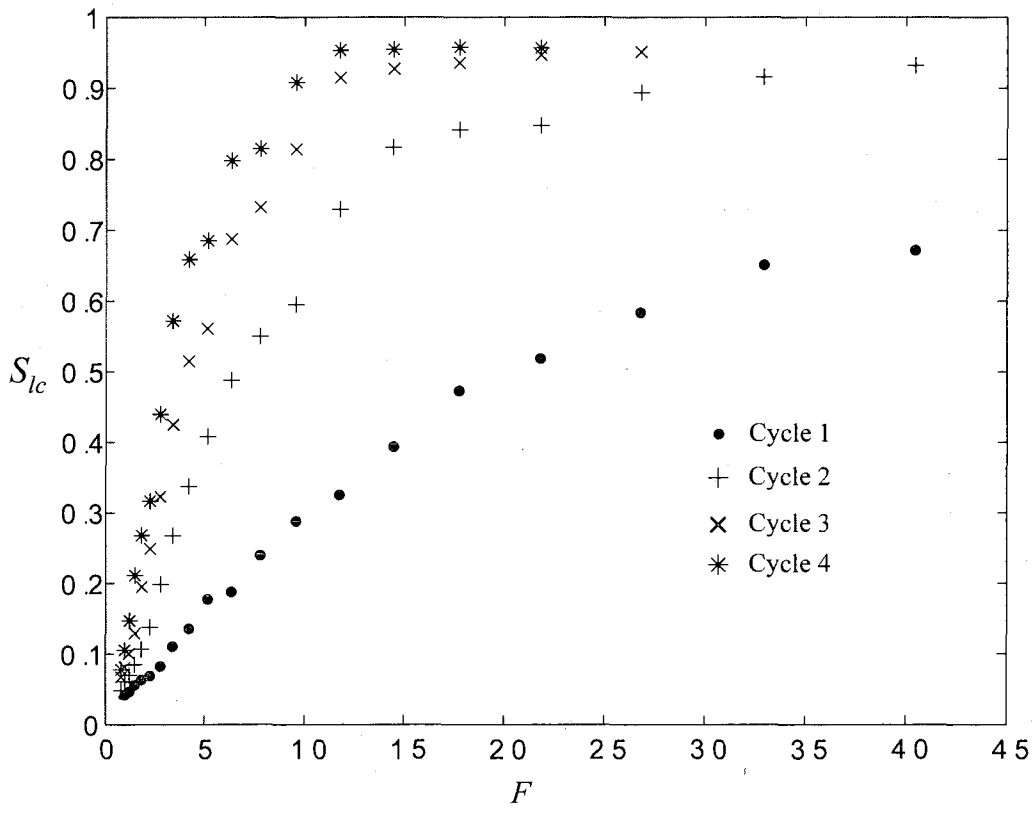

Figure 3.8. Calculated extent of mixing (S_{lc}) vs. the mixer effectiveness (F) measured at the outlet of the first four electrode cycles for a mixer with the overall cycle pattern $[ABCD]_n$

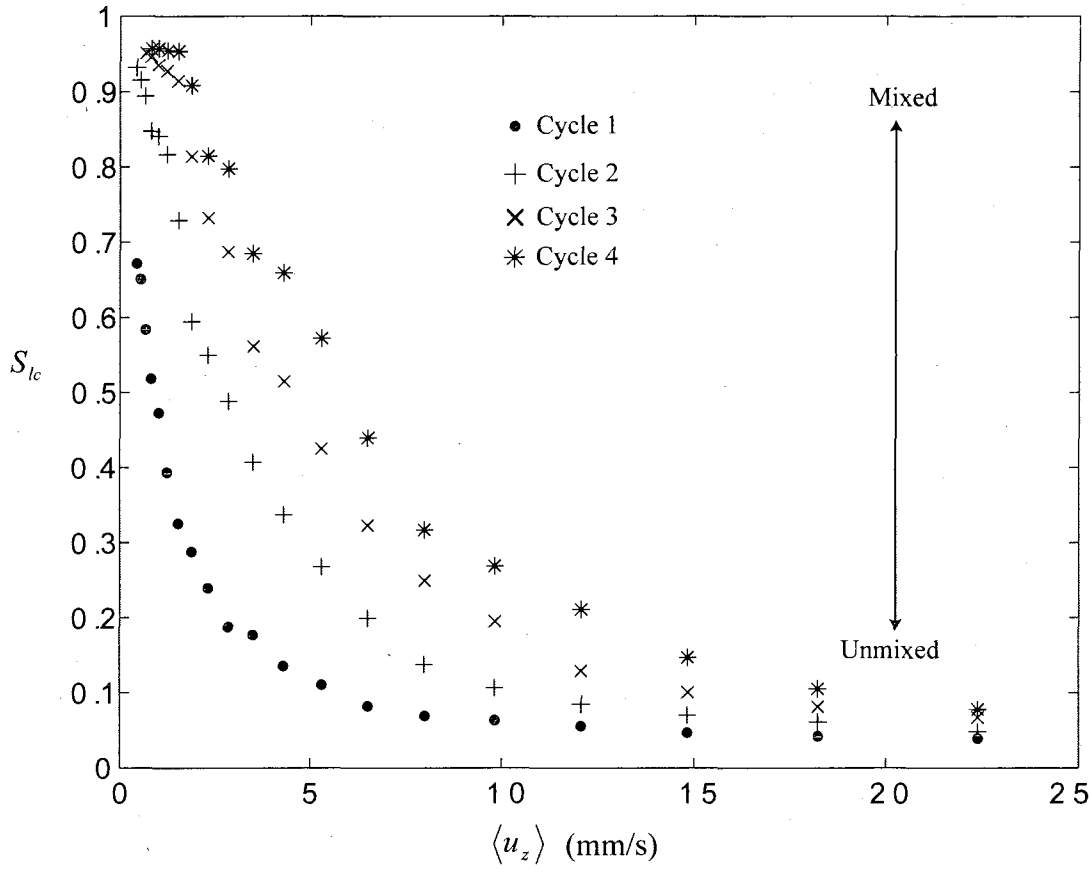

Figure 3.9. Calculated extent of mixing S_{lc} vs. the average axial fluid velocity $\langle u_z \rangle$ for a mixer with h = 60 μm, w = 140 μm, l_e = 400 μm, and $\Delta\phi$ =2.0 V. The mixer corresponds to the overall electrode cycle pattern $[ABCD]_n$

3.5 Experimental Results

3.5.1 Extent of Mixing Analysis

Based on the above analysis, a four electrode mixer $[ABCD]_3$ (Fig. 3.10*A*) was chosen for experimental studies. The dimensions of the mixer were w = 140 μm, h = 58 μm, and l_e = 400 μm, where the individual electrode cycles matched those shown in Fig. 3.3 and Fig. 3.9, with 70 μm axial spacing between individual electrodes. Mixing experiments were conducted such that two channel inlets containing a buffer solution (TES) were joined in a T-junction immediately upstream of the mixing electrodes, where one inlet stream contained a fluorescent dye (0.1 mM Rhodamine B). The flow rates of the two inlet streams were adjusted so that the volumetric flow rate of the pure buffer stream was twice that of the stream containing the fluorescent dye. The performance of the mixer was evaluated over a range of bulk flow rates, yielding average linear velocities of the dye/buffer solution were within the range $0.5 < \langle u_z \rangle < 12$ mm s^{-1}. After the flow had stabilized, an applied DC potential of $\Delta\phi$ = 2.0 V was placed across the electrode pairs. Fig. 3.10*B* displays top down fluorescence microscopy images 5.6 mm downstream of the t-junction pertaining to the before ($\Delta\phi$ = 0 V) and after ($\Delta\phi$ = 2.0 V) states, for $\langle u_z \rangle$ = 1.6 mm s^{-1}. Using a series of time averaged images (200 ms), fluorescent line scans across the channel width (averaged over 10 μm) of the mixer situated adjacent to an electrode cycle outlet were used to compute the adjusted extent of mixing (δ_a) via Eqn. (3.20).[i] In these animations, dye initially segregated to one half of the micro-channel is rapidly mixed throughout the channel cross-section upon application of a potential drop across the electrode pairs.

[i] Animations displaying the on/off operation of the mixing procedure may be viewed at http://navier.engr.colostate.edu/eof/ .

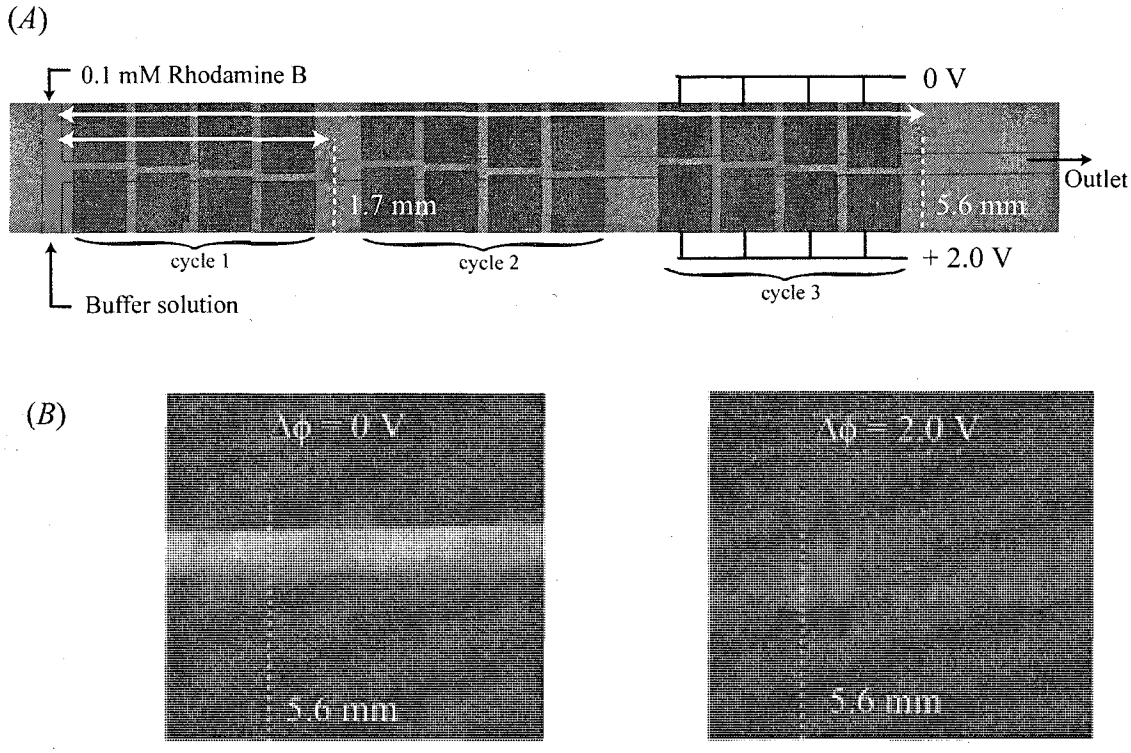

Figure 3.10. (*A*) Top down microscopic image of the experimental mixer used in this study. (*B*) Fluorescence images regarding $\Delta\phi = 0$ V and $\Delta\phi = 2.0$ V for the experimental mixer operated at $\langle u_z \rangle$ = 1.6 mm s^{-1}

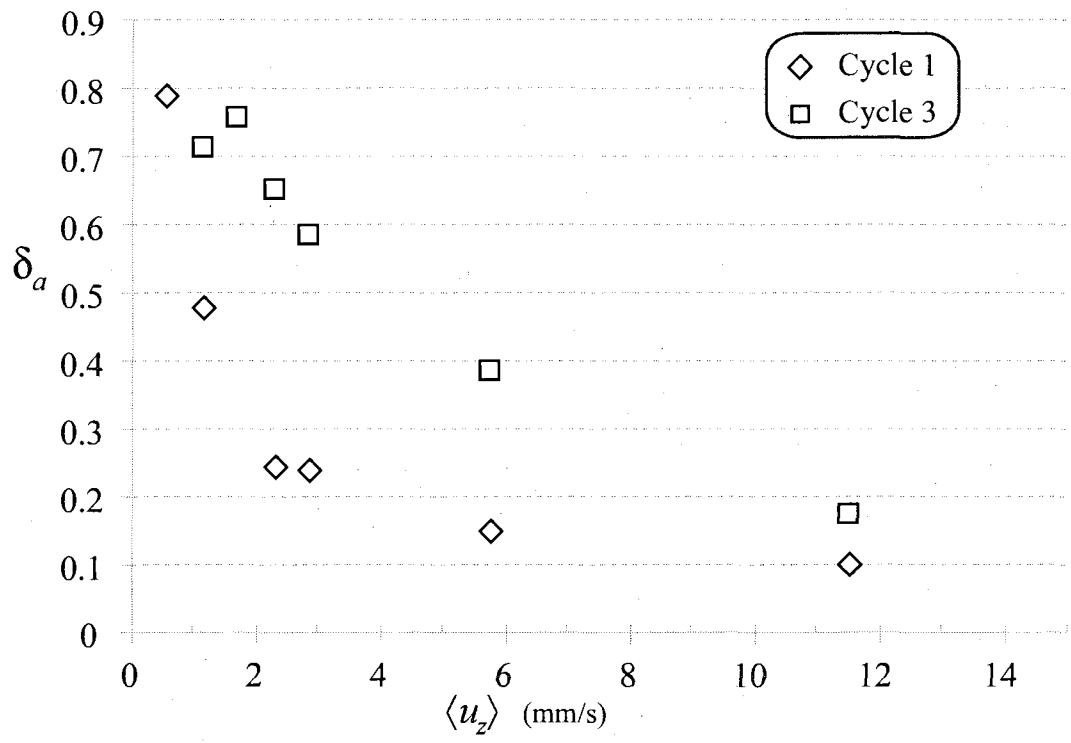

Figure 3.11. Adjusted extent of mixing (δ_a) vs. $\langle u_z \rangle$ for the mixer shown in Fig. 3.10.

Figure 3.11 presents δ_a as a function of $\langle u_z \rangle$ for the mixer shown in Fig. 3.10 operated with $\Delta\phi = 2.0$ V. The intensity values were acquired immediately downstream of the first (diamonds) and third electrode cycles (squares) shown in Fig. 3.10. Mixing was enhanced for all flow rates considered, if only to a small extent at higher bulk flow rates. The adjusted extent of mixing increases dramatically as $\langle u_z \rangle$ is decreased, experiencing a sharp rise when $\langle u_z \rangle < 3$ mm s^{-1}. As may be expected, δ_a measured after cycle 3 is greater than all respective values measured after cycle 1. It should be noted that, although δ_a provides a good estimate for the overall extent of mixing in the channel cross-sections, it cannot distinguish between a well mixed solution and a solution which is horizontally laminated with fluorescent and non-fluorescent solutions.[54] Because top-down microscopic methods were used in this study, these two states are indistinguishable. However, if at any point the channel cross-section were artificially mixed in this manner, one would expect high to

low transitions in δ_a values as the effectiveness F of the mixer is increased, e.g. lowering of $\langle u_z \rangle$ shown in Fig. 3.11. In practice this effect is never observed. Furthermore, the results displayed in Fig. 3.11 qualitatively agree with those shown in Fig. 3.9, created with the numerical model utilizing the same geometrical and operating parameters as the experimental device.

3.5.2 Localized Electrolysis

In general, application of a potential across an electrolyte solution will result in electrolysis of water on the surfaces of the integrated electrodes, with acid production localized to the anode and base production on the cathode.[37] Along with localized production of acid and base is the potential for formation of macroscopic O_2 and H_2 bubbles, respectively. Due to the removal of electrolysis products by axial flow, the mixer could be operated continuously ($\Delta\phi < 3.5$ V) for all of the flow rates displayed in Fig. 3.11 without any apparent formation of gas bubbles. However, at lower bulk flow rates ($\langle u_z \rangle < 0.5$ mm s^{-1}), local acid production can initiate a significant loss of the quantum efficiency of Rhodamine B, making quantification of the extent of mixing via Eqn. (3.20) problematic. Localized regions of low pH can furthermore be detrimental to a mixer of this type through protonation of the micro-channel walls, lowering the overall ζ-potential of the surfaces, and reducing the overall magnitude of EOF within the local regions. For the closed channel recirculating device shown by Lammertink *et al.*,[37] EOF between two integrated electrodes diminished 30 s after application of a potential difference between the electrodes. Similarly, in the limit $\langle u_z \rangle \rightarrow 0$ the transverse flow mixer in this study experiences the same phenomenon, where the limit of operation is determined by such factors as $\Delta\phi$, ζ, and the ionic concentration of the buffer solution.

To determine where this lower limit of operation might occur, 0.5 μm diameter fluorescent polymer microspheres (Duke Scientific) were used as a visualization tool. Due to their overall negative surface charge, electrostatic forces dominate in regions of

low fluid velocities, and the microspheres attract to the positive electrode. However, fluid velocities within the primary recirculation are high enough to entrap the particles, and helical flow can be viewed within this region.[ii] Using these microspheres as a visualization tool, it was found that, for bulk flows corresponding to $\langle u_z \rangle > 0.3$ mm s^{-1} and $\Delta\phi = 2.0$ V, no loss of transverse EOF over a period of 30 min was observed, during this period the current across the electrode gap remained constant, reaching steady state within several seconds. For very low fluid velocities ($\langle u_z \rangle \approx 0.05$ mm s^{-1}), the magnitude of transverse EOF was found to be significantly degraded within 2 minutes. From the animations, a large degree of fluid interaction within the inter-electrode space is evident for inter-electrode distances of 70 μm, where there exists transitional helical flow between the staggered electrode gaps. Although the numerical model discussed above neglects this flow, it is clear that, along with flow above each electrode gap, this inter-electrode flow can be used to promote a mixing environment. These flow interactions are the focus of future work.

3.5.3 Operational implications

From Fig. 3.9 and Fig. 3.11, it is seen that this type of mixer performs best at lower bulk flow rates. The extent of mixing after each electrode cycle at higher bulk flow rates can be increased via an increase of the mixer effectiveness F, which may be accomplished utilizing several strategies. For example, F may be increased directly via an increase in $\Delta\phi$ or l_e. However, these can increase the potential for both macroscopic gas formation and electrochemical interactions, both of which may promote unfavorable side effects. Furthermore, an increase in l_e leads to a mixer that requires greater axial space. The most effective method to increase F is to decrease the size of the electrode gap (w_g), which simultaneously increases the magnitude of the electric field and transverse electro-

[ii] Animations of fluorescent microsphere entrapment within the primary recirculation region may be viewed at http://navier.engr.colostate.edu/eof/.

osmotic velocity (constant $\Delta\phi$) between the gap. The decrease in w_g creates a primary recirculation flow profile that exhibits higher fluid velocities yet occupies less space along the channel floor; however, decreasing w_g may result in significant Joule heating effects. Thus, more focus must be placed not only on the overall mixing cycle pattern, but onto the temperature distributions within such a system. Also, the creation of more effective flow patterns may be possible by utilizing more electrodes per mixing unit, whereby electrodes can be placed along both the top and bottom walls of a micro-channel. The overall effects of new mixing configurations, along with a minimization of the total electrode surface area in the micro-channel, are the focus of future work.

3.6 Future Work

Since the completion these studies, there have been a number of investigations focused on applying transverse electric fields onto the cross-section of axial driven flow in a microchannel. Chang and Yang studied spatial and temporal changes in the ζ-potential distributions of the walls of a microchannel subjected to axial electro-osmotic flow.[55] By optimizing the temporal changes to the system, a chaotic mixing state was theorized within an axial distance of $z = 20w$, determined via both study of the Lyapunov exponent of the system as well as Poincaré mapping techniques. In another study, Pacheco *et al.* produced a chaotic mixing state in a two-dimensional cavity by introducing random temporal fluctuations into the applied potential on 4 individual electrodes located on the channel sidewalls.[56] This concept was then applied to a theoretical three-dimensional device, where optimal temporal fluctuations were found to produce a chaotic mixing state.[57] In these studies, no attempts concerning the fabrication and operation of an experimental device were made. Futhermore, these theorized devices would involve complex fabrication techniques, generally unavailable to standard clean room laboratories.

The device in this study has great promise for incorporation into lab-on-a-chip devices where rapid mixing of fluids is required within short axial distances. The following subsections detail potential methods to optimize the mixing characteristics of the device while minimizing the electrolytic impact on the contents of the microchannel.

3.6.1 Optimization of Mixing Electrode Design

The mixing electrodes in this study were fabricated with simple patterns such that the individual electrodes possessed a constant surface area along the channel axis. As a result of this design there is a large amount of electrode surface area immediately in contact with the electrolyte solution. Areas of the electrode surface located away from the electrode gap have several negative effects on the properties of the device, namely (1) no EOF occurs on the electrode surface, and these electrode regions act to inhibit the overall magnitude of helical flow within the secondary recirculation region, and (2) these regions of the electrode serve to negatively modify the properties of the electrolyte solution through electrolytic effects. Therefore it seems reasonable to minimize the surface area of the electrodes in a fashion such that the overall shape of the electrode gap is maintained. Figure 3.12 displays the shape of these proposed electrodes. With this new electrode shape the overall surface area of the electrode can be reduced by an order of magnitude or more, while preserving the magnitude of the EOF in between the electrode gap. Figure 3.13 displays the ϕ-contour profile and fluid streamlines of a microchannel with w = 100 μm, h = 25 μm, and w_g = 40 μm for both the original and proposed electrode designs. The contour plots shown in Fig. 3.13 were calculated using the methods discussed above. The primary recirculation region in both electrode designs is qualitatively the same, while the secondary recirculation region for the new design appears to encompass more fluid near the microchannel floor. With these qualities in mind it is expected that the performance of the proposed design be at least as high as the current mixer.

Using traditional clean room laboratory techniques, it is expected that the integrated micro-electrodes would be limited to widths on the order of 5-10 μm. To further reduce the electrolytic effects of these electrodes, an insulating layer could be placed on top of the electrodes. This layer, constructed from either a hard material (SiO_2) or soft polymer (Su-8), would need to adhere to the electrodes over a large applied potential range and be fabricated such that the edge of the electrodes remain open to the electrolyte solution. It is unclear if very thin coatings of a insulating layer covering the entire electrode would serve to produce useful EOF velocities.

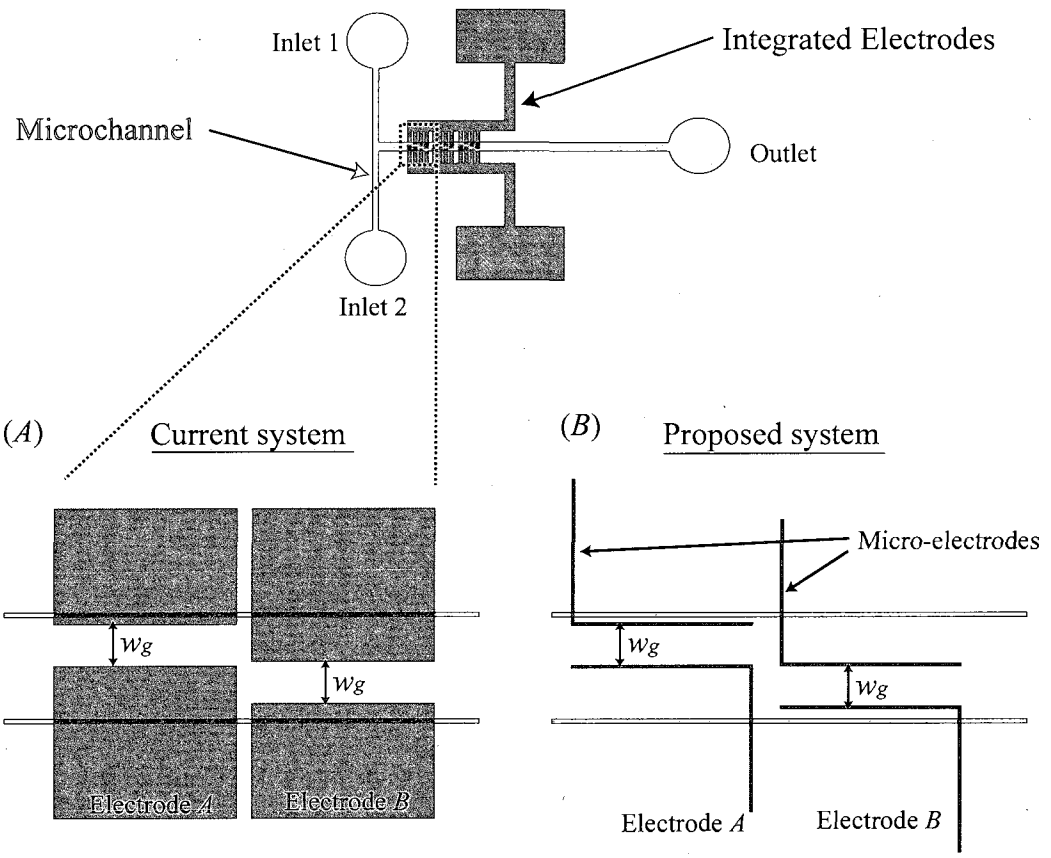

Figure 3.12. Proposed electrode design. By maintaining the outline of the original integrated electrodes, the function of the electrode gap is preserved.

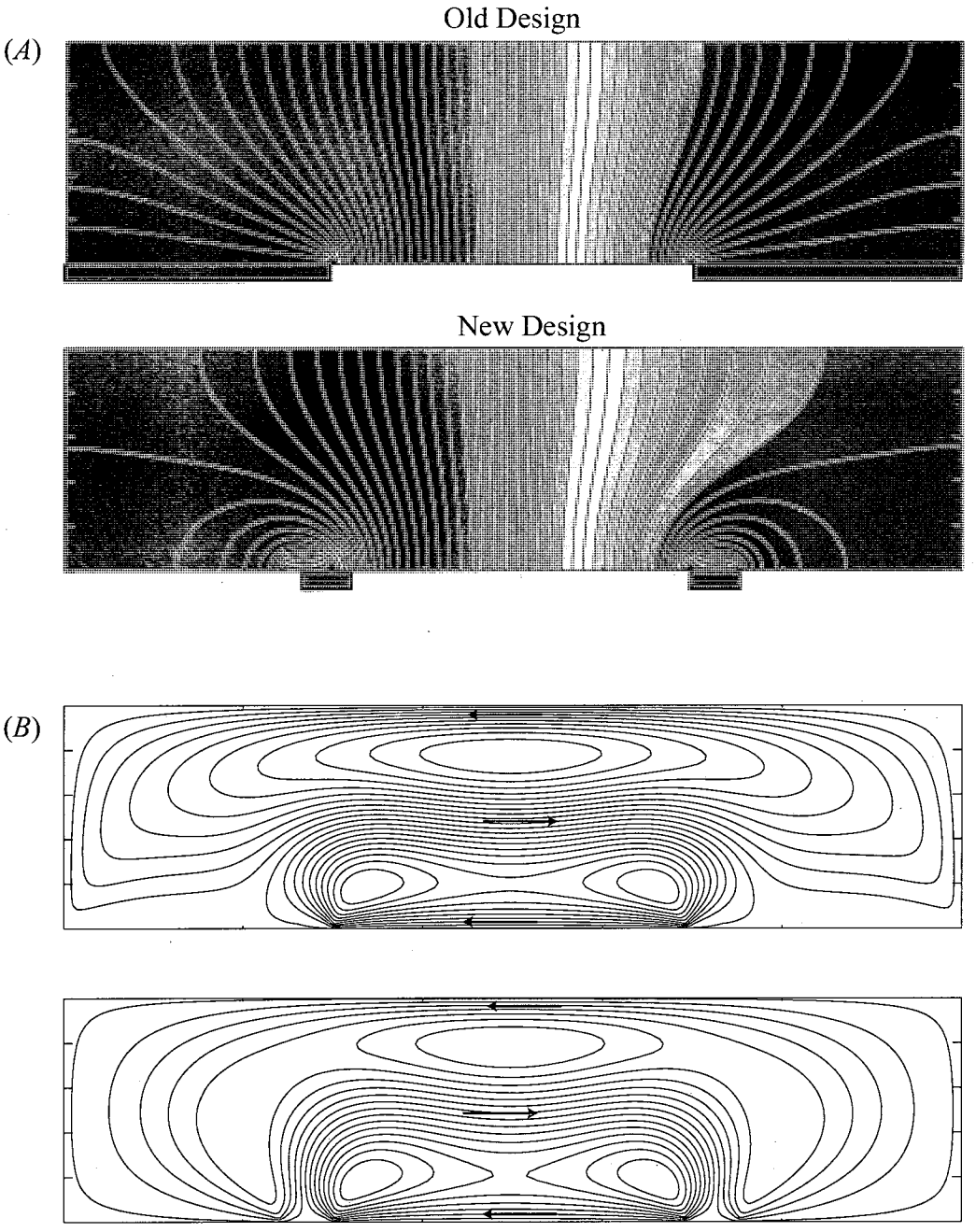

Figure 3.13. (*A*) ϕ-contour plot and (*B*) fluid streamlines for a microchannel with w = 100 μm, h = 25 μm, w_g = 40 μm, and $\Delta\phi$ = 1.0V.

3.6.2 Incorporation of Mixing Electrodes on Two Surfaces

From the results shown in this study, it is clear that the region of space directly between each electrode gap contributes to the creation of the primary recirculation region, which is responsible for the bulk of the mixing effectiveness in such a device. The high velocities within the primary recirculation region are due to the high potential gradient existing between the electrode gap, therefore it seems reasonable to fabricate a system of electrodes such that the potential gradient remains high along the entire cross-sectional surface area. This can be accomplished both by adding more electrodes along the bottom surface as well as the addition of multiple electrodes on the top surface. Multiple electrodes on each floor facilitate the creation of multiple high-velocity recirculation regions using smaller electrode gaps, requiring lower potential differences for each gap and minimizing electrolytic effects to the fluid. Figure 3.14 displays cross-sectional ϕ-contour profiles and stream lines for a device with three or four 10 μm wide electrodes located on both the top and bottom of the channel. By a simple alteration of the micro-electrode geometry for each electrode cycle, an efficient mixing profile can be created.

Fabrication of these multi-layer devices can be accomplished via electrode deposited onto two glass substrates, which are bonded with a layer of Su-8 polymer with thickness *h*. Such a device has been successfully fabricated in the CSU clean room; however, all multiple electrode devices failed when subjected to experimental testing due to problematic artifacts of the experimental methods at the time. The details of the fabrication of such a device can be seen in Chapter 7. Unless modified by post-fabrication methods, the Su-8 based sidewalls of this type of mixer will not support EOF; however, it is expected that efficient mixing profiles can still be created with the top and bottom floors alone, as seen in Fig 3.14.

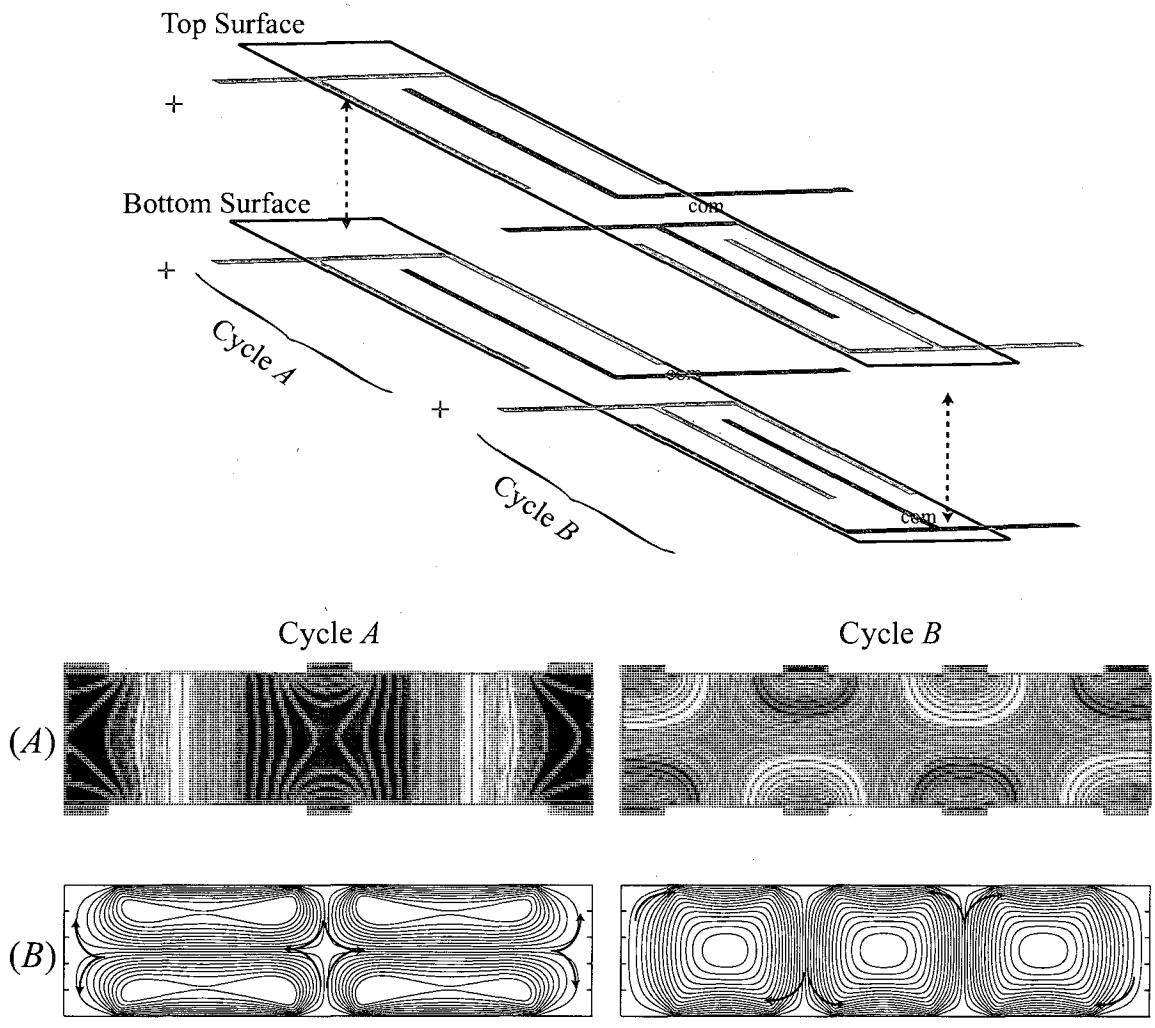

Figure 3.14. (*A*) ϕ-contour plots and (*B*) fluid stream lines for the proposed mixer with multiple micro-electrodes per cycle. The sidewalls in this case possess a value of $\zeta = 0$.

3.6.3 Optimization of Microchannel Geometries

As previously discussed, the rate at which a fluid can be mixed is, generally, directly associated with the magnitude of non-axial helical flow within a closed conduit. This principal applies directly to the mixer within this study, displayed in Fig. 3.8, as increases in the mixer effectiveness (F) lead to decreases in the overall axial channel length required to completely mix a fluid. Because the primary mixing mechanism, EOF, is a surface based phenomenon, it is reasonable to assume that microchannel geometries of $h/w \approx 1$ would lead to non-axial flow profiles that are non-optimal for mixing purposes. Concerning the fabrication methods used in this study, optimal mixing profiles would consist of increasing the ϕ-potential gradient in the x-direction and utilizing channel geometries of $h/w < 1$. An optimal microchannel/electrode design would include a balance of enhanced non-axial flow patterns utilizing high aspect ratio channels with a channel geometry that allows for reasonable flow rates with a given axial pressure drop. With such a design, effective mixing of fluids with higher axial velocities than those displayed in Fig. 3.11 might be possible. Determination of an overall optimal design, including the microchannel geometry as well as the geometry of the electrodes, would be determined utilizing the computational methods utilized in this study. In this study, no effort was given to study the effects of the channel dimensions on mixing effectiveness.

3.7 Conclusions

This study demonstrates the capability of a new microfluidic mixing device that combines transverse electro-osmotic flow and axial pressure driven flow. The mixer is readily fabricated, and operation requires only a low-voltage power supply and standard methods of fluid delivery. Non-axial flow is produced within the device via transverse electric fields generated by a potential drop across integrated metal electrodes. The degree of mixing over each electrode gap is related to the effectiveness parameter F, which can be directly controlled via geometric parameters (w_g, l_e) or operational conditions ($\langle u_z \rangle$, $\Delta\phi$).

A simplified model combining two-dimensional EOF with Poiseuille flow is used to describe the three-dimensional velocity field in the mixer. Utilizing particle tracking of passive tracers, the model is applied to an initial survey of the key geometric and operational parameters describing the system. It is shown that the extent of mixing at specified x,y-planes increases as F increases, where these results can be transformed to describe the mixers' performance as a function of $\langle u_z \rangle$. A laboratory device has been fabricated using soft lithographic methods, and the extent of mixing using fluorescent microscopy measured as a function of bulk axial flow. The laboratory mixer displays excellent mixing properties at low values of $\langle u_z \rangle$. Furthermore, the numerical model predictions are in excellent agreement with data acquired from the laboratory device. This study presents the first experimental device to utilize combinations of localized transverse electric fields to promote mixing within axial driven flow.

3.8 References

1. H. A. Stone, A. D. Stroock and A. Ajdari, (2004) Engineering flows in small devices: Microfluidics toward a lab-on-a-chip *Annual Review of Fluid Mechanics*, **36**, 381-411.
2. J. Cha, J. Kim, S. K. Ryu, J. Park, Y. Jeong, S. Park, S. Park, H. C. Kim and K. Chun, (2006) A highly efficient 3D micromixer using soft PDMS bonding *Journal of Micromechanics and Microengineering*, **16**, 1778-1782.
3. H. Chen and J. C. Meiners, (2004) Topologic mixing on a microfluidic chip *Biophysical Journal*, **86**, 482a-482a.
4. C. Neils, Z. Tyree, B. Finlayson and A. Folch, (2004) Combinatorial mixing of microfluidic streams *Lab on a Chip*, **4**, 342-350.
5. D. Therriault, S. R. White and J. A. Lewis, (2003) Chaotic mixing in three-dimensional microvascular networks fabricated by direct-write assembly *Nature Materials*, **2**, 265-271.
6. Y. N. Xia and G. M. Whitesides, (1998) Soft lithography *Annual Review of Materials Science*, **28**, 153-184.
7. F. Jiang, K. S. Drese, S. Hardt, M. Kupper and F. Schonfeld, (2004) Helical flows and chaotic mixing in curved micro channels *Aiche Journal*, **50**, 2297-2305.
8. F. Schonfeld and S. Hardt, (2004) Simulation of helical flows in microchannels *Aiche Journal*, **50**, 771-778.
9. A. P. Sudarsan and V. M. Ugaz, (2006) Fluid mixing in planar spiral microchannels *Lab on a Chip*, **6**, 74-82.
10. Y. Yamaguchi, F. Takagi, T. Watari, K. Yamashita, H. Nakamura, H. Shimizu and H. Maeda, (2004) Interface configuration of the two layered laminar flow in a curved microchannel *Chemical Engineering Journal*, **101**, 367-372.
11. Y. Yamaguchi, F. Takagi, K. Yamashita, H. Nakamura, H. Maeda, K. Sotowa, K. Kusakabe, Y. Yamasaki and S. Morooka, (2004) 3-D simulation and visualization of laminar flow in a microchannel with hair-pin curves *Aiche Journal*, **50**, 1530-1535.
12. J. T. Yang, K. J. Huang and Y. C. Lin, (2005) Geometric effects on fluid mixing in passive grooved micromixers *Lab on a Chip*, **5**, 1140-1147.
13. A. D. Stroock, S. K. Dertinger, G. M. Whitesides and A. Ajdari, (2002) Patterning flows using grooved surfaces *Analytical Chemistry*, **74**, 5306-5312.
14. A. D. Stroock, S. K. W. Dertinger, A. Ajdari, I. Mezic, H. A. Stone and G. M. Whitesides, (2002) Chaotic mixer for microchannels *Science*, **295**, 647-651.
15. D. S. Kim, S. W. Lee, T. H. Kwon and S. S. Lee, (2004) A barrier embedded chaotic micromixer *Journal of Micromechanics and Microengineering*, **14**, 798-805.
16. H. Sato, S. Ito, K. Tajima, N. Orimoto and S. Shoji, (2005) PDMS microchannels with slanted grooves embedded in three walls to realize efficient spiral flow *Sensors and Actuators a-Physical*, **119**, 365-371.
17. H. Suzuki, C. M. Ho and N. Kasagi, (2004) A chaotic mixer for magnetic bead-based micro cell sorter *Journal of Microelectromechanical Systems*, **13**, 779-790.
18. K. P. Selverov and H. A. Stone, (2001) Peristaltically driven channel flows with applications toward micromixing *Physics of Fluids*, **13**, 1837-1859.

19. J. West, J. P. Gleeson, J. Alderman, J. K. Collins and H. Berney, (2003) Structuring laminar flows using annular magnetohydrodynamic actuation *Sensors and Actuators B-Chemical*, **96**, 190-199.
20. A. Dodge, M. C. Jullien, Y. K. Lee, X. Niu, F. Okkels and P. Tabeling, (2004) An example of a chaotic micromixer: the cross-channel micromixer *Comptes Rendus Physique*, **5**, 557-563.
21. X. Z. Niu and Y. K. Lee, (2003) Efficient spatial-temporal chaotic mixing in microchannels *Journal of Micromechanics and Microengineering*, **13**, 454-462.
22. X. Z. Niu, L. Y. Liu, W. J. Wen and P. Sheng, (2006) Hybrid approach to high-frequency microfluidic mixing *Physical Review Letters*, **97**, -.
23. C. C. Chang and R. J. Yang, (2007) Electrokinetic mixing in microfluidic systems *Microfluidics and Nanofluidics*, **3**, 501-525.
24. N. Sundaram and D. K. Tafti, (2004) Evaluation of microchamber geometries and surface conditions for electrokinetic driven mixing *Analytical Chemistry*, **76**, 3785-3793.
25. J. Park, S. M. Shin, K. Y. Huh and I. S. Kang, (2005) Application of electrokinetic instability for enhanced mixing in various micro-T-channel geometries *Physics of Fluids*, **17**, -.
26. M. H. Oddy, J. G. Santiago and J. C. Mikkelsen, (2001) Electrokinetic instability micromixing *Analytical Chemistry*, **73**, 5822-5832.
27. H. Lin, B. D. Storey, M. H. Oddy, C. H. Chen and J. G. Santiago, (2004) Instability of electrokinetic microchannel flows with conductivity gradients *Physics of Fluids*, **16**, 1922-1935.
28. T. S. Leu and F. C. Ma, (2005) Novel EHD-pump driven micro mixers *Journal of Mechanics*, **21**, 137-144.
29. T. J. Johnson and L. E. Locascio, (2002) Characterization and optimization of slanted well designs for microfluidic mixing under electroosmotic flow *Lab on a Chip*, **2**, 135-140.
30. C. Y. Lee, G. B. Lee, L. M. Fu, K. H. Lee and R. J. Yang, (2004) Electrokinetically driven active micro-mixers utilizing zeta potential variation induced by field effect *Journal of Micromechanics and Microengineering*, **14**, 1390-1398.
31. J. L. Lin, K. H. Lee and G. B. Lee, (2005) Active mixing inside microchannels utilizing dynamic variation of gradient zeta potentials *Electrophoresis*, **26**, 4605-4615.
32. H. Y. Wu and C. H. Liu, (2005) A novel electrokinetic micromixer *Sensors and Actuators a-Physical*, **118**, 107-115.
33. E. Biddiss, D. Erickson and D. Q. Li, (2004) Heterogeneous surface charge enhanced micromixing for electrokinetic flows *Analytical Chemistry*, **76**, 3208-3213.
34. C. C. Chang and R. J. Yang, (2004) Computational analysis of electrokinetically driven flow mixing in microchannels with patterned blocks *Journal of Micromechanics and Microengineering*, **14**, 550-558.
35. C. C. Chang and R. J. Yang, (2006) A particle tracking method for analyzing chaotic electroosmotic flow mixing in 3D microchannels with patterned charged surfaces *Journal of Micromechanics and Microengineering*, **16**, 1453-1462.

36. T. E. McKnight, C. T. Culbertson, S. C. Jacobson and J. M. Ramsey, (2001) Electroosmotically induced hydraulic pumping with integrated electrodes on microfluidic devices *Analytical Chemistry*, **73**, 4045-4049.
37. R. G. H. Lammertink, S. Schlautmann, G. A. J. Besselink and R. B. M. Schasfoort, (2004) Recirculation of nanoliter volumes within microfluidic channels *Analytical Chemistry*, **76**, 3018-3022.
38. I. Gitlin, A. D. Stroock, G. M. Whitesides and A. Ajdari, (2003) Pumping based on transverse electrokinetic effects *Applied Physics Letters*, **83**, 1486-1488.
39. S. Z. Qian and H. H. Bau, (2002) A chaotic electroosmotic stirrer *Analytical Chemistry*, **74**, 3616-3625.
40. S. Z. Qian and H. H. Bau, (2005) Theoretical investigation of electro-osmotic flows and chaotic stirring in rectangular cavities *Applied Mathematical Modelling*, **29**, 726-753.
41. J. R. Pacheco, K. P. Chen and M. A. Hayes, (2006) Rapid and efficient mixing in a slip-driven three-dimensional flow in a rectangular channel *Fluid Dynamics Research*, **38**, 503-521.
42. R. J. Hunter and R. H. Ottewill, *Zeta potential in colloid science : principles and applications*, Academic Press, London ; New York, 1981.
43. J. L. Anderson, (1989) Colloid Transport by Interfacial Forces *Annual Review of Fluid Mechanics*, **21**, 61-99.
44. V. V. Meleshko, (1998) Biharmonic problem in a rectangle *Applied Scientific Research*, **58**, 217-249.
45. A. D. Stroock and G. J. McGraw, (2004) Investigation of the staggered herringbone mixer with a simple analytical model *Philosophical Transactions of the Royal Society of London Series a-Mathematical Physical and Engineering Sciences*, **362**, 971-986.
46. I. Altas, J. Dym, M. M. Gupta and R. P. Manohar, (1998) Multigrid solution of automatically generated high-order discretizations for the biharmonic equation *Siam Journal on Scientific Computing*, **19**, 1575-1585.
47. Z. B. Stone and H. A. Stone, (2005) Imaging and quantifying mixing in a model droplet micromixer *Physics of Fluids*, **17**, -.
48. M. Camesasca, M. Kaufman and I. Manas-Zloczower, (2006) Quantifying fluid mixing with the Shannon entropy *Macromolecular Theory and Simulations*, **15**, 595-607.
49. M. Camesasca, I. Manas-Zloczower and M. Kaufman, (2005) Entropic characterization of mixing in microchannels *Journal of Micromechanics and Microengineering*, **15**, 2038-2044.
50. J. N. Lee, C. Park and G. M. Whitesides, (2003) Solvent compatibility of poly(dimethylsiloxane)-based microfluidic devices *Analytical Chemistry*, **75**, 6544-6554.
51. J. A. Vickers, M. M. Caulum and C. S. Henry, (2006) Generation of hydrophilic poly(dimethylsiloxane) for high-performance microchip electrophoresis *Analytical Chemistry*, **78**, 7446-7452.
52. S. Bhattacharya, A. Datta, J. M. Berg and S. Gangopadhyay, (2005) Studies on surface wettability of poly(dimethyl) siloxane (PDMS) and glass under oxygen-

plasma treatment and correlation with bond strength *Journal of Microelectromechanical Systems*, **14**, 590-597.

53. A. Sze, D. Erickson, L. Q. Ren and D. Q. Li, (2003) Zeta-potential measurement using the Smoluchowski equation and the slope of the current-time relationship in electroosmotic flow *Journal of Colloid and Interface Science*, **261**, 402-410.
54. M. S. Munson and P. Yager, (2004) Simple quantitative optical method for monitoring the extent of mixing applied to a novel microfluidic mixer *Analytica Chimica Acta*, **507**, 63-71.
55. C. C. Chang and R. J. Yang, (2008) Chaotic mixing in a microchannel utilizing periodically switching electro-osmotic recirculating rolls *Physical Review E*, **77**, -.
56. J. R. Pacheco, K. P. Chen, A. Pacheco-Vega, B. S. Chen and M. A. Hayes, (2008) Chaotic mixing enhancement in electro-osmotic flows by random period modulation *Physics Letters A*, **372**, 1001-1008.
57. J. R. Pacheco, (2008) Mixing enhancement in electro-osmotic flows via modulation of electric fields *Physics of Fluids*, **20**, -.

Chapter 4

Passive Microfluidic Pumping Using Coupled Capillary/Evaporation Effects

Portions of this chapter appear in the following:

- Lynn N.S., Henry C.S., and Dandy D.S. (2009) Evaporation from Microreservoirs *Lab on a Chip*, **9**, 1780-1788
- Lynn N.S. and Dandy D.S. *Submitted, Lab on a Chip*

4.1 Introduction

4.1.1 Passive Pumping

Perhaps the most important unit operation within microfluidics based lab-on-a-chip (LOC) devices lies in the handling and transport of fluids. Often overlooked, the ability to provide continuous flow with high precision can dramatically improve the efficiency and reliability of devices utilizing the fundamentals of separation, reaction, and detection for bioanalytical purposes and point-of-care diagnostics.[1] These different processes are often carried out in a complex network of microchannels comprising a microfluidic network (μFN) that links the inlet/outlet regions serving as interfaces for analyte delivery or product and waste collection. The traditional active mechanisms for fluid transport within μFNs generally rely on either pressure-driven flows from syringe pumps and pressurized chambers or flows derived from electrokinetic phenomena.[2]

A large class of active micropumps relies on the oscillatory or rotational movements of internal components (or the microchannel walls) to displace finite volumes of fluid in a periodic fashion. Because of the low Reynolds numbers associated with these devices, nearly all require the use of check valves arranged in a manner that unidirectional flow is

accomplished as a result of the oscillatory movements. These micro-check valves become susceptible to failure upon introduction of particulate matter, and usually work only in limited flow rates and oscillatory frequencies. Early pumps featuring a reciprocating diaphragm actuated by piezoelectric means in order to pump fluids through a directed check valve arrangement were first demonstrated by several groups, where the pumping units possessed size footprints greater than a square centimeter.[3-5] The creation of oscillatory movements via piezoelectric materials requires somewhat high potentials (> 100 V) for the creation of relatively small stroke lengths (< 15 μm). Multiple studies aimed at both the optimization of stroke volumes and fabrication methods regarding these piezoelectric actuated micropumping systems have been realized with varying success.[6, 7] Due to the many problems associated with piezoelectric actuation, there has been a significant amount of work aimed at the creation of reciprocating micropumps actuated by a variety of means, including electrostatic,[8] thermopneumatic,[9-11] and electromagnetic interactions.[12] However, devices utilizing this pumping mechanism are highly susceptible to failure upon introduction of small gas bubbles into the pumping chamber; to date there have been only several self-priming pumps utilizing this mechanism that are tolerant to this problem.[11, 12] Other microfluidic pumping devices using reciprocating actuation that operate without the use of valves have also been reported.[13, 14]

In contrast to the actuated pumps discussed above that possess moving parts, a large class of microfluidic pumps has been developed that take advantage of various electromagnetic phenomena. These pumps possess no moving parts, and can usually be fabricated with simple microfabrication procedures available in many clean room environments; however, the pumps become severely limited by the properties of the fluid in question. Microfluidic pumps based on eletrohydrodynamic forces can pump fluids with flow rates spanning multiple orders of magnitude, requiring only modest potential drops;[15, 16] however, these pumps can only be used with non-ionic fluids with low conductivity (e.g. water, methanol). For the handling of ionic fluids, electroosmotic

pumps (operating via DC or AC currents) are capable of providing adjustable steady-state flows in a variety of microchannel geometries and substrates.[17]

Although these active delivery methods are able to provide adjustable volumetric flow rates spanning multiple orders of magnitude, they possess a number of negative features, including: respecively large dead volumes, complicated sample/interface connections, and a minimum requirement of $O(1)$ mL sized sample volumes. Furthermore, the utilization of these methods, along with less common flows based on centrifugal forces,[18] surface acoustic waves,[19] or micromechanical actuation,[20-22] generally require equipment that is significantly larger in size than the μFN itself and can severely restrict device portability.

Due to these limitations, there has been a significant amount of work focused on the creation of passive flows within μFNs. Demanding no external power input, passive flow methods require only fluid delivery to an inlet region (usually via pipette), after which filling of the μFN is spontaneous and the subsequent continuous flow is a function of the device design. Free from the size restrictions and power requirements of external equipment, LOC devices utilizing passive flow have great potential for use in point-of-care diagnostics and portable micro-total analysis systems.

Because of the inverse dependence of capillary pressure on the characteristic radius of curvature for an air/liquid interface, capillary forces are a convenient driving force for the creation of pressure-driven flow in hydrophilic microchannels. Passive flow from capillary forces in microchannels can be accomplished utilizing either static air/liquid menisci existing external to the μFN or menisci internal to the μFN whose positions move with time. Capillary pumps using internal menisci can be created via expanding channel networks in parallel such that the characteristic size of the outlet air/liquid meniscus remains on the order of the size of the microchannel.[23] These systems provide the ability to create very high differential pressures throughout the μFN and have been successfully applied to heterogeneous affinity assays, supplying near-constant continuous

flow over the course of several minutes.[24, 25] However, the pumping regions are $O(1)$ cm^2 in size and must be enlarged to maintain continuous flow for longer periods of time.

By transferring the menisci responsible for the driving capillary force to a position external to the μFN, the overall footprint of a capillary pump can be reduced substantially. Passive capillary pumping has been demonstrated utilizing the difference in curvature for liquid drops placed on the inlet and outlet reservoirs of a μFN,[26] where the overall size of the pumping region is $O(1)$ mm^2. Continuous flow between the reservoirs can be accurately described using simple analytical models accounting for the shape of each droplet;[27, 28] however, these models do not account for liquid loss through evaporation. Because the combined effects of evaporation and convective flow from each reservoir will act to change the overall capillary forces present in the system, the flow is transient and can only be sustained for several minutes.[29] Additionally, prediction of flow rates within these droplet-based passive pumping systems may be problematic in situations where the position of the air/liquid meniscus drops below the top of the reservoir, where the shape of the meniscus becomes sufficiently complicated as the liquid volumes approach sub-μL quantities that the effects of evaporation cannot be determined using simplified models.

Although there exists a great deal of literature focusing on the kinematics of filling a μFN via capillary forces, where filling times are typically less than 100 s, few studies have focused on the creation of sustained continuous flows, and little to no data exist concerning the state of flow within a μFN after filling has completed. In this chapter, a passive microfluidic pumping mechanism is demonstrated that combines the ability to create steady flows at high differential pressures within a mm^2 footprint. Through microfluidic particle tracking, we have observed a flow mechanism in simple systems consisting of a microchannel connecting two small micro-reservoirs, as seen in figure 4.1. After sample introduction to an inlet reservoir, capillary forces drive fluid through a μFN spontaneously such that a small meniscus is created along the corner regions of an outlet

reservoir. The reservoirs in Fig 4.1 have upper diameter D_1, lower diameter D_2, and height H and are connected by a microchannel with width w, height h, and length L. The system quickly reaches steady state and is able to provide constant flow rates through a μFN for more than an hour. Utilizing a simple model that accounts for both the rate of evaporation and the shape of an air/liquid interface for a given system, accurate predictions of laboratory flow rates as a function of reservoir and μFN geometries are demonstrated. This approach may be applied to nearly all LOC devices utilizing pressure-driven flow. As an illustrative example, this pumping technique is applied for the passive generation of temporally stable chemical gradients.

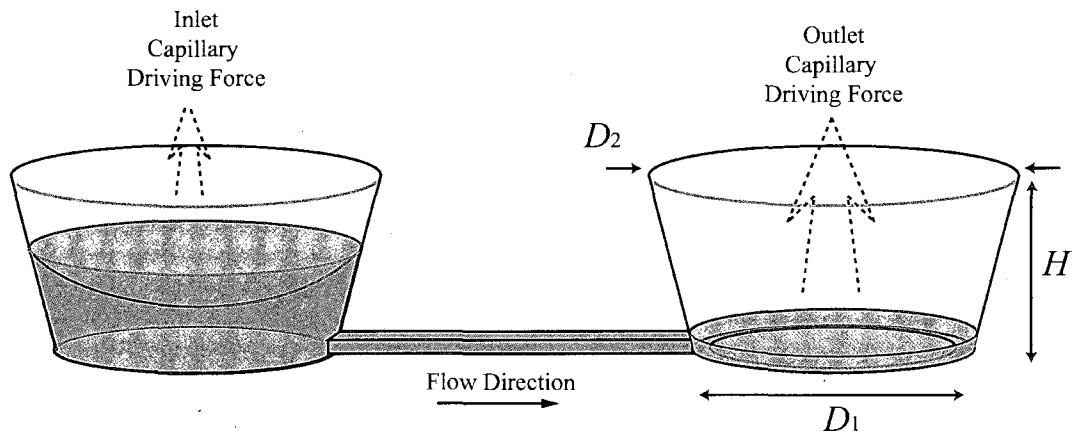

Figure 4.1. Diagram of overall system. The small meniscus along the corner regions of the outlet reservoir serves to drive fluid through a microchannel at high differential pressures.

4.1.2 Evaporation from Microreservoirs

Because of the high surface area to volume ratios in micro-fluidic systems, loss of fluid through evaporation and permeation becomes increasingly important.[30] Evaporation may rapidly increase the local concentration of solutes in systems that include an open air/liquid interface, which can lead to detrimental effects in an analytical system. If not

controlled, evaporation effects in systems containing sub-μL liquid volumes is of critical concern, as times required for the complete evaporation of a liquid sample can be less than a minute. In all microfluidic systems containing an open air/liquid interface, local evaporation rates and their dependence on local conditions and reservoir geometries must be taken into consideration.[29, 31, 32]

In many open microfluidic systems, attempts are made to either mitigate or enhance evaporation effects. Reducing the evaporation rate is generally required to maintain analyte concentrations when performing chemical analysis on aqueous fluids introduced or extracted in microreservoirs. If no action is taken to replenish the reservoir solvents, sub-μL sized volumes can dry out within a few minutes,[33] requiring a sufficiently fast analytical procedure.[34] Perhaps the easiest way to control evaporation from these reservoirs is via isolation of the air/liquid interface with either a solid lid[35] or an immiscible liquid cap, such as mineral oil[36] or another organic liquid.[33, 37] Other direct approaches involve control of the relative humidity directly above the air/liquid interface, usually performed via sample placement near a water bath to keep the surrounding air saturated with water vapor.[29, 38] More complicated approaches involve the fabrication of micro-reservoir arrays from agarose gel.[39] These gel-based arrays consist of over 90% water, saturating the local environment above each reservoir and substantially reducing evaporation rates.

Evaporation enhancement in lab-on-a-chip applications is generally associated with passive micro-fluidic pumping applications. A simple and efficient approach to evaporation-based passive pumps can also be realized by exposing the outlet regions of a μFN to the atmosphere, where evaporation occurring at the outlet region of a the μFN serves to drive fluid from an inlet reservoir through the system at substantial volumetric flow rates. Evaporation in these systems can then be enhanced by either forced convective air motion,[40] heating the outlet regions using microfabricated elements,[41] or

by increasing the air/liquid interface surface area at the μFN outlet with hydrophilic membranes[42] or filter paper plugs.[43]

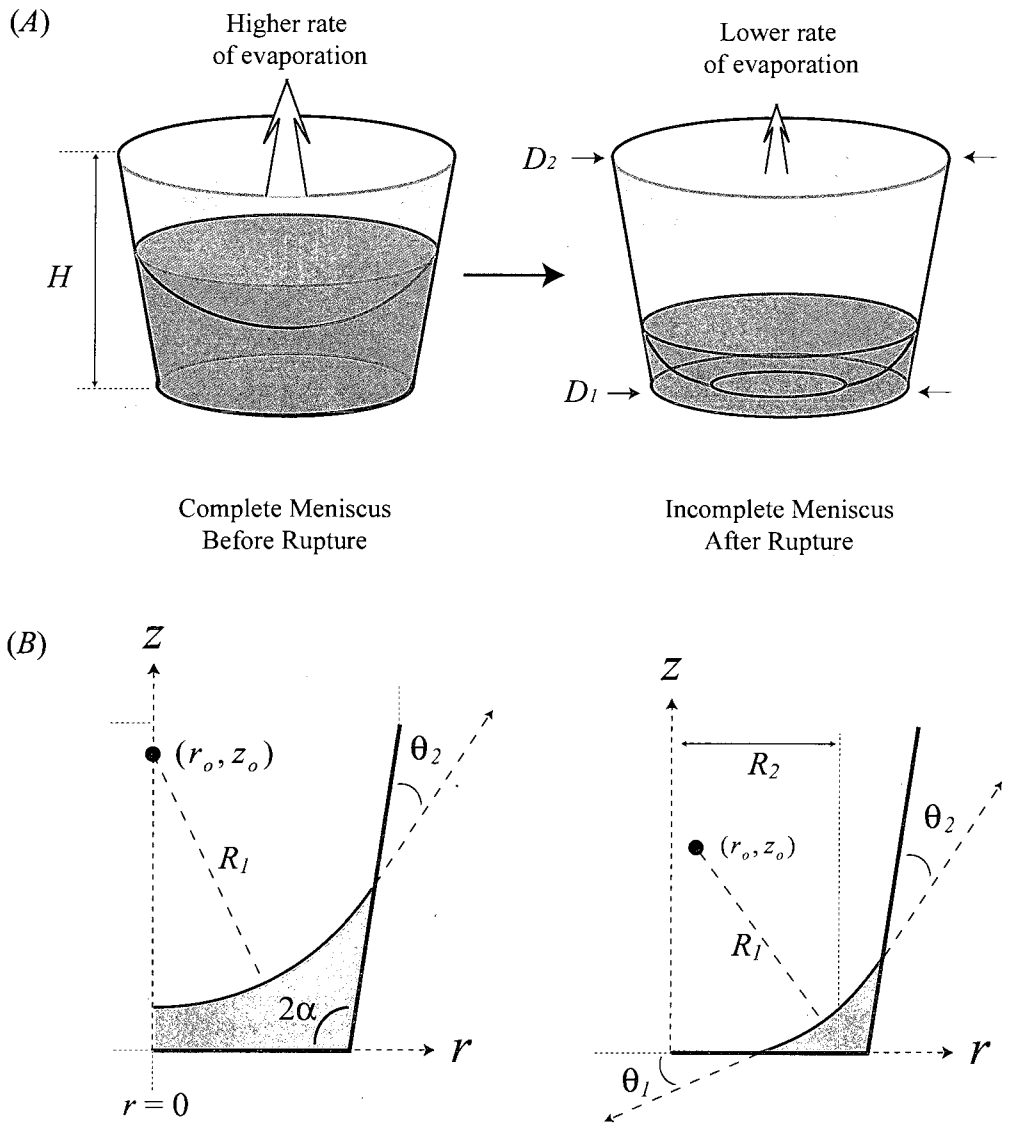

Figure 4.2. (*A*) As a meniscus recedes towards the bottom of a reservoir, it will rupture into an incomplete state. (*B*) Geometric parameters describing a meniscus in a microreservoir in the *r*,*z*-plane.

There are many LOC designs where uncontrolled evaporation can lead to unwanted changes to the initial experimental conditions and, if given enough time, failure of the device. In the case of passive pumping methods based on capillary forces, either between two droplets of water[26, 27] or liquid in an open faced micro-channel,[44] evaporation will continuously reduce the volume of water present in the system. This loss may lead to changes in the capillary forces driving liquid through the system, thus acting to increase (or decrease) the overall observed flow rate. In the case of μNFs used for the immobilization of immunoglobulins to a surface,[45] excessive evaporation from the inlet reservoir can lead to reservoir dry out and non-homogeneous deposition of material. This behavior may affect the overall reliability of devices that depend on uniform surface coverage of capture ligands, such as those used in various micromosaic immunoassays detailed in chapter 5.[46, 47]

In many LOC devices it becomes important to calculate not only the dependence of device performance on the evaporation rate, but also the time at which that device might undergo failure. The rate of evaporation from an air/liquid interface (Q_e) is dependent on both the conditions of the environment above the meniscus as well as the geometry of the meniscus itself. Historically, the study of the evaporation rate and shape of a liquid meniscus from μL-sized volumes has focused on the role of evaporation of a sessile drop for deposition of solids onto a flat surface.[48-51] While the evaporation of sessile drops remains important for many LOC applications, there is little information regarding evaporation of a droplet of water confined to a micro-reservoir constructed from hydrophilic materials. Previously, this topic has been restricted to experimental studies concerning evaporation of droplets in shallow nanoliter wells, with the focus on solute deposition from the droplets,[52] evolution of the meniscus with time,[53, 54] evaporation rate of the droplets,[55] or particle tracking studies of flow induced via evaporation.[56] In those studies meniscus shape evolution and the transient behavior of the evaporation rate were not estimated or predicted. The absence of these data may very well be due to the

complexity of the dynamics: as water in a micro-reservoir recedes to the point where the bottom of the meniscus reaches the reservoir floor, the meniscus will rupture due to the discontinuity of the surface energies between the initial air/liquid interface and the eventual solid/liquid interface along the reservoir floor (Fig. 4.2). In the small geometry of the reservoir, it may be assumed that body forces have negligible impact on the interface shape such that, prior to rupture the meniscus is spherical. However, after rupture the meniscus takes on a more complicated shape.

In order to accurately model the dynamics of flow for a system similar to that shown in Fig. 4.1, information regarding the instantaneous rate of evaporation from the meniscus must be known. In section 4.3.2 we examine the evaporation rate and shape evolution of an air/water meniscus situated in a cylindrical micro-reservoir modeled after those used in many LOC devices,[45-47] specifically, with a reservoir height , floor diameter, and upper diameter all on the order of a millimeter. A simple geometric model is proposed to determine the shape of a meniscus representing a given volume of water in a reservoir having a circular, but not necessarily constant, cross-section. With the interface geometry known, the evaporation rate of the water in the well can then be determined utilizing computational fluid dynamics (CFD). The combined geometric/CFD model is shown to reliably predict the evolution of air/water menisci in experimental systems. It is demonstrated that evaporation of water from micro-reservoirs can be either enhanced or suppressed, depending on the geometry of the reservoir. Other than passive pumping in microfluidic systems, the methods utilized within this chapter will prove useful in a wide array of applications such as the secondary measurement of the surface properties of a cylindrical shaped substrate, the concentration of solutes within a microreservoir, and the controlled deposition of solids onto the reservoir floor.

4.2 Experimental Methods

4.2.1 Solutions

For particle tracking experiments, solutions of 0.5 μm diameter fluorescent polystyrene microspheres (Duke Scientific) in nanopure water (Barnstead) were stabilized with tween-20 (Sigma) at a concentration of 1.5×10^{-7} M. The number density of the spheres ranged from 1.3×10^{7} to 6.5×10^{7} mL^{-1} depending on the height of the microchannel and speed of flow. For experiments involving evaporation of water from a reservoir with no flow, the number density of the spheres was 10^{6} mL^{-1}. For experiments involving the passive creation of chemical gradients, buffered solutions of fluorescently tagged immunoglobulin (IgG) were prepared as follows. Purified solutions of polyclonal IgG (Invitrogen) were fluorescently labeled with the Alexa Fluor 488 protein labeling kit (Invitrogen) and diluted to the proper concentrations in PBS (150 mM NaCl, 50 mM Na_2HPO_4, pH 7.4) along with 1.0 mg mL^{-1} of bovine serum albumin (Sigma), 1.5×10^{-7} M tween-20, and a microsphere density of 1.3×10^{6} mL^{-1}. All solutions were aggressively vortexed for 30 s before sample introduction to the inlet reservoir to ensure uniform distribution of the microspheres.

4.2.2 Fabrication of Microchannels and Reservoirs

The microchannels in this study were created using the soft lithographic methods developed by Xia *et al.*[57] Microchannel molds were composed of the negative photoresist Su-8 (Microchem) on 4" diameter polished silicon wafers (University Wafers). Protocols suggestions are available from MicroChem (www.microchem.com); however, optimal procedures vary from day-to-day and these protocols should be taken only as suggestions. Lithography of Su-8 is best accomplished on a clean wafer dehydrated at 180 °C prior to the spin coat process. After pouring a small amount (< 10 mL) of photoresist onto the wafer, the spin rate is slowly increased (166 rpm s^{-1}) to a spin speed of 800 rpm and held for 30 seconds. The spin rate is then increased (488 rpm s^{-1}) to a final spin rate and held

for an additional 30 seconds, after which the spin rate is slowly decreased to zero (166 rpm s^{-1}). The final spin rate and the viscosity of the photoresist solution are the predominant methods to control the overall thickness h of the Su-8 film; however, it should be noted that all of the coating steps have a strong effect on both the magnitude and uniformity of h. The wafer is then placed on a 65 °C hotplate for one minute (minimum) and transferred to a 95 °C hotplate for a period determined by h, generally longer than 10 minutes. The wafer is then exposed with UV radiation through both a 350 nm longpass filter (Omega PL-360LP) and dark field photomask (FineLine Imaging) for a period again determined by h and the intensity of the UV source. After exposure, the wafer is placed on a 95 °C hotplate for a minimum of 10 minutes and allowed to cool to room temperature. The wafer is then lightly stirred in propylene glycol methyl ether acetate (Sigma) to dissolve the unpolymerized Su-8 for several minutes, rinsed with isopropyl alcohol (Sigma) and blow dry with nitrogen. At this point the photoresist is rendered insoluble to all liquids and can only be removed via etching or stripping processes. The heights of the microchannel molds were measured with a profilometer, and widths were measured with a calibrated microscope. Only microchannel molds having microchannel heights with a standard deviation of less than 1 were used in this study.

Open faced microchannels were created by curing a degassed 1:10 curing agent:base mixture of poly(dimethylsiloxane) (PDMS, Sylgard 184, Dow Corning) prepolymer over the Su-8 molds at 110 °C for 120 minutes. The channel networks were then peeled from the molds and cut to final size with a razor blade. High precision biopsy punches (Technical Innovations) were then used to create the reservoir chambers, making sure the punch direction was as close to vertical as possible. The biopsy punch creates a conical cavity, which allows for an expanding ($D_2 > D_1$) or contracting ($D_2 < D_1$) reservoir, depending on which side the of the PDMS mold the reservoir is sealed. After the creation of the reservoirs, the PDMS molds were treated via an extraction, which has been shown

to stabilize the hydrophilic nature of an oxidized PDMS surface for up to 7 days.[58] The PDMS molds were rendered hydrophilic by exposure to air plasma (25 W, 900 mTorr, 30 s), after which the reservoirs were irreversibly sealed to a cleaned glass slide. For studies involving evaporation, some reservoirs were sealed to a flat PDMS mold.

4.2.3 Experiment Initialization and Image Acquisition

Experiments were generally conducted within 20 minutes after fabrication; however, experimental observations did not vary with respect to time after device fabrication for a period of up to several days. A microliter pipette was used to inject aqueous solutions into a microreservoir with liquid volume V_o ranging from 0.2 to 4 μL, depending on the reservoir and microchannel geometry under consideration. The temperature and relative humidity of the external environment was recorded at the onset of the experiment (Fluke 971 temperature humidity meter), and typically remained within 2 °C and 1.5 % RH of the initial conditions for several hours. Care was taken to eliminate the introduction of particulate matter into the reservoirs. Immediately after liquid introduction into the inlet reservoir ($t = 0$), the microchannels were placed on an inverted microscope equipped with an epifluorescence attachment (Nikon TE-2000U) fitted with a monochrome CCD camera (Coolsnap fx) using the program Metamorph (Molecular Devices).

4.2.4 Evolution of a Meniscus during Evaporation

For evaporation studies, pictures of the reservoir floor were taken at $\Delta t = 10$ s intervals starting at $t = t_c$ (meniscus rupture) and extending until the reservoir was completely dry (t_{end}). This series of images were then used to measure the diameter of the inner meniscus (D_{cap}) as a function of time. Figures 4.3*A* and 4.*3B* show the diagram of the experimental setup and images displaying the meniscus before and after rupture. Figure 4.3*C* displays D_{cap} as a function of time for an initial liquid volume of $V_o = 0.65$ μL in a reservoir with $D_1 = 1.38$ mm, $D_2 = 0.77$ mm, and $H = 2.2$ mm. The rupture event

occurred at t_c = 42.9 min with an initial rupture diameter of $D_{cap}(t_c)$ = 0.47 mm, and the reservoir was completely dry at t_{end} = 64.7 min.

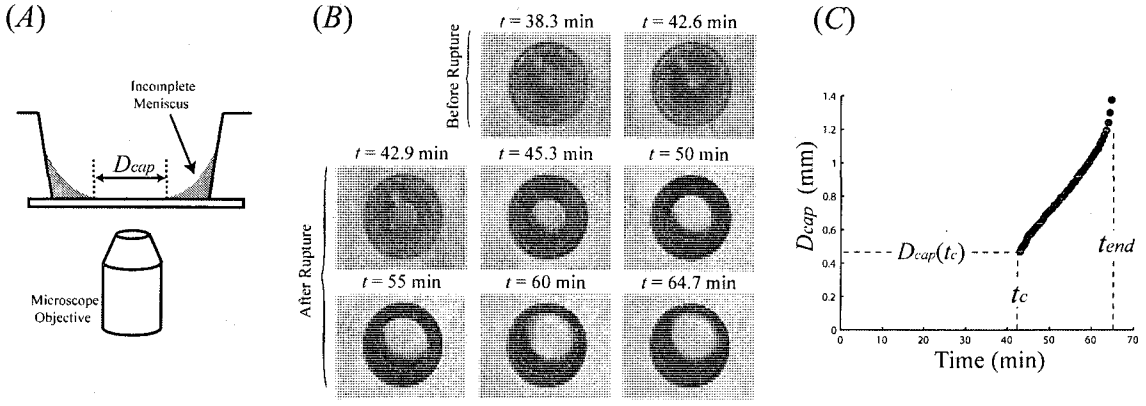

Figure 4.3. (*A*) Illustration of the experimental techniques in this study. (*B*) Experimental images of a ruptured meniscus for a reservoir at T = 28 °C, RH = 31%, with geometry D_1 = 1.38 mm, D_2 = 0.77 mm, and H = 2.2 mm. (*C*) Experimental values of D_{cap} vs. t for the images shown in (*B*).

4.2.5 Particle Tracking

For particle tracking, images were acquired sequentially at 100× magnification with an exposure time of 5 ms and Δt = 30 ms between exposures. Particle tracking studies were performed using the methods developed by Crocker and Grier.[59] Near instantaneous measurements of the average fluid velocity v for unidirectional flow were accomplished by capturing a minimum of 150 sequential images displaying positions of the fluorescent tracer beads. Each image was refined with a bandpass filter to suppress pixel noise, after which the location of individual tracer beads was determined using a minimum intensity threshold. Particle locations were then refined to give estimates of the centroid positions, shown for three images in Fig 4.4*A* for 0.5 μm diameter beads flowing in a microchannel of h = 5μm and w = 50 μm at an average velocity of v = 860 μm s^{-1}. A data set consisting of the x- and y-postitions of each observation at time t is used with the algorithm

developed by Crocker *et al.* to link particles into individual trajectories, as shown in Fig 4.4*B* for the three images shown in Fig 4.4*A*. As an example, Fig. 4.4*C* displays the linked trajectories of 45 particles taken over 100 consecutive images. After the particle trajectories were calculated, particle velocities were estimated using $v_{particle} = \Delta x/\Delta t$. Utilizing experimental measurements of w and h, average fluid velocities were then calculated from an average of the top 50 maximum particle velocity (v_{max}) observations along with a relation of v vs. v_{max} acquired from the Boussinesq series solution for viscous flow in a rectangular duct [60]. Due to the small size of the tracer particles and the low Reynolds numbers present in this system, it may be assumed that $v_{particle} = v_{fluid}$ for particles in channel locations where the fluid is at a maximum velocity.[61]

The algorithms illustrated in Fig. 4.4 do not give accurate results if the flow is sufficiently fast and the particle densities are such that there is less than 10μm between each particle. The CCD camera used in this study was limited to times between consecutive images of $\Delta t = 30$ ms. As a result, accurate measurements were limited to flows of $v < 3.5$ mm s^{-1}. Flow rates exceeding $v > 1$ mm s^{-1} required very dilute particle concentrations such that each image contained less than 5 particles at a given time. For purposes of accuracy, the results of this study were limited to flows such that $v < 2$ mm s^{-1}. The particle tracking algorithms were verified by manual location of individual particle tracks for a stream of images.

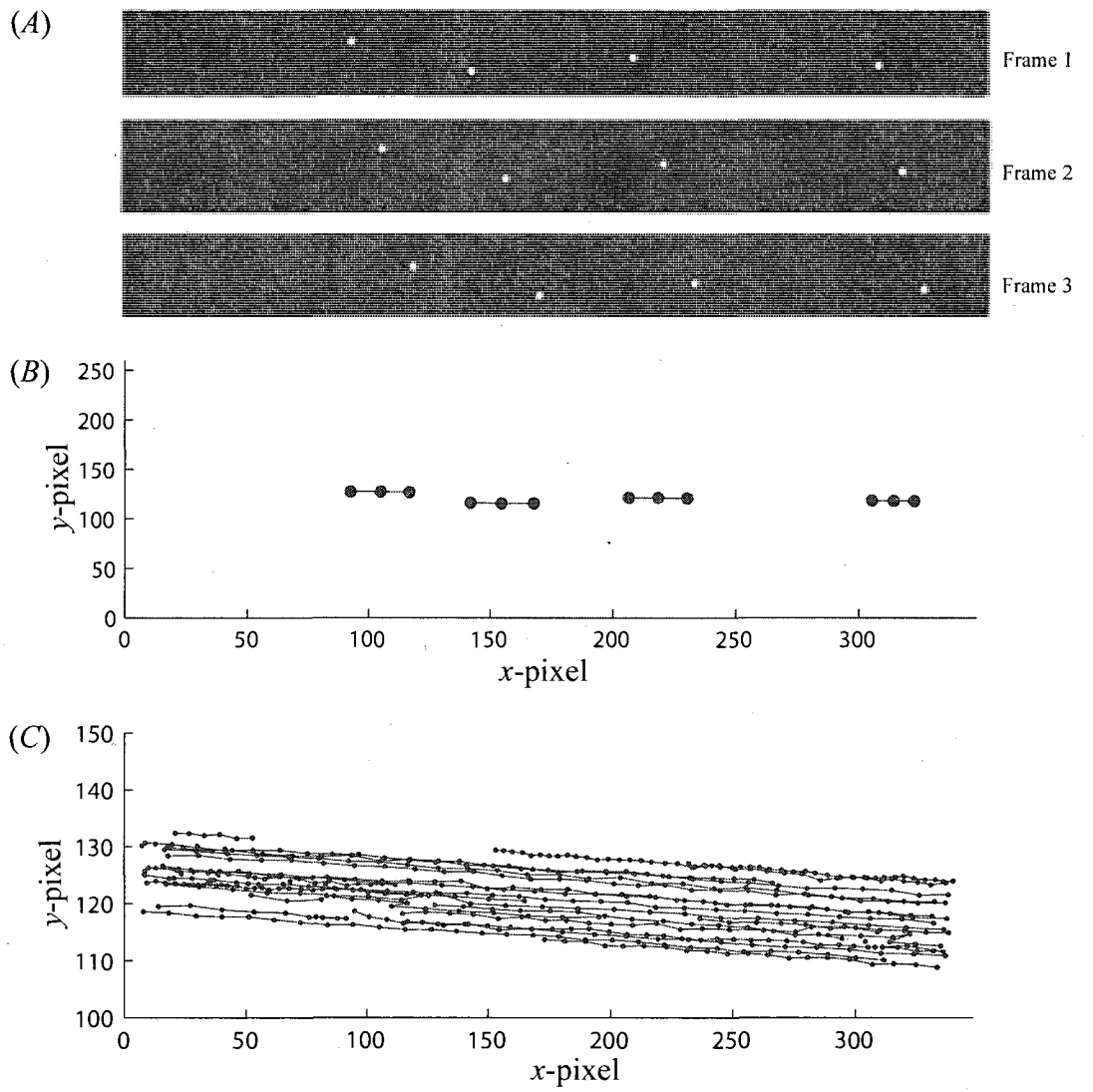

Figure 4.4. (*A*) Three consecutive frames (taken at Δt = 30 ms apart) showing the particle locations of 4 individual beads after particle location refinement. (*B*) y- vs. x-pixel trajectories linked by individual particles for the positions shown in (*A*). (*C*) Trajectories of 45 particles (over 100 images) in a channel of h = 5 μm and w = μm flowing at an average linear velocity of v = 860 μm s^{-1}.

4.3 Model

Upon introduction of an aqueous solution into the inlet reservoir, liquid spontaneously fills a hydrophilic microchannel and the corner regions of an outlet reservoir similar to the case shown in Fig. 4.1, such that fluid moves between the reservoirs with a time-dependent volumetric flow rate Q_f. The laboratory systems used here are composed of poly(dimethylsilixane) (PDMS) microchannels and reservoirs bonded to a glass slide. It is important to develop a mathematical model to accurately predict $Q_f = Q_f(t)$ occurring in laboratory microchannels with height h, width w, and length L connecting reservoirs with height H, lower diameter D_1, and upper diameter D_2. In each reservoir the apparent contact angles between the aqueous solution and the reservoir floor and sidewalls are θ_1 and θ_2, respectively. For a liquid of density ρ and viscosity μ moving with average axial linear velocity $v = Q_f / wh$, typical Reynolds numbers ($Re = hv\rho/\mu$) in these μFNs are often smaller than 0.1 and flow is well within the laminar regime for all cases.

Via application of the Washburn equation, it is estimated that the time required for capillary forces to fill the μFNs relevant to this study is on the order of 1 s [62]. Wetting of the corner regions of the outlet reservoir (forming an incomplete meniscus) has been observed experimentally to be completed within 10 s. The cross-sectional view of an air/liquid interface within a reservoir can be seen in Fig. 4.2*B*. Performing a mass balance on the liquid contents of a single reservoir yields

$$\frac{dV}{dt} = Q_f - Q_e - Q_{perm}\,, \tag{4.1}$$

where $V(t)$ is the liquid volume present in the reservoir, Q_e is the loss due to evaporation from the air/liquid meniscus, Q_{perm} is the volumetric rate of permeation into the reservoir sidewalls, and Q_f is defined to be positive if fluid is moving into the reservoir. Because of the small characteristic length scales of the reservoirs the system may be assumed to be at

pseudo steady state such that flow will respond nearly instantaneously to changes in the liquid volume present in either reservoir. The volumetric flow rate between the reservoirs can be determined from a flow resistance analogy as

$$Q_f = \frac{-\Delta p}{K}, \tag{4.2}$$

where K is the viscous resistance to flow within the microchannel, $\Delta p = p_{l,out} - p_{l,in}$ is the differential fluid pressure between the two reservoirs, and the subscripts *in* and *out* denote the inlet and outlet reservoirs, respectively. Neglecting secondary effects due to the sudden contraction and expansion from the reservoir to the microchannel, the viscous resistance to laminar flow may be calculated as [63]

$$K = \frac{12\mu L}{w^3 h}\left[1 - \frac{192w}{\pi^5 h}\sum_{n=1,3,5..}^{\infty}\frac{1}{n^5}\tanh\left(\frac{n\pi h}{2w}\right)\right]^{-1}. \tag{3}$$

For quiescent liquid conditions the pressure differential Δp_i between the liquid and gas phase across a curved interface can be calculated using the Young-Laplace equation

$$\Delta p_i = p_v - p_l = \gamma\left(\frac{1}{R_1} + \frac{1}{R_2}\right), \tag{4}$$

where R_1 and R_2 are the two principal radii of curvature pertaining to the air/liquid meniscus (Fig. 4.2*B*), γ is the air/liquid interfacial tension, and the subscripts v and l indicate the vapor and liquid phase, respectively. Because the dimensions of a microchannel can be accurately measured using several experimental techniques, Eqn. (3) can be calculated with a high degree of accuracy. Knowledge concerning the interfacial flux of water into the PDMS substrate can be found in the study by Randall *et al.*,[30] therefore Q_{perm} can be deduced if the interfacial area $A_{s,l}$ between the liquid and PDMS sidewalls is known. To solve Eqn. (4.1), it follows that relationships of $Q_e = Q_e(V)$,

$A_{s,l} = A_{s,l}(V)$, $R_1 = R_1(V)$, and $R_2 = R_2(V)$ must be obtained. These relationships are discussed in the next section.

4.3.1 Shape of a Meniscus in a Microreservoir

The geometries of the menisci and reservoirs used in this study are shown in Fig. 4.2. To predict the rate of evaporation from a micro-reservoir containing a given volume of liquid, one needs to know the shape of the air/liquid meniscus. Because the shape of the meniscus is dependent on the surface properties of the reservoir, a relationship is needed between those properties and the geometric parameters of the system. For systems in quasi-thermodynamic equilibrium, the relationship between the properties of the surface and the air/liquid interface can be described by Young's equation,

$$\gamma_{sv} = \gamma\cos(\theta) + \gamma_{sl}, \tag{4.5}$$

where θ is the apparent contact angle between the liquid and surface and γ_{sv} and γ_{sl} represent the surface and interfacial free energies of the solid-vapor and solid-liquid interfaces, respectively. For reasonably dilute aqueous solutions changes in θ will represent the relative hydrophilic/hydrophobic extent of the surface. In this study, θ_1 is defined as the contact angle between water and the reservoir floor and θ_2 as the contact angle between water and the reservoir sidewalls. The shape of the meniscus is then dependent on the geometry of the reservoir and surface conditions of the reservoir sidewalls and floor (D_1, D_2, H, θ_1, θ_2) as well as the given volume of water within the reservoir (V).

Determination of the shape of a free interface in mechanical equilibrium with a solid edge is not a straightforward process. Analytical solutions may only be found for a small number of cases, and numerical methods are usually required.[64] Furthermore, experimental measurements concerning the shape of menisci in micro-reservoirs via confocal[55] or interference-contrast microscopy[54] suffer from poor resolution near the reservoir walls. The problem can be simplified, however, by noting that the reservoirs

will usually have a floor diameter of $D_1 < 1$ mm, such that for water with density ρ the Bond number can be calculated as $B_o = \rho g D_1^2 / 4\gamma_{lv} \leq 0.05$; hence, surface tension forces will dominate gravitational forces. In this case it may be assumed that the two principal radii of curvature, R_1 and R_2, do not vary with respect to position along the interface. In Fig. 4.2*B*, R_1 is defined as the radius of curvature of the meniscus in the r,z-plane, having a center of curvature based at the point (r_o, z_o). R_2 is defined (for incomplete menisci) as the radius of curvature in the r,θ-plane, extending from $r = 0$ to the average radial position of the meniscus. For a given reservoir liquid volume, the shape of the meniscus is then calculated from a curve that intersects the reservoir floor and sidewalls with intersection angles θ_1 and θ_2, respectively, and whose volume when integrated with respect to r, θ, and z is equivalent to the given volume of liquid in the reservoir. Because there is no explicit expression for r_o, z_o, and R_1 given H, D_1, D_2, θ_1, θ_2, and V, an iterative method must be utilized.

Here we present a simple method to calculate the shape of a meniscus for expanding reservoirs ($D_2 > D_1$), where the angle of intersection between the reservoir floor and sidewalls is such that $2\alpha > \pi/2$ as shown in Fig. 4.2*B*. The derivations associated with cylindrical ($D_1 = D_2$, $2\alpha = \pi/2$) or contracting ($D_1 < D_2$, $2\alpha < \pi/2$) reservoirs are very similar and will not be shown here. The reservoir walls can be described by the line $r = F(z) = a_1 z + a_2$. Additional geometric information for this system are the angles

$$\beta_1 = 2\alpha - \frac{\pi}{2}, \tag{4.6}$$

$$\beta_2 = \pi - 2\alpha - \theta_2, \tag{4.7}$$

$$\beta_3 = 2\alpha + \theta_2 - \frac{\pi}{2}, \tag{4.8}$$

as shown in figure 4.5.

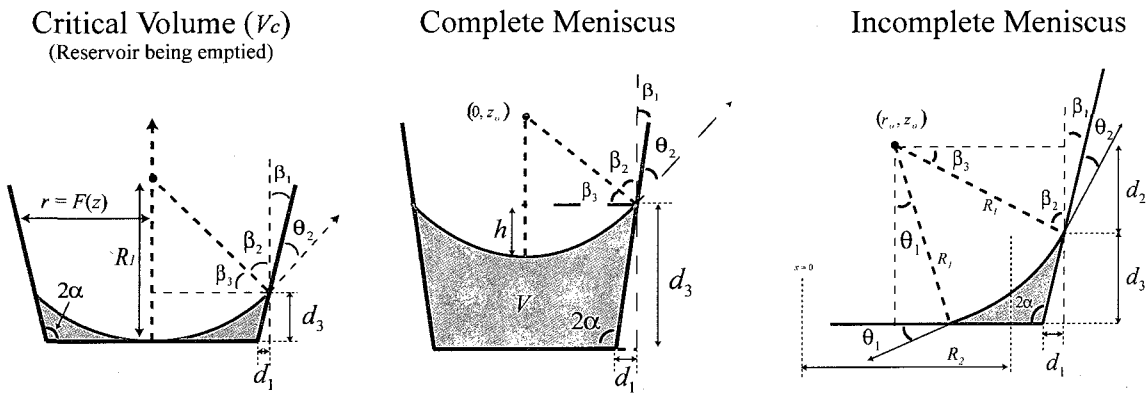

Figure 4.5. Geometries used in the calculation of the meniscus shape.

Critical volume (V_{ca}). The critical volume V_{ca} is the volume at which the meniscus will rupture from a continuous state to form a moving contact line. This event occurs at the liquid volume under conditions that $dV/dt < 0$ where the bottom of the meniscus reaches the reservoir floor ($z_o = R_1$), and depends only on the reservoir geometry and θ_2. The first radius of curvature for this system can be found by equating two relationships for the z-position of the meniscus intersection with the reservoir sidewalls,

$$d_3 = \frac{2R_1\cos(\beta_3) - D_1}{2\tan(\beta_1)}, \tag{4.9}$$

$$d_3 = R_1\left(1 - \sin(\beta_3)\right), \tag{4.10}$$

which leads to

$$R_1 = \frac{D_1}{2\left(\cos(\beta_3) + \tan(\beta_1)\sin(\beta_3) - \tan(\beta_1)\right)}. \tag{4.11}$$

From this value of R_1, the critical volume can be obtained by $V_c = V_2 - V_1$, where

$$V_2 = \pi\int_0^{d_3} F^2 dz = \frac{\pi}{3a_1}\left((a_1 d_3 + a_2)^3 - a_2^3\right), \tag{4.12}$$

$$V_1 = \frac{\pi}{6}h\left(3R_m^2 + h^2\right), \tag{4.13}$$

using the relationships $R_m = R_1 \cos(\beta_3)$ and $h = R_1(1-\sin(\beta_3))$.

Similarly, there exists a critical volume V_{cb} where the meniscus transitions from an incomplete to a complete state under conditions such that $dV/dt > 0$ and the distance between $r = 0$ and the position of the inner contact line approaches zero ($R_1 \sin(\theta_1) \rightarrow 0$). The calculation of V_{cb} is similar to that of V_{ca} and is not discussed here.

Complete Meniscus. This case arises when $V > V_{ca}$ under conditions such that $dV/dt < 0$, or when $V > V_{cb}$ under conditions such that $dV/dt > 0$, where in both situations $d_3 < H$. From the trigonometric relationships

$$d_1 = R_1 \cos(\beta_3) - D_1/2, \tag{14}$$

$$d_3 = \frac{d_1}{\tan(\beta_1)}, \tag{15}$$

we solve the equation $V = V_2 - V_1$ for R_1, where V_2 and V_1 are given above. The explicit solution for R_1 is very complicated and will not be repeated here. The center of curvature for the meniscus will then be (0, z_o), where $z_o = d_3 + R_1\sin(\beta_3)$.

Incomplete Meniscus. This case arises when $0 < V < V_{ca}$ under conditions such that $dV/dt < 0$, or when $0 < V < V_{cb}$ under conditions such that $dV/dt > 0$ (as well as the additional criteria that $d_3 < H$). Using the trigonometric relationships

$$d_2 = R_1 \sin(\beta_3), \tag{16}$$

$$d_3 = R_1 \cos(\theta_1) - d_2, \tag{17}$$

$$d_1 = d_3 \tan(\beta_1), \tag{18}$$

the equation $V = V_2 - V_1$ is solved for R_1, where V_2 is given above, and V_1 may be written as

$$V_1 = \pi \int_0^{d_3} F^2 dz = \pi \int_0^{d_3} \left(r_o + (R_1^2 - (z - z_o)^2)^{\frac{1}{2}} \right)^2 dz. \tag{19}$$

Here, r_o and z_o are the center of curvature of the meniscus, and can be found via

$$r_o = \frac{D_1}{2} + d_1 - R_1 \cos(\beta_3), \tag{20}$$

$$z_o = d_3 + d_2. \tag{21}$$

No analytical solution can be found for R_1 for this geometry, thus the solution must be found iteratively. Starting with an initial guess for R_1, we calculate $V_{calc} = V_2 - V_1$ from Eqns. (4.12) and (4.19). If $V_{calc} > V$, R_1 is slightly decreased and *vice versa*. The iteration is ceased when $V_{calc} = V$.

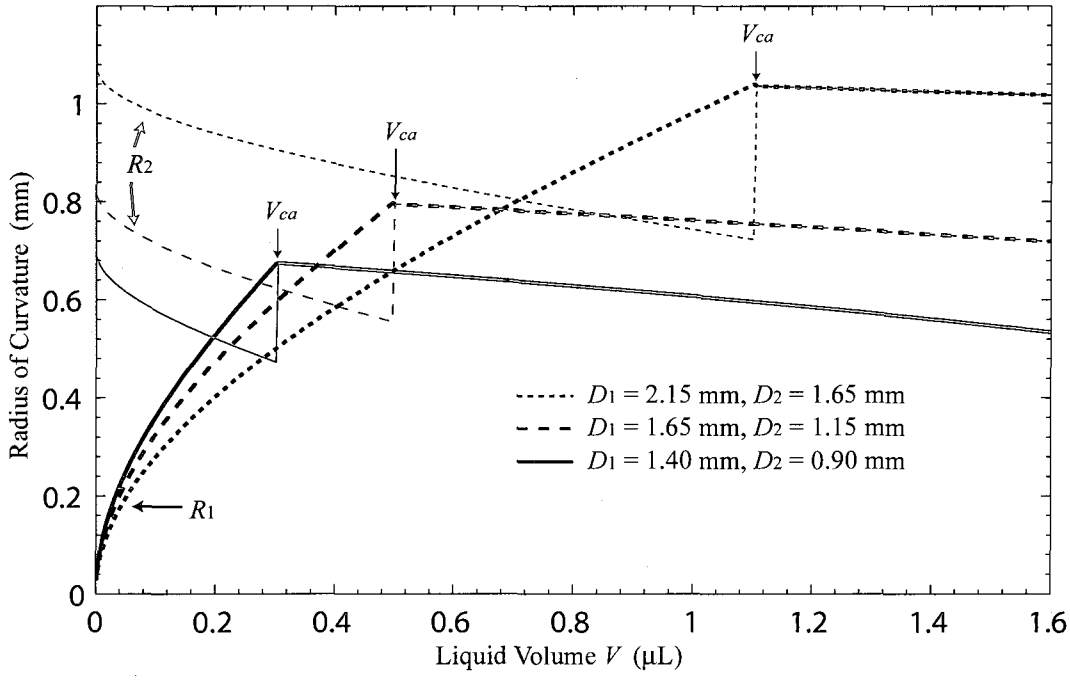

Figure 4.6. (*A*) Predicted values of the two primary radii of curvature, R_1 (black, thick line) and R_2 (red, thin line), plotted as a function of the liquid volume V contained in reservoirs with $H = 2.0$ mm and varying diameters.

Figure 4.6 displays calculated values of R_1 and R_2 for several reservoirs with varying upper and lower diameters, $H = 2.0$ mm, and contact angles $\theta_1 = 4°$ (glass) and $\theta_2 = 18°$ (oxidized PDMS), typical of experimental values in this study. Because the cross-sectional area of these reservoirs decrease as z increases ($D_2 < D_1$), the magnitude of R_1 ($=R_2$) will increase as V decreases for $V > V_{ca}$ for complete menisci, where the opposite is true for expanding reservoirs ($D_1 < D_2$). When evaporation causes the liquid volume in the reservoir to reach $V = V_{ca}$, the meniscus will rupture into an incomplete state. Values of R_1 and R_2 asymptote to zero and $D_1/2$, respectively, as the liquid volume V approaches zero. In this limit of $V \to 0$, $R_1 \propto V^{1/2}$, seen for all reservoirs. The Laplace pressure for menisci in reservoirs with low V will thus scale as $\Delta p_i \propto V^{-1/2}$. Because the liquid pressure p_l in these reservoirs will be below atmospheric pressure—consistent with Eqn. (4.4)—flow in a common μFN connected by multiple reservoirs of the same dimension will always have flow directed toward the reservoir with smallest liquid volume, provided the meniscus in that reservoir is incomplete. The dependence of R_1 and R_2 on V is complicated and cannot be captured with simple analytical expressions. For incomplete menisci at a given value of V, R_1 will decrease with both increasing D_1 and decreasing θ_1 and θ_2.

Considering a situation where a very large reservoir (negligible Laplace pressures) with arbitrarily large capacity feeds an outlet reservoir with a stable outlet meniscus with liquid volume V similar to that shown in Fig. 4.1, one can solve for the instantaneous flow rates through the microchannel as a function of outlet reservoir liquid volume V by substituting Eqns. (4.3) and (4.4) into Eqn. (2). Figure 4.7 plots instantaneous values of Q_f as a function of V in this situation for three microchannels of different width. At the critical volume $V_{cb} = 1.23$ μL, the meniscus transitions from an incomplete to a complete state and values of Q_f drop due to the sudden increase in R_2. For values of $V < 10^{-2}$ μL, the volumetric flow rate increases rapidly, scaling as $Q_f \propto V^{-1/2}$, which is consistent with

the results shown in Fig. 4.6. When the liquid volume is held constant, Q_f increases rapidly with increasing w, consistent with Eqns. (4.2) and (4.4).

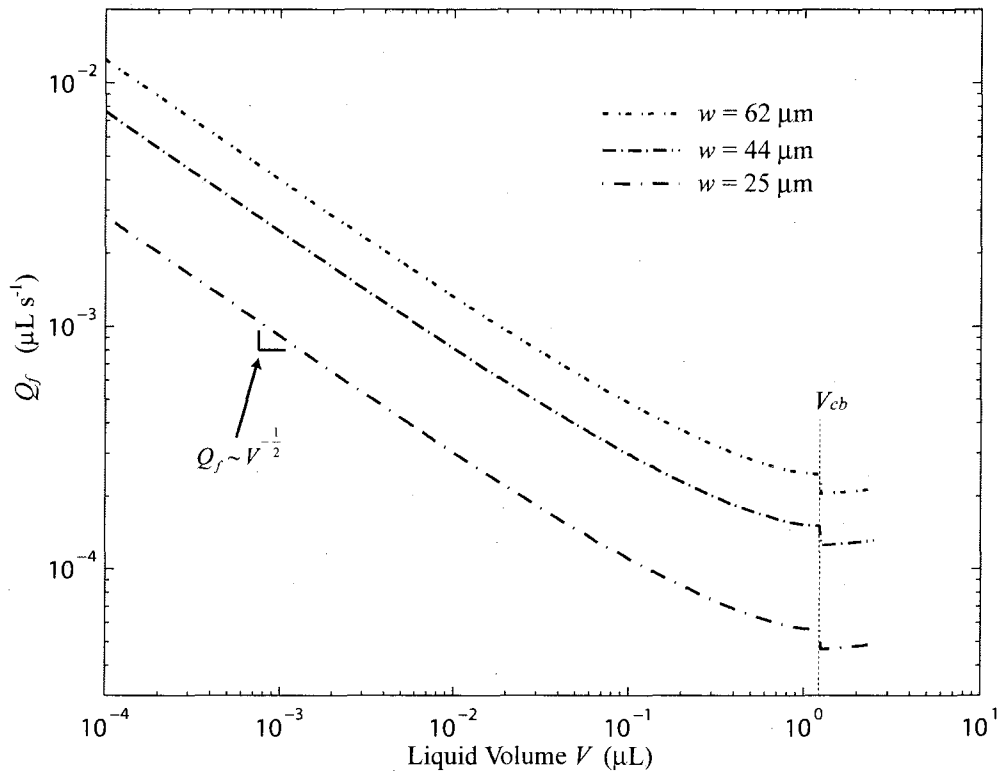

Figure 4.7. Q_f vs. V calculated from Eqn. (2) for microchannels with h = 25 μm and varying width connected to an outlet reservoir with D_1 = 2.15 mm, D_2 = 1.65 mm, and H = 2.0 mm where the capillary forces associated with the inlet reservoir were neglected.

4.3.2 Rate of Evaporation from a Meniscus in a Microreservoir

An accurate relationship between the instantaneous evaporation rate Q_e and the liquid volume $V(t)$ is needed to accurately predict the evolution of a meniscus over time. From Fig. 4.2, it may be seen that for a given reservoir geometry, Q_e will depend on the volume of water in the reservoir and cannot be assumed constant as in previous studies.[54-56] This transient behavior is primarily due to the increase in the average distance needed for

water vapor diffusion as well as changes to the interfacial area as the meniscus recedes towards the reservoir floor. To proceed further with the development of the model it is necessary to make several additional, but physically justifiable assumptions.

The micro-reservoirs used in this study have an average diameter and height on the order of a millimeter. For these geometries it is reasonable to assume the gas (air) and liquid in the reservoir are essentially quiescient, and that water vapor is transported upward solely via diffusion. The mole fraction of water vapor just above the well (x_{a2}) is assumed constant, determined by the relative humidity (RH), pressure (p), and absolute temperature (T) of the system. The gas phase at the air/water meniscus reaches near-instantaneous equilibrium, and the mole fraction of water vapor at the interface (x_{a1}) may be determined using Raoult's law. Because the meniscus recedes very slowly as evaporation proceeds the system is at pseudo steady-state, and it can futher be assumed that, due to the high surface-area to volume ratio, the system will be isothermal.

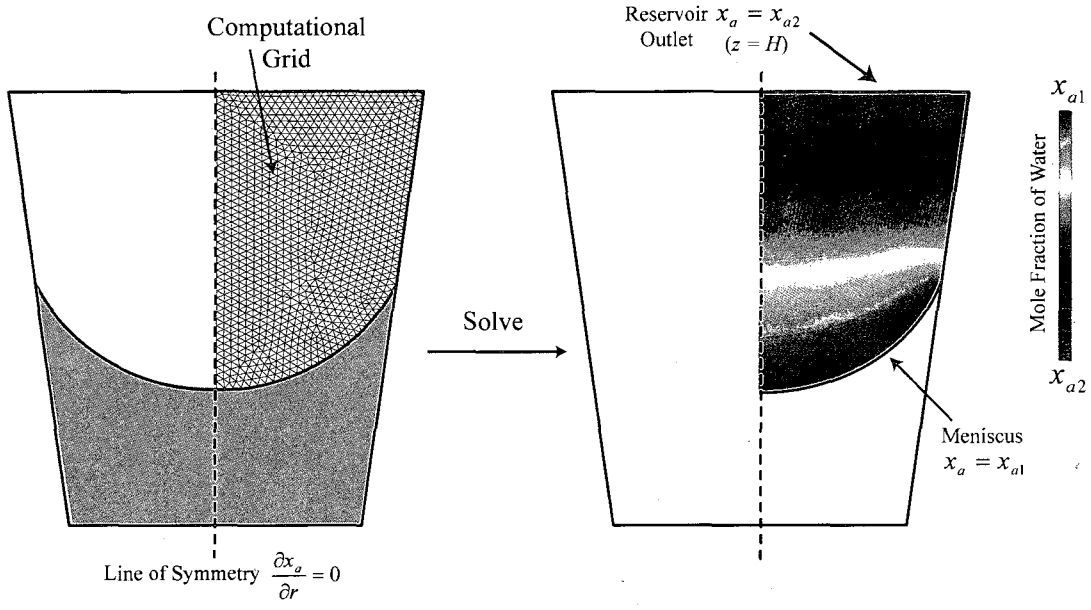

Figure 4.8. Illustration of the axi-symmetric CFD model utilized in this study. The computational grid is for presentation purposes only.

For dilute concentrations of water vapor at constant pressure, the volumetric evaporation rate from the meniscus can then be expressed as

$$Q_e = \frac{-pM_w\mathcal{D}}{\rho RT}\int_A \frac{\partial x_a}{\partial \hat{n}} dA, \tag{22}$$

where A is the cross-sectional area of integration normal to $\hat{n}$, R is the gas constant, M_w is the molecular weight, ρ is the liquid density, and $\mathcal{D}$ is the diffusion coefficient of water vapor in air. Because of the curved geometry of the meniscus, exact solutions for $x_a = x_a(r, z)$ in the gas phase cannot be derived and numerical methods must be applied to determine the evaporation rate from reservoirs with given parameters H, D_1, D_2, θ_1, θ_2, and V. For this study, integration of Eqn. (4.22) is performed along a plane of constant z, where conservation of mass requires that the plane of integration must be situated at a z-position located higher than the top edge of the meniscus.

Figure 4.8 illustrates the domain modeled in this study. Numerical calculations to determine the water vapor mole fraction distribution are performed using a 2-D axisymmetric CFD model. For each reservoir with given surface properties and external conditions a minimum of 25 simulations were performed, each pertaining to a specific reservoir liquid volume, where the shape of the meniscus was predetermined using the geometric model described above. The CFD preprocessing package Gambit® was used to discretize the gas phase within the reservoir into 4-node elements, with typical element dimensions on the order of $D_1/100$. This discretization scheme has been pre-determined in this system to have sufficient resolution to ensure the predicted concentration field is independent of the mesh density. The finite volume CFD package FLUENT® was then used to solve the 2-D concentration distribution for water vapor within the r,z-plane, where the mole fractions of water vapor along the meniscus and at the reservoir outlet were set to x_{a1} and x_{a2}, respectively. The species conservation equation for water vapor was solved using a second-order accurate scheme, and the simulations were considered

converged when the normalized residuals fell below 10^{-7}. After the solution for x_a has converged the evaporation rate is calculated using Eqn. (4.22), where the integration is performed along the reservoir outlet plane at $z = H$.

4.4 Discussion

4.4.1 Effect of Reservoir Geometries and Surface Properties on Evaporation

Experimentally observed evaporation rates of liquids contained in shallow reservoirs ($D_1/H \gg 1$) have been shown to be proportional to the diameter of the reservoir and independent of time.[54-56] These functional relationships do not hold true for taller reservoirs such as those in this study ($D_1/H \approx 1$). Figure 4.9 displays mole fraction distributions and evaporation rates for water vapor within several reservoir geometries and reservoir liquid volumes. The difference in geometry between the expanding and contracting reservoirs would result from a reversed punch direction regarding a PDMS substrate. Several geometrical relationships affecting Q_e can be seen in Fig. 4.9. In general, a decrease in Q_e is seen with decreasing liquid volumes due to the increase in the average distance needed for diffusion as the meniscus recedes towards the reservoir floor. However, the evaporation rate is not only dependent on this diffusion distance, but also on the overall interfacial area as well as the geometry of the reservoir itself. The difference in evaporation rates for different reservoir geometries can be quite dramatic; for example, the evaporation rate for an expanding reservoir (for the conditions shown in Fig. 4.9) with $V = 0.1$ μL ($Q_e = 0.36$ pL s^{-1}) is only slightly lower than the case for a contracting reservoir with $V = 1$ μL ($Q_e = 0.42$ pL s^{-1}), even though there is clearly a difference in the interfacial area and diffusion length between the two cases. For a given volume of liquid, Q_e will be higher for an expanding reservoir than a contracting reservoir for several reasons: (*i*) the position of the meniscus will be higher in an expanding reservoir at a given volume, reducing the distance needed for diffusion and (*ii*) evaporation rates are enhanced in expanding reservoirs due to the increase in the

available area for diffusion area as z increases. The latter effect is made clear by examining one-dimensional diffusion in a well, and is examined in more detail in the appendix for this chapter.

To determine a functional relationship between Q_e and V for a given reservoir with overall volume V_{res}, a minimum of 25 CFD simulations such as those shown in Fig. 4.9 were performed, with each simulation pertaining to a different reservoir liquid volume. The simulations are carried out such that a minimum of 10 simulations are evenly spaced along the range of $V_{ca} < V < V_o$, corresponding to a complete meniscus, and a minimum of 15 simulations are evenly spaced along the range of $-6 < \log(V) < \log(V_{ca})$ for an incomplete meniscus. Interpolation between the resulting data points is accomplished by fitting Q_e vs. V to the following relationships,

$$\text{complete meniscus } (V > V_c) \quad Q_e = a_1 V^2 + a_2 V + a_3, \tag{4.23}$$

$$\text{incomplete meniscus } (V < V_c) \quad Q_e = b_1 \log(V) + b_2 \log\left(\frac{V}{V_{res}}\right)^{b_3}, \tag{4.24}$$

where V_{res} is the overall volume of the reservoir. The two distinct relationships are needed due to the discontinuous nature of the meniscus before and after rupture. The regression analysis within this study yielded R^2 coefficient values greater than 0.95 for systems that exhibit stable menisci (to be discussed later). There is little physical meaning associated with the fitting parameters in Eqns. (4.23) and (4.24) and the parameters describing the system, and as such their values are not reported here.

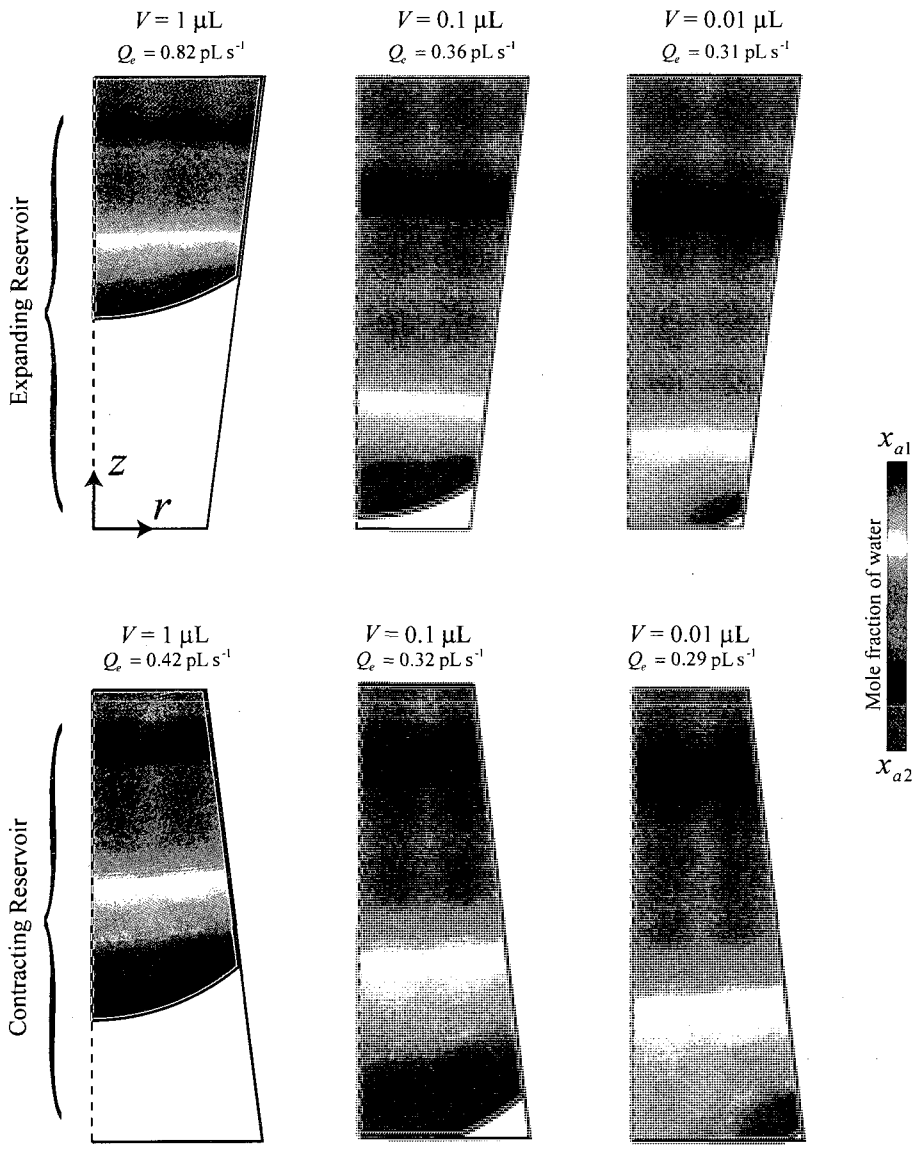

Figure 4.9. CFD simulations displaying the mole fraction of water vapor in several reservoirs with differing volumes. The simulations pertain to a reservoir with $\theta_1 = 25°$, $\theta_2 = 50°$, $H = 2$ mm, $T = 28$ °C, $p = 686$ Torr, and RH = 25%, with an expanding reservoir ($D_1 = 1$ mm, $D_2 = 1.5$ mm) and a contracting reservoir ($D_1 = 1.5$ mm, $D_2 = 1$ mm).

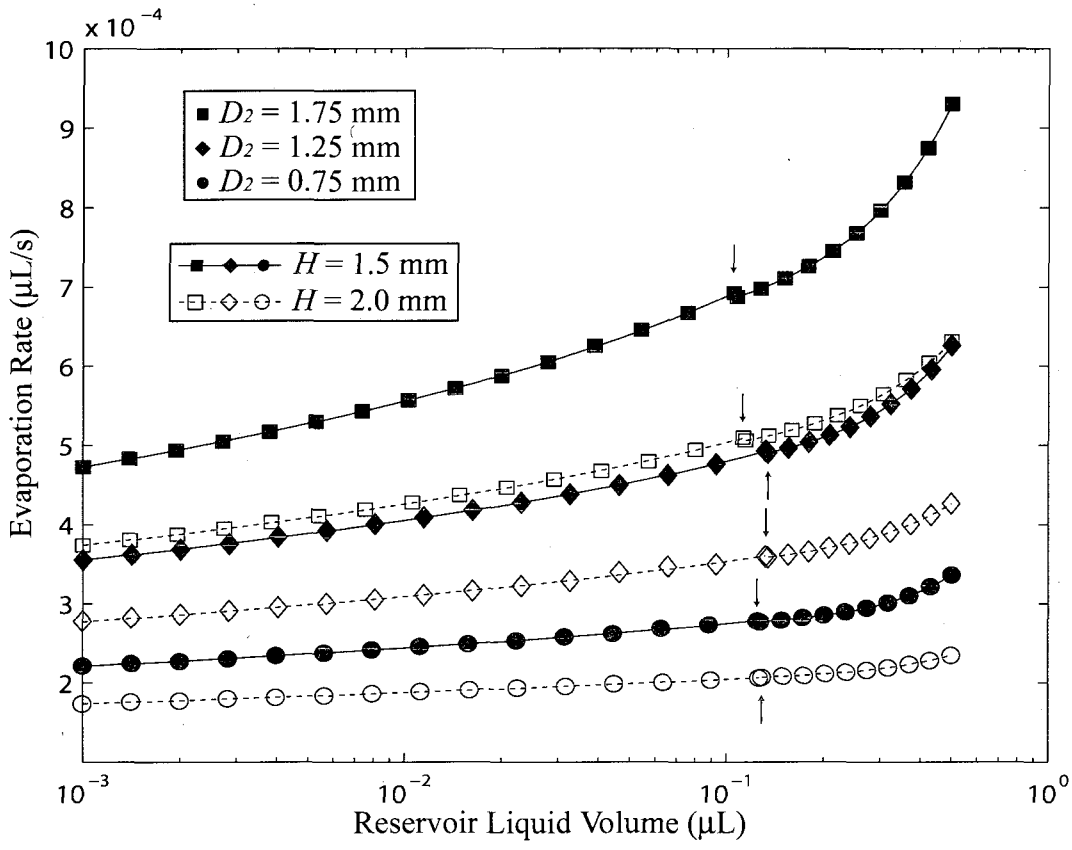

Figure 4.10. Effect of reservoir geometry on evaporation rate for constant contact angles of $\theta_1 = 25°$ and $\theta_2 = 50°$ and $D_1 = 1.25$ mm, for a system with $T = 28$ °C, $p = 686$ Torr, and RH = 25%. The arrows indicate the critical volume at which the meniscus ruptures ($V = V_{ca}$).

Figure 4.10 displays Q_e vs. V for a variety of reservoir diameters and heights for a set value of $D_1 = 1.25$ mm and contact angles of $\theta_1 = 25°$ and $\theta_2 = 50°$, representative of a typical inlet reservoir in this study constructed entirely from PDMS. Although the two curves for complete and incomplete menisci are discontinuous at $V = V_c$, the difference in Q_e between the two states at $V = V_c$ is predicted to be small. For a given reservoir, the decrease in Q_e with decreasing V is clear in all reservoirs; for example, for the case in of $D_2 = 1.75$ mm and $H = 1.5$ mm, there is a decrease in the evaporation rate by 49% from the liquid volume $V = 0.5$ μL ($Q_e = 0.93$ pL s^{-1}) to $V = 10^{-3}$ μL ($Q_e = 0.47$ pL s^{-1}). Furthermore, the effect of the reservoir geometry is very significant, as evaporation rates in expanding reservoirs at a given liquid volume can be much greater than rates in contracting reservoirs: for the liquid volume $V = 0.3$ μL, the $D_2 = 1.75$ mm, $H = 1.5$ mm reservoir ($Q_e = 0.80$ pL s^{-1}) has an evaporation rate 260% greater than the $D_2 = 0.75$ mm reservoir of the same height ($Q_e = 0.30$ pL s^{-1}). The overall dependence on reservoir height is also important, as decreases in a reservoir height of $H = 2.0$ mm to $H = 1.5$ mm leads to increases in Q_e of 38% and 34% for the $D_2 = 1.75$ mm and $D_2 = 0.75$ mm reservoir ($V = 0.1$ μL), respectively.

In addition to the effects of the reservoir geometry, the surface properties of the reservoir also have an effect on the evaporation rate, albeit to a lesser degree. Figure 4.11 displays this effect, as decreases in both θ_1 and θ_2, that is, increased hydrophilicity, will serve to increase the evaporation rate from both expanding and contracting reservoirs. This effect is more pronounced at higher reservoir liquid volumes associated with complete menisci, where Q_e depends only on θ_2, and is mainly due to the increase in the interfacial area with decreasing liquid/reservoir contact angles. Figure 4.11also displays the dependence of θ_2 on V_c, as increases in θ_2 lead to decreases in V_c for all reservoir geometries.

For the reservoirs studied here, changes in temperature, pressure, and humidity on the evaporation rate are independent of the reservoir liquid volume and will not be discussed

in detail. It should be noted that to ensure accuracy regarding the results in Fig. 4.10 and 4.11, the maximum reservoir liquid volume was limited so that the average distance from the meniscus to the top of the reservoir was less than $H/2$, and this will be discussed below.

The results shown in Figs. 4.10 and 4.11 are useful in the prediction of the evolution of a meniscus under conditions such that $dV/dt < 0$. The ranges of V in these figures are typical of those seen in the inlet reservoir of the passive pumping mechanism detailed in this chapter. For experimental menisci associated with the outlet reservoir similar to that shown in Fig. 4.1, we are interested in the overall effect of the size of the reservoir on Q_e for incomplete menisci with liquid volumes in the range of $V < 10^{-1}$ μL. Figure 4.12 illustrates the evaporation rate as a function of V/V_{res} in reservoirs with height H = 1.0 mm for several diameters with the constraint $D_1 = D_2$. It can be seen that the dependence of Q_e on V is very weak as $V \rightarrow 0$ and $D_1 \rightarrow 0$. These results suggest that the overall diameter of the reservoir will have a significant effect on the overall flow rate of systems utilizing this passive pumping mechanism, provided that $V_{out}/V_{res} < 0.1$.

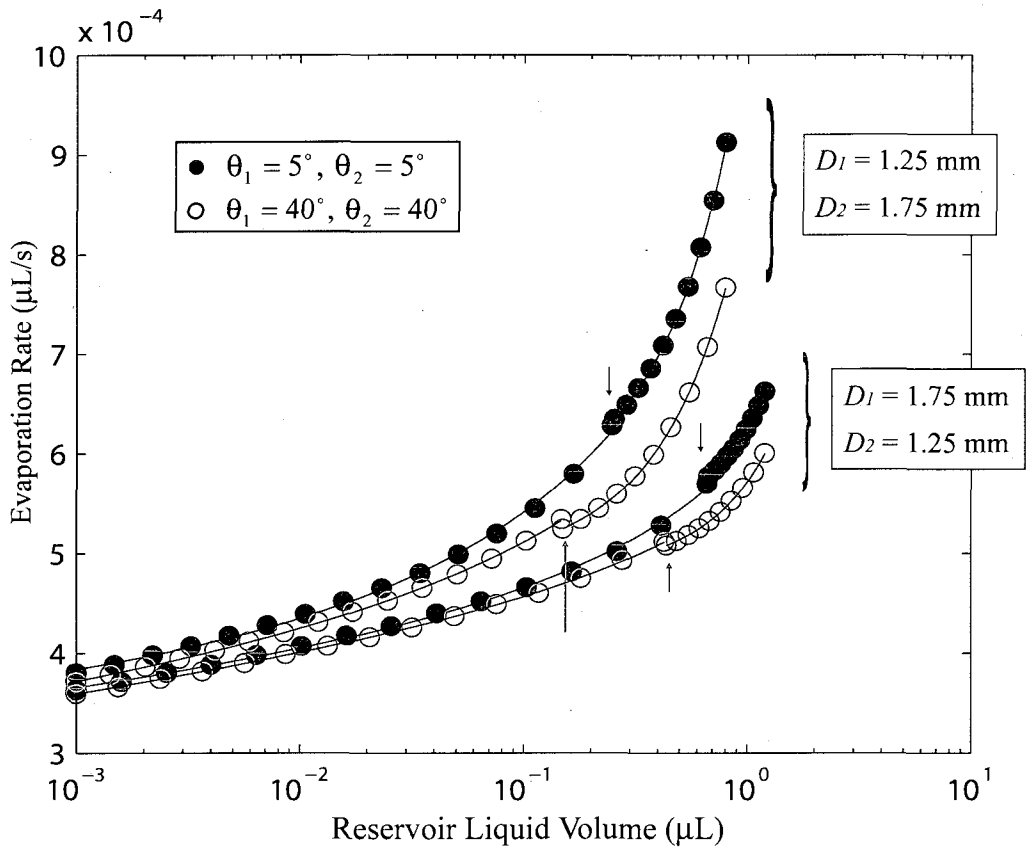

Figure 4.11. Effect of reservoir contact angles on evaporation rates from two reservoir geometries with $H = 2.0$ mm for a a system with $T = 28$ °C, $p = 686$ Torr, and RH = 25%. The arrows indicate the critical volume at which the meniscus ruptures ($V = V_{ca}$).

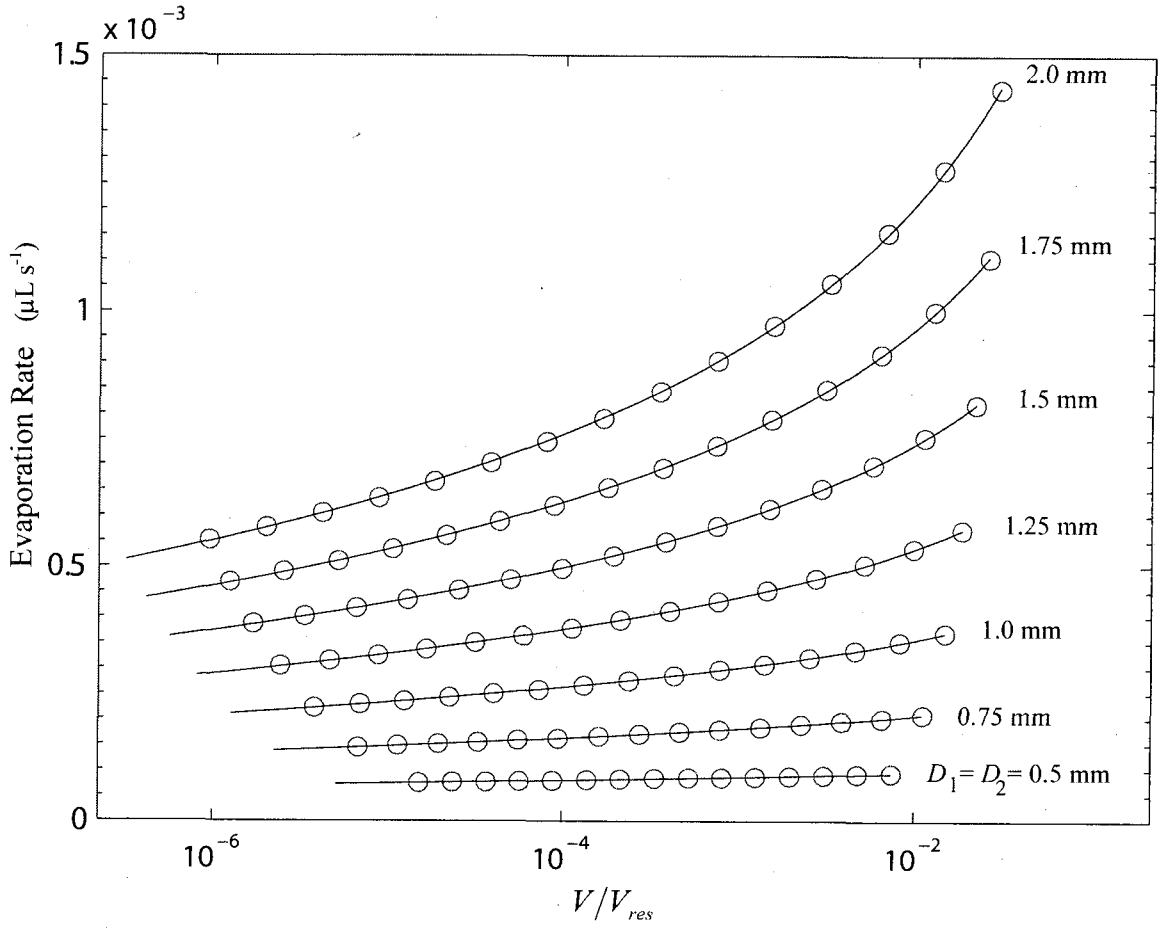

Figure 4.12. Evaporation rate as a function of the normalized liquid reservoir volume (V/V_{res}) for several reservoir diameters with H = 1.0 mm, T = 25 °C, and RH = 20%. The symbols represent individual CFD simulations and the lines represent fits to Eqn. (24).

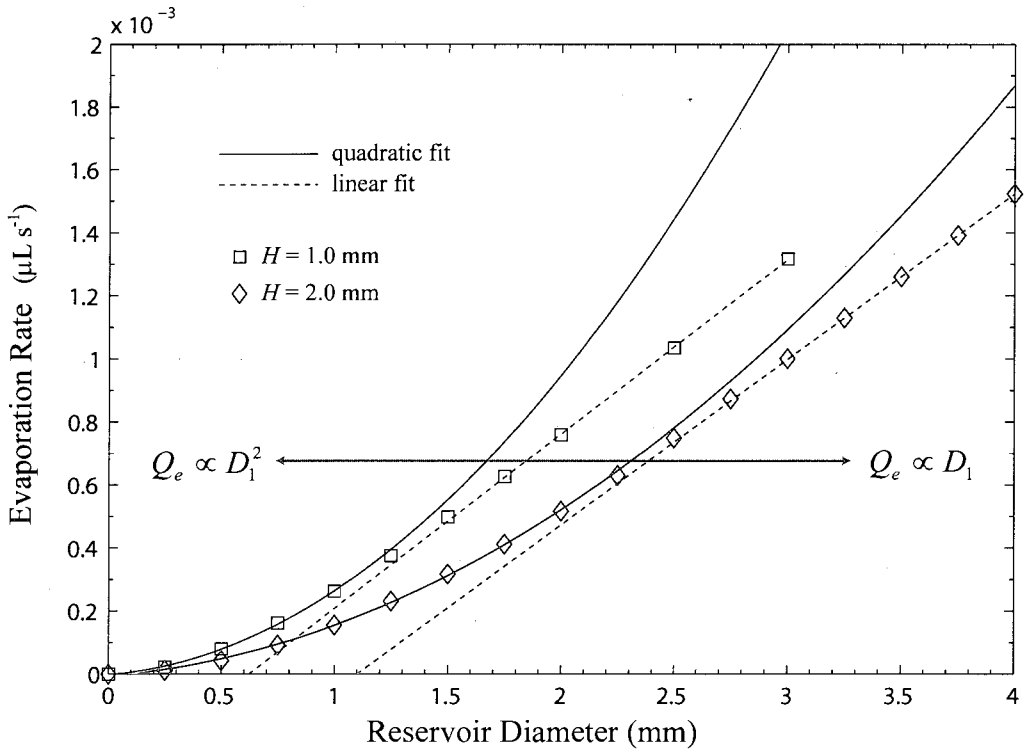

Figure 4.13. Evaporation rate as a function of the reservoir diameter for reservoirs with $H = 1.0$ and 2.0 mm and $V/V_{res} = 10^{-4}$ for the data shown in Fig. 4.12. The solid lines represent linear and quadratic fits to individual CFD simulations.

Figure 4.13 displays the dependence of Q_e on the reservoir diameter (for cylindrical reservoirs) for systems with $H = 1.0$ and 2.0 mm. For all cases, Q_e increases with D_1; however, for smaller values of D_1, $Q_e \propto D_1^2$, while $Q_e \propto D_1$ for larger values of D_1, with the transition between the two scaling rates occurring at $D_1/H = O(1)$. This difference in scaling rates can be explained by examining the case for steady-state diffusion in a cylinder of diameter D_1 and height H with a small amount of water present along the bottom perimeter of the cylinder. In this case the mass fraction of water obeys $\nabla^2 x_a = 0$, with the bottom corner of the reservoir acting as a point source $x_a(D_1/2,0) = x_{a1}$, along with no flux conditions $dx_a/d\hat{n} = 0$ along the boundaries $r = a$ and $z = 0$. For the limiting case $D_1/H \ll 1$, the upper wall acts as a sink such that $x_a(r,H) = x_{a2}$, and the solution will resemble one-dimensional diffusion such that $\partial x_a/\partial r \approx 0$

and $dx_a/dz \approx (x_{a1} - x_{a2})/H$, thus Q_e will scale with the reservoir height as $Q_e \sim H^{-1}$. Furthermore, the differential area dA in Eqn. (4.22) can be calculated along a plane of constant-z, thus $Q_e \sim rdrd\theta \propto D_1^2$. Conversely, for systems where $D_1/H \gg 1$, the system resembles diffusion from a thin ring of diameter D_1 into a semi-infinite medium. In this limiting case the evaporation rate will scale as the circumference of the meniscus, such that $Q_e \propto D_1$, which is consistent with several experimental studies concerning the evaporation rate from shallow wells [53, 54]. This scaling law can also be derived by examining the analogous situation regarding the electrical potential distribution due to a uniformly charged circular ring of diameter D_1 [65]. These two scaling laws are valid for all reservoirs where $V_{out}/V_{res} < 0.1$ and provide a good approximation for reservoirs with non-cylindrical geometries.

4.4.2 Prediction of Meniscus Evolution During Evaporation

Given a specific reservoir geometry (D_1, D_2, H) and specific experimental conditions (T, p, RH, V_o), one only needs to know values of to θ_1 and θ_2 to predict the evolution of an evaporating meniscus over time. Standard experimental methods cannot be used to measure the value of θ_2 due to the confined geometry of the reservoir sidewalls. However, because the critical volume of the reservoir depends only on θ_2, knowledge about the initial rupture diameter can be used to gain insight regarding predicted values of θ_1 and θ_2. Figure 4.14 shows a contour plot of the predicted dependence of θ_1 and θ_2 on $D_{cap}(t_c)$ for a reservoir with D_1 = 1.2 mm, D_2 = 1.6 mm, and H = 1.8 mm. A specific value of θ_2 determines V_c for a given reservoir geometry, which in turn establishes a relationship between θ_1 and $D_{cap}(t_c)$. Using experimental values for $D_{cap}(t_c)$, such as that shown in Fig. 4.3*C*, a functional relationship for θ_1 in terms of θ_2 may then be determined. Thus, one needs only experimental values for $D_{cap}(t_c)$ and an initial guess for θ_2 to predict the parameters V, r_o, z_o, R_1 and R_2 as a function of time.

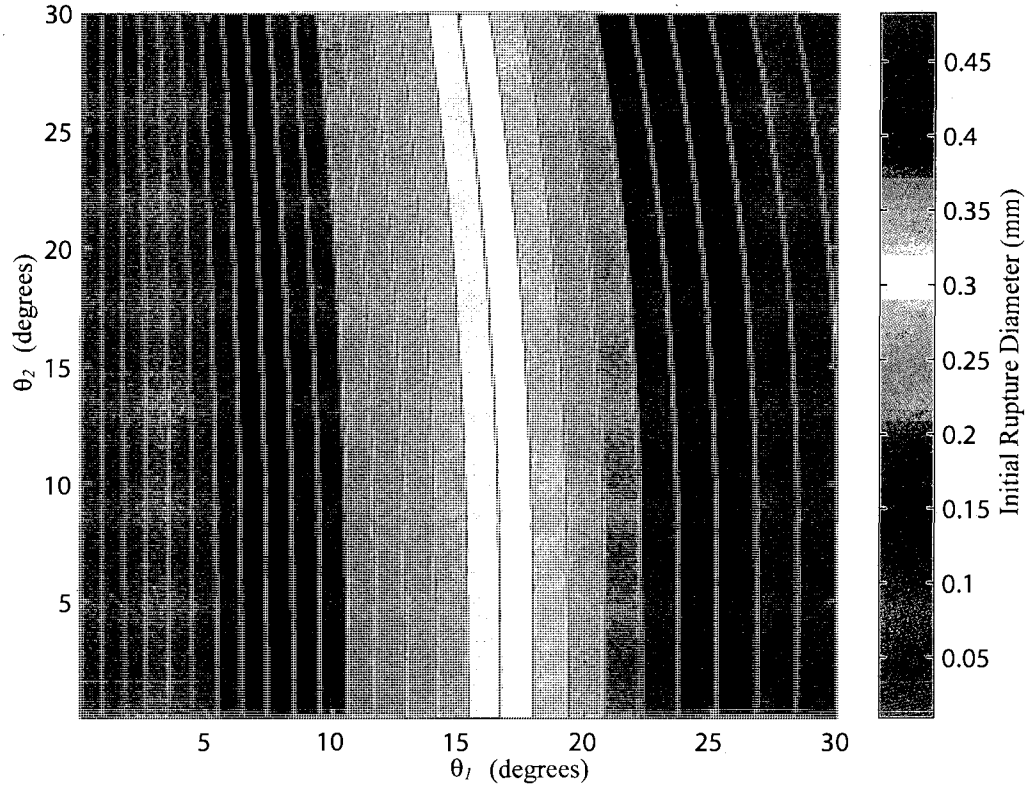

Figure 4.14. Contour plot displaying the predicted initial rupture diameter $D_{cap}(t_c)$ of a meniscus as a function of θ_1 and θ_2 for a reservoir with D_1 = 1.2 mm, D_2 = 1.6 mm, and H = 1.8 mm.

To predict the evolution of a meniscus during evaporation, the time rate of change for the volume within a reservoir is discretized using a first order forward difference

$$V^{n+1} = V^n - Q_e \Delta t \ , \tag{4.25}$$

where V^n represents the volume of the liquid at time $t = n\Delta t$. The simulation is initialized with a liquid volume V_o, and values of Δt are adjusted such that $Q_e \Delta t < 10^{-4}$ μL. An initial guess for θ_2 and the experimental value for $D_{cap}(t_c)$ are used to determine a matching value for θ_1. These values are then used along with the experimental values of D_1, D_2, H, T, p, and RH as inputs to a series of CFD simulations to determine the parameters (a_1, a_2, a_3, b_1, b_2, b_3) associated with Eqns. (4.23) and (4.24). These parameters determine the relationship between Q_e and V, which in turn is used in Eqn. (4.25) to calculate V as a

function of time. The predicted values of D_{cap} as a function of time (for $t > t_c$) can then be calculated using the geometric model (Appendix I in the ESI). Typically, several iterations involving a guess for θ_2 are required for a good fit to the experimental data, where each iteration involves calculation of the parameters associated with Eqns. (4.23) and (4.24).

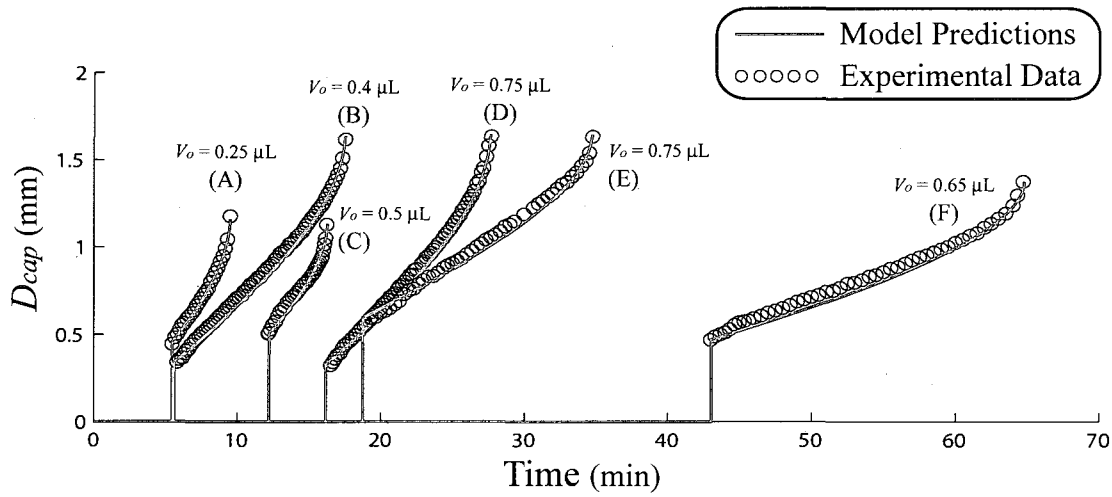

Figure 4.15. Experimental and predicted data showing the inner ruptured meniscus (D_{cap}) as a function of time. The parameters for the predictions are shown in Table 4.1. These values were taken in an aqueous solution with a Tween-20 concentration of 10^{-7} M.

Figure 4.15 compares experimental measurements to predicted values of D_{cap} as a function of time for several reservoir geometries and constructs (PDMS reservoir, glass or PDMS floor). The parameters associated with the results shown in Fig. 4.15 are displayed in Table 4.1. The solutions used to measure D_{cap} vs. t had a tween-20 concentration of 10^{-7} M, typical of solutions placed in the inlet reservoir in this chapter. Aside from small scale differences in D_{cap} persisting for roughly 3 minutes after the meniscus rupture, the model does very well with respect to predicting experimental measurements. The geometric/CFD model predicts the time of meniscus rupture and overall time of the experiment (t_{end}) within 1.5 and 0.5 minutes, respectively, for all cases

(16 total experiments). The effect of reservoir geometry on the overall evaporation rate may be seen from the results in Fig. 4.15. For example, the difference between an expanding and contracting reservoir can clearly be seen between the case (C) and (F), where times for reservoir dry out for a 0.5 μL droplet in an expanding reservoir was 16.2 min compared with 64.7 minutes for dry out of a 0.65 μL droplet in a smaller contracting reservoir. The reservoir in case (F) had 30% more liquid, yet took nearly 300% more time to dry out under roughly the same conditions. The initial slopes of D_{cap} shown in Fig. 4.15 are a complicated relationship between the reservoir geometries, surface conditions, and external conditions. This behavior is unlike the evaporation of water from shallow wells, where time derivatives of D_{cap} are independent of the reservoir geometry and volume.[53] The discrepancy between the two cases is most likely due to the pinning of the meniscus around the upper rim of a shallow reservoir while the lower meniscus edge recedes freely. Neither the upper or lower edge of menisci in the reservoirs in this study has been observed to be static. If either of the two contact lines of the meniscus were to be pinned in a micro-reservoir, the combined CFD/geometric model would likely not show the accuracy displayed in Fig. 4.15, since the geometric model assumes a contact line that can move freely along both the reservoir floor and sidewalls.

	Type	D_1 (mm)	D_2 (mm)	H (mm)	V_o (μL)	T (°C)	RH (%)	θ_1 (deg.)	θ_2 (deg.)	Vc (μL)
(A)	PDMS/glass	1.17	1.65	2.1	0.25	27	23	21.5	48	0.095
(B)	PDMS/glass	1.65	1.15	2.0	0.4	28	31	9.5	54	0.259
(C)	PDMS/PDMS	1.14	1.65	1.7	0.5	26	20	28.5	42	0.102
(D)	PDMS/glass	1.65	1.15	1.9	0.75	28	26	9.8	50	0.280
(E)	PDMS/PDMS	1.65	1.13	2.0	0.75	25	38	23.8	50	0.306
(F)	PDMS/PDMS	1.38	0.77	2.2	0.65	28	31	28.5	43	0.192

Table 4.1. Experimental and Predicted parameters for the results shown in figure 4.15.

A total of 16 experiments were fit to predictions such as those shown in Fig. 4.15 corresponding to a range of parameters from $0.77 \leq D_1, D_2 \leq 2.2$ mm, $1.0 \leq H \leq 3.5$ mm, $9.8 \leq \theta_1 \leq 30°$, and $41 \leq \theta_2 \leq 58°$. The predicted contact angle of water and a glass floor was $\theta_{1,glass} = 14 \pm 5.6°$, whereas the predicted value pertaining to a PDMS floor was $\theta_{1,PDMS} = 26 \pm 3.4°$ (based on 8 experiments each). These values compare very well to experimental contact angle measurements of clean glass and PDMS oxidized with the conditions in this experiment (25W, 900 mTorr air, 20 s).[66] The predicted contact angle of water and the PDMS reservoir was $\theta_{2,PDMS} = 49 \pm 4.7°$, where there was no significant difference between $\theta_{2,PDMS}$ values pertaining to PDMS/PDMS and PDMS/glass reservoirs. The difference between $\theta_{1,PDMS}$ and $\theta_{2,PDMS}$ may be attributed to several factors, including the increase in surface roughness of the reservoir sidewalls as a result of the punching process[67] and the lower efficiency of plasma penetration to the smaller diameter cavity. The small variance in the fitted parameters $\theta_{1,PDMS}$, $\theta_{1,glass}$, and $\theta_{2,PDMS}$ with respect to the large range of experimental parameters in this study highlight the effectiveness of the combined geometric/CFD model.

Regardless of the discrepancy between $\theta_{1,PDMS}$ and $\theta_{2,PDMS}$, these averaged parameters may be used to predict the evolution of a meniscus with high accuracy. Table 2 displays the errors associated with t_c and t_{end} for the evolution of a meniscus in the reservoirs shown in Fig. 4.15 using the averaged parameters $\theta_{1,PDMS}$, $\theta_{1,glass}$, and $\theta_{2,PDMS}$ given above. As expected, the values of Δt_c and Δt_{end} are strongly dependent on $\Delta\theta_2$, the difference between the averaged value $\theta_{2,PDMS}$ and the value θ_2 shown in table 1. Because of the small dependence of Q_e on θ_1 and θ_2, as shown in Fig. 4.11, the error in Δt_{end} is much smaller than Δt_c, accurately predicting reservoir dry out within a minute for all cases.

	experimental		prediction				error	
	t_c (min.)	t_{end} (min.)	t_c (min.)	t_{end} (min.)	$\Delta\theta_1$ (deg.)	$\Delta\theta_2$ (deg.)	Δt_c (min.)	Δt_{end} (min.)
(A)	5.5	9.5	5.52	9.47	-7.2	-0.4	0.02	0.03
(B)	5.8	17.5	4.23	18.2	3.5	-4.4	-1.57	0.7
(C)	12.2	16.2	12.95	16.4	3.8	6.6	0.75	0.02
(D)	16.5	27.6	16.0	27.4	3.7	-2.4	-0.5	-0.02
(E)	19.3	34.7	19.5	35.3	-0.1	1.6	0.02	0.6
(F)	43	64.7	44.2	65.1	1.0	4.6	1.2	0.4

Table 2. Errors of prediction for the cases shown in figure 7 by utilizing the averaged parameters $\theta_{1,glass} = 14°$, $\theta_{1,PDMS} = 26°$, and $\theta_{2,PDMS} = 49°$.

4.4.3 Prediction of Time-Dependent Flow

Numerical Methods. To validate the proposed flow model, the time-dependent average velocity v of 0.5 μm diameter fluorescent tracer beads was measured in PDMS/glass microchannels for an initial liquid volume V_o in the inlet reservoir. Predictions of $v(t)$ were obtained from the solution to Eqn. (4.1) using measured values of D_1, D_2, H, h, w, L, T, RH, θ_1, and θ_2 (i.e., no adjustable parameters). To predict the time-dependent flow occurring in these systems Eqn. (4.1) can be discretized using a first-order difference method as

$$V^{n+1} = V^n + \left(Q_e^n + Q_f^n + Q_{perm}^n\right)\Delta t, \tag{4.26}$$

where V^n is the liquid volume in a given reservoir at time $t = n\Delta t$. Given the shape of a meniscus in a reservoir, the evaporation rate $Q_e = Q_e(V)$ can be calculated using Eqn. (4.23) or (4.24) and Q_{perm} can be calculated using the liquid/PDMS interfacial area determined by the geometric model and a permeation flux of $J = 7\times10^{-6}$ kg m^{-2} s^{-1} taken from the experimental measurements of Randall *et al.* [30] Using Eqns. (4.2), (4.3), and (4.4), $Q_f = Q_f(V)$ can be calculated using the relationship

$$\Delta p = \Delta p_{i,in} - \Delta p_{i,out} = \gamma_{in}\left(\frac{1}{R_{1,in}} + \frac{1}{R_{2,in}}\right) - \gamma_{out}\left(\frac{1}{R_{1,out}} + \frac{1}{R_{2,out}}\right). \quad \textbf{(4.27)}$$

Predictions of $v(t)$ were obtained by solving Equation (4.26) for both reservoirs with a time step of $\Delta t = 0.1$ s, where at each time step values of Q_f^n, Q_e^n, and Q_{perm}^n were calculated from V_{in}^n and V_{out}^n. Because the tracer bead solutions used here are stabilized with a surfactant (tween-20) at a concentration of $C_s = 1.5\times10^{-7}$ M, decreases in both γ, θ_1, and θ_2 are expected over time as the surfactant concentration increases in both reservoirs due to evaporative effects. The surfactant concentration in the reservoirs can be calculated utilizing Eqn. (4.26) along with

$$C_{s,out}^{n+1} = \left(M_{s,out}^{n} + Q_f^n C_{s,in}^n \Delta t\right)/V_{out}^n, \quad \textbf{(4.28)}$$

where M_s is the molar mass of surfactant in each reservoir. From the results of Niño *et al.* [68], changes in the interfacial tension with surfactant concentration can be accounted for via $\gamma = \alpha_1 \log(C_s) + \alpha_2$ for the range 4×10^{-7} M $< C_s < C_{s,crit}$, where $\alpha_1 = -21.6$ g s^{-2} and $\alpha_2 = -65.8$ g s^{-2}; $\gamma = 73$ g s^{-2} for the range $C_s < 4\times10^{-7}$ M; and $\gamma = 33$ g s^{-2} for the range $C_s > C_{s,crit}$, where the critical micelle concentration (CMC) for tween-20 in water is $C_{s,crit} = 2.5\times10^{-5}$ M.

For aqueous solutions with surfactant concentrations well above the CMC of $C_s = 8\times10^{-5}$ M, the contact angles for the outlet reservoir were measured using the techniques shown in Fig. 4.15. Figure 4.16 displays experimental and predicted values of D_{cap} vs. t for two reservoirs with $D_1 = 2.15$ mm, $D_2 = 1.65$ mm, and $H = 1.8$ mm using solutions a fluorescent beads with a tween-20 concentration of 8×10^{-5} M. It can be seen that the initial rupture diameter for the two reservoirs is much smaller than the reservoirs shown in Fig. 4.15. This is due to the increase in surfactant concentration, where decreases in both θ_1 and θ_2 will lead to a decrease in $D_{cap}(t_c)$ as expected from the results shown in Fig. 4.14. Using the results shown in Fig. 4.16, the contact angles for the outlet reservoir were measured to be $\theta_{1,out} = 4.2 \pm 1.0°$ and $\theta_{2,out} = 18.2 \pm 2.5°$ (8 total experiments). °. In

contrast, for dilute aqueous solutions with $C_s = 1.5\times10^{-7}$ M, contact angles were $\theta_{1,in} = 13 \pm 5.4°$ and $\theta_{2,in} = 49.6 \pm 4.7°$ from the results in Fig. 4.15. These values are used as inputs to the geometric model discussed above to establish predictions for R_1 and R_2 as a function of V_{out}. Because the capillary forces associated with the inlet reservoir are small ($R_{1,in}$,$R_{2,in}$ » $R_{1,out}$) and $C_{s,in}$ does not increase appreciably until close to reservoir dry out, it is reasonable to neglect variations in $\theta_{1,in}$ and $\theta_{2,in}$ with time.

Regarding variation of Q_e with temperature, values of T and RH are measured at the onset and completion of an experiment. For predictive reasons it is assumed that any changes are linear with time and values of Q_e are calculated accordingly. With respect to the environment surrounding the reservoir, according to Eqn. (4.22) the evaporation rate scales as $Q_e \propto x_{a1}\mathcal{D}T^{-1}$, independent of the reservoir volume.

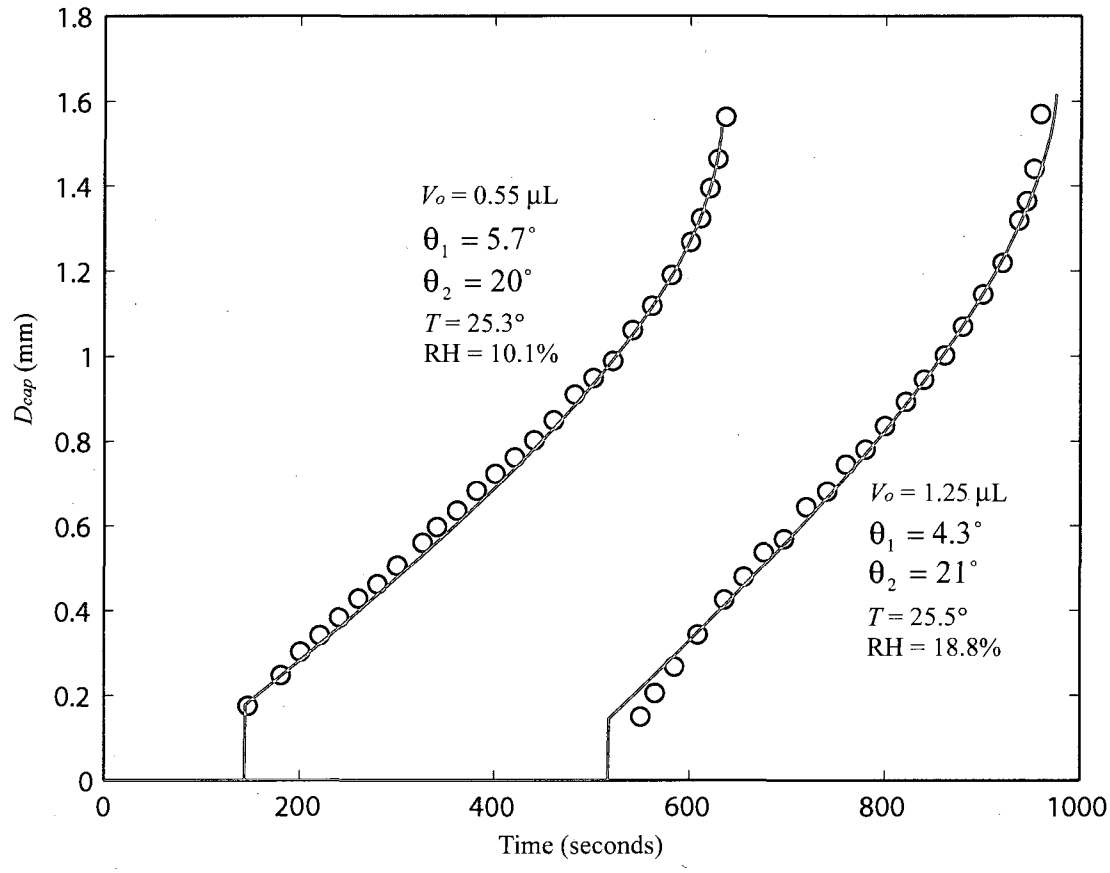

Figure 4.16. Experimental and predicted data showing the inner ruptured meniscus (D_{cap}) as a function of time for reservoirs with D_1 = 2.15 mm, D_2 = 1.65 mm, and H = 1.8 mm. These values were taken in an aqueous solution with a Tween-20 concentration of 8×10^{-5} M.

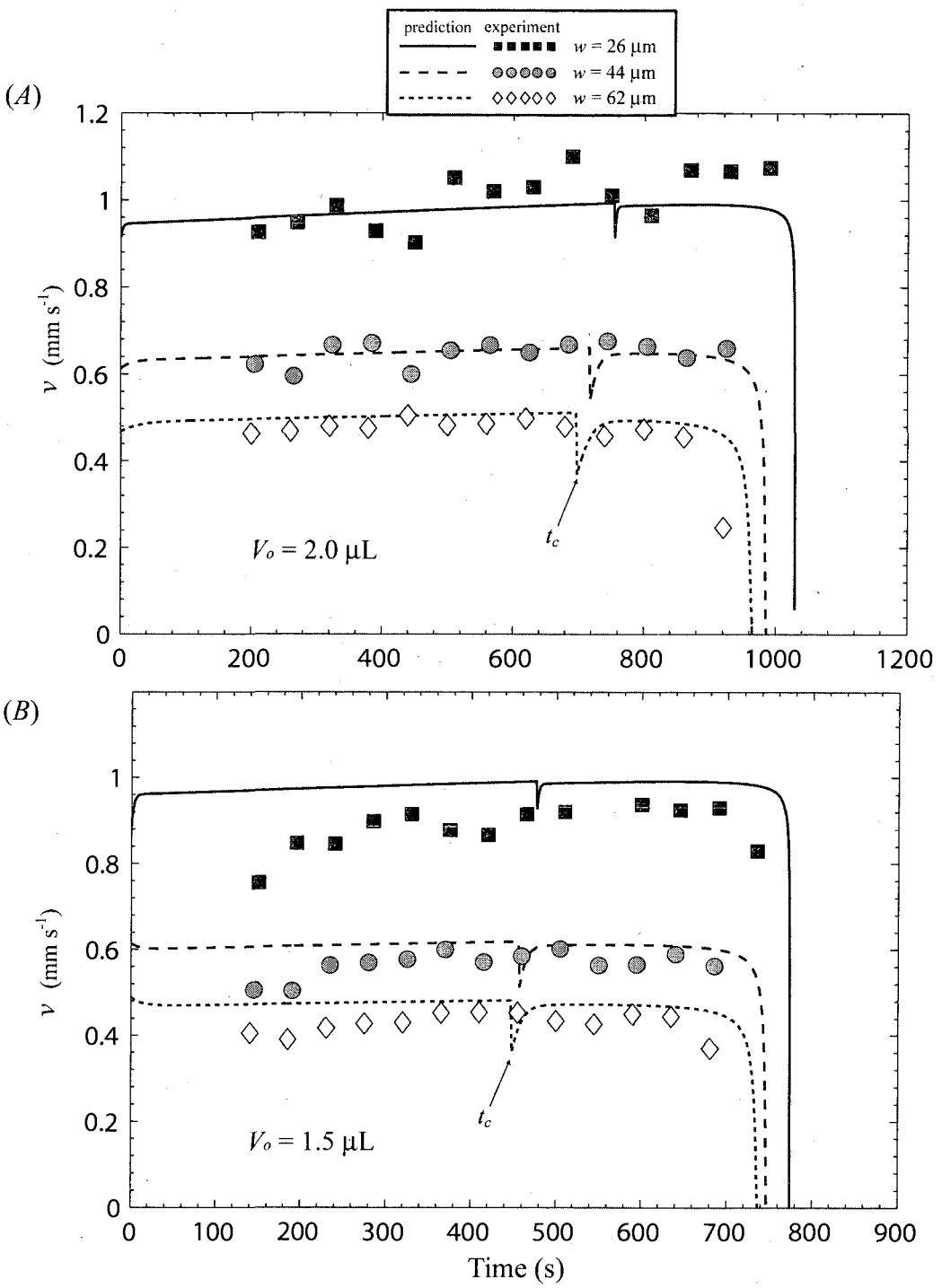

Figure 4.17. Experimental and theoretical predictions of the average fluid velocity v as a function of time in microchannels with $h = 28$ μm, $L = 20$ mm, and varying width with reservoirs with dimensions $D_1 = 2.15$ mm, $D_2 = 2.65$, $H = 2.5$ mm and contact angles $\theta_{1,in} = 13°$, $\theta_{2,in} = 49°$, $\theta_{1,out} = 4.2°$, and $\theta_{2,out} = 18.2°$. (*A*) Initial inlet reservoir volume $V_o = 2.0$ μL. Experimental conditions were $T_{begin} = 24.2$ °C $\rightarrow T_{end} = 25.7$ °C. $RH_{begin} = 0.167 \rightarrow RH_{end} = 0.177$. (*B*) $V_o = 1.5$ μL with experimental conditions $T_{begin} = 25.0$ °C $\rightarrow T_{end} = 25.8$ °C. $RH_{begin} = 0.173 \rightarrow RH_{end} = 0.162$. For all figures, $Q_f \rightarrow 0$ within 45 s of the last data point.

Results. Figure 4.17 displays both laboratory measurements and model predictions of the average fluid velocity as a function of time in microchannels (h = 28 μm, L = 20 mm) with different widths connecting expanding inlet/outlet reservoirs (D_1 = 2.15 mm, D_2 = 2.65 mm, H = 2.5 mm). Figures 4.17*A* and 4.17*B* correspond to initial volumes V_o = 2.0 μL and 1.5 μL, respectively, placed in the inlet reservoir at $t = 0$. Although channels with larger w have lower steady fluid velocities, they possess larger values of both Q_f and $Q_{e,out}$; therefore both the time at which the inlet meniscus ruptures to an incomplete state (t_c) and the time at which the both reservoirs are empty (t_{end}) decrease with increasing w in Fig. 4.17. Measured and predicted values of t_{end} were within 45 s of one another for all cases shown in Fig. 4.17.

The results shown in Fig. 4.17*A* indicate that steady flows persist for roughly 18 minutes before $Q_f \rightarrow 0$, during which time over 50% of the liquid in the inlet reservoir was lost to evaporation. The duration of flow can be extended significantly by the use of several straightforward modifications, including (*i*) eliminating $Q_{e,in}$ by use of a immiscible liquid cap or a saturated cotton swab placed on top of the inlet meniscus, or (*ii*) by reducing $Q_{e,in}$ by decreasing D_1 and D_2, such that $D_1 > D_2$, and increasing H to appropriate values as shown in section 4.4.1. Using these techniques, steady flows have been observed to persist for times lasting longer than an hour with little to no variation in the magnitude of v from the initial values in systems with constant T and RH.

For each experiment shown in Fig. 4.17, substantial flow rates are generated as long as there is a sufficient volume of water in the inlet reservoir ($V_{in} \gg V_{out}$), and flow quickly approaches zero at $t = t_{end}$ as $V_{in} \rightarrow 0$ due to the equalization of the capillary forces in each reservoir ($R_{1,in} \rightarrow R_{1,out}$). A brief decrease in Q_f follows the meniscus rupture from a complete to an incomplete state at a time $t = t_c$, after which Q_f quickly returns to a value close to that seen before rupture. Predicted values of $V_{out} = V_{out}(t)$ reach steady state

within 30 s as long as the initialization value $V_{out}(t=0)$ is smaller than the steady value, but the magnitude of the outlet initialization volume had no effect on the ultimate steady value of Q_f. The steady values of V_{out} ($t > 0$) yield volumetric flow rates that change very little with time as shown by both the predicted and measured values in Fig. 4.17. The small changes observed in Q_f over time may be attributed to (*i*) increases in $\Delta p_{i,in}$ from evaporation and convection losses acting to decrease Q_f as time increases (since $D_1 > D_2$); and (*ii*) increases in T (with small changes in RH) acting to increase Q_f as time increases. Therefore, a system with large inlet reservoirs ($\Delta p_{i,in} = 0$) at constant T and RH will exist at a steady state such that $dV_{out}/dt \approx 0$.

4.4.4 Prediction of Steady-State Flow Rates

When utilizing this passive flow approach for LOC based applications, it is important to understand the dependence of Q_f on the microchannel and reservoir geometries, as well as on the local values of T and RH. To investigate the range of steady-state volumetric flow rates achievable in simple two-reservoir geometries, particle tracking analysis was performed on systems with varying h, w, $D_{1,out}$, $D_{2,out}$, and H_{out} with a large inlet reservoir to ensure that small changes in V_{in} had little effect on Q_f. Values of v were measured for a μFN with 9 channels of varying width and constant height, where measurements were taken within 2 minute after introduction of liquid to the inlet reservoir, with all measurements taken within 5 minutes such that values of T and RH could be assumed constant. Figure 4.18 displays experimental and predicted values of v vs. w for two microchannels with h = 28 μm and L = 20 mm connected to different outlet reservoir geometries. Steady state values of v were predicted using Eqn. (4.1) with $dV/dt = 0$, given laboratory measurements of D_1, D_2, H, T, RH, θ_1, θ_2, and the assumption that $\Delta p_{i,in}$ = 0. The experimental data points represent averaged values of v taken from 3 separate μFNs fabricated from the same mold, where there were 8 measurements per sample. All nine microchannels in the μFN were lined up parallel to each other with 40 μm spacing

between each channel. A single stream of 150 sequential images (100x magnification) was capable of measuring v for a minimum of 4 channels.

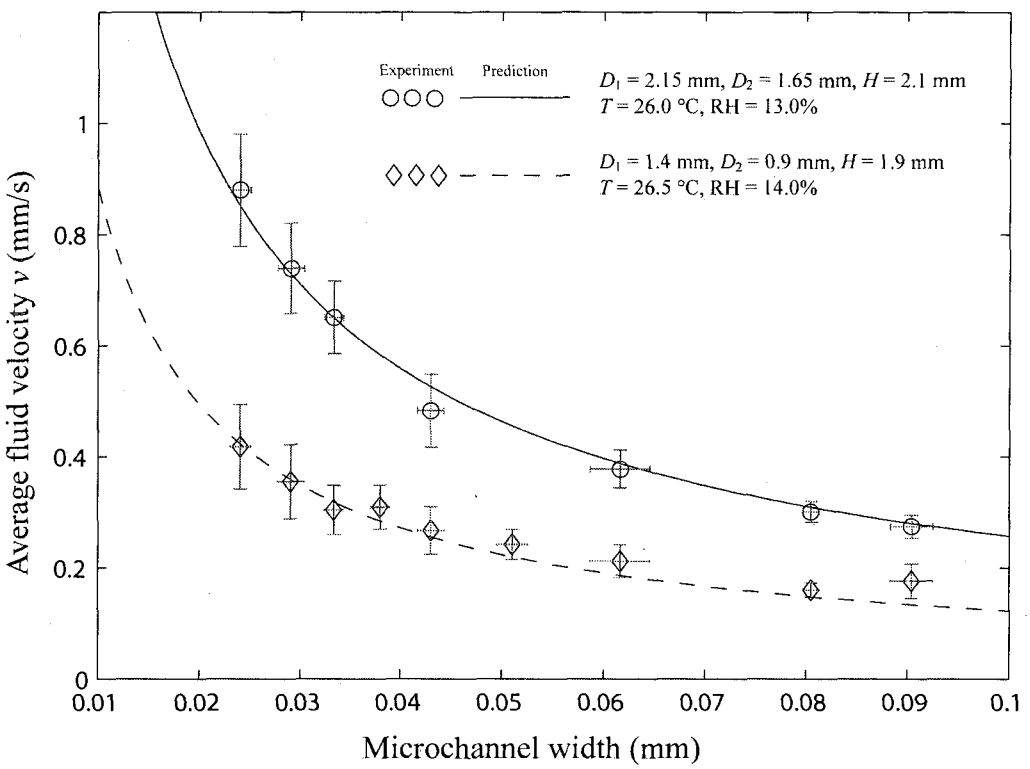

Figure 4.18. Average fluid velocity v vs. microchannel width w for two microchannels with h = 28 μm and L = 20 mm connected to different outlet reservoirs.

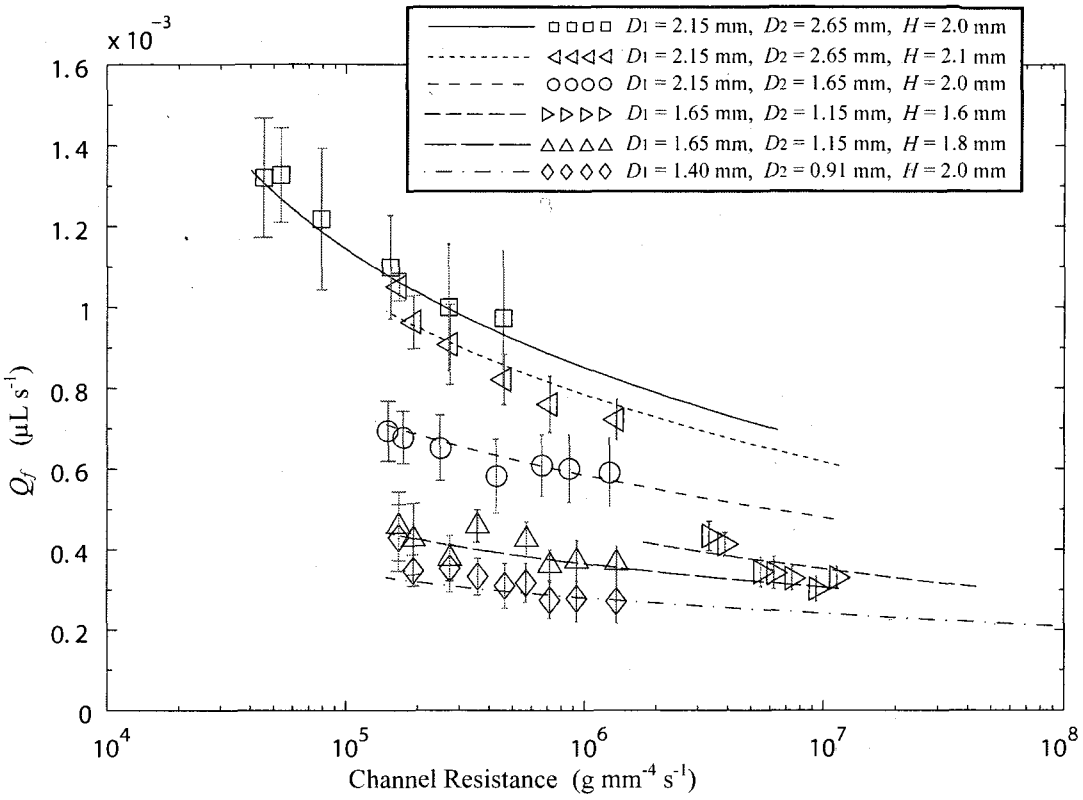

Figure 4.19. Experimental and theoretical predictions for the Volumetric flow rate Q_f vs. the viscous channel resistance K for systems with varying microchannel and outlet reservoir dimensions. Experimental conditions for both figures are (□) T = 26 °C, RH = 0.215, (◁) T = 25.8 °C, RH = 0.16, (○) T = 26 °C, RH = 0.13, (▷) T = 25 °C, RH = 0.11, (△) T = 25.8 °C, RH = 0.16, (◊) T = 26.5 °C, RH = 0.14.

Figure 4.19 displays measured and predicted steady state values of Q_f as a function of the viscous resistance K for microchannels with varying outlet reservoir dimensions. These results highlight the accuracy of the combined geometric/CFD model coupled with Eqns. (4.1) through (4.4) in predicting the dependence of Q_f on the parameters h, w, D_1, D_2, H, T and RH that define a system. The average deviation of the measured values from theoretical predictions for the results shown in Fig. 3*A* was 6.2% with a maximum deviation of 25.3%. The results shown in Fig. 4.19 illustrate the dependence of Q_f on the dimensions of the outlet reservoir. For example, for a microchannel with w = 90 μm, h = 28 μm, and L = 20 mm (K = 1.7×10^5 g mm^{-4} s^{-1}), increasing the overall diameter of the

outlet reservoir from (D_1, D_2) = (1.4 mm, 0.91 mm) to (2.15 mm, 2.65 mm) will increase the volumetric flow rate by 224%, from $Q_f = 0.33$ μL s^{-1} to $Q_f = 1.07$ μL s^{-1}.

For all of the systems shown in Fig. 3, $V_{out}/V_{res} < 0.1$, such that the wetted sidewall area in the outlet reservoir is predicted to be small and it follows that $Q_{perm} \ll Q_e$. Thus, responses of Q_f to changes in reservoir geometry are mirrored in Q_e. For cylindrical reservoirs with $D_1/H \ll 1$, the volumetric flow rate is predicted to scale with the reservoir dimensions as $Q_f \propto D_1^2$ and $Q_f \propto H^{-1}$, per the results shown in Fig. 4.13. For shallow reservoirs ($D_1/H \gg 1$) the volumetric flow rate will scale as $Q_f \propto D_1$, with the transition between the two scaling rates occurring near $D_1/H \approx 1$. The latter results are consistent with experimental observations of evaporation of liquid from shallow wells.[53, 54] Interestingly, a switch of the outlet reservoir diameters D_1 and D_2 at a constant value of H (accomplished by reversing the punch direction in fabrication) leads to only small (< 5%) changes in Q_f.

Figure 4.19 also displays the relationship between Q_f and K for a given reservoir, with Q_f increasing slightly with decreasing K. The exact relationship between Q_f and K is complicated, since for a given reservoir decreases in K lead to higher values of V_{out} and thus lower values of Δp, leading to only slight increases in Q_f. This relatively weak dependence will prove beneficial for LOC devices utilizing this flow mechanism, as small deviations in microchannel dimensions from variability in the fabrication process will have a commensurately small effect on Q_f. This effect is not seen in traditional capillary driven LOC devices where the meniscus curvature is restricted according to the geometry of the device and flow rates scale as $Q_f \propto K^{-1}$, as given by Eqn. (4.2). Figure 4.20 displays the predicted dependence of the steady values of Δp and V_{out} on K for the values shown in Fig. 4.19 (experimental measurements are omitted for clarity). For channels with large viscous resistances ($K > 10^8$ g mm^{-4} s^{-1}), outlet menisci extended a short distance along the perimeter adjacent to the microchannel outlet. In this large K limit the overall size of the meniscus tends to be on the order of the microchannel size,

and discrepancies in Q_f between measurement and prediction were larger than those shown in Fig. 4.19.

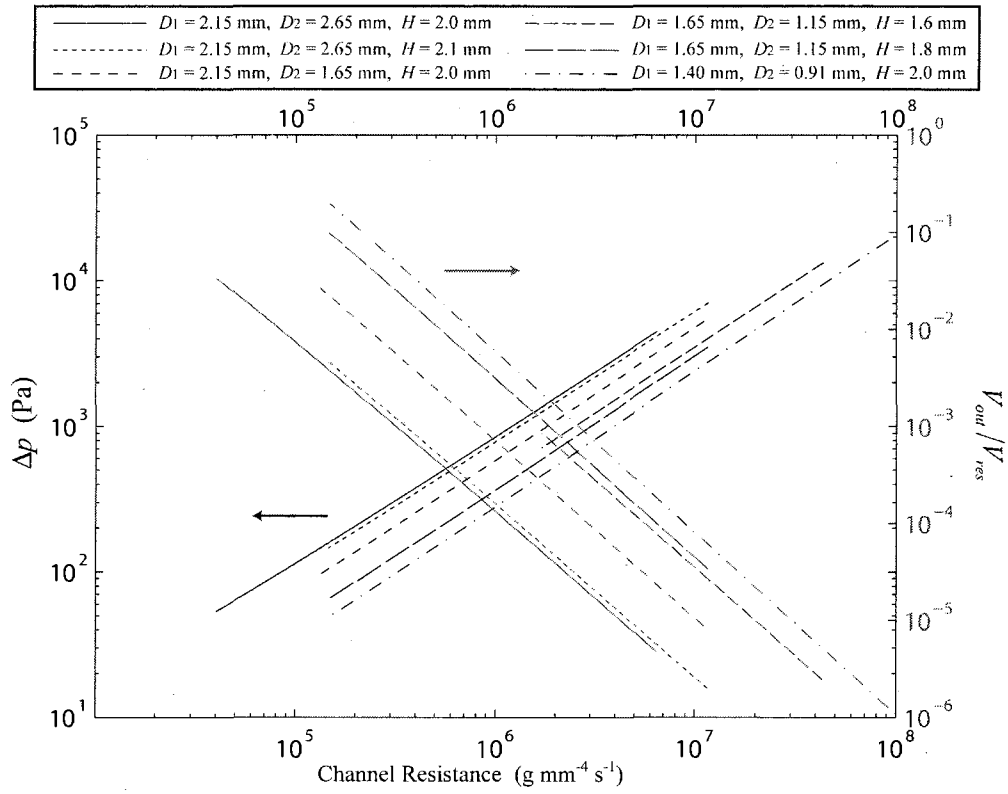

Figure 4.20. Theoretical predictions for Δp and V_{out}/V_{res} vs. K for the values shown in Fig 4.19.

4.4.5 Meniscus Stability and Model Accuracy

It is hypothesized that there exists a stability criterion for a ruptured meniscus (as shown in Fig. 4.2) similar to that of a 2D meniscus lying on a solid edge with angle 2α. Following the example presented by Langbein,[69] it is expected that for values of $2\alpha + \theta_1 + \theta_2 < \pi$ the ruptured meniscus will be stable in the concave form shown in Fig. 4.2. Beyond this stability criterion, for values of $2\alpha + \theta_1 + \theta_2 > \pi$, the ruptured meniscus is expected to exist in either a convex form or a shape not readily described mathematically. For experimental systems (PDMS/PDMS) made hydrophilic with a lower quality plasma (200 mTorr, 15W, 20s), the meniscus indeed ruptures to a state not defined by the geometric model proposed here; however, the boundary between the two states of stability has not been resolved.

Because of the dilute nature of the fluorescent bead solution in the inlet reservoirs for the data shown in Figs. 4.18 and 4.19, it is doubtful that θ_1 or θ_2 will change as a function of reservoir liquid volume. However, because the liquid within the reservoir reaches a point of infinite concentration as $t \rightarrow t_{end}$, it is unlikely that solutions containing realistic solute concentrations would display constant apparent contact angles over the duration of the experiment. To model these systems, one would only need a relationship between θ_1 or θ_2 and the solute concentration, which in principle are obtainable through experiment. As long as solute precipitation does not interfere with the position of the mensiscus, or the stability criterion shown above is not violated, these systems could most likely be predicted with the same accuracy as the cases shown in Fig. 4.19.

In this study, care was taken to ensure that the average meniscus position was at a z-position lower than $H/2$ at the onset of the experiment. As the meniscus height approaches the top of the reservoir, or $V \rightarrow V_{res}$, the evaporation rate calculated by Eqn. (4.22) increases in inverse proportion to the distance from the meniscus to the reservoir outlet. Under those conditions Eqn. (4.22) will over predict the evaporation rate from the meniscus, resulting in an under prediction of t_c and t_{end}. Because Eqn. (4.22) achieves

significant accuracy as the liquid volume decreases, the model can be used for all systems with $V \leq V_{res}$ to estimate the minimum time for reservoir dry out. To accurately describe the evolution of a meniscus in a micro-reservoir for the conditions described above, one must (*i*) develop a model that accounts for the steady-state diffusion of water vapor into the semi-infinite space above the reservoir and (*ii*) develop a function that gives a smooth transition between the two models as a function of the liquid volume in the reservoir.

4.5 Applications

4.5.1 Control over Evaporation Effects

Rather than utilizing complex fabrication strategies or inclusion of unnecessary experimental protocols, the techniques in this study can be used to design inlet reservoirs such that the inlet concentration is within acceptable limits over a predetermined time. The simplicity of this approach is in significant contrast with some previous technologies; for example, the assay system developed by Zimmermann *et al.* requires an inlet reservoir to the μFN to be cooled to 2 °C above the dew point in order for a 0.6 μL water droplet to persist for over an hour.[41] A reservoir such as that shown in Fig. 4.15, case (F), achieves the same result without the need to control the external environment. We have also fabricated reservoirs with D_1 = 1.1 mm, D_2 = 1.6 mm, and H = 3.5 mm that allow a 0.6 μL droplet to persist for over 90 minutes. For that case, it is predicted that (provided $V_o/Q_f \gg t_{end}$) at t = 20 min, V/V_o = 0.9, which is sufficient for most analytical measurements. This same approach may also be used to enhance evaporation in systems that require analyte pre-concentration for detection. An inlet reservoir designed with dimensions that produce higher evaporation rates used in micro-fluidic based assays would lead to systems with lower detection limits, as the reservoir solution could be concentrated by an order of magnitude within several minutes.

4.5.2 Passive Pumping from Multiple Inlets

Due to the ability to provide near-constant continuous flow rates for periods lasting over an hour, this passive pumping system can be applied to nearly all LOC devices that require pressure-driven flow. With precise control of sample-to-sample microchannel and outlet reservoir dimensions, this pumping mechanism has the potential to enhance the repeatability of heterogeneous assays requiring continuous flow for multiple hours, including affinity relationships possessing poor association kinetics or assays based on analytical measurements of live cells. Appropriate design of the inlet reservoirs of such systems would require only pipette delivery of sample volumes $V_o < 10$ μL, eliminating the need for syringe pumps or pressurized vessels.

Because the capillary forces associated with the inlet reservoirs are very small relative to those in the outlet reservoir, a single outlet reservoir can be used to pump fluids from multiple inlet reservoirs with volumetric flow rates from each reservoir dictated by the dimensions of the μFN. A representative example of this reservoir/μFN arrangement can be found in the passive generation of chemical gradients utilizing the techniques displayed by Jeon *et al.*[70] The configuration of a μFN used to passively create varying protein concentrations within a series of 8 outlet channels from two inlet reservoirs is shown in Fig. 4.21*A*, where the μFN had individual channel dimensions of w = 24 μm and h = 20 μm connected to an outlet reservoir with D_1 = 2.15 mm, D_2 = 1.65 mm, and H = 1.5 mm. The two inlet reservoirs were charged sequentially with solutions containing 1 μg mL^{-1} and 10 μg mL^{-1} of fluorescently labeled IgG (V_o = 3.0 μL), after which capillary filling of the μFN was completed in less than 30 s. Steady flow was maintained for over 75 min ($Q_f = 6.1\times10^{-4}$ μL s^{-1}, $K = 1.2\times10^{6}$ g mm^{-4} s^{-1}), where the average fluid velocity along each of the 8 outlet channels was measured to be 158 ± 6 μm s^{-1} (predicted velocities for the microchannel/reservoir system was v = 154 μm s^{-1}). Fluorescence images of the region near the outlet meniscus can be seen in Fig. 4.21*B* (t =

60 min); all 8 channels developed steady fluorescent profiles within 3 minutes, as shown in Fig. 4.22. By capping each inlet reservoir with 1.0 μL of heavy mineral oil, the concentrations of the aqueous solutions in each reservoir is maintained over time ($Q_{e,in}$ = 0), and the fluorescent intensity profile of the outlet channels at t = 60 min remains within 15% of the profile seen at t = 3 min. The slight increase in fluorescence intensity is most likely due to the adsorption of fluorescently labeled protein onto the microchannel walls over time. Conversely, if nothing is done to mitigate evaporation from the inlet reservoir the concentrations in each outlet channel increases steadily over time, resulting in nearly a 100% increase in fluorescent intensity within each channel at t = 30 min. Because evaporation occurs from all reservoirs in that case, steady flow was only maintained for 35 min.

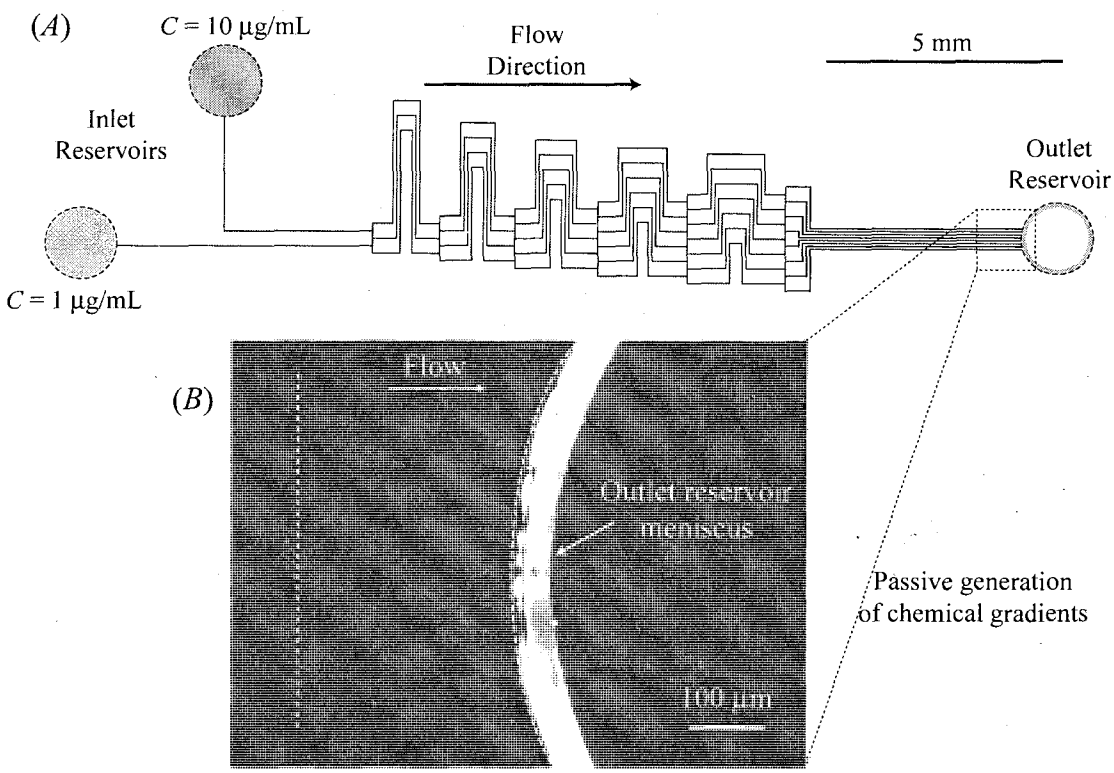

Figure 4.21. (*A*) Overall μFN design for the passive generation of chemical gradients in 8 outlet channels from 2 inlet reservoirs. (*B*) Fluorescence intensity (t = 60 min) for the 8 outlet channels for the case with the inlet channels containing 10 μg mL^{-1} and 1 μg mL^{-1} of fluorescently labeled IgG, respectively. The position of the incomplete meniscus did not change over time.

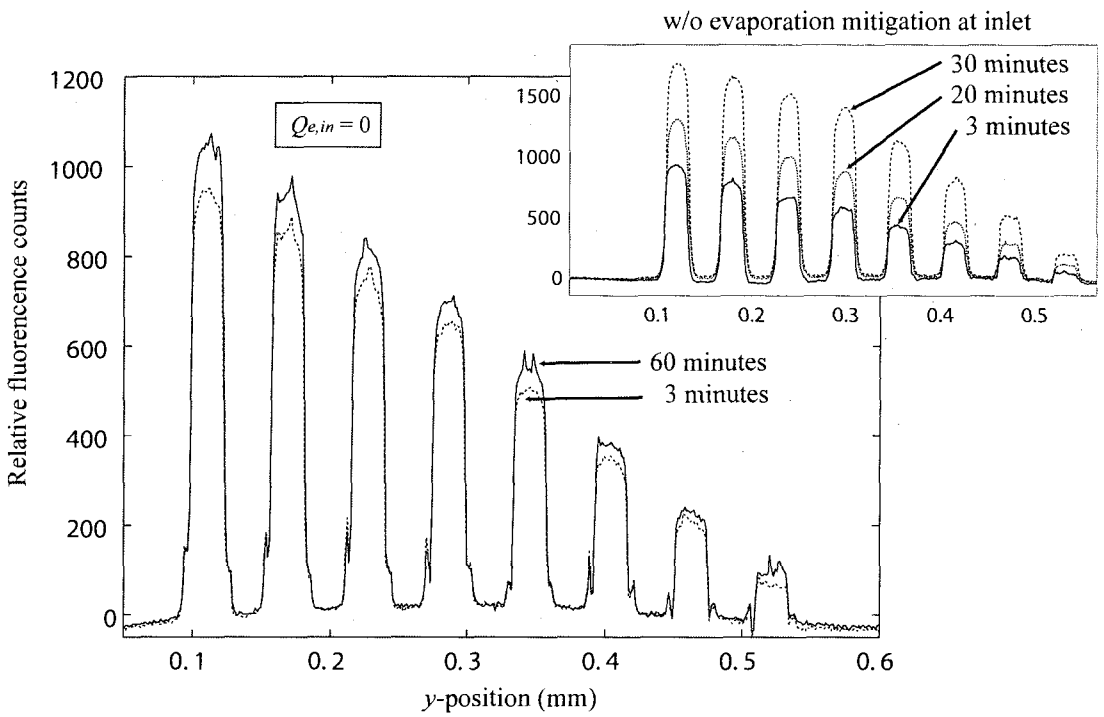

Figure 4.22. Relative fluorescence intensity across the 8 outlet channels for 3 and 60 minutes when the inlet reservoirs were capped with mineral oil. The inset displays the same profile when the inlet reservoirs were open to evaporation.

4.6 Future Work

4.6.1 Rapid Concentration of Solutes

Suspended or dissolved material within the inlet reservoir is rapidly concentrated in the outlet reservoir in these systems due to the small, $O(1)$ pL, steady-state values of V_{out}. Furthermore, the recirculation profiles present in the outlet reservoir serve to mix the reservoir contents and help maintain a uniform concentration throughout the solution. These recirculation profiles are clearly seen in the tracer bead movements within experimental outlet reservoirs, where fluid velocities are on the order of 100-1000 μm s^{-1}.

This effect is evident in the fluorescence image shown in Fig. 4.21*B*, where there is a sharp increase in fluorescence intensity between the microchannels and outlet reservoir meniscus. For this case a steady value of V_{out} = 2.0 pL is predicted, and after 60 minutes of flow the material in the outlet reservoir is concentrated by over 3 orders of magnitude above the inlet value. For systems where evaporation is eliminated from the inlet reservoir ($Q_{e,in} = 0$), the concentration of a solute in the outlet reservoir can be calculated from Eqn. (4.28). As shown in Fig. 4.20, the steady-state liquid volume V_{out} will decrease with a decrease in the dimensions of a microchannel (for outlet reservoirs with a constant dimension). Figure 4.23 displays predicted values of the normalized concentration of a generic solute (C_{out}/C_{in}) vs. t for the data shown in Fig. 4.17. In this figure microchannels of h = 28 μm and different width are connected to an outlet reservoir with D_1 = 2.15 mm, D_2 = 2.65 mm, and H = 2.5 mm. The predicted steady state values for the w = 26, 44, and 64 μm microchannels are V_{out} = 1.4, 8.1, and 15.7 pL, respectively. It can be seen that C_{out}/C_{in} increases rapidly with time, where the rate of increase is dependent on the microchannel width due to the inverse dependence of $C_{out}/C_{in}(t)$ on V_{out}, as shown in Eqn (4.28). The outlet reservoir pertaining to the microchannel with w = 26 μm will concentrate the solution in the inlet reservoir by nearly 3 orders of magnitude within 15 minutes.

This passive controlled concentration of confined fluids in the outlet reservoir would prove beneficial to many LOC applications, such as the qualitative detection of an analyte via the use of heterogeneous immunoassays as seen in Fig. 4.24. The details of a heterogeneous assay are described in chapter 5. By performing the assay within the confines of the outlet reservoir rather than in the microchannels leading to the outlet reservoir, it is possible that the limits of detection for a given analyte can be reduced by up to 3 orders of magnitude due to this localized concentration of solute.

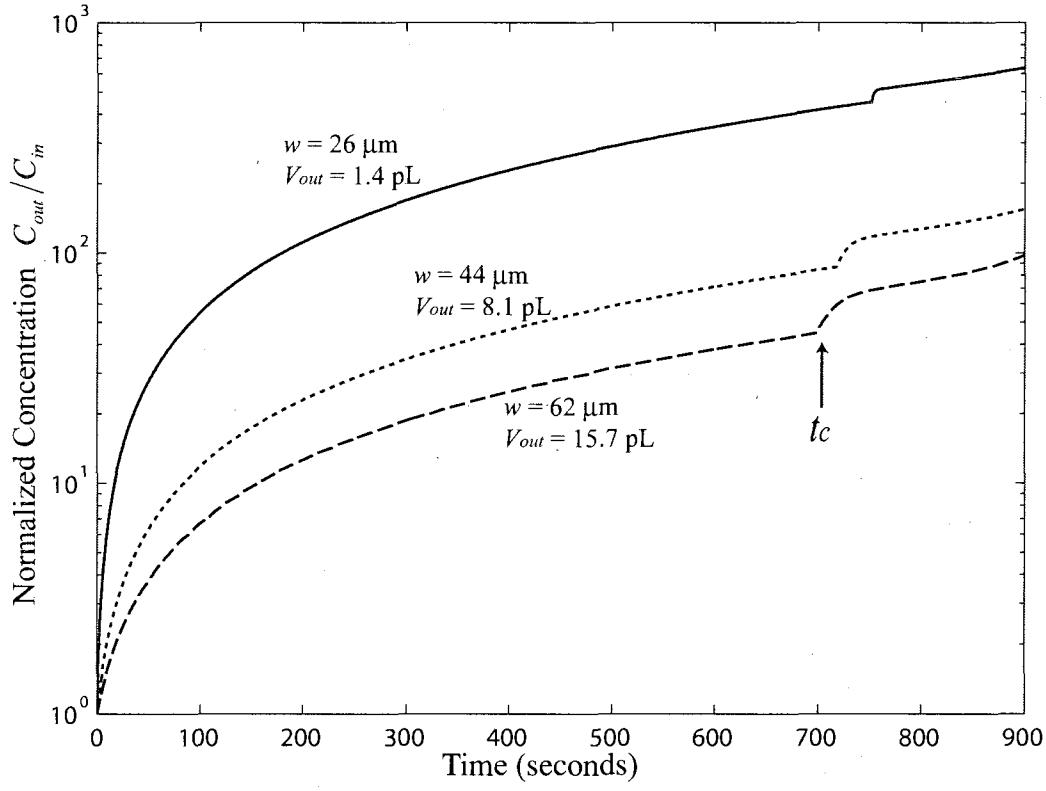

Figure 4.23. Predicted values of C_{out}/C_{in} vs. time for microchannels of different width connected to an outlet reservoir with D_1 = 2.15 mm, D_2 = 2.65 mm, and H = 2.5 mm. This system is the same as shown in Fig. 4.17.

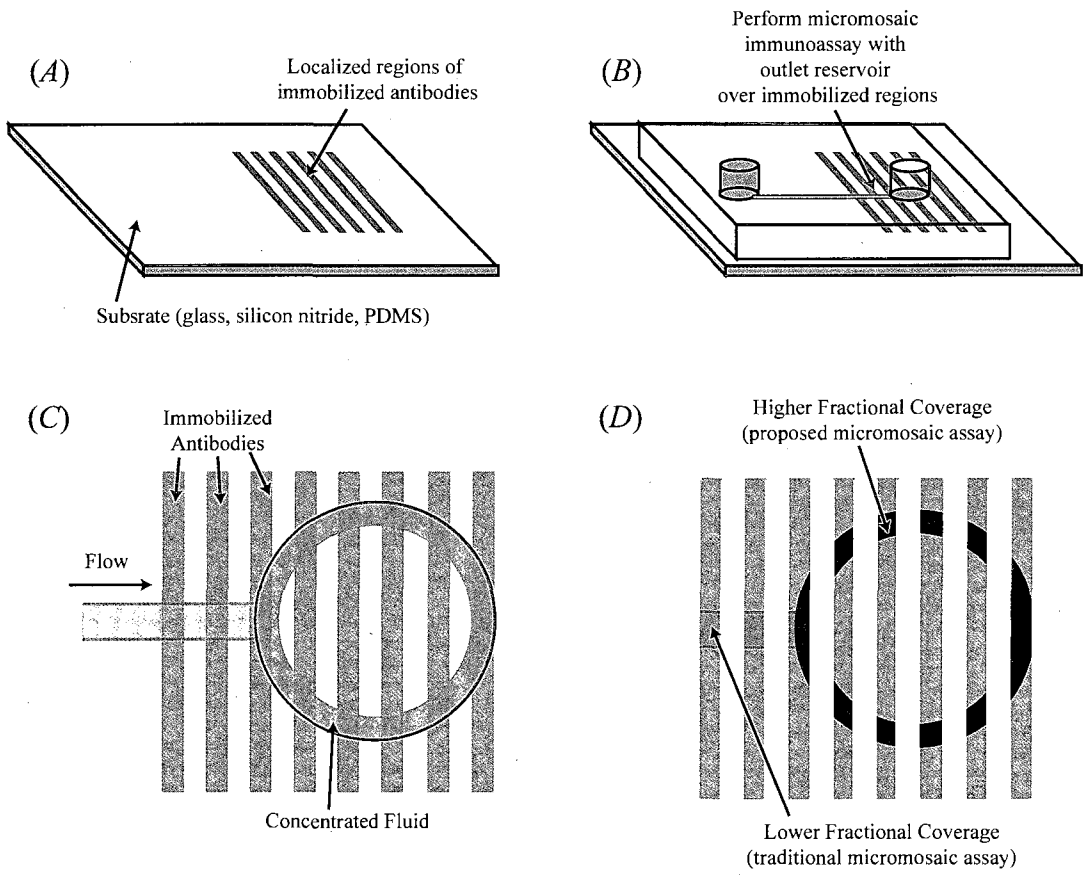

Figure 4.24. By performing a heterogeneous micromosaic immunoassay under the microchannel outlet reservoir rather than the microchannel, higher fractional coverages (higher signals) can be obtained at dilute analyte concentrations.

4.6.2 Passive Pumping with Multiple Outlet Reservoirs

The concentration of material in the outlet reservoir limits the overall flow duration for a given system as solutes crystallize near the outlet meniscus; however, material tends to crystallize in the reservoir at the point farthest from the microchannel outlet, allowing flow to continue at a controlled rate for extended times. The overall duration of flow for a single outlet reservoir is thus limited by both the concentration and solubility of the solutes in the inlet reservoir. To date, the operational limits of this flow mechanism are not known. Regardless, this operational limitation should be alleviated by the use of multiple outlet reservoirs, where multiple reservoirs with small diameters can produce larger steady-state values of V_{out} such that the rate of concentration in each reservoir is minimized and flow can be maintained for longer periods of time. In addition, the use of multiple outlet reservoirs should provide a larger range of Q_f compared to those shown in Fig. 4.19, because volumetric flow rates may be increased (approximately) in proportion to the number of outlet reservoirs. A circuit diagram of a system with one inlet reservoir and three outlet reservoirs is shown in Fig. 4.25. Ignoring permeation effects and capillary forces in the inlet reservoir, steady-state flow in this type of system can be solved with the following equations

$$Q_{fo} = \frac{p_o - p_m}{K_o} = Q_{f2} + Q_{f3} + Q_{f4}, \tag{4.29}$$

where $p_o = p_{atm}$, the atmospheric pressure in the surrounding environment. Eqn. (4.29) describes the flow from the inlet reservoir to the junction point. Flow in the remaining channels are described by

$$Q_{fi} = \frac{p_i - p_m}{K_i} = b_{1,i}\log(V_i) + b_{2,i}\log(V_i)^{b_{3,i}}, \tag{4.30}$$

$$p_i = p_{atm} - \frac{\gamma}{c_i}V_i^{\frac{1}{2}}, \tag{4.31}$$

where $i = 1,2,3$, c_i is a function of the reservoir geometry, and $b_{1,i}$, $b_{2,i}$, and $b_{3,i}$ are parameters fit from Eqn. (4.24). The unknowns in Eqns. (4.29) to (4.30) are V_i, the liquid volume in each reservoir, p_m, the fluid pressure at the junction. Therefore, predicting Q_f in μFNs with N outlet reservoirs involves the solution to N+1 non-linear equations.

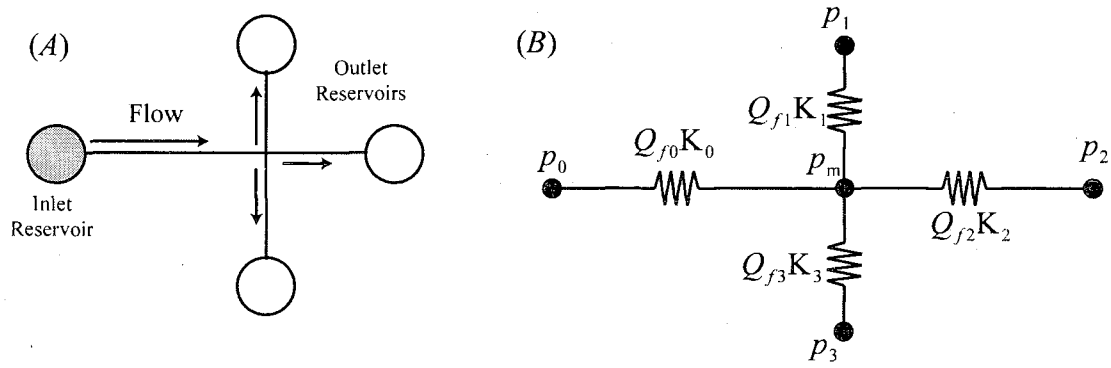

Figure 4.25. (*A*) Simple diagram of a system with one inlet reservoir and three outlet reservoirs. (*B*) Circuit diagram of the system shown in (*A*).

4.7 Appendix: One-Dimensional Diffusion in a Well

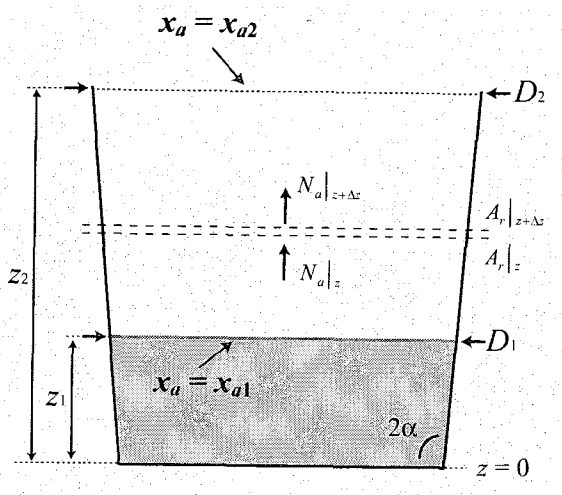

Figure 4.26. Geometric parameters describing one-dimensional diffusion in a well.

Consider a well with height $H = z_2$ and liquid level positioned at $z = z_1$ with upper diameter (D_2) and diameter at the meniscus (D_1) as shown in Figure 4.26. Assuming the average interface position (z_1) is not moving very fast, we can perform a quasi steady-state mass balance between the plane z and $z + \Delta z$ to find

$$\frac{d}{dz}(A_r N_a) = 0, \tag{4.32}$$

where A_r is the cross-sectional area of the reservoir and N_a is the molar flux of water vapor in the z-direction. Using Fick's first law of binary diffusion, we can also express the molar flux as

$$N_a = -\frac{c\mathcal{D}}{1 - x_a}\frac{dx_a}{dz}. \tag{4.33}$$

where c is the molar concentration of the gas phase, $\mathcal{D}$ is the diffusion coefficient of water vapor, and $x_a = x_a(z)$ is the mole fraction of water vapor. Again, the reservoir walls can be described by the line $r = F(z) = a_1 z + a_2$, thus A_r can be expressed as a function of z

$$A_r = \pi(a_1 z + a_2)^2. \tag{4.34}$$

Assuming that both the molar concentration and diffusion coefficient are constant with dilute values of x_a, substitution of equations (4.34) and (4.33) into equation (4.32) and simpifying yields

$$\frac{d}{dz}\left(\frac{(a_1 z + a_2)^2}{1 - x_a}\frac{dx_a}{dz}\right) = 0. \tag{4.35}$$

Integration of equation (4.35) twice with respect to z yields

$$\ln(1 - x_a) = \frac{C_1}{a_1(a_1 z + a_2)} + C_2. \tag{4.36}$$

The boundary conditions for this problem are then

$$x_a = x_{a1} \text{ at } z = z_1, \tag{4.37}$$

$$x_a = x_{a2} \text{ at } z = z_2, \tag{4.38}$$

where x_{a1} and x_{a2} represent the mole fraction of water vapor at the air/liquid interface and reservoir entrance, respectively. Noting that $D_1 = 2(a_1 z_1 + a_2)$ and $D_2 = 2(a_1 z_2 + a_2)$, the mole fraction distribution can then be found as

$$x_a = 1 - \exp(Y), \tag{4.39}$$

where

$$Y = \frac{D_1 D_2}{2(D_2 - D_1)(a_1 z + a_2)}\ln\left(\frac{1 - x_{a1}}{1 - x_{a2}}\right) + \frac{D_1 \ln(1 - x_{a2}) - D_1 \ln(1 - x_{a1})}{D_2 - D_1}. \tag{4.40}$$

Eqn. (4.39) can be used with Eqn. (4.22) to calculate the overall one-dimensional evaporation rates. Figure 4.27 displays the liquid evaporation rate $Q_e = N_a A_r M_w / \rho$ as a function of the dihedral angle 2α for several different reservoir geometries, where M_w and ρ correspond to the molecular weight and density of water, respectively. It can be seen that for all reservoir geometries, Q_e increases with increasing α and increasing values of D_1, consistent with the results of this study.

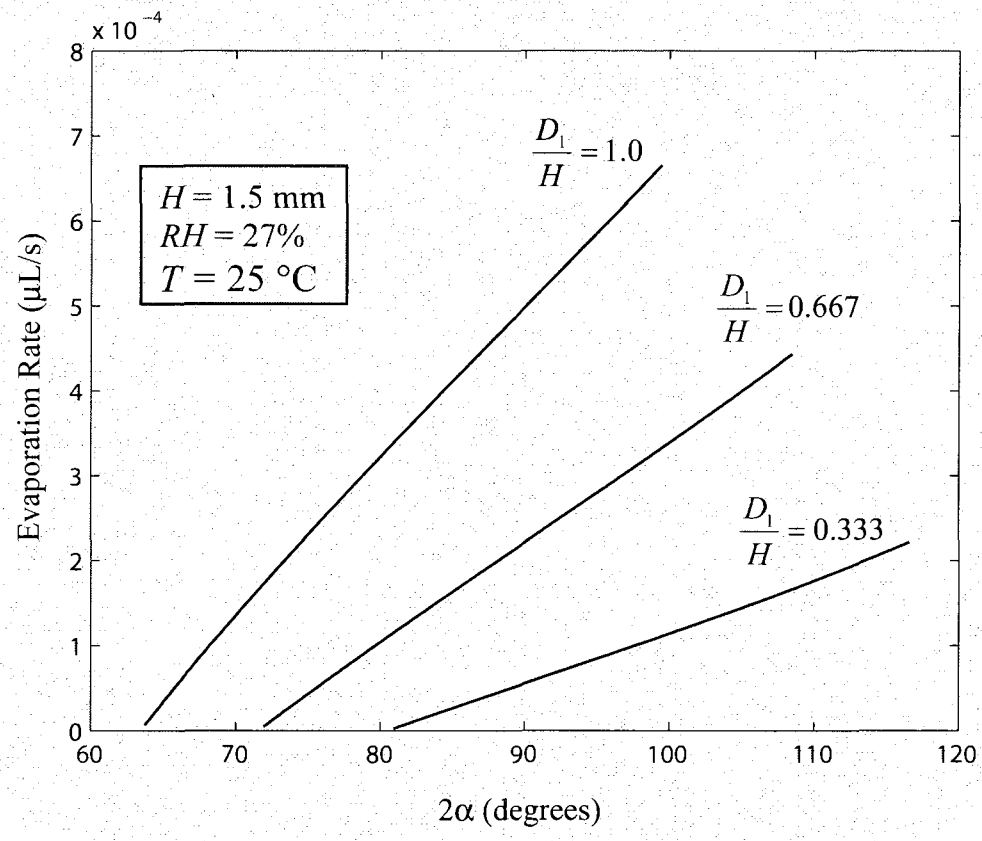

Figure 4.27. Overall evaporation rate (Q_e) vs. the dihedral angle 2α for three different reservoirs with varying values of D_1.

4.8 Conclusions

In summary, a passive pumping strategy has been demonstrated that provides near-constant flow rates from $O(1)$ μL sample volumes for periods exceeding an hour . To gain insight into the dynamics of flow for a given system, a simple geometric model is proposed that accounts for the shape of an air/liquid meniscus present in a cylindrical micro-reservoir with variable cross section. This model is utilized as a template for studying the rates of evaporation from the liquid volume via computational fluid dynamics. The combined geometric/CFD approach has been shown to both (*i*) quantitatively predict the evolution of a meniscus over time in experimental systems and (*ii*) quantitatively predict the volumetric flow rates occurring in simple systems consisting of two microreservoirs connected by a microchannel. All predictions using this combined geometric/CFD approach possess very high accuracy.

This method can be used with any liquids as long as the geometry of the reservoir and solution properties obey the relation $2\alpha + \theta_1 + \theta_2 < \pi$. Because the passive pumping mechanism shown here requires only that the microchannel/reservoir system be sufficiently hydrophilic, these systems can be fabricated from multiple constructs and are not limited to PDMS or glass substrates. Appropriate flow rates for a given μFN are accomplished via control over the dimensions of both the microchannels and outlet reservoirs. The techniques used in this study may be used to optimize a variety of lab-on-a-chip applications that either involve a holding reservoir open to the environment or require steady state passive flow for extended durations of time.

4.8 References

1. K. Ohno, K. Tachikawa and A. Manz, (2008) Microfluidics: Applications for analytical purposes in chemistry and biochemistry *Electrophoresis*, **29**, 4443-4453.
2. S. Pennathur, (2008) Flow control in microfluidics: are the workhorse flows adequate? *Lab on a Chip*, **8**, 383-387.
3. J. G. Smits, (1990) Piezoelectric Micropump with 3 Valves Working Peristaltically *Sensor Actuat a-Phys*, **21**, 203-206.
4. W. J. Spencer, W. T. Corbett, L. R. Dominguez and B. D. Shafer, (1978) Electronically Controlled Piezoelectric Insulin Pump and Valves *Ieee Transactions on Sonics and Ultrasonics*, **25**, 153-156.
5. H. T. G. Vanlintel, F. C. M. Vandepol and S. Bouwstra, (1988) A Piezoelectric Micropump Based on Micromachining of Silicon *Sensors and Actuators*, **15**, 153-167.
6. M. Koch, A. G. R. Evans and A. Brunnschweiler, (1998) The dynamic micropump driven with a screen printed PZT actuator *J Micromech Microeng*, **8**, 119-122.
7. C. J. Morris and F. K. Forster, (2000) Optimization of a circular piezoelectric bimorph for a micropump driver *J Micromech Microeng*, **10**, 459-465.
8. T. Bourouina, A. Bosseboeuf and J. P. Grandchamp, (1997) Design and simulation of an electrostatic micropump for drug-delivery applications *J Micromech Microeng*, **7**, 186-188.
9. M. C. Acero, J. A. Plaza, J. Esteve, M. Carmona, S. Marco and J. Samitier, (1997) Design of a modular micropump based on anodic bonding *J Micromech Microeng*, **7**, 179-182.
10. F. C. M. Vandepol, H. T. G. Vanlintel, M. Elwenspoek and J. H. J. Fluitman, (1990) A Thermopneumatic Micropump Based on Micro-Engineering Techniques *Sensor Actuat a-Phys*, **21**, 198-202.
11. A. Wego and L. Pagel, (2001) A self-filling micropump based on PCB technology *Sensor Actuat a-Phys*, **88**, 220-226.
12. S. Bohm, W. Olthuis and P. Bergveld, (1999) A plastic micropump constructed with conventional techniques and materials *Sensor Actuat a-Phys*, **77**, 223-228.
13. D. H. Jun, W. Y. Sim and S. S. Yang, (2007) A novel constant delivery thermopneumatic micropump using surface tensions *Sensor Actuat a-Phys*, **139**, 210-215.
14. J. C. Yoo, Y. J. Choi, C. J. Kang and Y. S. Kim, (2007) A novel polydimethylsiloxane microfluidic system including thermopneumatic-actuated micropump and Paraffin-actuated microvalve *Sensor Actuat a-Phys*, **139**, 216-220.
15. A. Richter, A. Plettner, K. A. Hofmann and H. Sandmaier, (1991) A Micromachined Electrohydrodynamic (Ehd) Pump *Sensor Actuat a-Phys*, **29**, 159-168.

16. V. Singhal and S. V. Garimella, (2005) A novel valveless micropump with electrohydrodynamic enhancement for high heat flux cooling *Ieee Transactions on Advanced Packaging*, **28**, 216-230.
17. X. Y. Wang, C. Cheng, S. L. Wang and S. R. Liu, (2009) Electroosmotic pumps and their applications in microfluidic systems *Microfluidics and Nanofluidics*, **6**, 145-162.
18. D. C. Duffy, H. L. Gillis, J. Lin, N. F. Sheppard and G. J. Kellogg, (1999) Microfabricated centrifugal microfluidic systems: Characterization and multiple enzymatic assays *Anal Chem*, **71**, 4669-4678.
19. A. Wixforth, C. Strobl, C. Gauer, A. Toegl, J. Scriba and Z. von Guttenberg, (2004) Acoustic manipulation of small droplets *Anal Bioanal Chem*, **379**, 982-991.
20. M. A. Unger, H. P. Chou, T. Thorsen, A. Scherer and S. R. Quake, (2000) Monolithic microfabricated valves and pumps by multilayer soft lithography *Science*, **288**, 113-116.
21. H. Andersson, W. van der Wijngaart, P. Nilsson, P. Enoksson and G. Stemme, (2001) A valve-less diffuser micropump for microfluidic analytical systems *Sensor Actuat B-Chem*, **72**, 259-265.
22. D. J. Laser and J. G. Santiago, (2004) A review of micropumps *J Micromech Microeng*, **14**, R35-R64.
23. M. Zimmermann, H. Schmid, P. Hunziker and E. Delamarche, (2007) Capillary pumps for autonomous capillary systems *Lab on a Chip*, **7**, 119-125.
24. S. Cesaro-Tadic, G. Dernick, D. Juncker, G. Buurman, H. Kropshofer, B. Michel, C. Fattinger and E. Delamarche, (2004) High-sensitivity miniaturized immunoassays for tumor necrosis factor a using microfluidic systems *Lab on a Chip*, **4**, 563-569.
25. D. Juncker, H. Schmid, U. Drechsler, H. Wolf, M. Wolf, B. Michel, N. de Rooij and E. Delamarche, (2002) Autonomous microfluidic capillary system *Anal Chem*, **74**, 6139-6144.
26. G. M. Walker and D. J. Beebe, (2002) A passive pumping method for microfluidic devices *Lab on a Chip*, **2**, 131-134.
27. E. Berthier and D. J. Beebe, (2007) Flow rate analysis of a surface tension driven passive micropump *Lab on a Chip*, **7**, 1475-1478.
28. I. J. Chen, E. C. Eckstein and E. Lindner, (2009) Computation of transient flow rates in passive pumping micro-fluidic systems *Lab on a Chip*, **9**, 107-114.
29. E. Berthier, J. Warrick, H. Yu and D. J. Beebe, (2008) Managing evaporation for more robust microscale assays - Part 1. Volume loss in high throughput assays *Lab on a Chip*, **8**, 852-859.
30. G. C. Randall and P. S. Doyle, (2005) Permeation-driven flow in poly(dimethylsiloxane) microfluidic devices *P Natl Acad Sci USA*, **102**, 10813-10818.
31. E. Berthier, J. Warrick, H. Yu and D. J. Beebe, (2008) Managing evaporation for more robust microscale assays - Part 2. Characterization of convection and diffusion for cell biology *Lab on a Chip*, **8**, 860-864.
32. J. C. T. Eijkel and A. van den Berg, (2005) Water in micro- and nanofluidics systems described using the water potential *Lab on a Chip*, **5**, 1202-1209.

33. E. Litborn and J. Roeraade, (2000) Liquid lid for biochemical reactions in chip-based nanovials *Journal of Chromatography B*, **745**, 137-147.
34. S. Neugebauer, S. R. Evans, Z. P. Aguilar, M. Mosbach, I. Fritsch and W. Schuhmann, (2004) Analysis in ultrasmall volumes: Microdispensing of picoliter droplets and analysis without protection from evaporation *Anal Chem*, **76**, 458-463.
35. R. Moerman, J. Knoll, C. Apetrei, L. R. van den Doel and G. W. K. van Dedem, (2005) Quantitative analysis in nanoliter wells by prefilling of wells using electrospray deposition followed by sample introduction with a coverslip method *Anal Chem*, **77**, 225-231.
36. C. D. T. Bratten, P. H. Cobbold and J. M. Cooper, (1997) Micromachining sensors for electrochemical measurement in subnanoliter volumes *Anal Chem*, **69**, 253-258.
37. M. Gratzl and C. Yi, (1993) Diffusional Microtitration - Acid-Base Titrations in Picoliter and Femtoliter Samples *Anal Chem*, **65**, 2085-2088.
38. E. Litborn, A. Emmer and J. Roeraade, (1999) Chip-based nanovials for tryptic digest and capillary electrophoresis *Analytica Chimica Acta*, **401**, 11-19.
39. M. Minarik, K. Kleparnik, M. Gilar, F. Foret, A. W. Miller, Z. Sosic and B. L. Karger, (2002) Design of a fraction collector for capillary array electrophoresis *Electrophoresis*, **23**, 35-42.
40. N. Goedecke, J. Eijkel and A. Manz, (2002) Evaporation driven pumping for chromatography application *Lab on a Chip*, **2**, 219-223.
41. M. Zimmermann, S. Bentley, H. Schmid, P. Hunziker and E. Delamarche, (2005) Continuous flow in open microfluidics using controlled evaporation *Lab on a Chip*, **5**, 1355-1359.
42. C. S. Effenhauser, H. Harttig and P. Kramer, (2002) An evaporation-based disposable micropump concept for continuous monitoring applications *Biomed Microdevices*, **4**, 27-32.
43. Z. R. Xu, C. H. Zhong, Y. X. Guan, X. W. Chen, J. H. Wang and Z. L. Fang, (2008) A microfluidic flow injection system for DNA assay with fluids driven by an on-chip integrated pump based on capillary and evaporation effects *Lab on a Chip*, **8**, 1658-1663.
44. Y. F. Chen, F. G. Tseng, S. Y. ChangChien, M. H. Chen, R. J. Yu and C. C. Chieng, (2008) Surface tension driven flow for open microchannels with different turning angles *Microfluidics and Nanofluidics*, **5**, 193-203.
45. E. Delamarche, A. Bernard, H. Schmid, B. Michel and H. Biebuyck, (1997) Patterned delivery of immunoglobulins to surfaces using microfluidic networks *Science*, **276**, 779-781.
46. A. Bernard, B. Michel and E. Delamarche, (2001) Micromosaic immunoassays *Anal Chem*, **73**, 8-12.
47. B. M. Murphy, X. Y. He, D. Dandy and C. S. Henry, (2008) Competitive immunoassays for simultaneous detection of metabolites and proteins using micromosaic patterning *Anal Chem*, **80**, 444-450.
48. R. D. Deegan, O. Bakajin, T. F. Dupont, G. Huber, S. R. Nagel and T. A. Witten, (2000) Contact line deposits in an evaporating drop *Physical Review E*, **62**, 756-765.

49. R. D. Deegan, O. Bakajin, T. F. Dupont, G. Huber, S. R. Nagel and T. A. Witten, (1997) Capillary flow as the cause of ring stains from dried liquid drops *Nature*, **389**, 827-829.
50. H. Hu and R. G. Larson, (2002) Evaporation of a sessile droplet on a substrate *Journal of Physical Chemistry B*, **106**, 1334-1344.
51. Y. Deng, X. Y. Zhu, T. Kienlen and A. Guo, (2006) Transport at the air/water interface is the reason for rings in protein microarrays *Journal of the American Chemical Society*, **128**, 2768-2769.
52. C. T. Chen, C. C. Chieng and F. G. Tseng, (2007) Uniform solute deposition of evaporable droplet in nanoliter wells *Journal of Microelectromechanical Systems*, **16**, 1209-1218.
53. C. T. Chen, F. G. Tseng and C. C. Chieng, (2006) Evaporation evolution of volatile liquid droplets in nanoliter wells *Sensor Actuat a-Phys*, **130**, 12-19.
54. L. R. van den Doel and L. J. van Vliet, (2001) Temporal phase-unwrapping algorithm for dynamic interference pattern analysis in interference-contrast microscopy *Appl Optics*, **40**, 4487-4500.
55. K. T. Hjelt, R. van den Doel, W. Lubking and M. J. Vellekoop, (2000) Measuring liquid evaporation from micromachined wells *Sensor Actuat a-Phys*, **85**, 384-389.
56. B. Rieger, L. R. van den Doel and L. J. van Vliet, (2003) Ring formation in nanoliter cups: Quantitative measurements of flow in micromachined wells *Physical Review E*, **68**, -.
57. Y. N. Xia and G. M. Whitesides, (1997) Soft lithography. *Abstracts of Papers of the American Chemical Society*, **214**, 348-PMSE.
58. J. A. Vickers, M. M. Caulum and C. S. Henry, (2006) Generation of hydrophilic poly(dimethylsiloxane) for high-performance microchip electrophoresis *Anal Chem*, **78**, 7446-7452.
59. J. C. Crocker and D. G. Grier, (1996) Methods of digital video microscopy for colloidal studies *J Colloid Interf Sci*, **179**, 298-310.
60. L. A. Belfiore, *Transport phenomena for chemical reactor design*, Wiley, New York, 2003.
61. M. E. Staben, A. Z. Zinchenko and R. H. Davis, (2003) Motion of a particle between two parallel plane walls in low-Reynolds-number Poiseuille flow *Phys Fluids*, **15**, 1711-1733.
62. E. W. Washburn, (1921) The dynamics of capillary flow. *Phys Rev*, **17**, 273-283.
63. W. M. Rohsenow, J. P. Hartnett and Y. I. Cho, *Handbook of heat transfer*, McGraw-Hill, New York, 1998.
64. G. Ryskin and L. G. Leal, (1984) Numerical-Solution of Free-Boundary Problems in Fluid-Mechanics .1. The Finite-Difference Technique *Journal of Fluid Mechanics*, **148**, 1-17.
65. P. Zhu, (2005) Field distribution of a uniformly charged circular arc *J Electrostat*, **63**, 1035-1047.
66. S. Bhattacharya, A. Datta, J. M. Berg and S. Gangopadhyay, (2005) Studies on surface wettability of poly(dimethyl) siloxane (PDMS) and glass under oxygen-plasma treatment and correlation with bond strength *Journal of Microelectromechanical Systems*, **14**, 590-597.

67. A. Shastry, M. J. Case and K. F. Bohringer, (2006) Directing droplets using microstructured surfaces *Langmuir*, **22**, 6161-6167.
68. R. R. Nino and J. M. R. Patino, (1998) Surface tension of bovine serum albumin and tween 20 at the air-aqueous interface *J Am Oil Chem Soc*, **75**, 1241-1248.
69. D. Langbein, (1990) The Shape and Stability of Liquid Menisci at Solid Edges *Journal of Fluid Mechanics*, **213**, 251-265.
70. N. L. Jeon, S. K. W. Dertinger, D. T. Chiu, I. S. Choi, A. D. Stroock and G. M. Whitesides, (2000) Generation of solution and surface gradients using microfluidic systems *Langmuir*, **16**, 8311-8316.

Chapter 5

Optimization of Microchannel Geometries Applied to Heterogeneous Immunoassays

This chapter is dedicated to the study of the effects of microchannel geometries and convective flow rates on the output signal of a heterogeneous immunoassay within a microfluidics based device.

5.1 Introduction

Due to the high specificity and sensitivity of the association between antigen and antibodies, aptamers, and complementary strands of DNA and RNA, biosensors based on affinity assays have become an indispensable tool for diagnostic and analytical purposes. Starting with the seminal work on these assays in the late 1950s and lasting roughly 30 years,[1] affinity assays were generally limited to the quantification of less than three analytes per test, where reagents pertaining to each analyte were tagged with a different label for detection purposes (e.g. fluorescence tagging or the use of radioisotopes). The proposed heterogeneous multi-analyte techniques by Ekins *et al.*[2] along with the demonstration of high throughput microarray printing techniques displayed by Schene *et al.*[3] moved multi-analyte affinity assays to the forefront of clinical diagnostics and research laboratories. These heterogeneous microarray affinity assays possess many advantages over their homogeneous predecessors, including (*i*) reduced required volumes of reagents and samples, (*ii*) the separation of analyte from the aqueous media, (*iii*) the

concentration of analyte in specific regions on a substrate, and (*iv*) the capability for detection of multiple analytes with a single label.

Current microarray techniques allow for the simultaneous quantification of thousands of analytes in a single experiment. In these experiments the analytes of interest range from DNA and RNA oligonucleotides,[4, 5] proteins,[6] and small tissue biopsies.[7] However, there are several problems and limitations with these technologies, including limited reproducibility and sensitivity to analyte concentrations.[8, 9] Microarray based assays are routinely conducted under static conditions such that analyte transport to the immobized capture regions occurs solely via molecular diffusion. Due to mass transfer limitations in these static assays, the creation of boundary layers void of analyte close to the immobilized capture regions creates a significant decrease in the time-dependent analyte capture rate. The relative rates of reaction and mass transfer are characterized by the Dahmköhler number $Da_1 = k_1 h C_{B,o}/D$, where k_1 is the forward reaction rate constant of the affinity relationship, h is the height of the microchannel, $C_{B,o}$ is the surface concentration of probe molecules, and D the molecular diffusion coefficient of analyte. Static systems involving biologically relevant analytes (proteins, DNA, RNA) commonly exhibit values of $Da_1 \gg 1$, and are thus severely mass transfer limited. As a result, affinity systems possessing poor reaction kinetics or low analyte concentration require hybridization times lasting longer than 24 hours.[10] The analyte depletion zones for a single capture spot can extend over several hundred microns, thus large errors can be induced when two spots situated near one another have competitive affinities for the same analyte.

Convective delivery of analyte over the capture spots can eliminate depletion layer effects and reduce the time required for complete hybridization; however doing so with modern microarray slides requires large sample volumes and is unpractical. When active fluid delivery occurs through a microfluidic platform, these volume requirements are reduced to those used by standard microarray procedures. Convective fluid delivery

through a μFN was first shown to reduce assay times by an order of magnitude or more with respect to conventional static assays,[11] and several groups have since developed microfluidic heterogeneous affinity assays using microarray printing technologies.[12-15] By using the immobilization techniques first demonstrated by Delamarche *et al.*,[16] several groups have developed microfluidic affinity assays without the need for expensive microarray printers.[17-22] The fundamentals steps of these microfluidic assays are shown in figure 5.1.

Although these microfluidic technologies have shown multi-analyte capability in a rapid, cost-effective format, they encompass a wide variety of microchannel geometries and convective flow rates and comparison of the different technologies is difficult. Performing the assay at a high flow rate comes at the cost of increased sample consumption; therefore the available time for the assay to be run in an active format will be limited. Conversely, if the assay is performed with a low flow rate the system becomes mass transfer limited and times required for hybridization to reach equilibrium can exceed that of traditional static assay, where the microchannels restrict the diffusion of analyte to one dimension. For purposes of assay accuracy, a large number of these continuous flow devices use multiple capture spots having an affinity for the same analyte. These spots are commonly situated along the microchannel axis separated from one another by a small distance. If the flow rate of the assay is sufficiently slow, a large analyte concentration boundary layer will be created downstream of the first capture spot. The reduction of analyte concentrations in this boundary layer results in a reduction of hybridization rates for the downstream capture spots. For quantitative assays constrained by time, the signal variance from these multiple spots can exceed 25%. Understanding the effects of flow rates and capture spot geometries on the output signal is vital in maintaining the accuracy and repeatability of these assays. The time dependent hybridization rate of an immobilized capture probe and a free analyte is a function of several parameters, including: the geometry and surface density of the immobilized

capture spot, the molecular diffusivity of the free analyte, the fluid velocity profile in the region surrounding each spot, and the reaction kinetics involved with the affinity interaction between the immobilized and free species. Fortunately, convection and diffusion on the microfluidic scale are well understood phenomena and there are several experimental systems to calculate the parameters associated with the kinetics of the affinity interaction.[23] There have been a variety of analytical methods proposed to calculate hybridization rates as a function of the parameters listed above; unfortunately, none possess the ability to reliably duplicate rates in experimental systems.[24-27] On the other hand, with the use of several computational methods, a variety of theoretical models have shown excellent prediction with experimental systems with complex geometries.[28-31] These computational methods can allow efficient exploration of the parameter space without the time requirements and high costs of experimental methods.

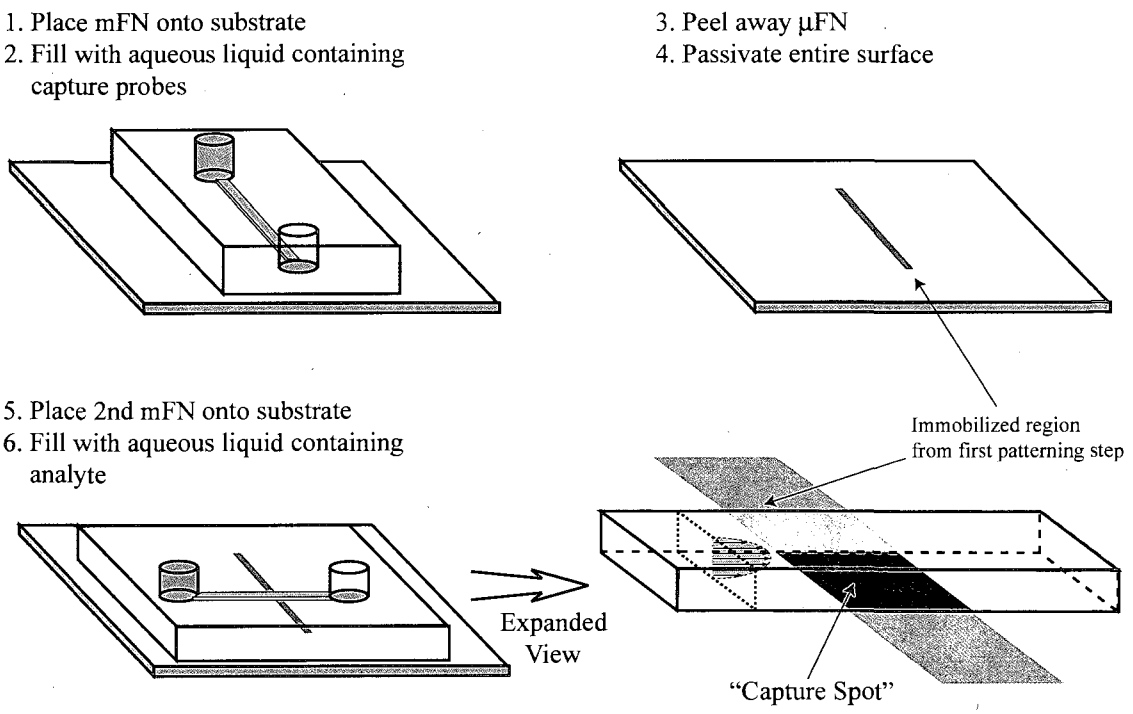

Figure 5.1. Micromosaic method to perform heterogeneous affinity assay on a substrate.

In this chapter we apply theoretical models similar to that of Zimmermann *et al.* and Parsa *et al.* to study the effects of microchannel geometry and convective flow rate on a heterogeneous immunoassay similar to those studied at Colorado State University.[32, 33] This dissertation proposes using the passive pumping methods described in figure 4 to deliver fluid to a capture spot situated on top of a local evanescent array coupled (LEAC) sensor.[34] This passive pumping mechanism is capable of providing steady state flow at a rate dictated by the geometries of the microchannel and outlet reservoirs. From previous numerical studies, it is clear that the axial velocity profile of the fluid situated above the capture spot has a large impact on the hybridization rate of the affinity assay;[29, 31] however, there has been no attention given to the effects of the microchannel geometries. This chapter discusses the benefits of reducing the overall height of microfluidic systems

applied to heterogeneous affinity assays. Keeping the microchannel width constant preserves the overall area of the capture spot and is beneficial for signal detection purposes. By reducing the height of a microchannel connecting two open reservoirs, the average fluid velocity over the capture spot can be significantly increased and the time for hybridization is reduced. Furthermore, we discuss possible alleviation methods to the effects of multiple capture spots for these systems.

5.2 Description of the System under Consideration

The micromosaic method for performing heterogeneous immunoassays is shown in Fig. 5.1, and details can be also be found in the literature.[20] Briefly, a network of open faced microchannels molded in PDMS is reversibly sealed to a substrate of interest to create a μFN. After sealing, an aqueous solution containing the capture probes is delivered through the microchannels using either passive flow mechanisms, or most commonly via syringe pumps. Capture probes flow through the μFN and bind to the substrate through passive adsorption, affinity interactions (e.g. biotin/avidin), or covalent bonds.[16] The μFN is then peeled away, after which the substrate is rinsed with a buffer and immersed in a passivating solution to prevent non-specific adsorption, such as an aqueous solution containing bovine serum albumin (BSA). These initial steps create precise spatial regions on the substrate surface where the capture agent is immobilized in patterns mirroring the design of the μFN. A second μFN is then sealed to the substrate (reversibly or irreversibly) such that microchannels of interest intersect the initial immobilized patterns. Aqueous solution containing the analyte of interest is placed in an inlet reservoir and passive flow drives fluid at a steady state through the μFN and over the immobilized capture spot regions. If passivation of the μFN is accomplished in the correct fashion, analyte will be free to bind to the capture bodies immobilized to the microchannel floor and will not interact with the remaining surfaces. Therefore, this system is reduced to that of laminar flow in a duct with a reactive boundary condition of

axial length l_s on the channel floor. Assuming the reaction kinetics favor the formation of the hybridized complex, the initial stages of the assay are similar to a modified Graetz problem such that the concentration of the analyte immediate to the capture spot approaches zero.

5.3 Model

The theoretical model used in this chapter describes the binding of an analyte to an capture body which has been immobilized to a specific region located on the floor of a microchannel under laminar flow, similar to the situation displayed in figure 1. The model is based on the direct binding of analyte to capture body and requires the following necessary, yet justifiable assumptions: (*i*) fluid flow occurring in the microchannel is in the laminar regime and body forces are negligible. (*ii*) the system is isothermal. (*iii*) the bound capture body surface coverage is homogeneous and all binding sites possess equal affinity constants. (*iv*) a single capture body is capable of reversibly binding no more than one analyte, and that interaction can be accounted for with a standard ligand-receptor model.

For steady-state, laminar, incompressible flow with constant fluid density, the velocity vector field $\mathbf{v} = \mathbf{v}(x, y, z)$ is represented by the Stokes equation,

$$-\nabla p + \mu \nabla^2 \mathbf{v} = 0, \tag{5.1}$$

along with the equation of continuity,

$$\nabla \cdot \mathbf{v} = 0. \tag{5.2}$$

where p and μ are the pressure and viscosity of the fluid, respectively. The solution to Eqns. (5.1) and (5.2) for viscous flow confined to a duct of width w and height h can be found in the following series solution,[35]

$$\frac{v_y}{\langle v_y \rangle} = \frac{2\left[\left(1-(z/h)^2\right)+4\sum_{n=0}^{\infty}(-1)^{n+1}M_n^{-3}\,\mathrm{sech}(M_n\,w/h)\cosh(M_n\,x/h)\cos(M_n\,z/h)\right]}{4\Big/3-(8h/w)\sum_{n=0}^{\infty}M_n^{-5}\tanh(M_n\,w/h)}, \quad \textbf{(5.3)}$$

where $M_n = (2n+1)\pi/2$. The concentration of an analyte in the bulk solution $C_A = C_A(x, y, z, t)$ is described by the unsteady-state convection-diffusion equation,

$$\frac{\partial C_A}{\partial t} + \mathbf{v}\cdot\nabla C_A = D\nabla^2 C_A, \quad \textbf{(5.4)}$$

where D is the molecular diffusion coefficient of the analyte present at low concentrations. The binding of analyte to capture body can be described using a standard ligand-receptor model

$$A(aq.) + B(s.) \underset{k_2}{\overset{k_1}{\leftrightarrow}} AB(s.), \quad \textbf{(5.5)}$$

where A denotes the aqueous analyte, B the immobilized capture body, and AB the immobilized bound complex. Assuming elementary reaction kinetics and ignoring surface diffusion, the surface concentration of the bound complex can be calculated as

$$\frac{\partial C_{AB}}{\partial t} = k_1 C_A\left(C_{B,o} - C_{AB}\right) - k_2 C_{AB}, \quad \textbf{(5.6)}$$

where k_1 is the association rate constant, k_2 is the dissociation rate constant, $C_{B,o}$ is the initial capture body surface concentration (or capture probe density), and $C_{B,o} = C_{AB} + C_B$. Equations (5.4) and (5.6) are coupled via the boundary condition along the reactive spot

$$\hat{n}\cdot\left(C_A\mathbf{v} - D\nabla C_A\right) = -k_1 C_A\left(C_{B,o} - C_{AB}\right) + k_2 C_{AB}, \quad \textbf{(5.7)}$$

where $\hat{n}$ is the unit vector normal to the plane of the reactive spot. The boundary conditions for the remaining surfaces of interest are listed as follows.

microchannel inlet, $C_A = C_{A,o}$, **(5.8)**

microchannel outlet, $\hat{n}\cdot D\nabla C_A = 0$, **(5.9)**

passivated surfaces, $\hat{n}\cdot\left(C_A\mathbf{v} + D\nabla C_A\right) = 0$, **(5.10)**

where $C_{A,o}$ is the concentration of analyte in the solution of interest. We define the fractional coverage of the bound-complex as

$$\theta_{AB} = \frac{C_{AB}}{C_{B,o}}, \tag{5.11}$$

where it follows that $0 \leq \theta_{AB} \leq 1$.

5.3.1 Well-Mixed Condition

In the case that the rate of transport of analyte to the capture surface is much greater than the rate of analyte binding to immobilized capture bodies, or $Da_I \ll 1$, we can assume that $C_A = C_{A,o}$ throughout the microchannel. In this well-mixed case, Eqn. (5.6) can be solved analytically with a solution of

$$\theta_{AB} = \frac{C_A}{C_A + K_d}\left[1 - e^{-(k_1 C_A + k_2)t}\right]. \tag{5.12}$$

At equilibrium, the fractional coverage of the bound-complex will reach a maximum possible value of

$$\theta_{AB,eq} = \frac{C_A}{C_A + K_d}. \tag{5.13}$$

This equilibrium coverage is the maximum surface density of the bound analyte/capture probe complex for a system given $C_{A,o}$ and a dissociation constant $K_d = k_2/k_1$. Equation (5.13) also applies when the concentration of analyte cannot be assumed constant. For these systems it is useful to know the minimum time required for an assay to reach a fractional coverage $\chi\theta_{AB,eq}$, where $0 \leq \chi \leq 1$. Solving Eqn. (5.12) for $t = t_{eq,min}$ and $\theta_{AB} = \chi\theta_{AB,eq}$ yields

$$t_{eq,\min} = \frac{-\ln(1-\chi)}{k_1 C_A + k_2}. \tag{5.14}$$

5.3.2 Numerical Methods

The finite volume suite Gambit/Fluent was employed to solve Eqns. (5.1), (5.2), (5.4), and (5.6) along with the boundary conditions (5.7) to (5.10). The geometries pertaining to a two-dimensional simulation are shown in Fig. 5.2. All simulations involved steady-state analyte flow over 4 capture regions, where each reactive spot had width w, length l_s, and were separated from one another by an axial distance l_s. This specific geometry was chosen as it represents experimental work performed in the department of chemistry.[33] The simulation geometry consisted of a minimum axial length of L = 1 mm, where the leading edge of spot 1 was situated 0.350 mm downstream of the inlet. The appropriate two- or three-dimensional geometries were typically discretized with a minimum of 40 computational nodes situated along both each reactive spot in the y-direction, and 30 computational nodes situated along height of the microchannel in the z-direction. These discritization schemes were predetermined such that solutions for the velocity field and analyte concentration were independent of the mesh density. The solution of the velocity field obtained by fixing the fluid velocity at the microchannel inlet to $\mathbf{v}(x,0,z) = \langle v_y \rangle$. The steady state solution to $\mathbf{v} = \mathbf{v}(x, y, z)$ was then obtained by successive iteration until the normalized residuals for the momentum and continuity equations fell below 10^{-5}. The uniform velocity profile along the microchannel inlet had no effect on the downstream velocity profile, where the solution to $\mathbf{v} = \mathbf{v}(x, y, z)$ near the reactive spot was verified by Eqn. (5.3) for a variety of microchannel geometries.

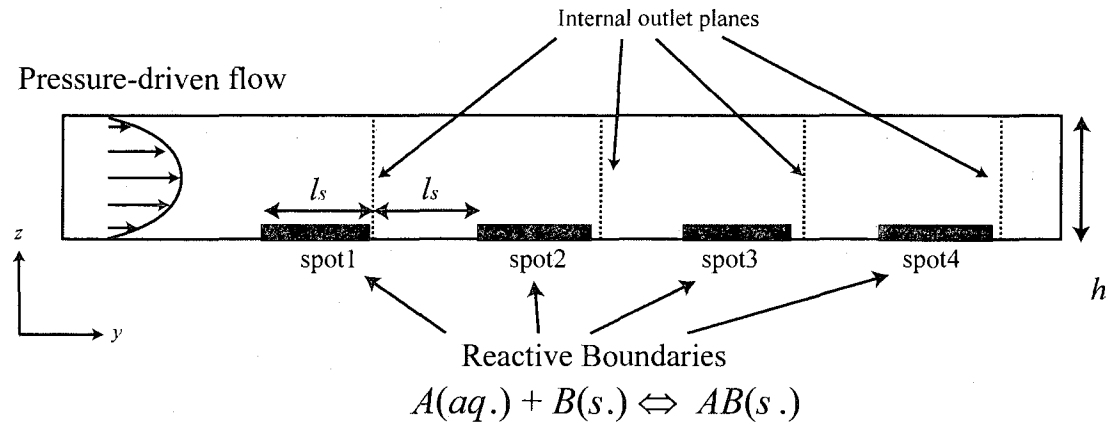

Figure 5.2. Simple diagram of two-dimensional simulations used in this chapter. The reactive spots have axial length l_s, and are separated from each other by the same distance.

After the solution to the velocity field was obtained, the unsteady state solutions for $C_A = C_A(x, y, z, t)$ and $C_{AB} = C_{AB}(x, y, z, t)$ were calculated using a dual time step method. For assay times of $t < 20$ s, a time step of $\Delta t = 0.01$ s was used in order to capture the initial hybridization rates under high mass transfer conditions. After $t = 20$ s, hybridization rates were lowered to the point that a larger time step of $\Delta t = 0.5$ s could be used. All calculations pertaining to the convection-diffusion equation used convergence criteria such that the normalized residuals for the species equations were below 10^{-7} at each time step. For these calculations, there was no difference solution pertaining to different values of Δt for $t > 20$ s as long as $\Delta t \leq 0.5$ s.

At each computed time step several variables were exported, including the average fractional coverage for each reactive spot and the average analyte concentration in planes of constant y-position situated immediately downstream of each spot (see Fig. 5.2). This solution method was verified for two-dimensional solutions with the solutions of Zimmermann *et al.*[31] and Hu *et al.*[29] by comparing curves of the time required to reach 95% equilibrium vs. the average axial fluid velocity, as seen in figure 5.3. In order to reduce the times required for computation, a series of simulations were implemented to

check if a two-dimensional simulation converged to a solution produced by the corresponding three-dimensional simulation. It was found that as long as the aspect ratio of a three-dimensional simulation was below the limit $h/w < 4$, there was no difference in curves regarding θ_{AB} as a function of time between the two simulations. Therefore all of the simulations in this chapter were discretized in two dimensions unless otherwise noted. Three-dimensional solutions were required to study the effects of helical flow on these assays, as noted in chapter 5.5.

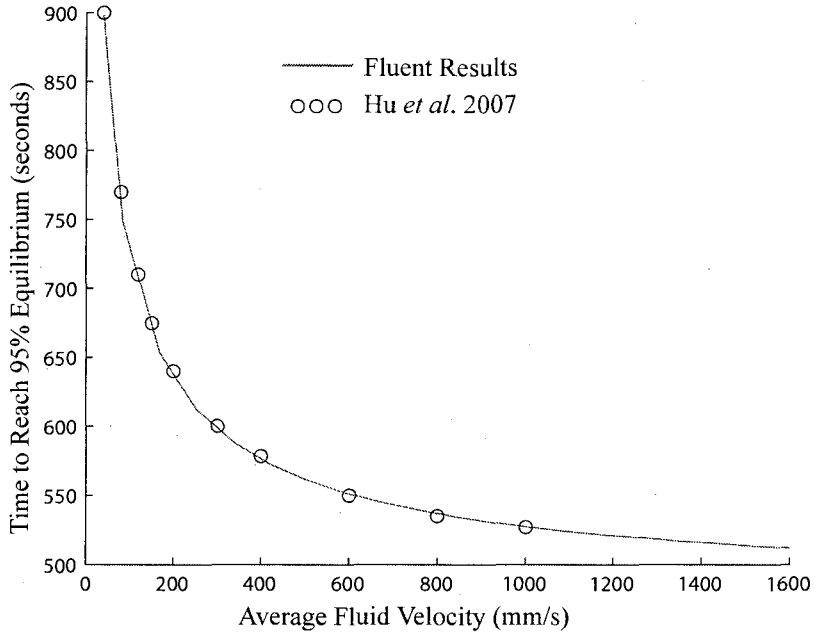

Figure 5.3. Verification of the numerical methods used in this study. These values pertain to electroosmotic flow over a reactive spot in a microchannel with h = 20 μm, l_s = 100 μm, $D = 10^{-11}$ m^2 s^{-1}, $k_1 = 10^5$ M^{-1} s^{-1}, $k_2 = 10^{-3}$ s^{-1}, and $C_{B,o} = 10^{-7}$ mol m^{-2}.

5.3.3 Parameter Space

In order to gain knowledge concerning the effects of convection and microchannel geometries of these microfluidic heterogeneous assays, parameters chosen for this study reflect those from experimental studies. Unless noted otherwise, the parameters used in this study are listed in table 5.1. Data involving the association and dissociation rate constant are typical of antigen binding to an immobilized antibody and are comparable to experimental values found in a variety of studies.[27, 36-38] Similarly, the values of the molecular diffusion coefficient, analyte concentration, and length of capture spot are typical of those seen in experimental studies at Colorado State University.[33] Although there is a substantial amount of data involving the quantification of capture probe density in experimental assays based on DNA and RNA hybridization, there is little to no information concerning the same data pertaining to immobilized antibodies or antigens, regardless of the methods of immobilization. The value of $C_{B,o} = 10^{-7}$ mol m^{-2} is expected to fall within the range of a typical immunoassay.

Parameter		Value
Association Rate Constant	k_1	10^{5} M^{-1} s^{-1}
Dissociation Rate Constant	k_2	10^{-3} s^{-1}
Capture Probe Density	$C_{B,o}$	10^{-7} mol m^{-2}
Analyte Inlet Concentration	C_A	10^{-7} M
Analyte Diffusion Coefficient	D	10^{-11} m^2 s^{-1}
Length of Capture Spot	w_s	25 μm

Table 5.1. Parameters used in this chapter.

5.4 Effect of the Mass Transfer Péclet Number on Assay

The most important parameter in these systems is the rate of convective fluid transport over the reactive spots, which is best described by the mass transfer Péclet number $Pe = \langle v_y \rangle h/D$, which relates the relative rate of axial convection to non-axial diffusion within the microchannel, where $\langle v_y \rangle$ is the average axial fluid velocity. Given a microchannel with a capture region described by the parameters l_s, D, k_1, k_2, and $C_{B,o}$, the system will exist in one of two states depending on the magnitude of $\langle v_y \rangle$. For sufficiently low rates of $\langle v_y \rangle$, the system is expected to exist in a mass transfer-limited regime, and times to reach equilibrium will be dictated by the geometries of the microchannel. In constrast, for sufficiently high rates of $\langle v_y \rangle$, the system is expected to exist in a reaction-limited regime, and times to reach equilibrium will be described by Eqn. (5.12) and have little dependence on the microchannel geometry.

Figure 5.4 displays the fractional coverage of the bound antigen/antibody complex as a function of time for two assays in a microchannel of height $h = 3$ μm with $\langle v_y \rangle = 200$ μm s^{-1} and $\langle v_y \rangle = 1$ μm s^{-1}. Using Eqn. (5.13), the equilibrium coverage is calculated to be $\theta_{AB,eq} = 0.91$, and the minimum time to reach 95% equilibrium is calculated to be $t_{eq,min}$ = 418 s using Eqn. (5.14). The large dependence of convective flow rate on these assays can be seen in Fig. 5.4, as the capture spots pertaining to the assay with a higher flow rate of $\langle v_y \rangle = 200$ μm s^{-1} reach an equilibrium state more than an order of magnitude faster than the assay with $\langle v_y \rangle = 1$ μm s^{-1}. For assays constrained by time, the difference between the two flow rates is significant. For example, at an assay time of $t = 418$ s, all four capture spots have fractional coverages greater than $\theta_{AB} > 0.8$ for the $\langle v_y \rangle = 200$ μm s^{-1} flow rate assay. On the other hand, only spot 1 in the $\langle v_y \rangle = 1$ μm s^{-1} flow rate assay has a significant amount of analyte coverage ($\theta_{AB} = 0.042$), whereas the remaining three spots have captured very little analyte ($\theta_{AB} < 0.01$). The results in Fig. 5.4 for the assay with $\langle v_y \rangle = 1.0$ μm s^{-1} suggest that nearly all of the analyte flowing over the first spot is

captured, as hybridization rates for spot 2 do not reach appreciable values until spot 1 is near equilibrium. This effect is highlighted in Fig. 5.5, which plots the normalized analyte concentration ($C_A/C_{A,o}$) averaged over planes of constant y-position situated just after each reactive spot (shown in Fig. 5.2). For the $\langle v_y \rangle$ = 1 μm s^{-1} assay, downstream reactive spots are subjected to analyte concentrations several orders of magnitude less than the upstream spot as long as the upstream spot is significantly below equilibrium. This effect is not seen in the assay with the higher flow rate, thus hybridization rates for all 4 spots in the $\langle v_y \rangle$ = 200 μm s^{-1} assay are similar, as seen in Fig. 5.4. The effect of analyte depletion on downstream capture spots is discussed in detail in section 5.4.

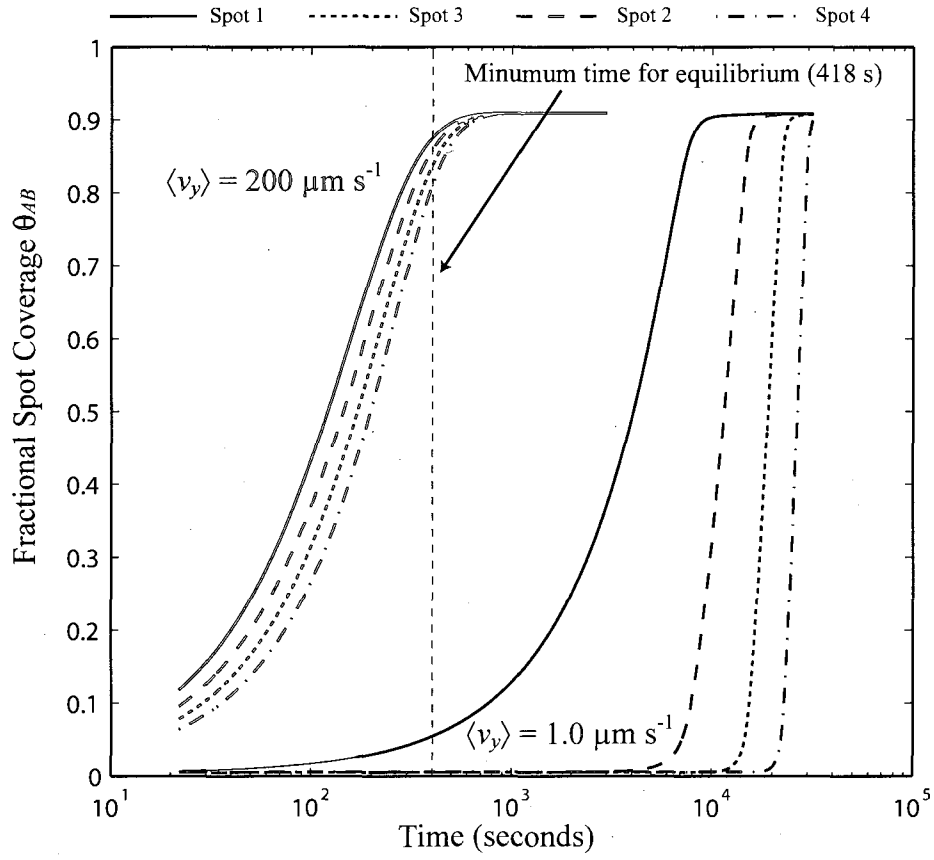

Figure 5.4. Fractional spot coverage θ_{AB} vs. time for two assays of different average flow rate in a microchannel with h = 3 μm.

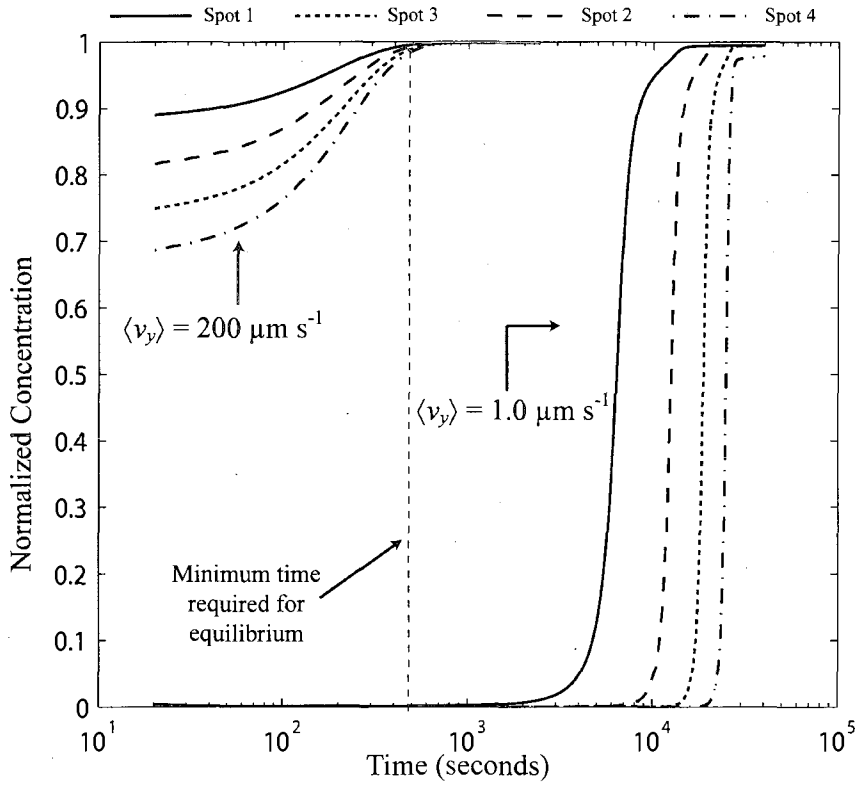

Figure 5.5. The normalized analyte concentration, averaged over planes of constant y-position situated immediately after each reactive spot, plotted as a function of time. This assay was simulated in a microchannel with $h = 3$ μm.

The results shown in Figs. 5.4 and 5.5 pertain to a microfluidic channel of height h = 3 μm situated above regions of immobilized capture bodies. These figures display the large dependence of the average fluid velocity above the capture spot on the fractional coverage θ_{AB} over the duration of several assays. To determine the effects of the fluid velocity on these heterogeneous affinity assays, a series of simulations similar to those shown in Figs. 5.4 and 5.5 were performed with the parameters listed in table 5.1 and varying fluid velocities ranging from 1-3500 μm s^{-1} and microchannel heights ranging from 2-20 μm. For each simulation, curves of θ_{AB} vs. t were used to calculate t_{eq}, the time for the assay to reach 95% of the equilibrium value determined by Eqn. (5.13). Figure 5.6 plots t_{eq} vs. $\langle v_y \rangle$ for spot 1 and 4 and a variety of microchannel heights.

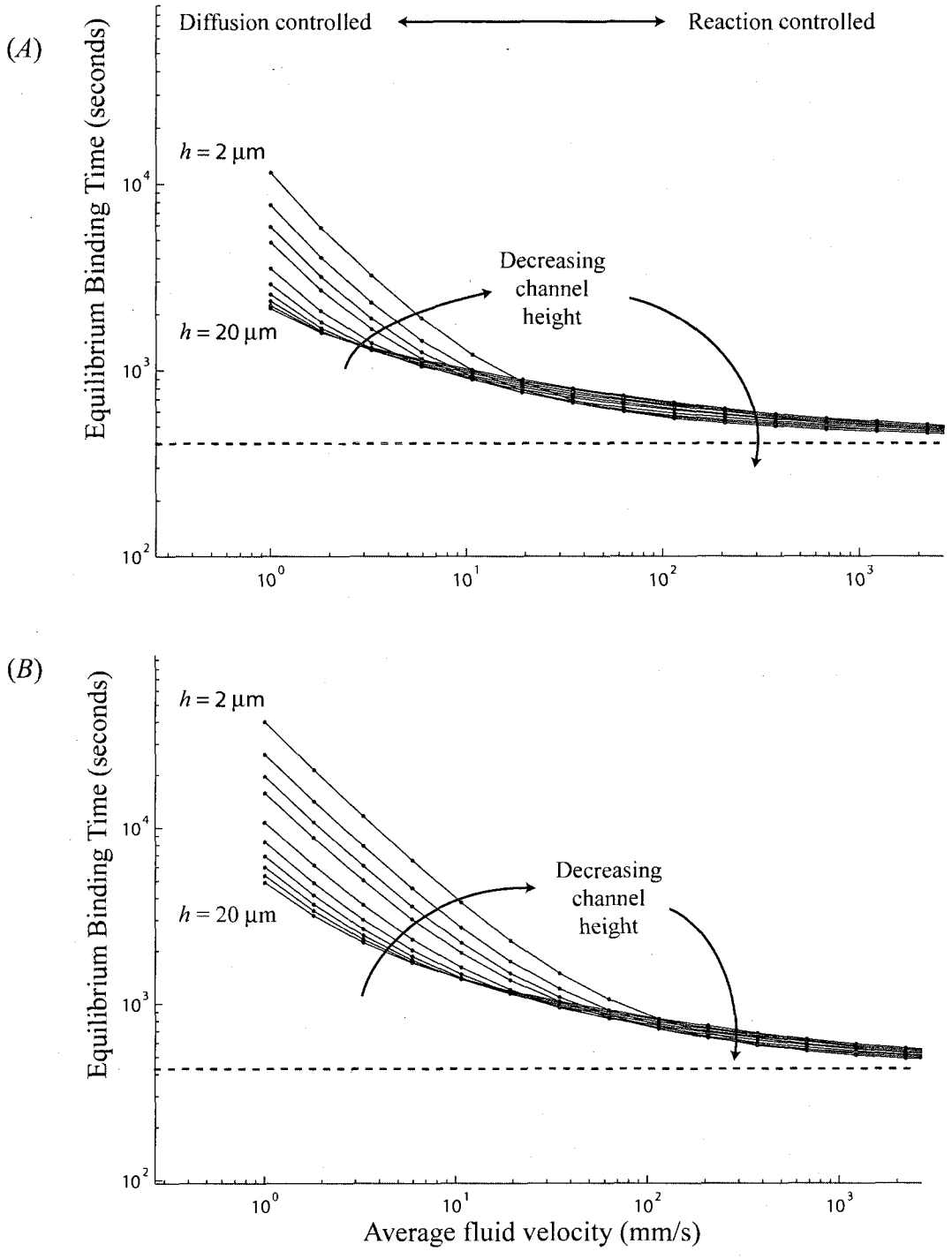

Figure 5.6. The time required to reach 95% equilibrium (t_{eq}) vs. the average fluid velocity for (*A*) spot 1 and (*B*) spot 4 (shown in Fig. 5.2). The simulation parameters are shown in table 5.1. The dashed line indicates $t_{eq,min}$. These simulations pertain to individual microchannel heights of h = 2, 3, 4, 5, 7.5, 10, 12.5, 15, 17.5, and 20 μm.

5.5 Effect of Microchannel Geometry on Assay

From the results shown in Fig. 5.6, it is clear that high fluid velocities are desirable in these heterogeneous affinity assays. In chapter 4, a method of passively creating steady state flows in microchannels is discussed, where the average fluid velocity can be accurately controlled by modification of the microchannel geometry. Specifically, the average fluid velocity can be increased dramatically by simply reducing the cross-sectional area of the microchannel. Prior to this study, the effects of the microchannel height on the assay performance were unknown, as all previous literature on the subject was constrained to microchannels of constant height.[27, 28, 31] Figure 5.6 displays the dependence of the microchannel height on these assays for the parameters listed in table 5.1. As expected, larger microchannels possess lower values of t_{eq} in the diffusion-controlled regime, as the overall cross-sectional area for diffusive flux is increased. The dependence of t_{eq} on the microchannel height in this regime is drastic; for example, at a flow rate corresponding to $\langle v_y \rangle = 1\ \mu m\ s^{-1}$, the times required to reach 95% equilibrium are $t_{eq} = 1.3$ h and $t_{eq} = 10.5$ h for the $h = 20\ \mu m$ and $h = 2\ \mu m$, respectively.

This dependence of t_{eq} on h is minimized as h becomes much larger than the size of the analyte concentration boundary layer at the downstream edge of each spot at a given value of $\langle v_y \rangle$. Interestingly, in the reaction-controlled regime this dependence is reversed as microchannels with smaller h have lower values of t_{eq}, albeit to a lesser degree when compared to the diffusion-controlled regime. For example, at a very high flow rate corresponding to $\langle v_y \rangle = 1000\ mm\ s^{-1}$, the times required to reach 95% equilibrium are $t_{eq} = 620$ s and $t_{eq} = 490$ s for the $h = 20\ \mu m$ and $h = 2\ \mu m$, respectively.

In these systems it is useful to know the overall efficiency of the capture spot to bind analyte from solution given specific assay conditions. We can calculate this efficiency by performing a mass balance on the analyte flowing past a single spot. We define the analyte utilization ξ as the ratio between the amount of analyte captured and the amount of analyte flowing past each reactive spot

$$\xi = \frac{\text{Analyte captured}}{\text{Analyte delivered}} = \frac{C_{A,o}t_{eq} - \int_0^{t_{eq}} C_A(t)dt}{C_{A,o}t_{eq}}. \quad \textbf{(5.15)}$$

Equation (5.15) is calculated by integrating the curves of $C_A = C_A(t)$ shown in Fig. 5.4 with respect to time until hybridization equilibrium is achieved. Using this definition, an assay that captures 100% of the available analyte would have a value of $\xi = 1$, whereas an assay that captures no analyte would have a value of $\xi = 0$. Figure 5.7 displays the analyte utilization as a function of $\langle v_y \rangle$ for the same assays shown in Fig. 5.6. As expected, ξ increases as $\langle v_y \rangle$ decreases due to the rates of convection approaching the rates of diffusion for analyte transport. In this case analyte within the entire cross-section of the microchannel is available to interact with the capture spots. Additionally, Fig. 5.7 displays the dependence of the analyte utilization on the microchannel geometry, where ξ increases as h decreases. This dependence is primarily due to the smaller distances required for diffusion of analyte to the capture spot as the microchannel height is reduced. High values of analyte utilization are very important to these assays when both sample volumes are limited and analyte concentrations are low. In this limiting case assays should be run at lower flow rates with small microchannels. For assays with varying inlet concentrations, we expect $\xi \propto \ln(C_{A,o})$ per the results of Zimmermann *et al.*[31]

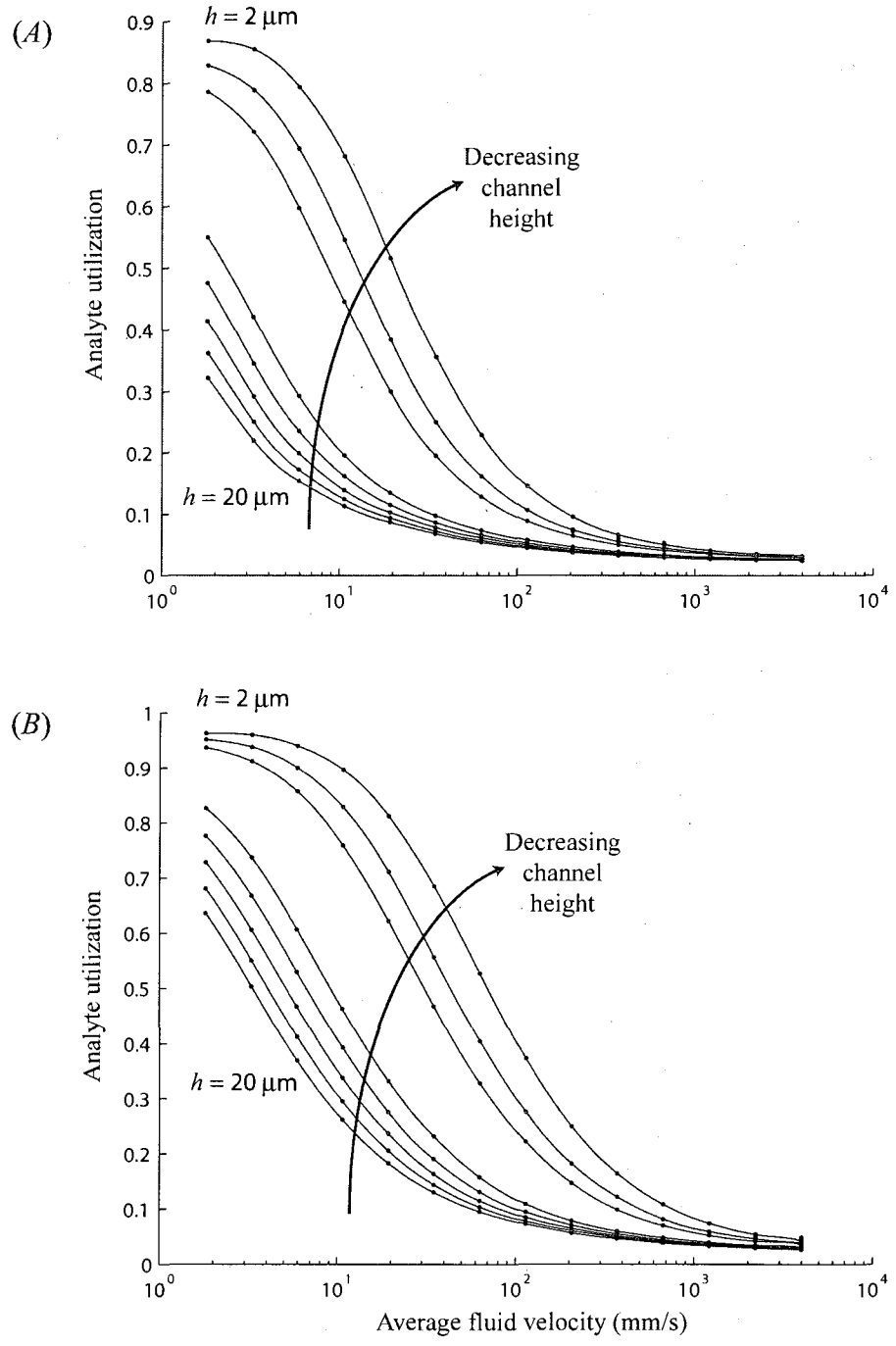

Figure 5.7. The analyte utilization (ξ) calculated as a function of the average fluid velocity for (*A*) spot 1 and (*B*) spot 4. The simulation parameters are shown in table 5.1. These simulations pertain to individual microchannel heights of h = 2, 3, 4, 10, 12.5, 15, 17.5, and 20 μm.

5.6 Effect of Helical Flow on Assay

Figures 5.5 and 5.6 highlight the problems associated with multiple sensing regions situated downstream from one another. As mentioned before, the creation of an analyte concentration boundary layer by the first reactive spot serves to deplete the overall concentration of analyte that the downstream spots are able to interact with. An example of an analyte concentration boundary layer typical of these systems with multiple reactive spots can be seen in Fig. 5.8. Figure 5.8*A* displays two-dimensional analyte concentration contours for a system with 4 reactive spots in a microchannel with $h = 30$ μm, $\langle v_y \rangle = 200$ μm s^{-1}, and the parameters listed in table 5.1. A progressive reduction in the analyte concentration gradients can be seen after each reactive spot, resulting in reduced magnitudes of analyte flux towards the downstream reactive spots. Therefore each downstream capture spot requires a longer time to reach hybridization equilibrium and furthermore, fractional coverages for each capture spot in time-restricted assays will be non-uniform. Figure 5.8*B* displays an experimental example of signal variance in time-restricted heterogeneous assays. This example, taken with permission from Murphy *et al.*,[33] pertains to a multi-analyte heterogeneous micromosaic competitive immunoassay performed in a manner similar to that shown in Fig. 5.1. The 2nd dimension of this assay was performed with a series of parallel microchannels situated vertically with respect to the experimental image, where the flow direction was from top to bottom. Artifacts resulting from the induced analyte depletion layer can be seen in several of the micromosaic capture regions in the lower right. For illustration purposes, an assay performed in a single microchannel is compared to a three-dimensional simulation of a time-restricted assay with $h = 30$ μm, $\langle v_y \rangle = 200$ μm s^{-1}, and $C_{A,o} = 10^{-9}$ M at an assay time of $t = 300$ s. Although the parameters pertaining to the assays performed by Murphy *et al.* are certainly different than those used in the simulation, there is a high degree in similarity regarding the qualitative comparison of the fractional coverage contours for the experimental vs. simulation cases.

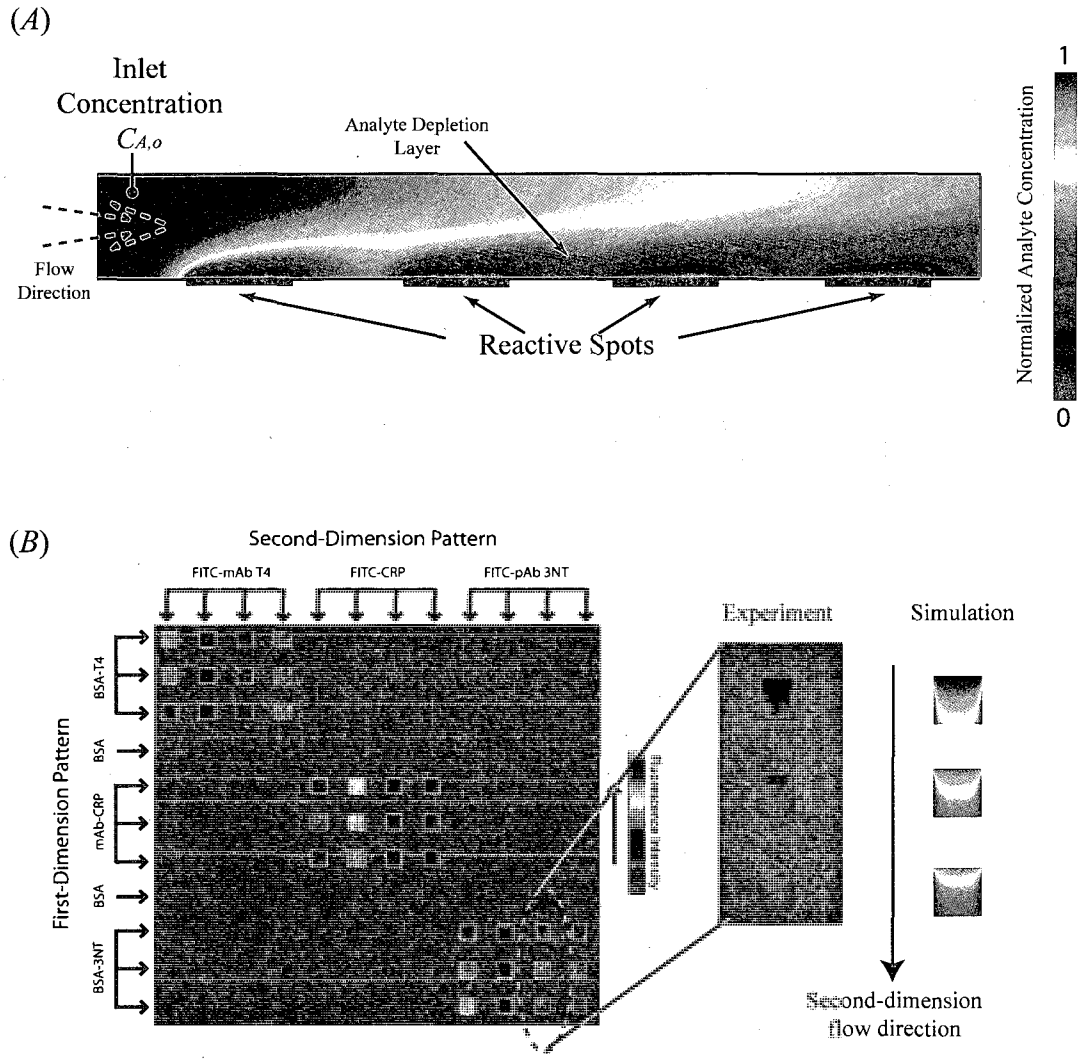

Figure 5.9. (*A*) Two-dimensional contours for the normalized analyte concentration ($C_A/C_{A,o}$) for an assay in a microchannel with h = 30 μm. (*B*) Experimental fluorescence image of a multi-analyte mosaic competitive immunoassay performed by Murphy *et al.*[33] The flow in the 2nd dimension is from top to bottom. Larger fluorescence intensities correspond to a higher fractional coverage of the bound antigen/antibody complex. There are several instances of the effects of an analyte depletion layer, of which one is highlighted to the right. The simulation pertained to an assay in a three-dimensional microchannel with h = 30 μm and $C_{A,o} = 10^{-9}$ M. Both figures used the parameters shown in table 5.1.

Although there has been a great deal of focus on the creation of different mixing strategies for microfluidic devices, there has been very little integration microfluidic mixing strategies applied to lab-on-a-chip systems other than the mixing of two fluid streams.[39-41] Several groups have investigated the use of oblique grooves situated on the top of a microchannel for use in heterogeneous microfluidic immunoassays. Pressure driven flow over the grooves induces helical flow within the microchannel in a manner such as to replenish analyte delivery to a reactive surface on the microchannel floor.[42-44] In another study, researchers used a microfluidic serpentine channel (capable of producing Lagrangian chaotic flow) situated on top of a reactive surface in order to improve analyte flux.[45] The inclusion of microfluidic mixing with these immunoassay devices improved the output signal for a variety of assay condtions; however, each study was conducted over a continuous reactive surface with $l_s/h \gg 1$ in microchannels with aspect ratios $h/w \approx 0.5$; therefore, it is unknown if these mixing devices would benefit assays pertinent to this study.

By placing these immunoassays in microfluidic channels imbedded with slanted grooves we hope to improve the response of the multi-spot time-restricted assays detailed above. The details of the creation and optimization of helical flow with slanted grooves can be found in chapter 2. Optimizing the geometry of the grooves for a microchannel situated above several reactive zones might create helical flow with a magnitude such that downstream capture spots are presented with a higher analyte concentration. Figure 2.8 highlights the efficiency of optimized grooves to induce high magnitudes of helical flow. To test the possible efficiency of such a device, three-dimensional flow of helical flow over reactive spots were simulated with a variety of groove designs and flow rates.

Figure 5.10 displays the fractional coverage of an assay simulated under three-dimensional helical flow with the parameters listed in table 5.1, $\langle v_y \rangle$ = 200 μm s^{-1}, and an assay time of t = 300 s. The microchannel had optimized groove geometries of $b/w = 0.15$, $a/w = 0.6$, $d/h = 1$, and $h/w = 0.271$ with a channel width of w = 74 μm

and reactive spot length l_s = 40 μm. From figure 5.10 it can be seen that the overall fractional coverage θ_{AB} has a different pattern with respect to the contours shown in Fig. 5.9, where the highest coverage follows the shape of the fluid streamlines in the mixer. Although these patterns are qualitatively different, there remain artifacts from the analyte depletion layers existing on the downstream capture spots. Even though the groove depth ratio is very large (with respect to the geometries studied in chapter 2), the relatively high magnitude of helical flow has little effect on the overall hybridization rates for the downstream spots. The simulation shown in figure 5.10 displayed values of $\theta_{AB}(t)$ that varied by less than 5% from the corresponding two-dimensional simulation (h = 20 μm, l_s = 40 μm) for the entire range of average fluid velocities studied (15 simulations, $1 \leq \langle v_y \rangle \leq 3500$ μm s^{-1}). This lack of assay improvement was also seen in all groove geometries (4 simulations) and groove styles (e.g. slanted, herringbone, v-shaped) simulated in this study. For these systems, the most important parameter to reduce variability between the fractional coverages of different capture spots is the average fluid velocity through a system. The next section details the design of microchannels using the passive pumping methods discussed in chapter 4 to increase $\langle v_y \rangle$ such that this capture spot variance is minimized.

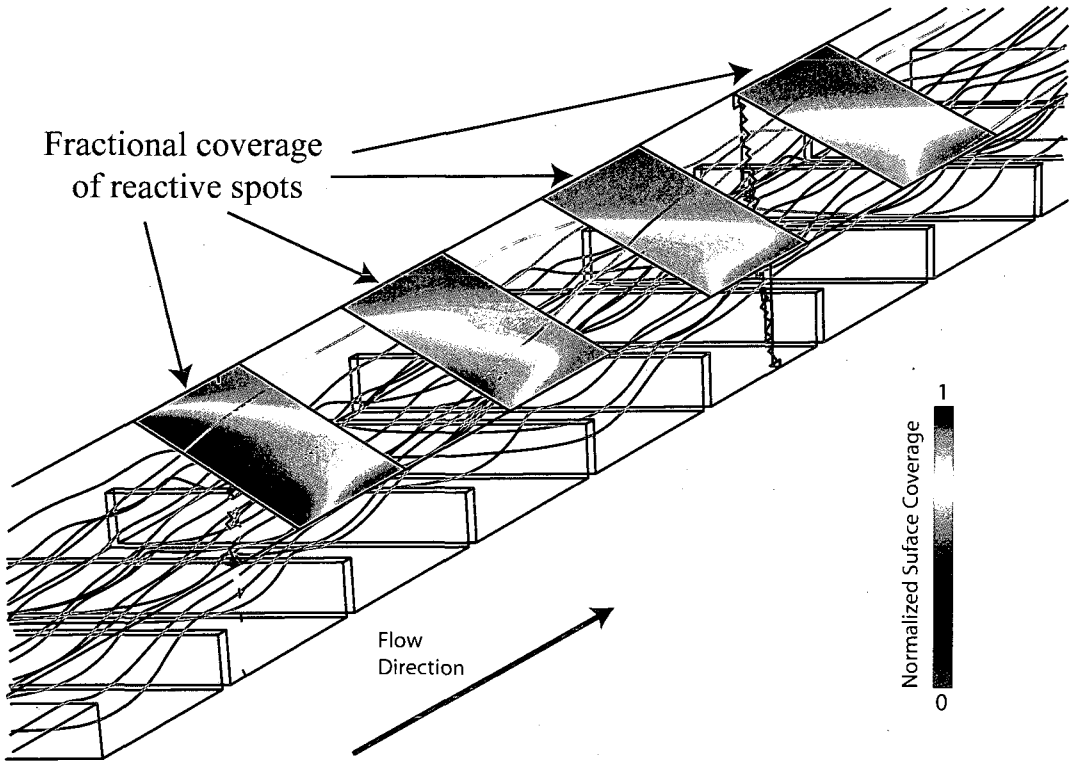

Figure 5.10. Assay simulated under three-dimensional flow. Note the shift in overall fractional coverage with respect to Fig. 5.9.

5.7 Affinity Assay Using a Passive Pumping Method

Figures 5.5 and 5.6 highlight the effects of the convective flow rates and microchannel geometries on heterogeneous affinity assays. The assays shown in these figures carried the assumption that individual assays can be performed at a flow rate independent of the microchannel geometry. This independence is true for systems using active means of fluid pumping, such as a syringe pump; however, for passive pumping systems the flow rate in a given system is a function of the microchannel geometry. Chapter 4 details a passive pumping mechanism that uses the coupled effects of capillary forces and evaporation effects to pump fluids through microchannels at controlled rates. In these systems the flow rate is a function of the microchannel geometry, as seen in Fig. 4.19. Therefore, it will be useful to couple the computational methods of chapter 4 to those shown in this chapter to predict the behavior of time-restricted assays occuring in microchannels of varying height.

To predict an assay response to changes in microchannel height, we utilize the methods detailed in chapter 4 to predict the volumetric flow rate as a function of microchannel geometry for a microchannel with w = 50 μm and length L = 4 cm connected to an outlet reservoir with lower diameter D_1 = 1.4 mm, upper diameter D_2 = 0.9 mm, and height H = 1.4 mm. These dimensions are typical of those used in experiment.[33] For an assay conducted at a temperature of T = 25 °C and relative humidity of 25%, the predicted steady state fluid velocities are shown as a function of the microchannel height within the inset of Figure 5.11. It can be seen that there a significant increase in $\langle v_y \rangle$ as h decreases, where for example $\langle v_y \rangle$ increases from 150 μm s^{-1} to 960 μm s^{-1} as the channel height is reduced from 20 μm to 2 μm. Using these values, the response of the assay can be predicted as a function of channel height. Figure 5.11 displays the predicted fractional coverage vs. the microchannel height for time-restricted assays of t = 300 s. For both reactive spots 1 and 4, there is a clear increase in fractional coverage as the channel height is reduced. More importantly, the difference in fractional

coverage between the spots is reduced substantially with smaller microchannels; for example, with a $h = 20$ μm channel there is a 17% decrease in fractional coverage from spot 1 to spot 4 (0.735 to 0.606), whereas for the $h = 2$ μm channel there is only a 3% difference (0.854 to 0.828). Futhermore, microchannels with smaller h provide reductions in the overall sample consumption. For the results in Fig. 5.11, the $h = 20$ μm assay possessed a volumetric flow rate of $Q_f = 0.13$ μL min^{-1}, whereas the $h = 2$ μm possessed a volumetric flow rate of only $Q_f = 0.08$ μL min^{-1}.

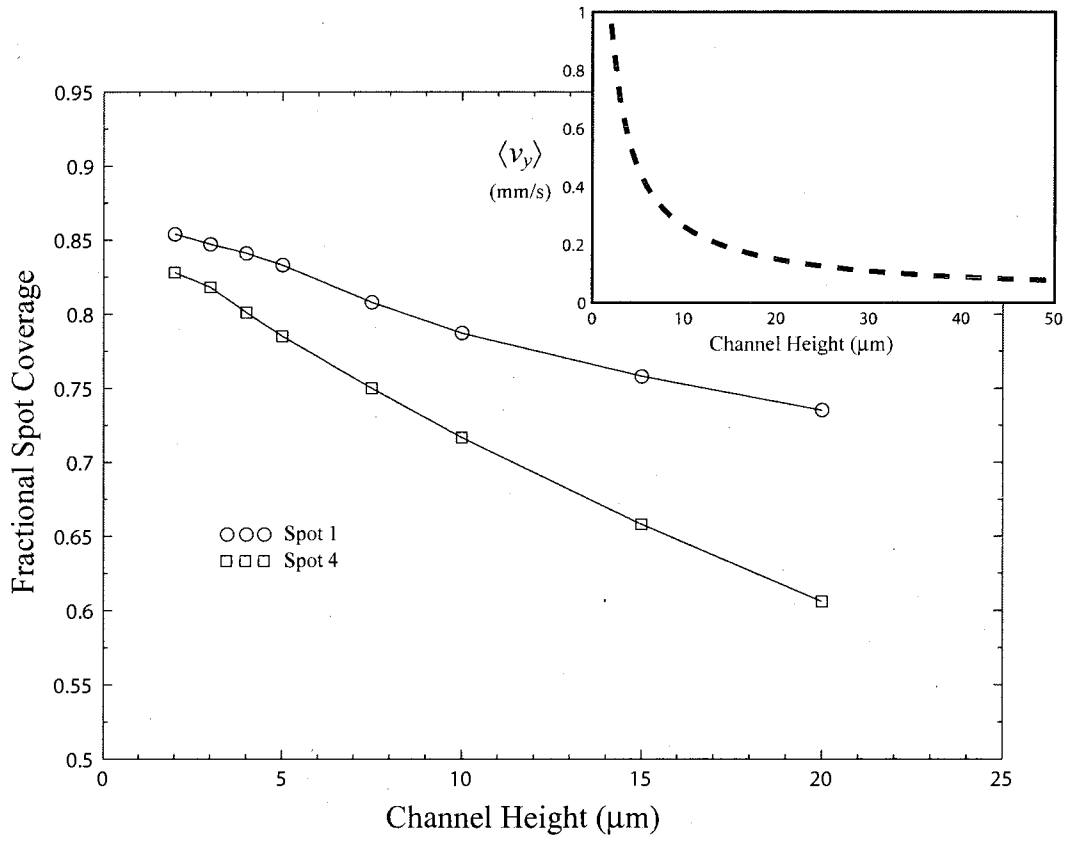

Figure 5.11. Computed fractional spot coverage (θ_{AB}) vs. microchannel height (h) for a 5 minute assay performed in a microchannel with $w = 50$ μm, $L = 4$ cm, connected to an outlet reservoir with height $H = 2.0$ mm, lower diameter $D_1 = 0.9$ mm, and upper diameter $D_2 = 1.4$ mm. The assay would be conducted at temperature $T = 25$ °C and 25% relative humidity. *Inset.* The average fluid velocity in this microchannel is calculated as a function of a microchannel height.

5.8 Conclusions

The results displayed in Figs. 5.6, 5.7, and 5.11 highlight the benefits of using microchannels with reduced characteristic dimensions for use in heterogeneous affinity assays. These benefits include (*i*) increased signal for time-restricted assays, (*ii*) reduced times required for hybridization equilibrium, (*iv*) reduced signal variance between multiple capture regions, and (iv) reduced sample consumption. In these systems, the introduction of passive non-axial flows through grooved microchannels provides only small assay enhancements, and should not be considered in experimental studies. We have shown that the most effective method to enhance analyte flux to the immobilized capture spots is through increasing $\langle v_y \rangle$ to the highest levels allowed by experiment.

In the passive pumping methods described in chapter 4, the average fluid velocity can be significantly increased through reducing the overall dimensions of the microchannel situated over the capture regions. When this pumping method is applied to these assays, the assay is significantly enhanced when the overall size of the channel is reduced, as seen in Fig. 5.11. This strategy can be used to alleviate the signal differences for multiple capture spots seen in experimental systems. When performing these assays with microchannels of very small *h,* experimental protocols must be examined to account for several potential sources of error.

When performing time-restricted assays, care must be taken that all microchannels are under convective conditions for the same amount of time. This becomes apparent when examining Fig. 5.4. Assays performed in the reaction-controlled regime collect material according to Eqn. (5.12). In the preliminary stages of an assay, the fractional coverage will exist in the range of $\theta_{AB} < 0.5$ and the hybridization rates will be substantially higher than those seen later in the assay. In this situation the fractional coverage for each spot is very sensitive to the assay time. Experimentally, these assays are generally performed with more than 8 microchannels with separate inlet reservoirs (2^{nd} dimension flow). The assay is initialized by the introduction of the analyte solution

to each reservoir via pipette and finalized by peeling off the μFN and quickly rinsing with buffer. Using these methods, it is common for the outer microchannels to vary in assay time by more than 30 s. For an assay in a microchannel with h = 10 μm, $\langle v_y \rangle$ = 200 μm s^{-1}, and the parameters shown in table 5.1, the fractional coverage of spot 1 for t = 120 s and t = 150 s is θ_{AB} = 0.36 and θ_{AB} = 0.43, a 19% difference.

When performing these assays with microchannels of h < 5 μm, extra care must be taken as to avoid the introduction of particulate matter into the channel. In the best case scenario, the particulate matter will increase the overall viscous resistance K of the microchannel resulting in flows with significantly lower values of $\langle v_y \rangle$. In the worst case scenario, particulate matter can eliminate convective flow in the microchannel, resulting in a static immunoassay and a significant reduction in hybridization rates.

5.9 Future work

5.9.1 Identification of the Important Dimensionless Products

Previous work. Figure 5.6 highlights the behavior of these heterogeneous assays under different operating conditions. For these assays there is a critical linear velocity v_c where the system undergoes a transition from a diffusion-limited to a reaction-limited regime. At flow rates of $\langle v_y \rangle \gg v_c$, the system responds as if it were well mixed and times to reach equilibrium tend towards $t_{eq,min}$. At flow rates of $\langle v_y \rangle \ll v_c$, the system becomes reliant on one-dimensional diffusion along the channel axis and t_{eq} increases by more than an order of magnitude from $t_{eq,min}$. In this situation ($\langle v_y \rangle \rightarrow 0$), the times required for equilibrium will asymptote towards a maximum value dictated by D, l_s, h, and $C_{A,o}$, where for all of the cases shown in Fig. 5.6, t_{eq} is in excess of 20 hours. These extended assay times present several difficulties concerning the computational methods used here, and it was decided to focus on flow rates pertaining to $\langle v_y \rangle$ > 1 μm s^{-1}. This restriction of parameter space is justified due to the difficulties present in obtaining a static flow field

for microfluidic systems composed of PDMS, as evaporative and permeation effects will induce fluid velocities in excess of 1 μm s^{-1} for the channel dimensions studied here.[46]

A first order estimate for v_c can be found via dimensional analysis of the system. There are 7 important independent variables associated with a two-dimensional heterogeneous assay, listed here as $\langle v_y \rangle$, k_1, D, $C_{A,o}$, $C_{B,o}$, h, and l_s. Note that we have disregarded the dissociation reaction constant k_2 as being unimportant, as we are only interested in the forward step of the ligand-receptor model. Using the Buckingham π-theorem, there will be four independent dimensionless products that describe the relationships between these variables. The first two dimensionless numbers can be obtained from non-dimensionalizing Eqns. (5.4) and (5.7) by using the following non-dimensional parameters

$$\bar{t} = \frac{\langle v_y \rangle t}{h},\ \overline{\nabla} = h\nabla,\ \overline{\nabla}^2 = h^2\nabla^2,\ \overline{\mathbf{v}} = \frac{\mathbf{v}}{\langle v_y \rangle},\ \overline{C}_A = \frac{C_A}{C_{A,o}},\ \overline{C}_B = \frac{C_B}{C_{B,o}},\ \overline{C}_{AB} = \frac{C_{AB}}{C_{B,o}}. \quad \textbf{(5.16)}$$

Substitution of these parameters into Eqn. (5.4) yields

$$Pe_m\left(\frac{\partial \overline{C}_A}{\partial \bar{t}} + \overline{\mathbf{v}} \cdot \overline{\nabla}\overline{C}_A\right) = \nabla^2 \overline{C}_A, \quad \textbf{(5.17)}$$

where $Pe_m = \langle v_y \rangle h / D$ is the mass-transfer Péclet number. Similarly, substitution of the parameters in Eqn. (5.16) into Eqn. (5.7) yields

$$\overline{\nabla}\overline{C}_A = Da_1 \overline{C}_A \overline{C}_B - Da_2 \overline{C}_{AB}, \quad \textbf{(5.18)}$$

where $Da_1 = k_1 h C_{b,o} / D$ and $Da_2 = k_2 C_{B,o} h / D C_{A,o}$ are the two Damköhler numbers related to these assays. As mentioned above, we choose Da_1 to be the important dimensionless product. Here we have chosen h, rather than l_s, as the important characteristic length scale pertinent to these systems. A third dimensionless product $\alpha = l_s / h$ can be chosen as the ratio of these two length scales. For the forth dimensionless

product, we choose $\beta = C_{A,o}h/C_{B,o}$. Provided that the correct choices were made concerning these important dimensionless products, two systems with different dimensional variables will exhibit similar behavior if they possess the same values of Pe_m, Da_1, α, and β. Unfortunately, this is not the case for the four dimensionless products we have chosen here. Figure 5.12 displays the dimensionless equilibrium binding time $\bar{t}_{eq} = Dt_{eq}/h^2$ as a function of the mass-transfer Péclet number (for spots 1-4) for systems with $Da_1 = 20$, $\alpha = 1$, and $\beta = 0.02$. In this case we choose a dimensionless time of $\bar{t} = h^2/D$. Although both simulations exhibit the same qualitative behavior, there is a clear difference in $\bar{t}_{eq}$ for the two simulations. This difference in behavior also exists when the equilibrium binding time is non-dimensionalized such that $\bar{t}_{eq} = t\langle v_y \rangle / h$.

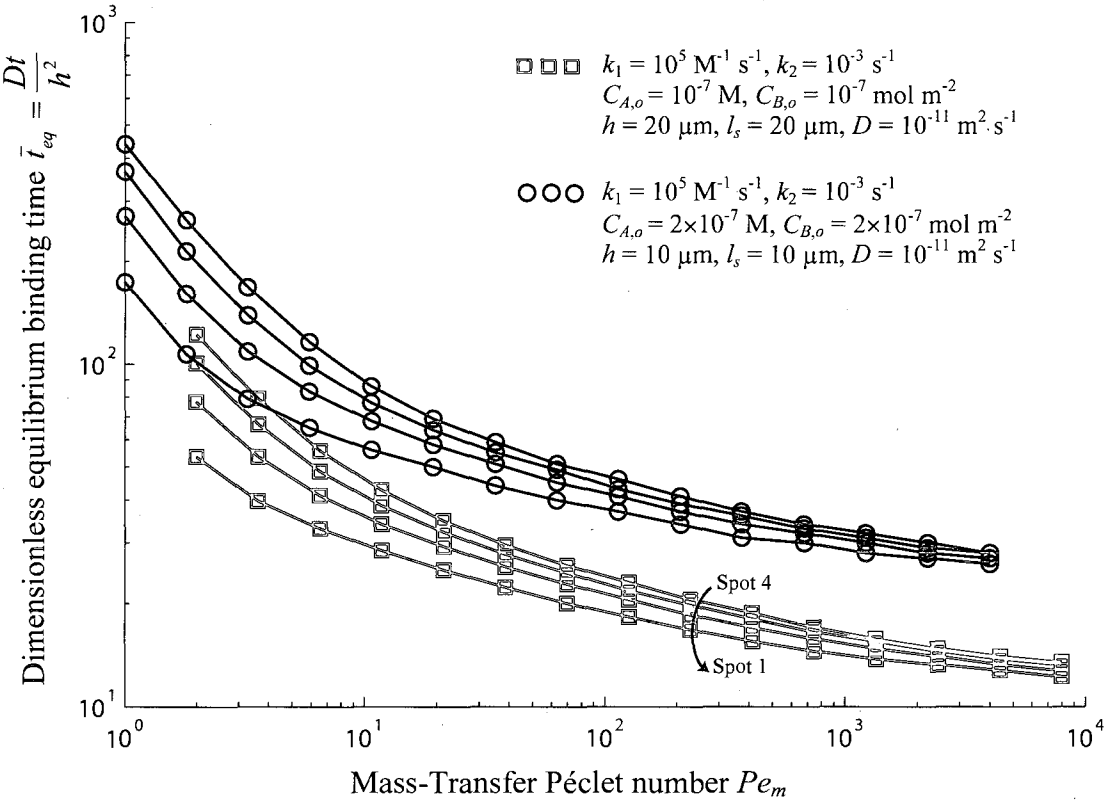

Figure 5.12. Non-dimensional behavior of the heterogeneous affinity assays in these systems. Both simulations pertain to $Da_1 = 20$, $\alpha = 1$, and $\beta = 0.02$.

Future work. After the completion of the work shown above, a similar study by Squires *et al.* addressed the non-dimensional behavior of the same heterogeneous affinity assays.[47] Although this study was fairly restricted in its computational nature, they provide a concise effort towards defining the important dimensionless products of these systems. The authors demonstrate that for conditions pertaining to $Pe_m \gg \alpha$, a system will exist in the reaction-controlled regime. By using an analysis similar to the classic Lévêque problem, they also show that the system is well represented by a 2nd mass-transfer Péclet number Pe_s, where for conditions such that $Pe_s = 6\alpha^2 Pe_m \gg 1$ the analyte concentration boundary layer thickness δ will exist such that $\delta \ll h$, a condition that ensures the system will exist in a reaction-controlled regime. The authors also provide a Damköhler number $Da_3 = k_1 C_{B,o}/DF$, where F is the dimensionless flux function $F = F(Pe_s)$. A functional form of F is given for only a limited number of operational regimes.

The computational methods within this chapter can be used to find functional relationships of F vs. Pe_s for the remaining 2 operating regimes noted by Squires *et al.* Futhermore, these computational methods can prove valuable in identification of the boundaries between operational regimes, easily identified with a phase diagram plotting α vs. Pe_m. A complete set of dimensionless products with the ability to properly describe the time-dependent characteristics of these assays has yet to be found. This might be possible, however, given enough time utilizing a large scale computational effort combined with the results of Squires *et al.*

5.9.2 Effect of Viscous Shear on the Assay

In section 5.7 we discuss the benefits of reducing the overall height of a microchannel used for these heterogeneous immunoassays. For a channel with dimensions such that $h/w \ll 1$, the shear rate at the capture spot surface is $\gamma = 6\langle v_y \rangle / h$. For systems using the passive pumping mechanism detailed in chapter 4, a reduction in microchannel height

creates a significant increase in $\langle v_y \rangle$, displayed in the inset to Fig. 5.11. From the results of chapter 4, microchannels with dimensions h = 5 μm, w = 20 μm, and length L = 20 mm connected to large outlet reservoirs can produce fluid velocities of $\langle v_y \rangle > 8$ mm s^{-1}. In these systems the shear rate above the capture spot can exceed 10,000 s^{-1}, which is much larger than all experimental heterogeneous immunoassays surveyed in the literature. To our knowledge, the effects of high shear rates on the kinetics of a heterogeneous immunoassay on a planar substrate are unknown. As the overall size of immobilized bound complex increases, it is possible the forces induced by the viscous shear can exceed the forces involved in an affinity reaction. Therefore performing assays within small microchannels might limit the equilibrium coverage given in Eqn. (5.13).

The passive pumping mechanism detailed in chapter 4 provides a large scale approach to the creation of parallel microchannels with varying shear rates. These pumping methods combined with the experimental methods of Murphy *et al.* might prove valuable in the determination of the effects of viscous shear on heterogeneous immunoassays. With an appropriate μFN design, experimental immunoassays with shear rates ranging several orders of magnitudes could be studied in a single experiment.

5.10 References

1. R. S. Yalow and S. A. Berson, (1959) Assay of Plasma Insulin in Human Subjects by Immunological Methods *Nature*, **184**, 1648-1649.
2. R. Ekins, F. Chu and E. Biggart, (1989) Development of Microspot Multi-Analyte Ratiometric Immunoassay Using Dual Fluorescent-Labeled Antibodies *Analytica Chimica Acta*, **227**, 73-96.
3. M. Schena, D. Shalon, R. W. Davis and P. O. Brown, (1995) Quantitative Monitoring of Gene-Expression Patterns with a Complementary-DNA Microarray *Science*, **270**, 467-470.
4. R. Plomin and L. C. Schalkwyk, (2007) Microarrays *Developmental Science*, **10**, 19-23.
5. R. B. Stoughton, (2005) Applications of DNA microarrays in biology *Annual Review of Biochemistry*, **74**, 53-82.
6. E. Kopf and D. Zharhary, (2007) Antibody arrays - An emerging tool in cancer proteomics *International Journal of Biochemistry & Cell Biology*, **39**, 1305-1317.
7. R. L. Camp, V. Neumeister and D. L. Rimm, (2008) A Decade of Tissue Microarrays: Progress in the Discovery and Validation of Cancer Biomarkers *Journal of Clinical Oncology*, **26**, 5630-5637.
8. P. Wu, D. G. Castner and D. W. Grainger, (2008) Diagnostic devices as biomaterials: a review of nucleic acid and protein microarray surface performance issues *Journal of Biomaterials Science-Polymer Edition*, **19**, 725-753.
9. C. L. Yauk, M. L. Berndt, A. Williams and G. R. Douglas, (2004) Comprehensive comparison of six microarray technologies *Nucleic Acids Research*, **32**, -.
10. G. Bhanot, Y. Louzoun, J. H. Zhu and C. DeLisi, (2003) The importance of thermodynamic equilibrium for high throughput gene expression arrays *Biophysical Journal*, **84**, 124-135.
11. S. Sjolander and C. Urbaniczky, (1991) Integrated Fluid Handling-System for Biomolecular Interaction Analysis *Analytical Chemistry*, **63**, 2338-2345.
12. R. Lenigk, R. H. Liu, M. Athavale, Z. J. Chen, D. Ganser, J. N. Yang, C. Rauch, Y. J. Liu, B. Chan, H. N. Yu, M. Ray, R. Marrero and P. Grodzinski, (2002) Plastic biochannel hybridization devices: a new concept for microfluidic DNA arrays *Analytical Biochemistry*, **311**, 40-49.
13. M. Noerholm, H. Bruus, M. H. Jakobsen, P. Telleman and N. B. Ramsing, (2004) Polymer microfluidic chip for online monitoring of microarray hybridizations *Lab on a Chip*, **4**, 28-37.
14. C. Peter, M. Meusel, F. Grawe, A. Katerkamp, K. Cammann and T. Borchers, (2001) Optical DNA-sensor chip for real-time detection of hybridization events *Fresenius Journal of Analytical Chemistry*, **371**, 120-127.
15. Y. Wang, B. Vaidya, H. D. Farquar, W. Stryjewski, R. P. Hammer, R. L. McCarley, S. A. Soper, Y. W. Cheng and F. Barany, (2003) Microarrays assembled in microfluidic chips fabricated from poly(methyl methacrylate) for the detection of low-abundant DNA mutations *Analytical Chemistry*, **75**, 1130-1140.

16. E. Delamarche, A. Bernard, H. Schmid, B. Michel and H. Biebuyck, (1997) Patterned delivery of immunoglobulins to surfaces using microfluidic networks *Science*, **276**, 779-781.
17. G. J. Wegner, A. W. Wark, H. J. Lee, E. Codner, T. Saeki, S. P. Fang and R. M. Corn, (2004) Real-time surface plasmon resonance imaging measurements for the multiplexed determination of protein adsorption/desorption kinetics and surface enzymatic reactions on peptide microarrays *Analytical Chemistry*, **76**, 5677-5684.
18. F. S. Ligler, M. Breimer, J. P. Golden, D. A. Nivens, J. P. Dodson, T. M. Green, D. P. Haders and O. A. Sadik, (2002) Integrating waveguide biosensor *Analytical Chemistry*, **74**, 713-719.
19. B. P. Nelson, T. E. Grimsrud, M. R. Liles, R. M. Goodman and R. M. Corn, (2001) Surface plasmon resonance imaging measurements of DNA and RNA hybridization adsorption onto DNA microarrays *Analytical Chemistry*, **73**, 1-7.
20. A. Bernard, B. Michel and E. Delamarche, (2001) Micromosaic immunoassays *Analytical Chemistry*, **73**, 8-12.
21. J. B. Delehanty and F. S. Ligler, (2002) A microarray immunoassay for simultaneous detection of proteins and bacteria *Analytical Chemistry*, **74**, 5681-5687.
22. M. Wolf, D. Juncker, B. Michel, P. Hunziker and E. Delamarche, (2004) Simultaneous detection of C-reactive protein and other cardiac markers in human plasma using micromosaic immunoassays and self-regulating microfluidic networks *Biosensors & Bioelectronics*, **19**, 1193-1202.
23. A. Szabo, L. Stolz and R. Granzow, (1995) Surface-Plasmon Resonance and Its Use in Biomolecular Interaction Analysis (Bia) *Current Opinion in Structural Biology*, **5**, 699-705.
24. J. Jenkins, B. Prabhakarpandian, K. Lenghaus, J. Hickman and S. Sundaram, (2004) Fluidics-resolved estimation of protein adsorption kinetics in a biomicrofluidic system *Analytical Biochemistry*, **331**, 207-215.
25. D. G. Myszka, X. He, M. Dembo, T. A. Morton and B. Goldstein, (1998) Extending the range of rate constants available from BIACORE: Interpreting mass transport-influenced binding data *Biophysical Journal*, **75**, 583-594.
26. L. Tang, H. J. Kwon and K. A. Kang, (2004) Theoretical and experimental analysis of analyte transport in a fiber-optic, Protein C immuno-biosensor *Biotechnology and Bioengineering*, **88**, 869-879.
27. R. A. Vijayendran, F. S. Ligler and D. E. Leckband, (1999) A computational reaction-diffusion model for the analysis of transport-limited kinetics *Analytical Chemistry*, **71**, 5405-5412.
28. J. Bishop, S. Blair and A. Chagovetz, (2007) Convective flow effects on DNA biosensors *Biosensors & Bioelectronics*, **22**, 2192-2198.
29. G. Q. Hu, Y. L. Gao and D. Q. Li, (2007) Modeling micropatterned antigen-antibody binding kinetics in a microfluidic chip *Biosensors & Bioelectronics*, **22**, 1403-1409.
30. H. Parsa, C. D. Chin, P. Mongkolwisetwara, B. W. Lee, J. J. Wang and S. K. Sia, (2008) Effect of volume- and time-based constraints on capture of analytes in microfluidic heterogeneous immunoassays *Lab on a Chip*, **8**, 2062-2070.

31. M. Zimmermann, E. Delamarche, M. Wolf and P. Hunziker, (2005) Modeling and optimization of high-sensitivity, low-volume microfluidic-based surface immunoassays *Biomedical Microdevices*, **7**, 99-110.
32. B. M. Murphy, D. S. Dandy and C. S. Henry, (2009) Analysis of oxidative stress biomarkers using a simultaneous competitive/non-competitive micromosaic immunoassay *Analytica Chimica Acta*, **640**, 1-6.
33. B. M. Murphy, X. Y. He, D. Dandy and C. S. Henry, (2008) Competitive immunoassays for simultaneous detection of metabolites and proteins using micromosaic patterning *Analytical Chemistry*, **80**, 444-450.
34. R. Yan, S. P. Mestas, G. Yuan, R. Safaisini, D. S. Dandy and K. L. Lear, (2009) Label-free silicon photonic biosensor system with integrated detector array *Lab on a Chip*.
35. L. A. Belfiore and NetLibrary Inc., *Transport phenomena for chemical reactor design*, J. Wiley, Hoboken, N.J., 2003.
36. T. Kashiwakuma, A. Hasegawa, T. Kajita, A. Takata, H. Mori, Y. Ohta, E. Tanaka, K. Kiyosawa, T. Tanaka, S. Tanaka, N. Hattori and M. Kohara, (1996) Detection of hepatitis C virus specific core protein in serum of patients by a sensitive fluorescence enzyme immunoassay (FEIA) *Journal of Immunological Methods*, **190**, 79-89.
37. P. Maillard, J. P. Lavergne, S. Siberil, G. Faure, F. Roohvand, S. Petres, J. L. Teillaud and A. Budkowska, (2004) Fc gamma receptor-like activity of hepatitis C virus core protein *Journal of Biological Chemistry*, **279**, 2430-2437.
38. Y. H. Zhou, Y. K. Shimizu and M. Esumi, (2000) Monoclonal antibodies to the hypervariable region 1 of hepatitis C virus capture virus and inhibit virus adsorption to susceptible cells in vitro *Virology*, **269**, 276-283.
39. C. C. Chang and R. J. Yang, (2007) Electrokinetic mixing in microfluidic systems *Microfluidics and Nanofluidics*, **3**, 501-525.
40. V. Hessel, H. Lowe and F. Schonfeld, (2005) Micromixers - a review on passive and active mixing principles *Chemical Engineering Science*, **60**, 2479-2501.
41. J. M. Ottino and S. Wiggins, (2004) Introduction: mixing in microfluidics *Philosophical Transactions of the Royal Society of London Series a-Mathematical Physical and Engineering Sciences*, **362**, 923-935.
42. J. O. Foley, A. Mashadi-Hossein, E. Fu, B. A. Finlayson and P. Yager, (2008) Experimental and model investigation of the time-dependent 2-dimensional distribution of binding in a herringbone microchannel *Lab on a Chip*, **8**, 557-564.
43. J. P. Golden, T. M. Floyd-Smith, D. R. Mott and F. S. Ligler, (2007) Target delivery in a microfluidic immunosensor *Biosensors & Bioelectronics*, **22**, 2763-2767.
44. J. D. Kirtland, G. J. McGraw and A. D. Stroock, (2006) Mass transfer to reactive boundaries from steady three-dimensional flows in microchannels *Physics of Fluids*, **18**, -.
45. R. A. Vijayendran, K. M. Motsegood, D. J. Beebe and D. E. Leckband, (2003) Evaluation of a three-dimensional micromixer in a surface-based biosensor *Langmuir*, **19**, 1824-1828.

46. G. C. Randall and P. S. Doyle, (2005) Permeation-driven flow in poly(dimethylsiloxane) microfluidic devices *Proceedings of the National Academy of Sciences of the United States of America*, **102**, 10813-10818.
47. T. M. Squires, R. J. Messinger and S. R. Manalis, (2008) Making it stick: convection, reaction and diffusion in surface-based biosensors *Nature Biotechnology*, **26**, 417-426.